Spring 2021

Novel piezo actuators for surface cleaning

Yezad H. Anklesaria
Missouri University of Science and Technology, yhar56@mst.edu

Department: Mechanical and Aerospace Engineering

NOVEL PIEZO ACTUATORS FOR SURFACE CLEANING

by

YEZAD ANKLESARIA

A DISSERTATION

Presented to the Graduate Faculty of the

MISSOURI UNIVERSITY OF SCIENCE AND TECHNOLOGY

In Partial Fulfillment of the Requirements for the Degree

DOCTOR OF PHILOSOPHY

in

AEROSPACE ENGINEERING

2021

Approved by:

Daniel Stutts, Advisor
Henry Pernicka
Lokeswarappa Dharani
Victor Birman
Wayne Huebner

ABSTRACT

Optical cameras are becoming increasingly common and are used in a variety of applications. With recent progress and transition toward more autonomous systems, the usage of optical systems will be common and widespread. Applications of the optical systems range from autonomous vehicles, home security systems, aviation, extraterrestrial vehicles, spacecraft, and satellites. Imaging systems are used in decision-making in many of these applications. Fouling of the field of view of the imaging system can impede the decision process. An active autonomous cleaning method for the optical surface of the optical systems reliably would be advantageous. The research work focuses on developing a novel piezo actuator that would keep a guard lens on an optical system clean of fouling contaminants using structural harmonic modes. Emphasis is given to camera systems in this work, with the view that the work can be easily expanded to other optical systems based on techniques developed here. The concept developed is to use ultrasonic vibrations and take advantage of the guard lens' structural harmonic modes to remove the contaminants. A process for design, optimization, and prototyping of the systems is presented. The prototype's efficacy is tested with various fluid and solid contaminants. Analytical models are developed in conjunction with this work to help understanding effects of eccentric load acting on circular plate.

ACKNOWLEDGMENTS

It has been many years since I arrived at Missouri University of Science and Technology. I have enjoyed working with several faculty and staff on campus who have helped me from my undergraduate degree to a doctoral degree.

This dissertation culminated in several years of work with Dr. Daniel Stutts on the Ultrasonic Lens cleaning project sponsored by Texas Instruments. I cannot express my gratitude enough toward Dr. Stutts for his guidance during research challenges. His mentorship through several projects over the course of my time at Missouri S&T is invaluable.

I also had the pleasure of working with Dr. Pernicka, who was my master's advisor committee member and mentor. Together, we worked on the satellite program and balloon sat program. My committee members, Dr. L. Dharani, Dr. V. Birman, and Dr. W. Huebner, their subject area expertise, has immensely helped my research. I have utilized every committee member's subject area lectures and in-person discussions in various research aspects.

I would like to acknowledge Texas Instruments (TI) for funding the research and Dr. Stephen Fedigan for his guidance. My sincere thanks to the Mechanical and Aerospace Engineering Department for allowing me to be a GTA, funding part of my education.

Special thanks to members of the Mechanical and Embedded Systems Integration Laboratory and several undergraduate students who have worked with me and helped in the research. It would be a long list to acknowledge every member, but Jacob Zorn, Dalton Stover, and Lauren Tomanek have made vital contributions.

Finally, this work would not have been possible without continuous and robust support from my family and parents, Katty and Hoshang Anklesaria. I am in debt to them for life.

TABLE OF CONTENTS

Page

LIST OF ILLUSTRATIONS

LIST OF TABLES

NOMENCLATURE

Symbol	Description
	Roman
A	Hamaker constant
a	Radius of the Plate
C	Capacitance
C_0	Parallel capacitance in BVD Model
C_1	Capacitance in BVD Model
D	Bending stiffness of the plate
d	Diameter of particle
d_{ij}	Piezoelectric charge constants. i,j=1-6
e	Dielectric constant
F	Test Frequency
f_a	Anti-Resonance Frequency
F_i	Electrostatic imaging force
f_r	Resonance Frequency
F_{cap}	Force due to capillary adhesion
$F_{\text{vdW deform}}$	van der Waals force due to deformation
$F_{\text{vdW total}}$	The total van der Waals force

F_{grav}	Force due to gravity
F_{vdW}	van der Waals force
g	Gravity
h	Thickness of the plate
h_g	Glass thickness
h_n	Normalizing thickness for glass
h_p	Thickness of PZT
h_w	Lifshitz-van der Waals constant
I_p	Peak to Peak Test Current
l	Distance between the charge centers
L_1	Inductance in BVD Model
P	True Power
Q	Reactive Power
q	Generalized force
$Q(r,\theta,t)$	Applied Pressure load
q_c	Charge
Q_m	Mechanical quality factor
r	Radial direction
r_0	Outer radius of the PZT
R_1	Resistance in BVD Model

r_c	Radius of particle
r_g	Radius of the Glass
r_i	Inner radius of the PZT
S	Apparent Power
S_{eqv}	Equivalent Stress in object
t	Time
T_{PZT}	Temperature of PZT
U	Potential difference
$U_3(r,\theta)$	Modal solution in thickness direction of plate
$u_3(r,\theta,t)$	Displacement of plate in thickness direction
V_p	Applied Peak to Peak Test Voltage
w_p	Width of the PZT
z	Atomic separation between the surfaces
$K^T{}_{ij}$	Relative dielectric constant at constant stress.1,j=1-6
$M_{\theta\theta a}$	Piezoelectric Moment load azimuthal
$M_{rr}{}^a$	Piezoelectric Moment load radial
$s^e{}_{ij}$	Elastic compliance at constant E. i,j=1-6

Greek

Δr	Separation of Pressure loads

δ	Unit impulse function
ϵ_0	Permittivity of free space
ϵ_{pzt}	Strain in the PZT
η_{mn}	Modal Participation factor
γ	Surface tension
λ_{mn}	Eigenvalue
∇	Laplacian biharmonic operator
ϕ	Phase lag of applied voltage and current
ρ	Density of contaminant
ρ	Mass density of the plate
ρ	Radius of surface adhesion
σ_E	von-Mises equivalent stress
σ_Y	Yield Strength of the material
σ_{glass}	Stress in the Glass
σ_{matl}	Stress in the Material
σ_{PZT}	Stress in the PZT
σ_{xx}	Normal stress - x direction
σ_{xy}	Shear stress - xy plane
σ_{yy}	Normal stress - y direction
σ_{yz}	Shear stress -yz plane

σ_{zx}	Shear stress - zx plane
σ_{zz}	Normal stress - z direction
θ	Azimuthal direction
u_3	Displacement in the thickness direction

Subscripts

$1, 2, 3$	Principal axis of Piezoelectric material
m	Number of radial node-lines
n	Number of diametrical node-lines
$r, \theta, 3$	Radial, Azimuthal and Thickness orientations

1. INTRODUCTION

Modern automated systems rely on imaging, and optical sensors make an autonomous decision. Atmospheric particulates surround everything and tend to adhere to surfaces. The contamination of optical surfaces is performance-limiting for many applications. The size and amount of contaminants on the optical surface can significantly degrade the image's quality or result in an unusable image. While many terrestrial applications can use some form of mechanical cleaning, such as wipers, removing contamination in harsh or remote environments is a significant challenge. Space systems such as spacecraft, rovers, and other remote surveillance equipment are susceptible to contamination on their imaging systems. These contaminants are likely to remain in place unless an active mechanism is used to clean the surface. The research aims to design, develop, prototype, and test surface cleaning piezo-actuators using structural harmonic modes (SHM).

The work was conducted under the research grant from Texas Instruments (TI) in two phases. In the first phase, work focused on analyzing prototype designs from Texas Instruments in finite element analysis software. The second phase, which forms the basis of this dissertation, focused on designing, building, and testing of prototypes of a guard lens system that would be self-cleaning, utilizing a piezoelectric actuator. A total of five designs were proposed and out of which four were designed, developed, prototyped, and efficacy-tested for potential lens cleaning ultrasonic actuators. Several challenges faced during the process have been detailed, and lessons learned will be useful for developing reliable future designs. Design optimization process was developed in ANSYS to better understand the ultrasonic lens cleaning actuator designs and custom post-processing routines were written to maximize the average surface acceleration in the optical region of the lens. The rationale behind maximizing surface acceleration stemmed from literature review and analysis completed in the phase I report submitted to Texas Instruments in April 2015, wherein it was explained that the principal means of separating contaminants adhering

to the lens surface was the inertial reaction force due to surface acceleration [1]. This conclusion led to the pursuit of designs optimized to operate at megasonic frequencies, but operation at megasonic frequencies presents additional challenges, which are detailed.

1.1. PURPOSE

The physics of the cleaning process is rather complicated, but there are at least two primary considerations: (1) achieving the necessary surface excitation to transfer sufficient energy to separate contaminants from the lens surface, and (2) achieving adequate distribution of the surface excitation to avoid contaminant accumulation in regions of low excitation – vibration nodes.

It was proposed to develop a cleaning system primarily independent of the surface that needs to be cleaned. This effort would result in designs that are easily adaptable to other systems. Since the primary applications of the ultrasonic cleaning actuator are geared towards cameras, a generic camera housing, suggested by TI, was modified to accommodate the proposed actuator designs. The camera housing design provided by TI is shown in Figure 1.1. Figure 1.2 shows the modified housing accommodating the actuator and lens cover. In all design optimizations, the camera housing dimensions shown in Figure 1.3 are kept constant.

1.2. DISSERTATION ORGANIZATION

Following the introduction, this work is organized into eight additional parts. To cover various aspects of the design and development process and to present analytical models developed.

- Section 2: focuses on literature and work done prior to this in areas of surface cleaning and adhesion forces.

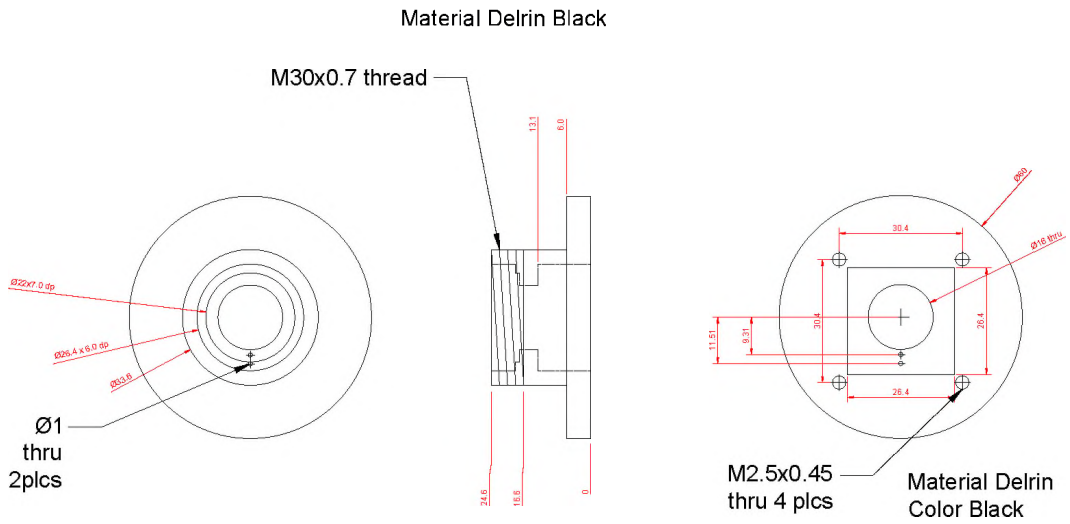

Figure 1.1. Camera Housing

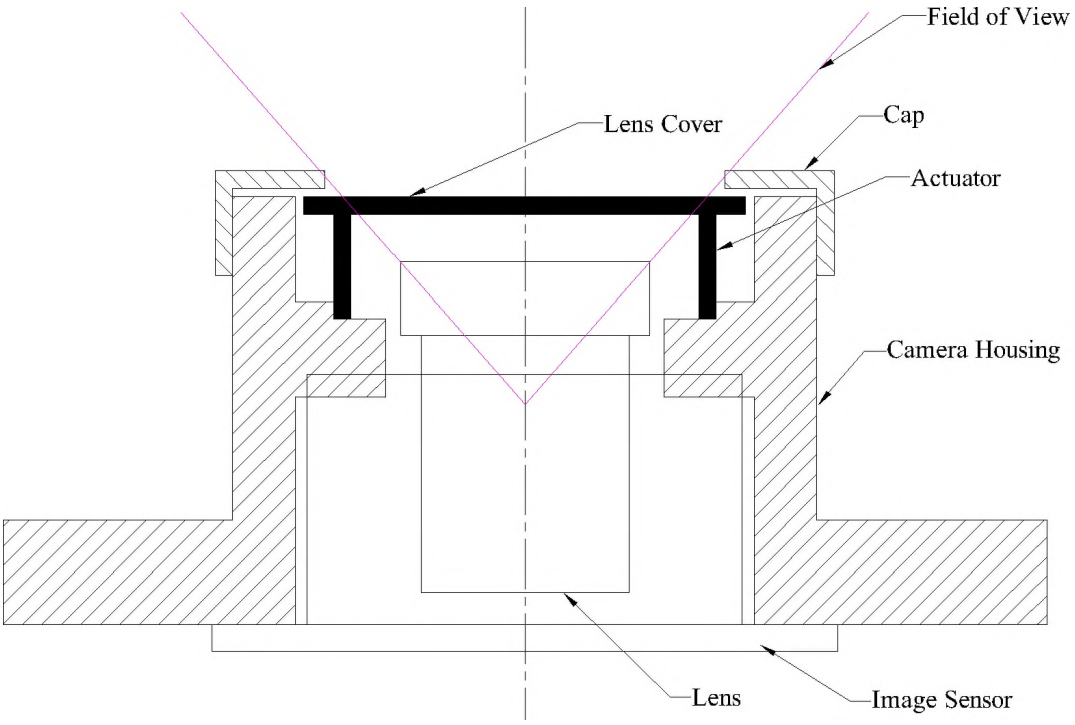

Figure 1.2. Modified Camera Housing

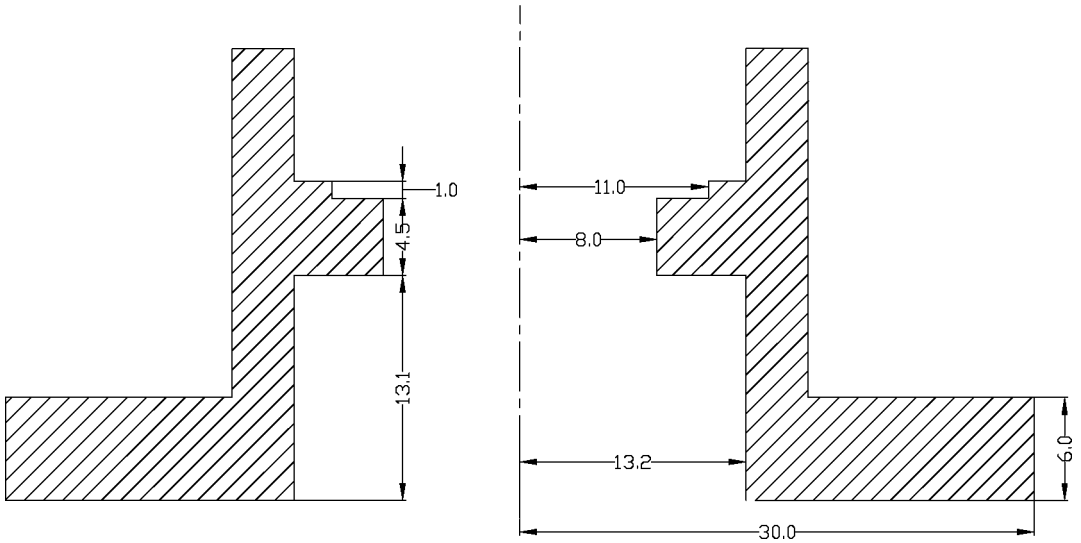

Figure 1.3. Camera Housing Dimensions in mm

- Section 3: covers the proposed designs to take advantage of structural harmonic modes to clean the surface of glass.
- Section 4: details the finite element analysis (FEA) procedure, optimization techniques and custom routines developed in FEA to design the actuator.
- Section 5: includes materials, manufacturing processes and failure modes of the materials.
- Section 6: discusses the prototype build and testing.
- Section 7 and 8: covers analytical methods to analyze eccentric pressure and moment load on a thin circular shell.
- Section 9: discusses the future work and concluding remarks on the designs.

2. LITERATURE REVIEW

There are three critical areas of interest: surface adhesion forces, surface cleaning techniques, and power electronics. The primary purpose of this research is to focus on the first two areas. A discussion of the relevant literature is provided in this section.

2.1. SURFACE ADHESION FORCES

Contaminants are all around in the atmosphere, and they are generated by a variety of means such as abrasion, chemical reaction, combustion process, human activities, etc. A fouling contaminant on a camera's optical path can lead to detrimental effects from low quality or partially blocked images to completely unusable images. Moreover, as systems rely heavily on optical devices to automate the processes and keeping the field of view of the optical device free of contaminants is essential. Contaminants tend to adhere to surfaces. The adhesion force between the contaminant and surface can be much higher than the gravitational force on the contaminant. Even inverting the surface would not lead to the removal of the contaminant [2]. Contaminants can be classified into three broad categories of solid, liquid, and mixture. Contaminants of the mixture category are primarily governed by liquid adhesion forces [3]. In nature, contaminant particles are nearly always in some mixture state and rarely in pure solids or liquids. Forces involving mixtures are difficult to quantify and classify if the adhesion is governed by liquid or solid adhesion force. In the study of adhesion forces, the literature focuses on solids or liquids. The influence of liquid or moistening of solid particles is also considered [2, 3]. Therefore, it is essential to understand what forces are involved and the magnitude of the forces involved as well as their relationship to the surface and contaminants.

Measuring adhesion forces is difficult as they are generally very small in magnitude. Adhesion forces are dependent on the particle size, type, and surface on which the particle rests. This requires several different contaminants and surfaces to be tested to capture

the complete adhesion force spectrum. There are no physical models to fully predict the adhesion force of a particle on a surface [2]. Adhesion strength is a combination of physical and chemical forces and mechanical stress and strain around the particle and surface interface. The forces involved in surface adhesion of a solid particle contaminant are the van der Waals forces, electrostatic forces, and magnetic forces [2, 4, 5, 6]. Van der Waals forces and electrostatic forces are the primary forces of attraction. Van der Waals forces are dominant for particles smaller than 50 microns, whereas the electrostatic forces are more important for larger particles [2]. Electrostatic contact potential (electrical double layer force) and excess charge image force are two subtypes of electrostatic forces [2].

2.1.1. Van der Waals Force. The polarization of atoms and molecules in a material containing dipoles and quadrapoles causes force between molecules. These also include both natural as well as induced instantaneous dipoles and quadrapoles [2]. This force is part of the van der Waals forces. Also included are nonpolar attractive forces, which are also known as London-van der Waals dispersion forces. London associated this force with the cause of optical dispersion [3]. The dispersion forces make a significant contribution to the intermolecular force, except when the polarizability is small and the dipole moment is large. These forces are considered to be additive for a combination of atoms and molecules, which is assumed in the Hamaker method. The Hamaker method uses a so-called Hamaker constant, A. The addition of forces has a limitation; it does not consider cross-correlation of charge. Lifshitz developed a better approach. Lifshitz started from the bulk optical properties of interfacing materials [3]. The Lifshitz-van der Waals constant, h_w, is defined as an integral function of the imaginary parts of the dielectric constants of the adhering materials [2]. At a very small distance between particle and surface, the Lifshitz-van der Waals constant, h_w, is related to material properties alone. The Lifshitz-van der Waals constant can be related to the Hamaker constant in some instances using Equation (2.1).

The Lifshitz-van der Waals constant ranges from 0.6 to 9.0 eV depending on the materials involved. The more absorptive the material means, the stronger the spontaneous fields, which results in larger van der Waals forces. The van der Waals force, F_{vdW}, per unit area between two parallel flat surfaces is given by Equation (2.2). In Equation (2.2), z is the atomic separation between the surfaces. Equation (2.2) can be further reduced to Equation (2.3) for a flat surface and a particle of radius, r.

$$h_w = \frac{4\pi A}{3} \tag{2.1}$$

$$F_{vdW} = \frac{h_w}{8\pi^2 z^3} \tag{2.2}$$

$$F_{vdW} = \frac{h_w r_c}{8z^2} \tag{2.3}$$

The force F_{vdW} in Equation (2.3) is the force necessary to remove the particle. Substituting diameter for radius and assuming separation distance, z, of 4 angstroms. The Equation (2.4) becomes:

$$F_{vdW} = 2 \times 10^{-8} h_w d \tag{2.4}$$

Table 2.1 shows the typical ranges of the constant h for some materials and the force per unit area for particle sizes in the range of 1 micron and 100 microns. These forces are large enough to deform the surface.

Table 2.1. Lifshitz-van der Waals Constant and Force Per Unit Area for 1 micron and 100 micron Particles [3]

Surface	Particle	h_w[eV]	F_{vdW} [dyne/cm^2] d = 1 micron	F_{vdW} [dyne/cm^2] d = 100 micron
Polymer	Polymer	0.6-0.9	1.78×10^5	1.78×10^6
Alumina	Alumina	4	1.02×10^9	1.02×10^7
Ge	Ge	6.6-7.6	1.81×10^9	1.81×10^7
Si	Si	6.8-7.2	1.78×10^9	1.78×10^7
Ge	Si	7.5	1.91×10^9	1.91×10^7
Graphite	Graphite	7.2	1.83×10^9	1.83×10^7
Graphite	Si	6.8	1.73×10^9	1.73×10^7
Cu	Cu	8.5	2.16×10^9	2.16×10^7
Ag	Ag	9.0	2.29×10^9	2.20×10^7

The additional van der Waals force due to deformation, $F_{\text{vdW deform}}$, is a function of the increased contact area caused by the deformation and is given by Equation (2.5). In Equation (2.5), ρ is the radius of the adhesion surface area in microns. For a z of $4A$, the equation becomes Equation (2.6).

$$F_{\text{vdW deform}} = \frac{h_w \rho^2}{8\pi z^2} \tag{2.5}$$

$$F_{\text{vdW deform}} = 9.96 \times 10^{-2} h_w \rho^2 \tag{2.6}$$

The total van der Waals force, $F_{vdWtotal}$, is given by Equation (2.7).

$$F_{\text{vdW total}} = F_{vdW} + F_{\text{vdW deform}} \tag{2.7}$$

Figure 2.1 shows van der Waals forces as a function of particle diameter for a graphite surface and silicon particle, with a Lifshitz-van der Waals constant of 6.8 eV and deformation forces for 1% and 5% radius of the adhesion surface area. If the particle is flattened and the particle's point contact is increased, the resulting contact radius is known as the radius of adhesion, as seen in Figure 2.2.

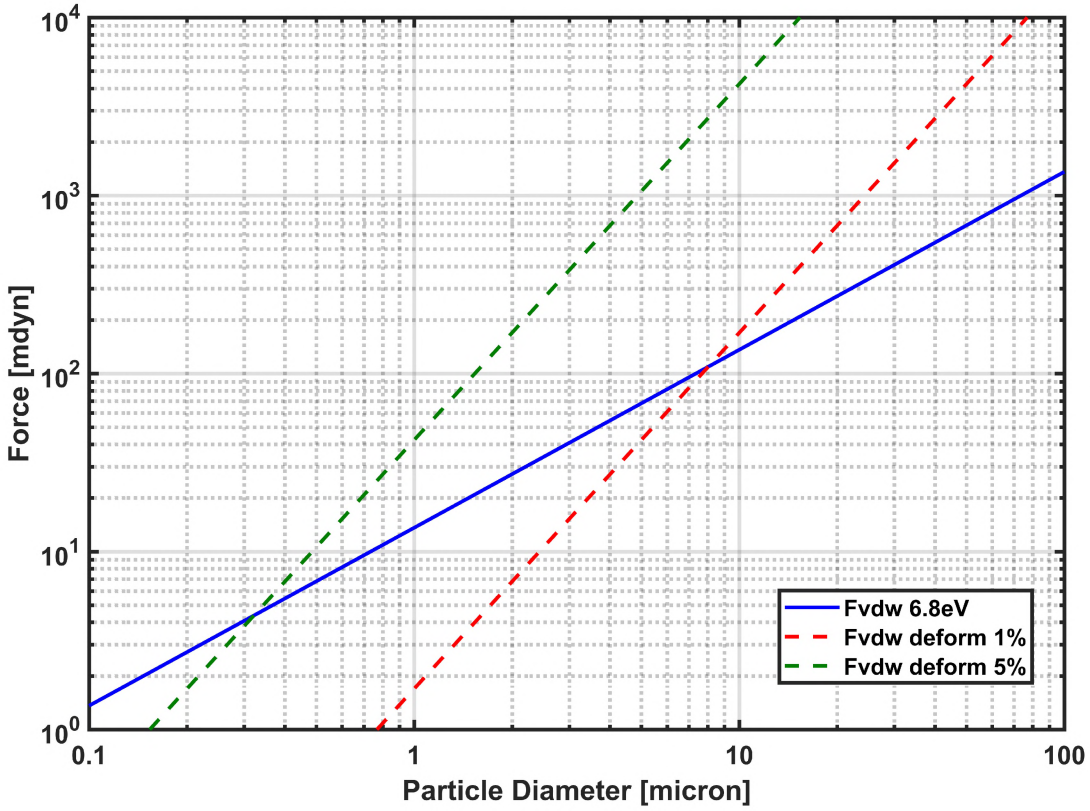

Figure 2.1. Van der Waals Force as a Function of Particle Diameter for Graphite-Silicon System

2.1.2. Electrostatic Force. As stated in Section 2.1, the electrostatic forces are comprised of two forces: contact potential double-layer force and imaging force. The electrostatic forces predominantly affect larger particles [5, 7]. The imaging electrostatic force arises from bulk excess charges on the particles that cause coulombic attraction to a surface. The imaging force is given by Equations (2.8) and (2.9) [2, 7]. In these equations, q_c is the charge, ϵ_0 is the permittivity of free space, e is the dielectric constant of the medium

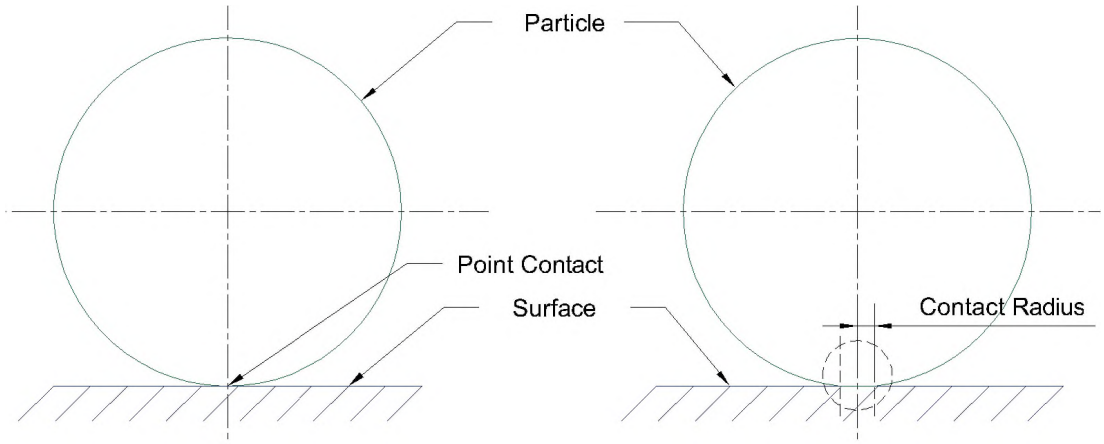

Figure 2.2. Particle with Point Contact and 10% Contact Radius with Surface

between the particle, l is the distance between the charge centers, C is the capacitance, and U is the potential difference in volts. The capacitance here has been expressed as a function of radius, r, via an approximation of the Euler equation [3].

$$F_i = \frac{{q_c}^2}{4\pi\epsilon_0 e l^2} \tag{2.8}$$

$$q_c = CU = 4\pi\epsilon_0 r U \tag{2.9}$$

$$F_i = 3 \times 10^{-2} d^2 \tag{2.10}$$

The other electrostatic force that is predominant on small particles is the electrostatic contact potential induced electric double-layer force. The two materials in contact develop a contact potential caused by the difference in local energy and work functions. Electrons flow from one material to the other until the potential charge equilibrium is reached. The resulting potential difference is called a contact potential, U, which generally ranges from 0 V to about 0.5 V. The electrostatic double-layer force can be calculated using Equation

(2.11). For a maximum potential difference of 0.5 V, the electrostatic double-layer force is approximated by Equation (2.12). Figure 2.3 compares the electrostatic force to the van der Waals forces for the graphite-silicon system. Figure 2.3 shows that the van der Waals forces dominate over electrostatic forces for very small particles. Double layer electrostatic forces also generally dominate over electrostatic image forces for small particles.

$$F_{el} = \frac{\pi \epsilon_0 r_c U^2}{z} \tag{2.11}$$

$$F_{el} = 4dU^2 \tag{2.12}$$

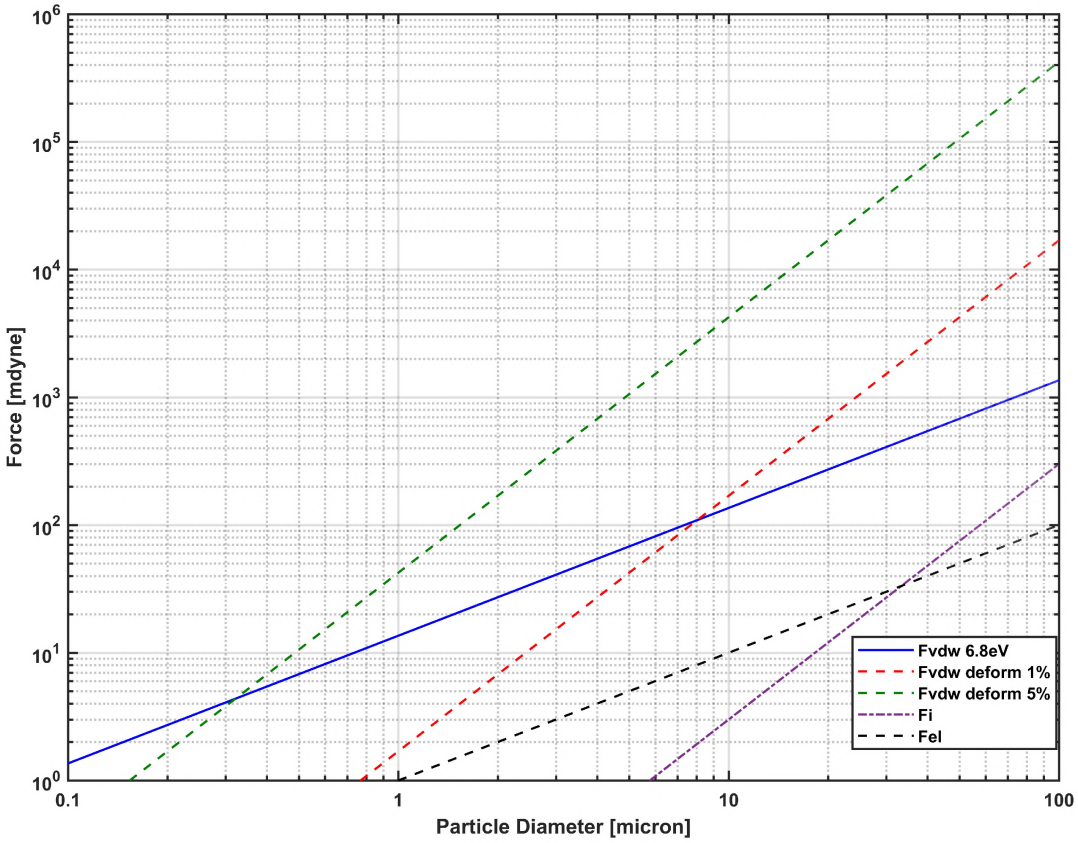

Figure 2.3. Comparison of Electrostatic Forces to van der Waals Force for Graphite Silicon System

Therefore, the total force to overcome the attraction between the contaminant and the surface is a summation of the Van der Waals Forces and the electrostatic forces.

The gravitational force on a particle is calculated using Equation (2.13). The total force and ratio of the total force to the gravitational force as a function of particle diameter are shown in Figure 2.4. The gravitational force never exceeds the total adhesion force for a dry system [3].

$$F_{\text{grav}} = \frac{4}{3}\pi r_c^3 \rho g \tag{2.13}$$

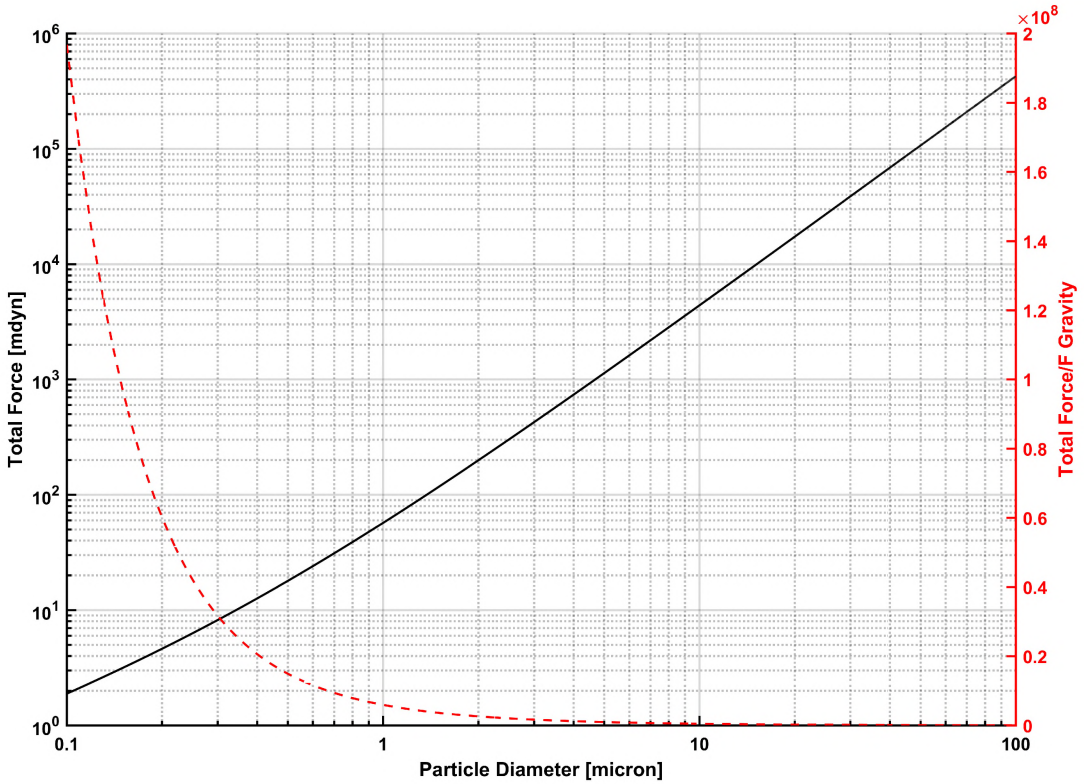

Figure 2.4. Total Adhesion Force and Ratio of Total Force to Gravitational Force as a Function of Particle Diameter

2.1.3. Effects of Humidity and Liquid on Adhesion. The calculated total adhesion force considers the system to be completely dry. If the contaminant is exposed to high humidity or if the surface system has been immersed and then withdrawn from a liquid,

a liquid film can form by capillary action between the particle and surface. The capillary force, given by Equation (2.14), can be significant and is a function of the particle radius, r, and surface tension, γ.

$$F_{\text{cap}} = 4\pi r_c \gamma \tag{2.14}$$

The capillary force may remain even after heating above the boiling point of the liquid [3]. The capillary force can be significantly higher than the van der Waals force.

For fluid contaminants, the essential parameters to be considered with respect to atomization are surface tension and viscosity [8, 9]. From the results of experimentation and literature, it can be concluded that the smaller the droplet size, the higher the frequency needs to be to atomize the droplet [8, 10]. The process of atomization is complex. First, a wave forms in the fluid, then capillary peaks form, and finally, atomization of the fluid occurs [11].

From these articles, it can be inferred that solid particles are mainly dependent on van der Waals forces, and require surface acceleration magnitudes inversely proportional to the particle diameter, and that fluid nebulization is best accomplished at higher frequencies.

2.2. CLEANING TECHNIQUES

Numerous authors examined several different methods of removing surface contaminants. Most of the papers focused on removing particles from semiconductor substrates [2, 5, 7, 12, 13]. It was determined that the best method to remove particles was an indirect method. It was also found that blowing pressurized fluid would not remove small particles and would be challenging to implement; thus, vibrational actuation was chosen [4, 7, 14]. One current application of vibrational actuation to remove particles is used in DSLR cameras that excite bending vibrations to remove dust particles. Olympus Optical Co. holds

several patents for dust removal mechanisms that use piezoelectric elements bonded to a glass light filter [15, 16]. No literature primarily focuses on fluid particle removal. There are, however, several articles discussing the nebulization of fluid for medical and chemical applications. Another method of atomizing fluid is the use of surface acoustic wave (SAW) actuators. SAW actuators can be used for a variety of particle sizes as the driving frequency can be changed. However, it was found that small particles have a weak dependency on the large driving frequency needed to atomize the fluid [17].

3. PROPOSED SURFACE CLEANING ACTUATOR DESIGNS

Early in the project, several potential design options were developed. After careful consideration, five unique designs were chosen and are described and shown in this section. Only the mechanical design, optimization variables, and procedures are described here.

3.1. SINGLE PZT SYSTEM (SPS)

The Single PZT System (SPS) design is the simplest compared to the other designs because it involves a single ring PZT element bonded to the glass, as shown in Figure 3.1. The design only requires a single phase drive signal, with the top and bottom electrodes connected to the signal and ground, respectively. The signal is DC-biased to reduce the tensile stress experienced by the PZT to extend the life of the PZT since repeated tensile stress cycles on PZT are undesirable. The magnitude of the DC-bias applied is dependent on whether a thickness or longitudinal mode is driven. The applied bias will oppose the motion of PZT such that it experiences a net-zero strain. When driving primarily in the thickness mode, the bias in the longitudinal direction seems desirable. However, when driving in the transverse effect, the opposite bias is preferred. There are a total of eight variables involved in this design, which are listed in Table 3.1. Out of the eight, there are only three mechanical design variables: the inner diameter, R_o, width, w_p, and thickness, h_p, of the PZT ring are optimized. The fourth variable is the DC-bias voltage, V_0, and is optimized to keep the effective stress in the PZT compressive in the desired mode actuation direction.

Table 3.1. Single PZT System (SPS) Design Parameters

Parameter	Description	Variable Type
R_i	Inner Radius of PZT	Optimized
R_o	Outer Radius of PZT ($R_o = R_i + W_p$)	Derived
R_g	Radius of Glass	Fixed
w_p	Width of PZT	Optimized
h_g	Thickness of Glass	Fixed
h_p	Thickness of PZT	Optimized
V_0	DC-bias Voltage	Optimized
V	Driving Voltage	Fixed

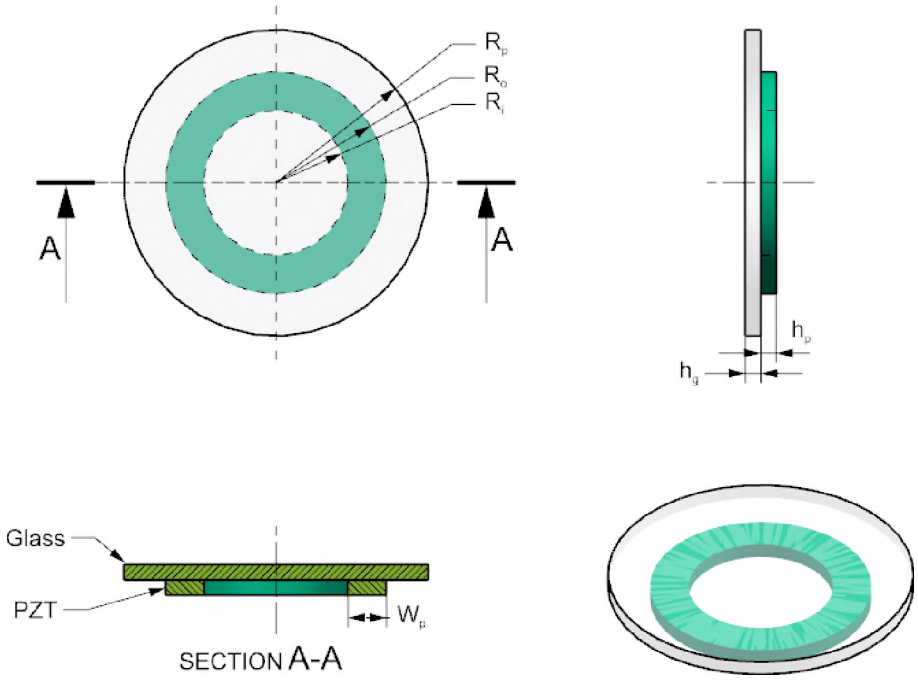

Figure 3.1. Single PZT System - SPS

3.2. MASS LOADED SINGLE PZT SYSTEM (MPS)

The mass loaded single PZT system (MPS) design is a modification of the SPS design. The MPS design has an additional steel ring bonded to the bottom of the SPS design's PZT, as shown in Figure 3.2. This design also only requires a single drive signal and is driven similarly to the SPS. There are a total of nine variables involved in this design, which are listed in Table 3.2. The MPS design has five optimized design variables. In

addition to the four variables optimized for the SPS design, the thickness of the mass, h_m, is also optimized. The additional mass's main advantage is to minimize the in-plane (radial) motion of the PZT and provide an inertial reaction for PZT to act against.

Table 3.2. Mass Loaded PZT System (MPS) Design Parameters

Parameter	Description	Variable Type
R_i	Inner Radius of PZT	Optimized
R_o	Outer Radius of PZT ($R_o = R_i + W_p$)	Derived
R_g	Radius of Glass	Fixed
w_p	Width of PZT	Optimized
h_g	Thickness of Glass	Fixed
h_p	Thickness of PZT	Optimized
h_m	Thickness of Mass	Optimized
V_0	DC-bias Voltage	Optimized
V	Driving Voltage	Fixed

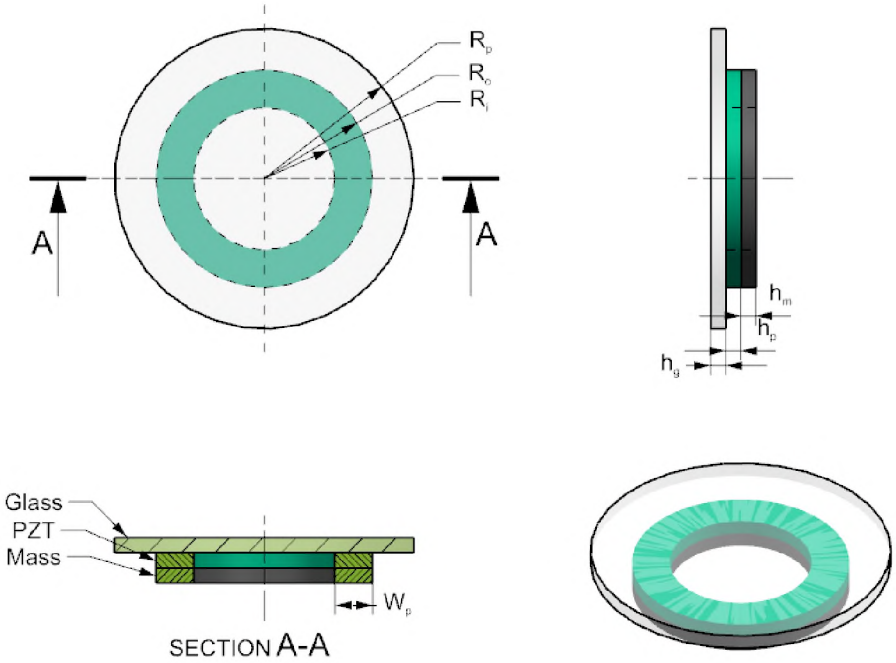

Figure 3.2. Mass Loaded Single PZT System - MPS

3.3. RADIALLY-SPLIT PZT SYSTEM (RPS)

This design can be realized in two ways: (1) using two PZT rings or (2) a split electrode on a single PZT element. This design's potential utility is the ability to drive two segments either in or out of phase, thereby exciting two axisymmetric modes of the PZT: one at a lower and the other at a higher frequency. When driven out-of-phase, a higher-frequency axisymmetric mode having a radial node line coincident with the separation between the two PZT rings, or the split in the electrode, is created. When driven in phase, a lower-frequency axisymmetric mode with a radial half-wavelength corresponding to the combined electrode width can be excited. In theory, by alternating between these two modes of excitation, potential radial node lines where contaminants might accumulate can be reduced or eliminated. This design allows for selecting variable widths of the two PZT rings or the two electrodes. The principal manufacturing challenge inherent in using two separate PZT rings is the difficulty in manufacturing rings thin enough and the subsequent concentric alignment of each. Presently, due to the relatively small size of the lens, it was found that the use of two separate PZT rings was unfeasible. Figure 3.3 and Table 6.13 show the design and optimized design parameters corresponding to RPS design respectively.

Table 3.3. Radially Split PZT System (RPS) Design Parameters

Parameter	Description	Variable Type
r_i	Inner Radius of PZT	Optimized
w_{p1}	Width of inner PZT ring	Optimized
w_{p2}	Width of outer PZT ring	Optimized
w_g	Gap between PZT ring or separation of electrodes	Optimized
r_o	Outer Radius of PZT ($r_o = r_i + w_{p1} + w_g + w_{p2}$)	Derived
r_g	Radius of Glass	Fixed
h_g	Thickness of Glass	Fixed
h_p	Thickness of PZT	Optimized
h_m	Thickness of Mass	Optimized
V_0	DC-bias Voltage	Optimized
V	Driving Voltage	Fixed

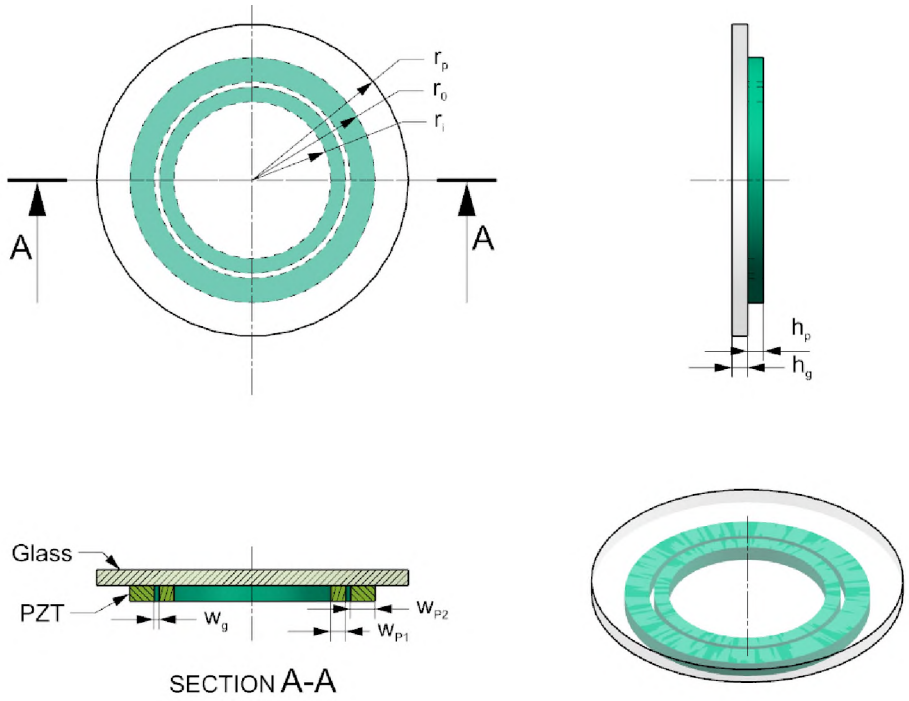

Figure 3.3. Radially-Split PZT System-RPS

3.4. SUPPORT-DRIVEN SYSTEM (SDS)

The support driven system (SDS) is a modification of the MPS design. The SDS has PZT elements bonded to the upper and lower surfaces as well as masses on each PZT element. The PZT ring elements are excited by an alternating voltage in such a manner that they expand and contract 180 degrees out-of-phase with one another, thereby inducing standing axisymmetric transverse bending waves in the glass corresponding to one or more of the higher frequency modes of the system. Figure 3.4 shows the SDS design and Table 3.4 provides the key parameters for optimization.

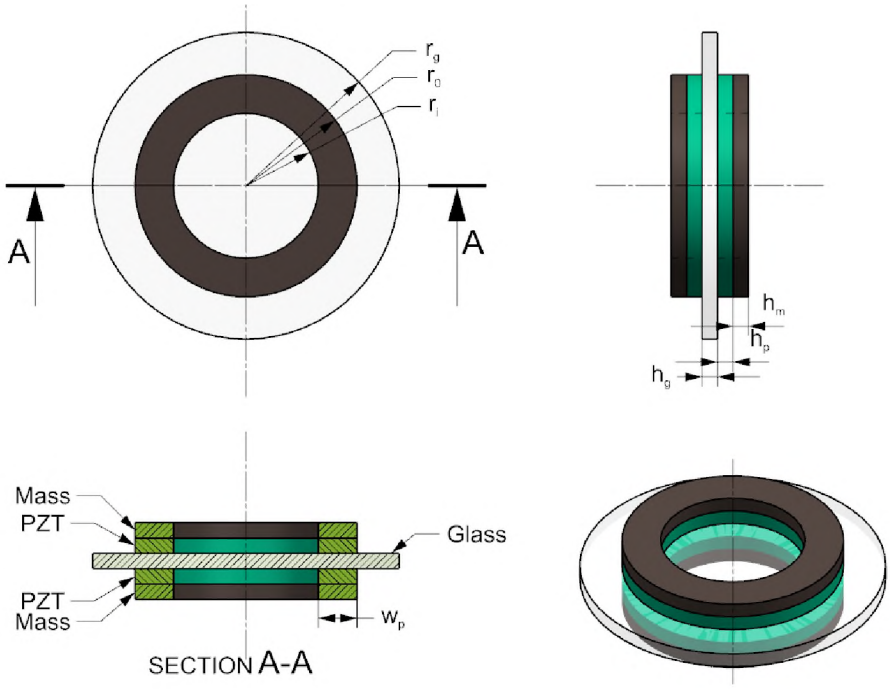

Figure 3.4. Support-Driven System-SDS

Table 3.4. Support Driven System (SDS) Design Parameters

Parameter	Description	Variable Type
r_g	Radius of Glass	Fixed
r_i	Inner Radius of PZT	Optimized
r_o	Outer Radius of PZT ($r_o = r_i + w_p$)	Derived
w_p	Width of PZT ring	Optimized
h_g	Thickness of Glass	Fixed
h_p	Thickness of PZT	Optimized
h_m	Thickness of Mass	Optimized
V_0	DC-bias Voltage	Optimized
V	Driving Voltage	Fixed

4. FINITE ELEMENT ANALYSIS AND OPTIMIZATION

The analysis of the lens cleaning actuator is a complex problem. Analytical solutions are limited to simple geometries, so the use of FEA is justified for the problem under investigation. ANSYS is an industry-standard FEA software that is capable of performing dynamic coupled-field analysis [18]. The coupled-field analysis technology allows solutions of multi-physics problems. In this investigation, mechanical and electrical problems are solved simultaneously. Therefore, ANSYS was chosen. Another reason to work with ANSYS is that it is the primary finite element analysis software available at Missouri S&T with a full research suite license and high-performance computing.

4.1. MODEL GEOMETRY AND ELEMENT SELECTION

Early in the analysis formulation phase of the research, it was decided to perform a full three-dimensional (3-D) analysis. The use of a full 3-D solution provided maximum insight into the cleaning action of the actuator. As details were added, the finite element models grew larger and more complex. One of the significant impacts on model size is the need to analyze designs in megasonic frequencies. Since all designs are axisymmetric, a simpler 2-D axisymmetric analysis was possible. This allowed for smaller models and the ability to analyze designs in high megasonic frequencies. Therefore, both 3-D elements and 2-D elements were selected for this research. Higher-order quadratic elements are chosen to represent the model and to allow for quadratic deformation in the design.

4.1.1. SOLID226. ANSYS SOLID226 is a 3-D 20-node coupled-field element. The element has five degrees of freedom per node. Structural capabilities include elasticity, plasticity, viscoelasticity, viscoplasticity, creep, large strain, large deflection, stress stiffening effects, and pre-stress effects. The element has multi-field capabilities, including

piezoelectric. Details on the element can be found in the ANSYS Mechanical APDL Element reference document [19]. The geometry of the SOLID226 can be seen in Figure 4.1. SOLID226 is used to model the piezoelectric elements in the analysis.

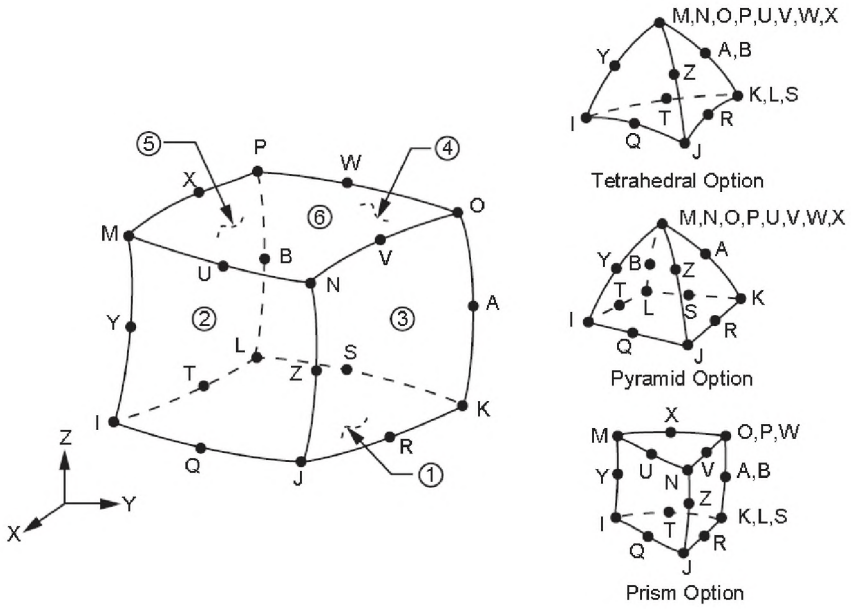

Figure 4.1. SOLID226 and SOLID186 Geometry [19]

4.1.2. SOLID186. ANSYS SOLID186 is a higher-order 3-D 20-node structural element. SOLID186 exhibits quadratic displacement behavior. The element supports plasticity, hyperelasticity, creep, stress stiffening, large deflection, and large strain capabilities. It also has mixed formulation capability for simulating deformations of nearly incompressible elastoplastic materials and fully incompressible hyperelastic materials. Details on the element can be found in the ANSYS Mechanical APDL Element reference document [19], and the geometry of the SOLID186 can be seen in Figure 4.1. It is used to model all non-piezoelectric components in the analysis.

4.1.3. PLANE223. ANSYS PLANE223 is a higher-order 2-D 8-node coupled-field element. The element has 8-nodes with up to four degrees of freedom per node. PLANE223's structural capabilities include elasticity, plasticity, hyperelasticity, viscoelasticity, viscoplasticity, creep, large strain, large deflection, stress stiffening effects, and

pre-stress effects. It also has mixed formulation capability for simulating deformations of nearly incompressible elastoplastic materials and fully incompressible hyperelastic materials. PLANE223 can be used to simulate plane stress, plane strain, and axisymmetric behavior. It also supports birth and death analysis, large deflection, large strain, a linear perturbation in piezoelectric analysis, nonlinear stabilization, and stress stiffening. Details on the element can be found in the ANSYS Mechanical APDL Element reference document [19]. The geometry of the SOLID186 can be seen in Figure 4.2. PLANE223 is used to model the piezoelectric element in the 2-D analysis.

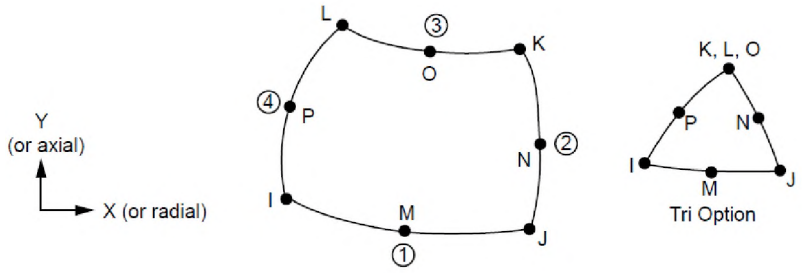

Figure 4.2. PLANE223 and PLANE183 Geometry [19]

4.1.4. PLANE183. ANSYS PLANE183 is a higher-order 2-D 6-node element. PLANE183 supports birth and death analysis, large deflection, large strain, linear perturbation in piezoelectric analysis, nonlinear stabilization, stress stiffening, fracture parameter calculation, material force evaluation, initial state, and rezoning. PLANE183 can be used to simulate plane stress, plane strain, plane stress with thickness, generalized plane strain, and axisymmetric behavior. Details on the element can be found in the ANSYS Mechanical APDL Element reference document [19]. Figure 4.2 shows a PLANE183 element. PLANE183 is used to model glass and other non-piezoelectric design geometries in the analysis.

4.1.5. Contact Element. The analysis applied in this study used contact elements to simulate the bond between different design components. ANSYS Workbench is allowed to select the contact element automatically, and the only parameter modified in the contact element is normal stiffness. The normal stiffness is governed by the type of contact and is based on the recommendation from the ANSYS contact element guide [20].

4.2. DESIGN ANALYSIS

This section describes the type of analysis performed, optimization strategy, and custom result algorithms developed and used in the design evaluation.

4.2.1. Mesh. The general emphasis was given to use Quadrilateral element Mapped Mesh (QMM) in all of the analyses. QMM is used in PZT elements, glass, and additional mass elements. Extremely fine mesh is used for any of the optimized designed bodies. The mesh element size used for each design analysis varies from 0.1 mm to 0.0001 mm. Since the camera housing is not a significant part of the actuator design, some of the models incorporated Free Quadrilateral Mesh (FQM) to reduce the number of elements and nodes in the model. The mesh element size used for the camera housing varies from 0.5 mm to 0.01 mm. Paving mesh strategy was used in meshing the camera housing; it involves using fine mesh where actuator design elements interact with the camera housing and then gradually increasing mesh size away from the design elements. The number of elements and nodes used in a design is directly related to the frequency span of interest. Modal analysis is the primary tool used to determine the natural frequency of the structures, and the number of natural modes extracted is directly proportional to the degrees of freedom in the finite element model [21]. A mesh convergence study is performed on each design model space similar to the ones outlined in Phase 1 of the project [1]. Since the meshing method used is based on model dimensions during each optimization pass, the mesh is updated to reflect

the design changes. This technique's advantage is that the ratio of the number of nodes to the per-unit length determined in the convergence study remains constant for a given dimension in each design optimization.

4.2.2. Type of Analysis. There are several analysis methods involved in solving a complex actuator problem. The four types of analysis of primary interest to the design effort are listed below.

- Static Analysis: Static analysis is the most common FEA analysis. It helps determine stress, strain, and displacement state under constant loading. This analysis is primarily used to determine pre-stress effects in design, due to either mechanical pre-load or DC-bias.

- Modal Analysis: Modal analysis is used to determine the natural modes (free-mode shapes) of the structure. It also calculates the modal participation factor in the primary axes of the structure for each of the modes. The modal participation factor can be used to determine the primary forcing axis, which would result in a maximum structural response. Modal analysis is used in conjunction with static analysis to determine the pre-stressed mode shapes of the structure.

- Harmonic Analysis: Harmonic analysis is used to determine the structure's response due to harmonic forcing. The harmonic analysis accounts for the pre-stressed effects in the solutions from a previous static analysis. Harmonic analysis can be performed by two methods: (a) Mode Superposition or (b) Full Harmonic Solution.

    - Mode Superposition method relies on modal analysis to calculate the harmonic response. It is a fast method of solution. One of the severe limitations of this method is the need to calculate a larger number of modes. A requirement to accomplish this analysis is that the lowest mode of all the calculated modes by the modal analysis must have a frequency of 1.5 times that of the frequency where the harmonic response is required [21]. For example, calculating a response

at 100 MHz would require that all of the modes up to 150 MHz be calculated in modal analysis. Since designs are optimized at megasonic frequencies to perform the mode superposition solution, the number of modes required can range from a couple of hundred to a couple of thousand modes.

- Full Harmonic Solution calculates the steady-state frequency response at the desired frequency. This method is computationally expensive and slow. The designs optimized for this project have been solved primarily using this method.

- Transient Analysis: Transient analysis is a full time-stepping method that allows the user to define non-periodic time-dependent loads. This method is computationally the most expensive method of all of the analysis methods. It would be useful when simulating multi-frequency designs, multiple time-dependent forcing conditions, or understanding the actuator's transient behavior.

4.2.3. Boundary Conditions and Forcing. The boundary conditions and loads are similar for each design; the only difference is in implementing them for each design as they are dependent on the design goals. As an example, the SDS design boundary conditions are shown in Figure 4.3. The boundary conditions are as follows:

1. Fixed Support: The nodes at the base of the camera housing are fixed to simulate being held in place at one location, so fixed support constraint is applied to eliminate motions from all degrees of freedom.

2. Frictionless Support: This constraint is applied to represent the axisymmetry of the model, and in a full 3-D model, the nodes at the center would not be allowed to move in the radial direction. Frictionless support constrains the nodes in the normal direction to the applied edge, but allows the body to deform and displace in the tangential or azimuthal direction.

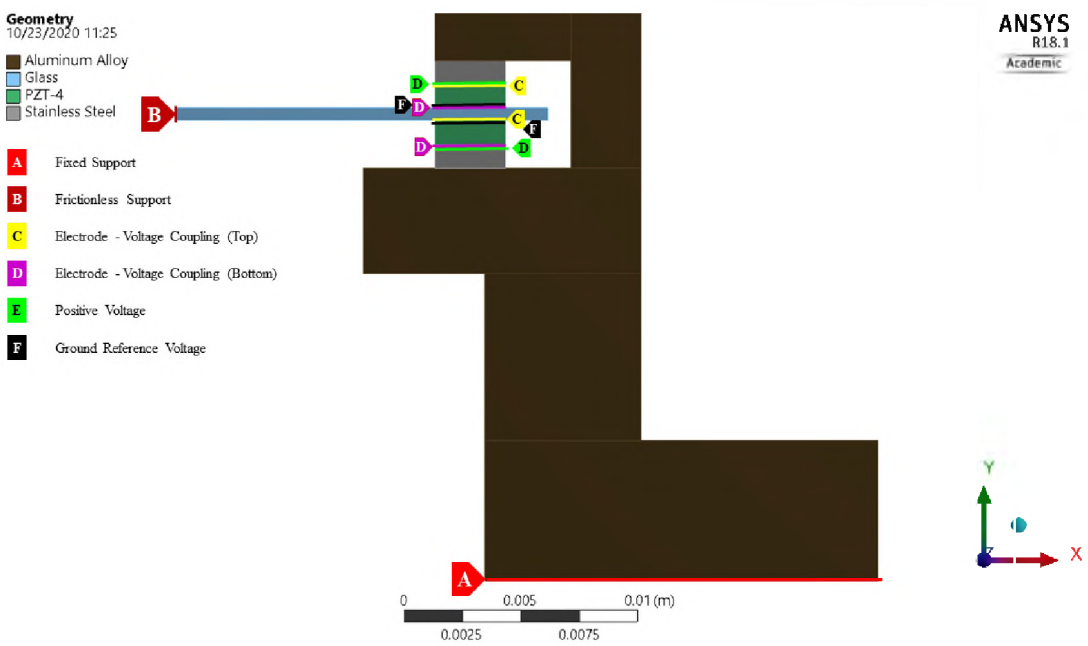

Figure 4.3. Boundary Conditions on SDS Model

3. Electrode Voltage Coupling: The electrodes on the PZT are represented by coupling the voltage degree of freedom on the PZT. All the nodes share a common node, allowing the edge to behave electrically as one, while mechanically still free to deform on its own.

4. Positive Voltage: This is the positive voltage forcing applied to the PZT via the coupled master node. The application of positive voltage to an electrode is dependent on the design under analysis. The DC-bias is applied to this coupled master node and optimized in static analysis to create pre-stress. In the case of harmonic analysis, a fixed voltage of 100 V_p is applied in all the designs as a positive voltage. The phase of the voltage applied is usually 0 degrees, unless a particular actuation sequence needs to be achieved; in that case, the phase applied may be 180 or 90 degrees.

5. Ground Reference Voltage: The negative or reference voltage is applied through this forcing. In all designs for both static and harmonic analysis, the applied voltage is 0 V_p.

The Figure 4.4 shows the boundary conditions and force applied to the four actuator designs in research. All designs have the common boundary condition of fixed support at the camera base and frictionless support at the glass center. The voltage couplings for each of the four designs are shown in Figures 4.4a, 4.4b, 4.4c and 4.4d for SPS, RPS and SDS designs respectively.

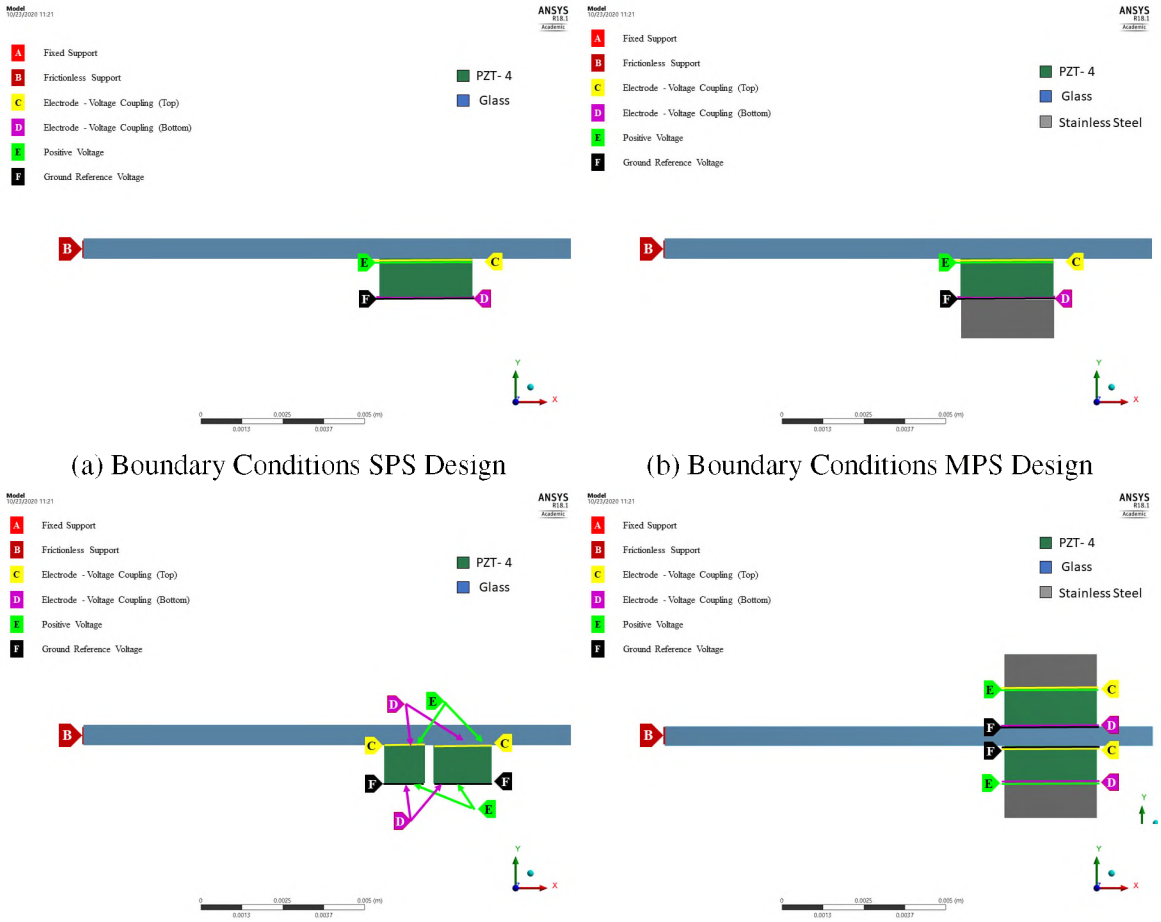

(a) Boundary Conditions SPS Design

(b) Boundary Conditions MPS Design

(c) Boundary Conditions RPS Design

(d) Boundary Conditions SDS Design

Figure 4.4. Actuator Design Boundary Conditions and Forcing

4.2.4. Design Optimization. Optimization of a design requires several types of analysis to be performed in combination to capture the design's behavior completely. Figure 4.5 displays a summary of the optimization. The analysis chain in the second row of the process diagram is used primarily to optimize the designs.

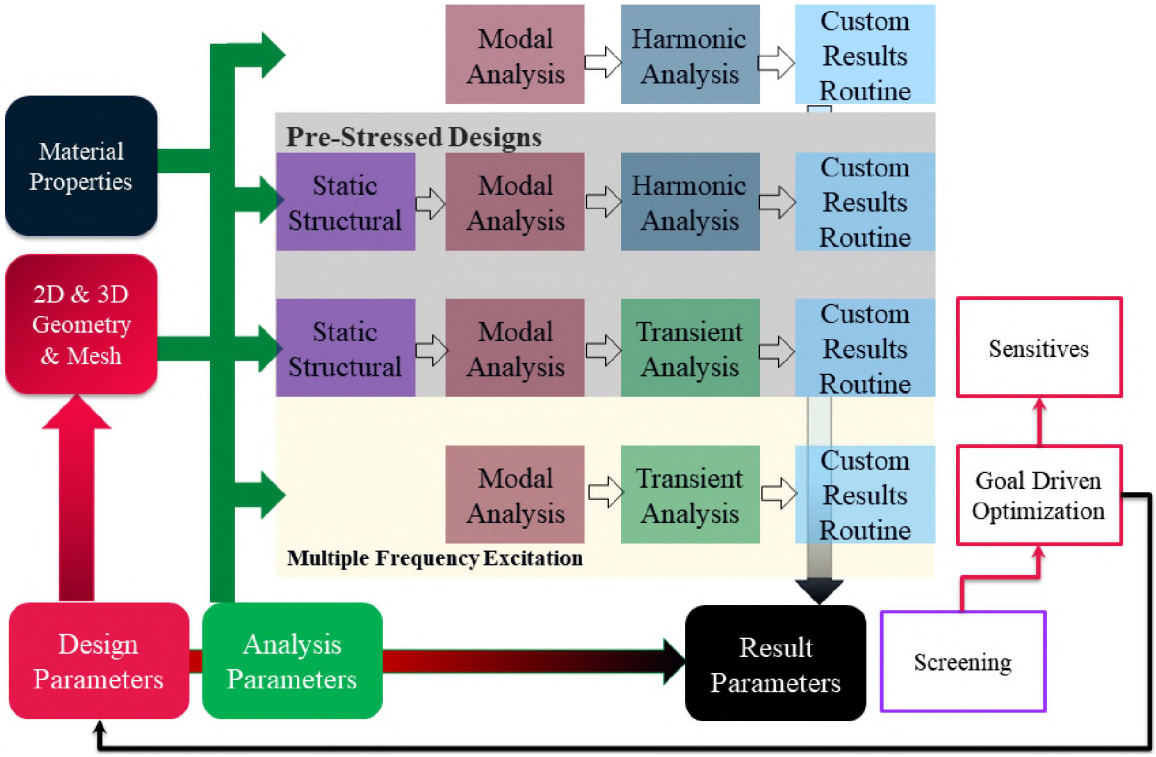

Figure 4.5. Design Optimization Summary

4.2.4.1. Optimization methodology. The process of optimization is as follows:

1. Define the dimensional optimization parameters and constant geometry dimensions.

2. Define the 2-D axisymmetric geometry and material properties described in Sections 3 and 5.

3. Perform a static analysis to calculate pre-stress due to mechanical pre-load or DC-bias. Pass static stress and strain results to the optimizer and check if they are within design limits for the materials.

4. Perform a modal analysis to identify modal participation factors and to understand the mode shapes. This step is only performed to understand design behavior and is not part of the optimization chain.

5. Steady-state harmonic analysis is performed twice in the frequency range of 10 kHz and 6 MHz. The results are then passed through a custom post-processing routine, and the step is repeated at five chosen frequencies from the routine. The Analysis and Post-processing routine algorithm is shown in Figure 4.6 and described in Section 4.2.4.2. The results from the analysis are passed on to one of the optimizers built into ANSYS.

6. Evaluate the new design point selected by the optimizer and repeat it until the optimization criteria are satisfied.

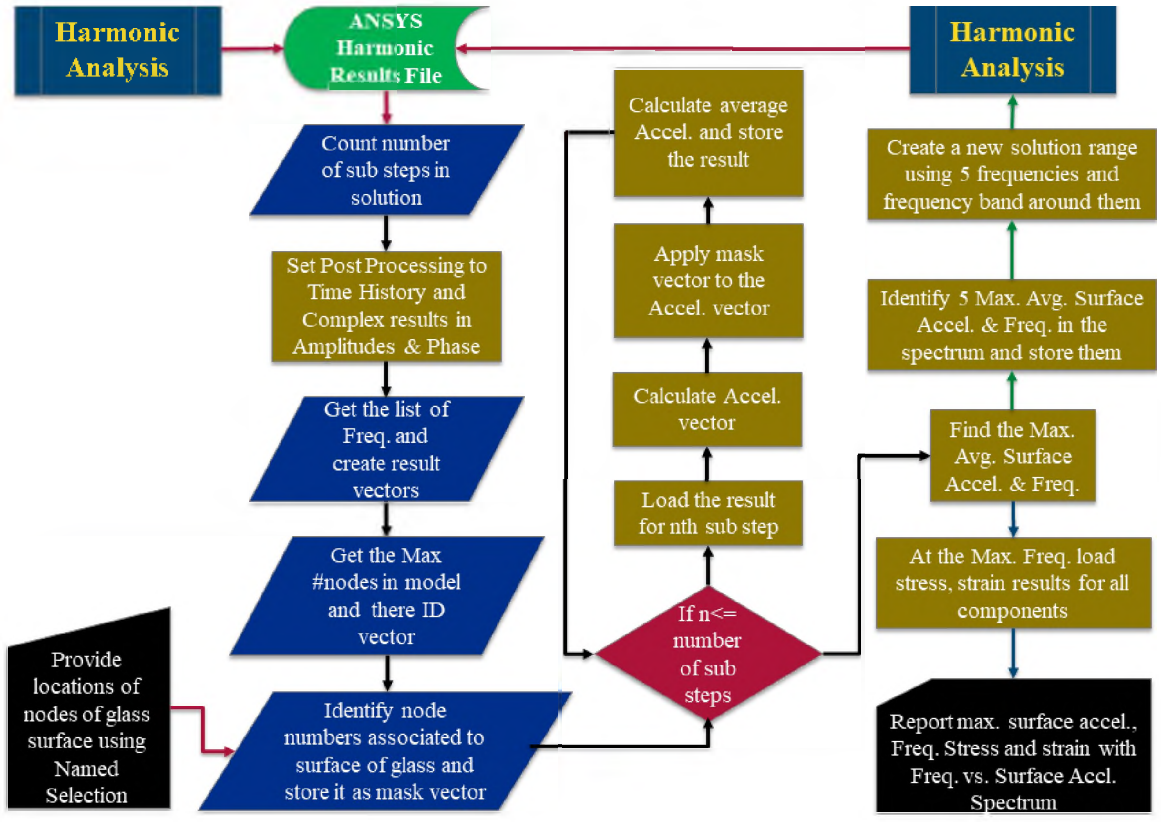

Figure 4.6. Analysis and Post Processing Routine

After the optimization has been completed, the best three design points are evaluated individually to create graphical results for each optimal design.

4.2.4.2. Analysis and post-processing routine. The Figure 4.6 illustrates the algorithm used in the analysis and post-processing of the design and is included in Appendix A3. The post-processing of the analysis is as follows:

1. The initial harmonic analysis is performed over the frequency range of 10 kHz to 6 MHz in 200 to 400 steps.

2. The routine identifies the number of sub-steps in the solution and converts the complex results at each step of the solution to magnitude and phase results.

3. Result vectors are predefined, and the frequencies at each solution step are stored.

4. A node vector is passed to the routine that identifies the nodes in the area of interest on the glass's surface. These node numbers are stored in a mask vector.

5. The results at each substep are loaded into the post-processor, and the normal surface acceleration is calculated for the design. The mask vector is applied to the results to isolate the nodes of interest. The acceleration of all the nodes are then averaged to get the average normal surface acceleration. This is repeated for all the substeps.

6. The results of average normal surface acceleration are then plotted with respect to frequency. The five frequencies with the maximum average surface acceleration in the spectrum are identified and then inputted to the second harmonic analysis.

7. A second harmonic analysis, repeating steps one through five, is then performed over a narrow 50 kHz band centered at each of the five design frequencies obtained in step six.

8. The results are then processed from the second harmonic analysis and passed to the optimizer.

    (a) Average normal maximum surface acceleration and the corresponding frequency are selected from the analysis performed in step seven, and the result is passed on to the optimizer.

(b) The stress and strain results in PZT, the stress in the glass, and other design elements are computed at the same frequency as the average normal maximum surface acceleration and passed on to the optimizer.

9. A composite frequency spectrum from the results of two harmonic analyses is plotted.

4.2.4.3. Optimization criteria. In general, all design optimizations are governed by the following objectives and constraints. Some of the designs require additional constraints to be defined; they are covered in the design studies section.

- Objective
  - Maximize the average normal acceleration in the field of view on the surface of the glass
  - Maximize the frequency
- Constraints
  - PZT
    - Normal stress in PZT: $\sigma_{PZT} \leq \sigma_Y$
    - Normal strain in PZT: $\epsilon_{PZT} \leq 0$
  - Normal stress in glass: $\sigma_{glass} \leq \sigma_Y$
  - Normal stress in other materials $\sigma_{matl} \leq \sigma_Y$
- Parameter Relations
  - Outer radius of PZT $r_o \leq r_g$
  - Inner radius of PZT $r_i \geq$ field of view radius of lens
  - Width of PZT $w_p \geq 0.75$ mm (this is to avoid small PZT width which is difficult to manufacture)

- Thickness of PZT $h_P \geq 0.254$ mm (this is to avoid very thin PZT which is difficult to acquire)

The stress criteria used in the optimizations are most likely impractical for the final design since they are set to the yield strength limits of the material. Yield stresses are used, so maximum surface acceleration is achieved on the glass, and currently, the weakest link in the prototype build is the epoxy interface between PZT electrodes and glass. A detailed discussion of the PZT bonding to glass is covered, and the challenges associated with it are covered in Section 5.4. An extensive study would be needed on the glass sealing bond with the PZT and is discussed in Section 5.4.4.2. In the final product design, the prototype's fatigue life would be considered, and studies would be undertaken to quantify the fatigue stress.

5. MATERIALS AND MANUFACTURING

The design and analysis aspects of the proposed designs are highly dependent on material properties. Before beginning a formal discussion of the results, a summary of the material properties used is presented. The other aspect that is significant to the successful design and testing of the actuator is manufacturing the prototypes. Some of the significant challenges faced during the manufacturing process are discussed here, along with their solutions.

5.1. LENS COVER - GLASS

A number of different types of glass are available to use as the lens cover. Some of the earlier designs involved the use of fused quartz (FQ). Other types of glass considered are ion-exchanged (Gorilla) glass and non-ion-exchanged glass from Corning.

5.1.1. Glass Types. In order to accommodate the 12 mm offset lens, as illustrated in Figure 1.2, it was decided to increase the diameter of the outer protective lens from 25.4 mm to 31.75 mm; this decision relaxed the minimum inner PZT ring radius constraint during the design optimization.

5.1.1.1. Fused quartz. FQ glass from Technical Glass Products was used initially for design studies. This glass was used because of its easy availability for the proof of concept prototypes. The limited number of thicknesses available constitutes the downside of this choice. The properties of FQ glass used in the design optimization and analysis are:

- Modulus of Elasticity: 72 [GPa]
- Poisson's Ratio: 0.17
- Density: 2200 [kg/m^3]
- Tensile yield strength: 40 [MPa]

5.1.1.2. Ion-exchanged glass and non-ion-exchanged glass. Ion-exchanged glass and non-ion-exchanged glass are used for some design studies. This glass was provided by Corning for prototyping[22]. The properties of glass used in the design optimization and analysis are:

- Modulus of Elasticity: 73.6 [GPa]
- Poisson's Ratio: 0.23
- Density: 2380 [kg/m^3]

5.1.2. Glass Thickness. Design optimizations of the 1.5875 mm thick FQ glass revealed high bending stresses. A design study was developed in ANSYS to see the effect of glass thickness on stress. Two studies were conducted on the SPS design; in both studies, the glass's thickness was the only mechanical parameter varied. The voltage applied to the design was varied for each study; in the first study, the applied voltage was held constant at 200 V_{pp}, while in the second study, the voltage was scaled and normalized to the thickness of glass to standard thicknesses of FQ glass. A voltage of 200 V_{pp}, was also used in Phase 1 of the project [1]. The applied forcing voltage in the second study is given by Equation (5.1):

$$V = 200\left(\frac{h_g}{h_n}\right) \tag{5.1}$$

where, V is the applied voltage, h_g is glass thickness, and the normalizing thickness of glass, h_n, (1/6" 1.5875mm). Displacement and stress results of the FQ glass were recorded for both studies and are shown in Tables 5.1 and 5.2. The displacement amplitude and phase are given in the radial (x) direction and thickness (y) direction, along with the vector sum magnitude of the corresponding directions of the FQ. Similarly, the stress amplitude and

phase in the radial (x), thickness (y), and shear (xy) along with von-Mises equivalent stress are given for the FQ glass. The von-Mises stress and the normal stress in the glass's thickness direction are plotted in Figures 5.1 and 5.2. Von-Mises equivalent stress is a scalar value that is derived from the stress tensor in a deformed material. According to the von-Mises yield criterion, the material under load will yield when the von-Mises equivalent stress reaches the yield strength of the material as defined in Equation (5.2) [23, 24], where σ_{ij} represents the components of stress in the x, y, and z directions.

$$\sigma_E = \sqrt{\sigma_{xx}^2 + \sigma_{yy}^2 + \sigma_{zz}^2 - \sigma_{xx}\sigma_{yy} - \sigma_{yy}\sigma_{zz} - \sigma_{zz}\sigma_{xx} + 3\sigma_{xy}^2 + 3\sigma_{yz}^2 + 3\sigma_{zx}^2} \tag{5.2}$$

This study shows that the bending stress scales more or less linearly with distance from the lens mid-plane under normalized voltage forcing as expected. Therefore, to avoid over-stress, the thinnest possible lens should be used. As a result of this study, an effort was made to find thinner glass with the diameter of interest. Thin Gorilla glass seemed to be most suitable for the application. Sourcing the Gorilla glass or a suitable alternative proved to be a challenge, but support was obtained from Corning in the form of ion-exchanged and non-ion exchanged glass samples [22].These samples were used to build the prototypes. Initially, both ion-exchanged and non-ion exchanged glasses were used, but it was soon found that the co-firing the silver electrode on to ion-exchanged glass was not possible. Consequently, prototypes were built using non-ion exchanged glass.

The fatigue life of glass is another important consideration and is most often predicted by stress-life and strain-life models for materials. However, these models do not accurately predict the fatigue life of brittle materials such as FQ glass. One of the common methods to characterize the fatigue life of FQ glass is the Weibull 2-parameter model. This model, for uniform dynamic stress, is mostly dependent on the surface finish with little dependence on the shape factor and stress area [25, 26].

Table 5.1. Design Study of the Effect of Glass Thickness on Stress with Constant Forcing

Thick-ness	Volt-age	Freq-uency	Deformation [μm]					Stress [MPa]						
			X (Radial)		Y (Thickness)		Vector	X (Radial)		Y (Thickness)		XY (Shear)		von-
t [mm]	V [V]	[kHz]	Ampl.	Phase	Ampl.	Phase	Sum	Ampl.	Phase	Ampl.	Phase	Ampl.	Phase	Mises
0.25	200	15	0.54	-60.56	12.25	-59.98	12.26	30.63	-62.05	6.02	-54.13	5.45	127.83	25.84
0.5	200	28	0.89	-80.62	10.55	-80.08	10.59	55.93	-82.52	13.34	-78.22	12.40	-83.64	47.88
0.75	200	38	0.94	-114.61	7.92	-114.17	7.98	63.20	-116.86	16.51	-113.47	16.02	-117.53	54.78
1	200	44	1.01	-102.71	6.89	-102.43	6.96	63.61	-105.45	18.48	-102.16	17.26	-105.97	54.77
1.25	200	48	0.96	-105.16	5.66	-105.05	5.74	57.44	-108.40	17.68	-105.00	16.37	-108.92	49.33
1.5	200	51	0.87	-115.39	4.52	-115.43	4.60	47.95	-119.13	15.36	-115.54	14.23	-119.64	41.12
1.5875	200	51	0.91	-71.38	4.54	-71.46	4.63	46.21	-75.38	15.79	-71.63	15.79	-75.92	38.96

Table 5.2. Design Study of the Effect of Glass Thickness on Stress with Scaled Forcing

Thick-ness	Volt-age	Freq-uency	Deformation [μm]					Stress [MPa]						
			X (Radial)		Y (Thickness)		Vector	X (Radial)		Y (Thickness)		XY (Shear)		von-
t [mm]	V [V]	[kHz]	Ampl.	Phase	Ampl.	Phase	Sum	Ampl.	Phase	Ampl.	Phase	Ampl.	Phase	Mises
0.25	31.50	15	0.13	-93.25	1.93	-59.98	1.93	-4.82	-62.05	0.95	-54.13	0.86	127.83	4.07
0.5	63	28	0.28	-80.62	3.32	-80.08	3.34	17.62	-82.52	4.20	-78.22	3.91	-83.64	15.08
0.75	95	38	0.45	-114.61	3.70	-114.17	3.77	29.86	-116.86	7.80	-113.47	7.57	-117.53	25.88
1	126	44	0.63	-102.71	4.34	-102.43	4.38	40.07	-105.45	11.64	-102.16	10.87	-105.97	34.5
1.25	157.5	48	0.76	-105.16	4.45	-105.05	4.52	45.23	-108.40	13.92	-105.00	12.89	-108.92	38.84
1.5	189	51	0.73	-115.39	3.81	-115.43	3.39	40.54	-119.13	12.96	-115.54	12.00	-119.64	34.69
1.5875	200	51	0.91	-71.38	4.54	-71.46	4.63	46.21	-75.38	15.79	-71.63	13.76	-75.92	38.96

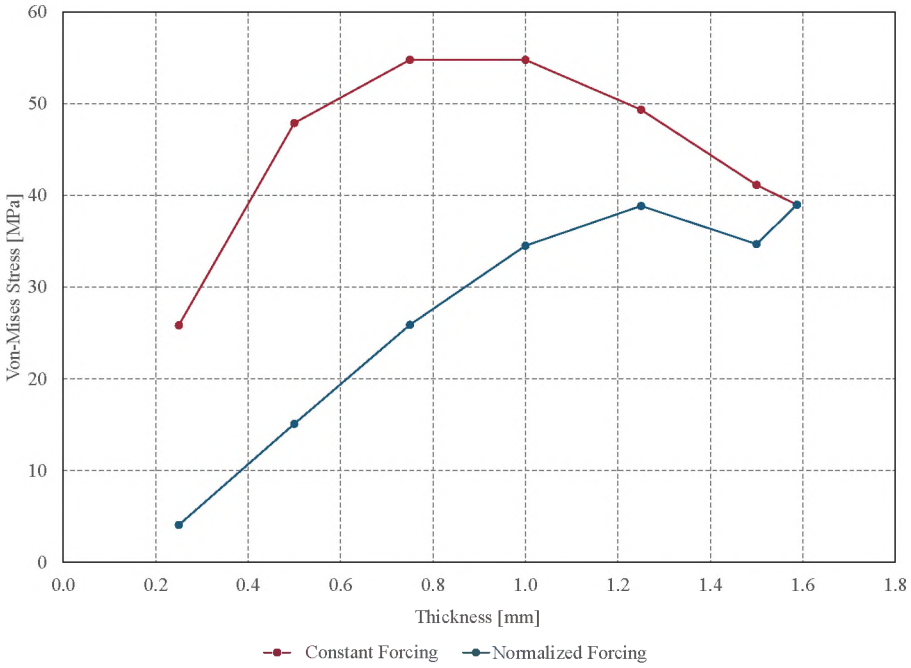

Figure 5.1. Von-Mises Stress Versus Glass Thickness

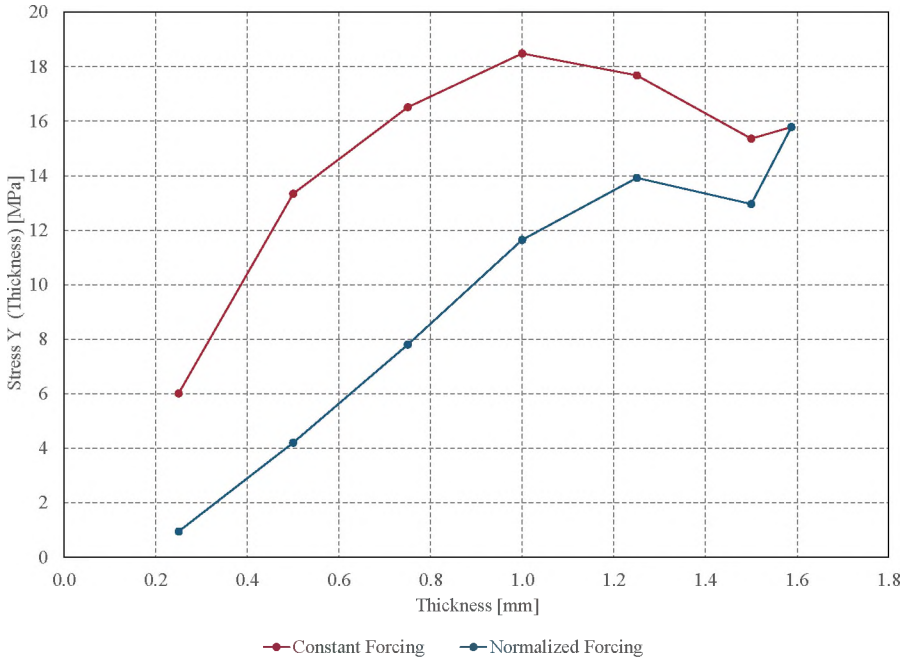

Figure 5.2. Normal Stress Versus Glass Thickness

It can be concluded from this study, and from the prototypes tested in the early designs, that the thickness of the glass has a significant role in the amount of stress developed. It is recommended that a thin glass with high yield strength and a large factor of safety be used for this application.

5.2. ACTUATOR-PZT

The type of PZT used significantly affects the life of the actuator and surface acceleration. Early in the design phase, one of the key questions was which PZT formulation would be best suited for the application. It was important to understand the effect of changing the PZT material in the design and its significance in optimizing the design. An ANSYS-based design study was formulated to evaluate four different types of PZT. The four materials were chosen based on if they were readily available from a manufacturer. The materials considered in this study were based on standard PZT formulations available from STEMiNC. The formulations studied were PZT4, PZT5A, PZT8, and PZT5H. The material properties used in this study are shown in Table 5.3. The SPS design was chosen to evaluate the different materials and is shown in Figure 5.3.

Axisymmetric symmetry was assumed in the 2-D SPS model, with the parameters and design choices listed below:

- Parameter and seed design
    - Input parameters
        - r_i = 6 mm
        - w_p= 3 mm
        - h_p = 1.02 mm
        - r_g = 12.7 mm
        - h_g = 1.5875 mm

- Derived parameters
  - r_o = 9 mm
  - Location of glass surface $h = h_p + h_g$ = 2.6075 mm
- Output parameters
  - Maximum of normal average acceleration amplitude on glass surface = A
  - Frequency at which A occurs = F
  - Stress in PZT = S_{eqv}

- Optimization Setup
  - Optimization method: Adaptive multi-objective
  - Design parameter domain
    - 6 mm $\leq r_i \leq$ 12 mm
    - 0.5 mm $\leq w_p \leq$ 5 mm
    - 0.254 mm $\leq h_p \leq$ 1.02 mm
  - Parametric and constraint relations
    - $r_o \leq r_g$ =12.7 mm
    - $S_{eqv} \leq$ 40 MPa
  - Objective
    - Maximize A
    - Minimize S_{eqv}

The design parameters were held constant, and the effects of the four different materials were studied. The average normal glass surface acceleration and peak surface acceleration are plotted with respect to frequency in Figures 5.4 and 5.5. The results of this study are summarized in Table 5.4. From the summary, it is seen that PZT4 has comparable average surface acceleration at a lower frequency compared to the other PZT formulations.

Table 5.3. Material properties of PZT [27]

Property	PZT4	PZT5A	PZT8	PZT5H
Navy Type	Type-I	Type-II	Type-III	Type-VI
STEMiNC	SM121	SM412	SM118	SM311
Density [kg/m^3]	7500	7750	7600	7500
$d_{31} \times 10^{-12}$ [m/V]	-123	-171	-97	-274
$d_{33} \times 10^{-12}$ [m/V]	289	274	225	593
$d_{15} \times 10^{-12}$ [m/V]	496	584	330	741
${s^e}_{11} \times 10^{-12}$ [m^2/N]	12.3	16.4	11.5	16.5
${s^e}_{33} \times 10^{-12}$ [m^2/N]	15.5	18.8	13.5	20.7
${s^e}_{12} \times 10^{-12}$ [m^2/N]	-4.05	-5.74	-3.7	-4.78
${s^e}_{13} \times 10^{-12}$ [m^2/N]	-5.31	-7.22	-4.8	-8.45
${s^e}_{44} \times 10^{-12}$ [m^2/N]	39.0	47.5	31.9	43.5
${s^e}_{66} \times 10^{-12}$ [m^2/N]	32.7	44.3	30.4	42.6
${K^T}_{11}$	1475	1730	1290	3130
${K^T}_{33}$	1300	1700	1000	3400
Mechanical Quality, Q_m	1000	100	1200	80

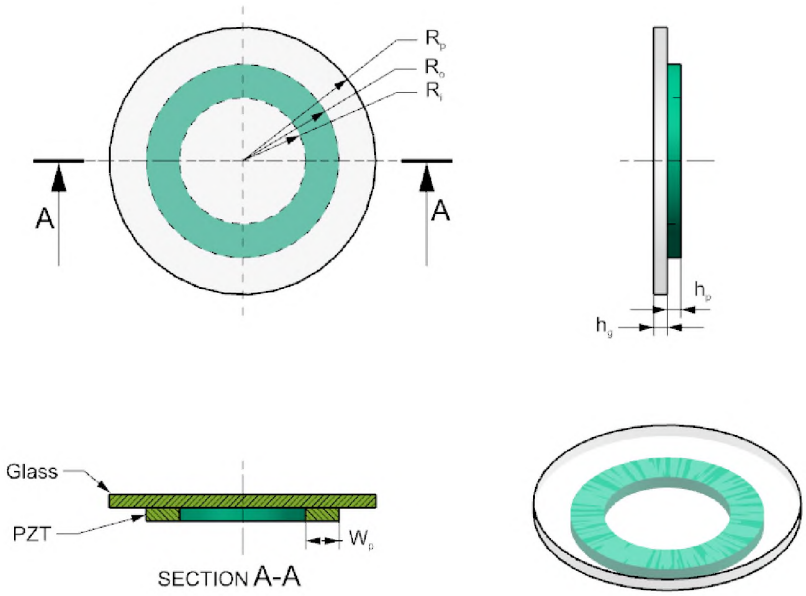

Figure 5.3. Single PZT System SPS

It is important to note that the peak acceleration on the surface occurs at that same frequency for all of the materials.

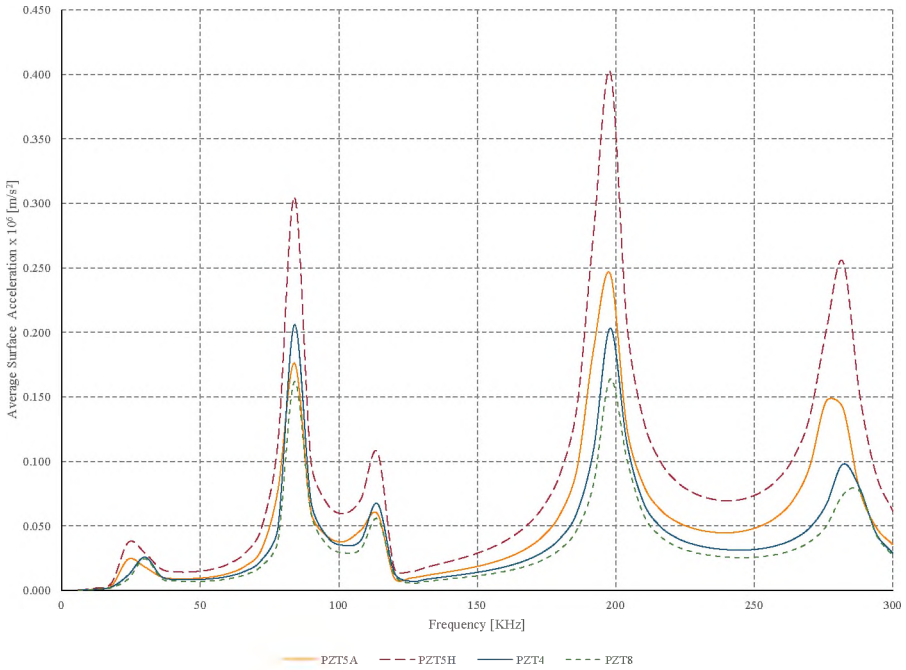

Figure 5.4. Average Surface Acceleration

Table 5.4. Summary of Results Material Study-Constant Design

Material	Average Surface Acceleration			Peak Surface Acceleration		
	Frequency [kHz]	Acceleration $\times 10^6$ [m/s^2]	S_{eqv} [MPa]	Frequency [kHz]	Acceleration $\times 10^6$ [m/s^2]	Phase [Deg.]
PZT5A	198	0.2456	11.94	198	0.85	-176.7
PZT5H	198	0.4020	19.355	198	1.3863	-176.5
PZT4	84	0.2060	27.558	198	0.7006	-175.4
PZT-8	198	0.1639	7.7341	198	0.5648	-175.1

Next, the optimization of the SPS design for the four different materials was undertaken. In each of the optimization runs, design constraints were kept fixed, and only the PZT material was varied. This study has a two-fold purpose: (1) to see if the material would perform better in a given set of constraints, and (2) to determine if the optimization process was significantly dependent on material property. The summary of optimization results

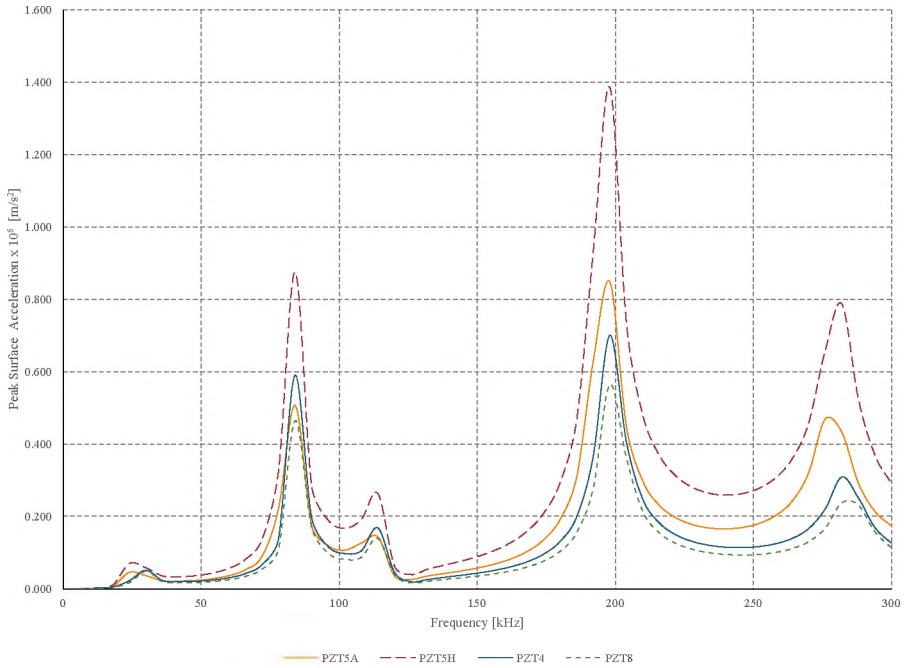

Figure 5.5. Peak Surface Acceleration

is shown in Table 5.5. For each optimization, two optimal design points are documented. Peak surface acceleration with respect to frequency is plotted in Figure 5.6. In Figure 5.7, the surface acceleration is plotted with respect to the radial dimension to determine which modes are excited at a given optimal frequency.

Based on the results in Table 5.5, it can be seen that the more consistent surface acceleration is achieved in the two design points of the PZT4 formulation. Upon further investigation, the surface acceleration profile of the PZT4 design shows that the higher surface acceleration is achieved at a lower mode compared to the PZT5A and PZT5H formulations. PZT4 has several advantages: (a) it is a hard formulation, has a lower electromechanical coupling coefficient, but much higher Q than other PZT's, (b) it can also be driven at much higher voltages without depoling, which can compensate for the lower coupling coefficient, and (c) is available in square plates, thus making it the best-suited candidate for the application.

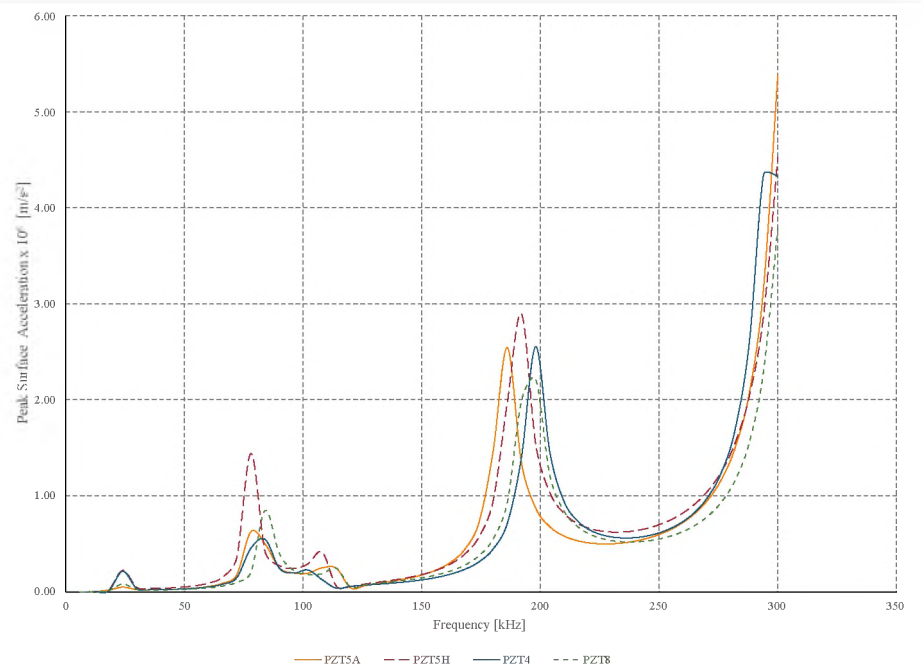

Figure 5.6. Optimal Design Peak Surface Acceleration Frequency

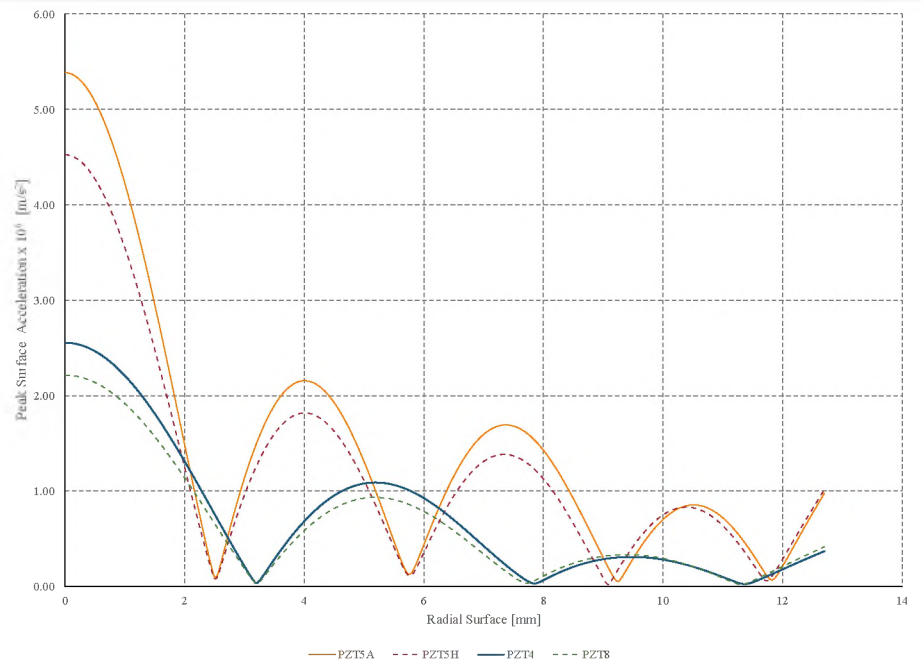

Figure 5.7. Surface Acceleration versus Radius of Glass

ANSYS requires that piezoelectric materials be fully defined. The material properties provided by ceramic manufacturers are in IEEE standard notation, which needs to be transformed to the axis of polarization and converted to ANSYS notation. A MATLAB

Table 5.5. Summary Of Material Study Optimization

Parameter	PZT5A		PZT5H		PZT4		PZT8	
	DP 1	DP2	DP 1	DP2	DP 1	DP2	DP 1	DP2
w_p [mm]	4.20	4.08	4.20	1.96	4.68	4.92	4.77	2.60
r_i [mm]	8.22	8.60	8.22	6.30	7.92	7.73	7.92	9.87
h_p [mm]	0.89	0.59	0.89	0.41	0.37	0.82	0.51	0.47
A [m/s^2]	0.8483	1.4559	1.2364	0.5147	1.2107	1.3056	1.0273	0.4767
S_{eqv}[MPa]	20.40	35.36	29.63	13.08	29.61	33.16	24.98	12.35
F [kHz]	300	300	300	300	300	300	300	300

script provided in Appendix A1 was written to achieve this. The script allows the user to choose from entering material properties independently or using one of the standard PZT formulations. It also allows the user to select the axis of polarization and output format for either ANSYS APDL or Workbench. PZT4 is used in all the design optimizations and prototype builds. The 2-D axisymmetric analysis of the design in ANSYS requires the polarization axis of material to be defined in the Y-axis.

- Density: 7750 [kg/m^3]
- Stiffnesses Matrix

$$C = \begin{bmatrix} 12.0346 & 7.5179 & 7.5090 & 0 & 0 & 0 \\ 7.5179 & 12.0346 & 7.5090 & 0 & 0 & 0 \\ 7.5090 & 7.5090 & 11.0867 & 0 & 0 & 0 \\ 0 & 0 & 0 & 2.2584 & 0 & 0 \\ 0 & 0 & 0 & 0 & 2.1053 & 0 \\ 0 & 0 & 0 & 0 & 0 & 2.1053 \end{bmatrix} \times 10^{10} \text{ [N/m}^2\text{]}$$

- Piezoelectric Constants Matrix

$$e = \begin{bmatrix} 0 & 0 & -5.3512 \\ 0 & 0 & -5.3512 \\ 0 & 0 & 15.7835 \\ 0 & 0 & 0 \\ 0 & 12.2948 & 0 \\ 12.2948 & 0 & 0 \end{bmatrix} \text{ [C/m}^2\text{]}$$

- Permittivity Matrix

$$K = \begin{bmatrix} 919 & 0 & 0 \\ 0 & 919 & 0 \\ 0 & 0 & 827 \end{bmatrix}$$

5.3. OTHER MATERIALS

Apart from the two main materials (PZT and Glass), the design also involves the lens holder which is made of Delrin. Some of the proposed designs call for additional mass to be attached to the PZT. The additional mass is designed using aluminum or steel, and the material properties of Delrin, stainless steel, and aluminum used in this analysis are listed below.

5.3.1. Delrin. The nominal properties of Delrin are used in the analyses and are listed below.

- Young's modulus: 2.413 [GPa]
- Poisson's ratio: 0.3
- Density: 1420 [kg/m^3]
- Tensile yield strength: 62.05 [MPa]

- Compressive yield strength: 35.85 [MPa]

5.3.2. Stainless Steel. In some designs (MPS and SDS) additional mass is added to the system. Nominal properties of stainless steel are used in the analyses and are listed below.

- Young's modulus: 193 [GPa]
- Poisson's ratio: 0.31
- Density: 7570 [kg/m^3]
- Tensile yield strength: 207 [MPa]

5.3.3. Aluminum. Nominal properties of aluminum are used in the analyses and are listed below.

- Young's Modulus: 71 [GPa]
- Poisson's Ratio: 0.33
- Density: 2770 [kg/m^3]
- Tensile yield Strength: 280 [MPa]

5.3.4. Epoxies, Conductive Ink and Conductive Paste. Several epoxies, conductive inks, and pastes have been used in the process of prototyping and testing. Their material properties are shown in Table 5.6. In the analysis, the bond is represented by contact elements. The nominal stiffness parameter in the contact element is used to define the bond strength [20].

- Epoxies: Epoxies are primarily used for bonding PZT directly to glass. Sometimes conductive epoxy is used to attach wires.
    - EPO-TEK 353ND is a high-temperature, high-strength optical epoxy used in early prototypes [28].

- EPO-TEK 301-2FL is a low-viscosity, low-temperature, and is formulated for optical use [29]. It can be both oven or room cured. It was initially used for bonding PZT to the glass for all the prototypes.
- EPO-TEK 323LP is a high-temperature, high-strength optical epoxy used in prototype building. It is the best epoxy for the application [30].
- EPO-TEK H20E is a silver-loaded conductive epoxy that can be cured in an oven or at room temperature. It is highly thixotropic and suitable for attaching wires [31].

- Conductive Ink: Conductive ink was primarily used as an electrode to attach the wire to glass. The conductive ink used was PELCO 16031 [32].
- Conductive Paste: ElectroScience ESL 9912-MM silver conductive paste was used for co-firing the PZT to the glass [33].

Table 5.6. Epoxy Properties

Epoxy	353ND	301-2FL	H20E	323LP
Mix ratio	10:1	100:35	1:1	10:1
Pot life [Hrs.]	≤ 3	10	60	24
Cure temperature [°C]	80	80	80	90
Cure time [Hrs.]	0.5	3	3	0.5
Glass transition temperature [$°C$]	≤ 90	≤ 45	≤ 80	≤ 100
Storage modulus [MPa]	3504	3110	5576	3062
Shore D hardness	85	70	75	88
Lap shear [MPa]	< 13.78	< 13.78	10.2	13.79
Die shear [MPa]	36.78	24.52	23.45	49.93
Density [g/cm^3]	1.11	1.01	2.44	1.19
Coefficient of thermal expansion				
CTE Below Tg [m/m °C]	54e-6	56e-6	31e-6	51e-6
CTE Above Tg [m/m °C]	206e-6	211e-6	158e-6	185e-6
Viscosity [cPs]	3000-5000	100-200	2200-3200	3500-5000

Studies were conducted on the epoxy bond thickness and visual quality of the bond using the epoxies listed in Table 5.6. In the first study, the bond between two microscope slides was studied with different epoxies and under different compression weights of 50 g,

100 g, and 200 g. The second study was repeated for the bond between glass and PZT. In both studies, the cure time and amount of epoxy used were kept constant. After bonding, the glass slides were cut in half using a diamond saw and studied using a high magnification microscope (Hirox-K7000) to record the average bond thickness and minimum bond thickness. Figure 5.8 shows a microscope measurement of the bond line for the Glass-PZT bond study. Figures 5.9 and 5.10 show the minimum bond thickness and average bond thickness measured. It was found that EPO-TEK 323LP was the best epoxy to achieve a thin and uniform bond line.

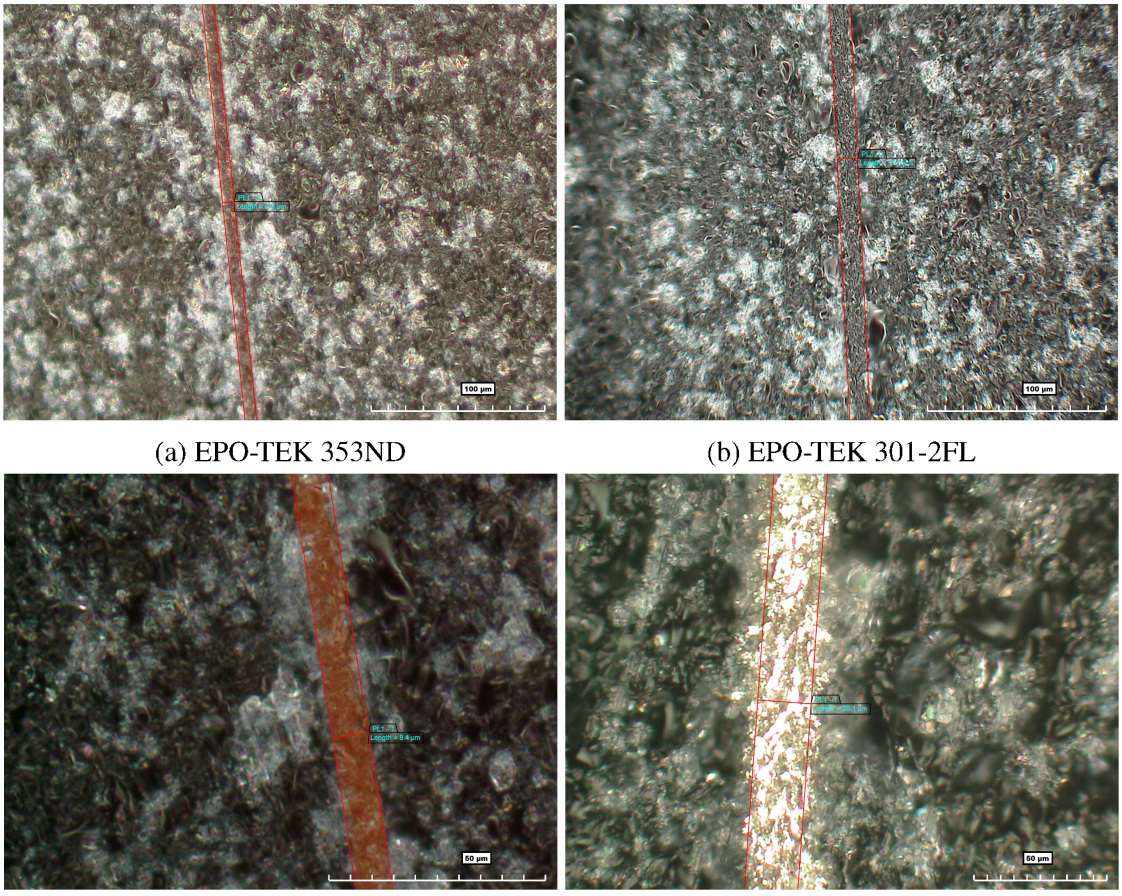

(a) EPO-TEK 353ND

(b) EPO-TEK 301-2FL

(c) EPO-TEK 323LP

(d) EPO-TEK H20E

Figure 5.8. Glass-PZT Epoxy Bond Thickness under 200g Weight

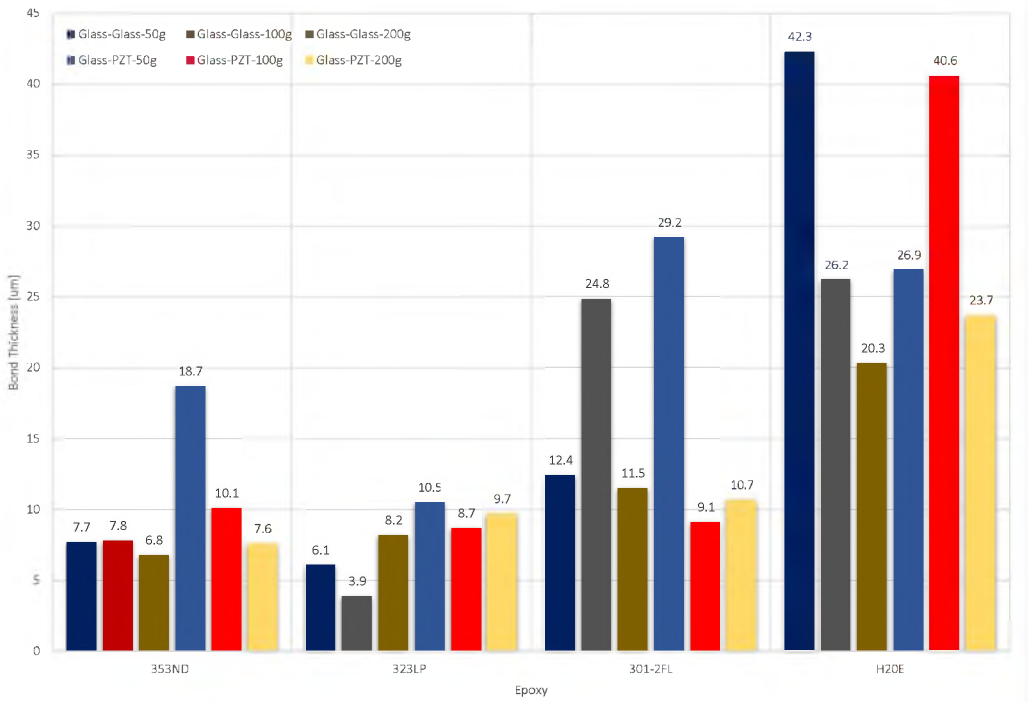

Figure 5.9. Minimum Bond Thickness

A good epoxy bond is a strong mechanical bond, and, according to bonding theory, an epoxy must fill in the valleys and crevices of the glass substrate and the PZT as well as displace the air trapped in the joint. Epoxy bonding should result in the interlocking of the adhesive and the adherend together [34]. A good epoxy bond is dependent on the bonding surfaces, should be less than five microns thick, and allow high point contact between the electrode on the glass and the PZT. Two principal challenges render the use of epoxy bonding inviable in the present application: (1) the electrode-epoxy interfaces are subjected to fairly high cyclic stresses, resulting in fatigue, and (2) glass is a relatively poor thermal conductor, so the interface is also subjected to cyclic heating which further exacerbates the fatigue problem. An alternative and potentially much more reliable approach will be discussed in Section 5.4.4.2.

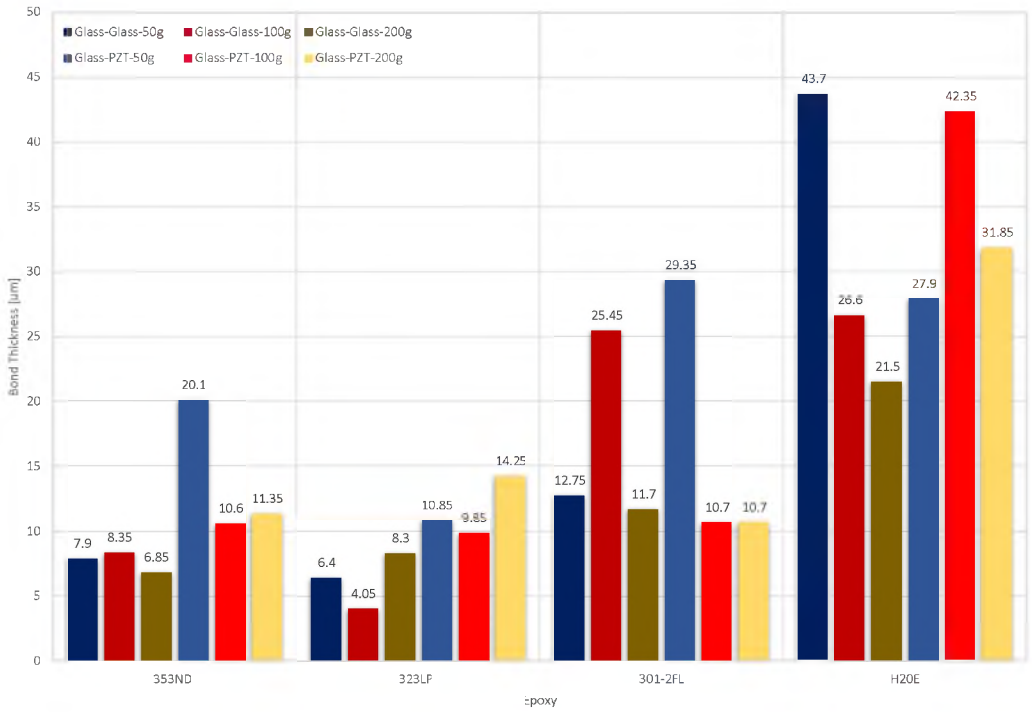

Figure 5.10. Average Bond Thickness

5.4. PZT RING CUTTING AND BONDING

5.4.1. PZT Cutting. The optimized designs required custom-sized rings; in actual production, this would be subcontracted. Efforts to find a subcontractor for prototyping proved to be challenging due to most of them requiring the purchase of rings in large quantities, at lower than required tolerance, and at a high cost. A total of five subcontractors were approached with a request for quotes (RFQ), out of which the only one offered a formal quote that proved to be cost, time, and quality prohibitive. An in-house slurry mill was developed to cut custom ring sizes with high-quality control. A custom fixture, shown in Figure 5.11, was developed to hold the flat PZT plates with relief for residual cut pieces of PZT. Also, a special tool was turned for each PZT ring from 1.5 inch copper cylindrical stock. Figure 5.12 shows a cross-section of a tool to cut a ring of outer diameter 22 mm, inner diameter 16 mm, and thickness of 1.59 mm, and tools used in making rings for the SPS and SDS designs. The tool is designed to cut the center hole of the ring first and then

cut the ring's outer circumference to about half the thickness of the PZT. After the first cut, the PZT plate is flipped over, and the remaining depth is cut out. The process used Silicon Carbide 320 grit lapping compound as the abrasive. The abrasive and spinning copper tool act to slowly grind the PZT plate. The process requires that gentle pressure be applied during grinding and is time-consuming. Thinner rings were challenging to cut and produced low yields using this method.

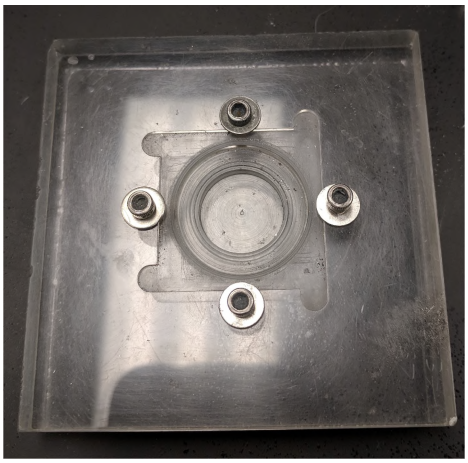

Figure 5.11. PZT Cutting Fixture

5.4.2. PZT Bonding. Conforming to the design specifications proved to be one of the challenges in building the prototype. Inability to align the PZT rings to glass resulted in asymmetric stresses in the glass and glass failure. The eccentricity of the prototypes also prompted the glass thickness study to understand the effect of eccentricity and glass thickness on stresses. Another issue encountered during manufacturing was the ability to access the PZT electrode attached to glass to drive the prototype. Both of these issues resulted in a substantial investment of time and work to overcome the limitations.

5.4.3. Alignment of the PZT Ring with the Glass. A visual alignment method was developed to assemble the prototypes. The visual alignment was achieved by using a template that is custom-made for each design and prototype. An example template for the SPS prototype is shown in Figure 5.13, and the assembled prototype on the template is shown in Figure 5.14. The template and fixturing were designed separately for each

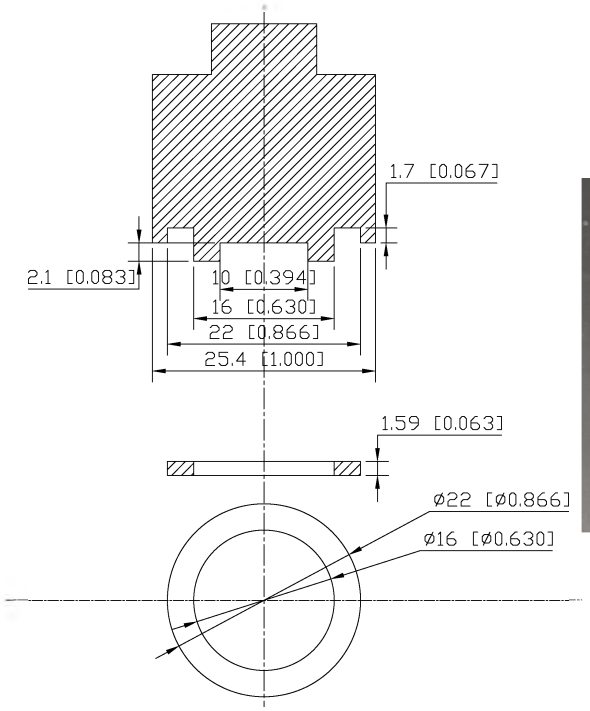

(a) Cross Section of Tool

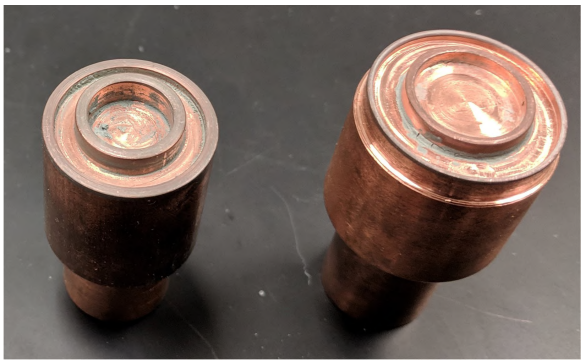

(b) Ring Cutting Tools

Figure 5.12. Ring Cutting Tool for PZT

prototype to account for variations in the individual component dimensions due to the manufacturing tolerance. The template is printed on transparent vellum paper and then placed on a tracing light-box. The prototype is then assembled on top of the template by first attaching the glass with double-sided tape. Then a thin layer of epoxy is applied to the PZT before placing it on to the glass, and the same is done to the additional mass, if applicable, to the prototype being built.

5.4.4. Electrical Contacts to PZT.

- Seven strand, silver plated, 32 AWG copper wire was used as the electrical contacts for all prototypes.
- Attaching wires to the PZT electrode bonded to glass proved to be more challenging. Numerous methods were tried and evaluated and are listed below:
    - Soldering to the side of the PZT

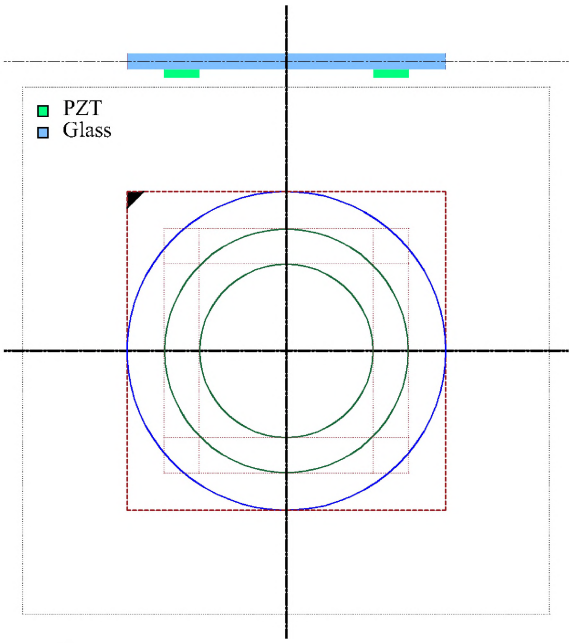

Figure 5.13. SPS Prototype Template

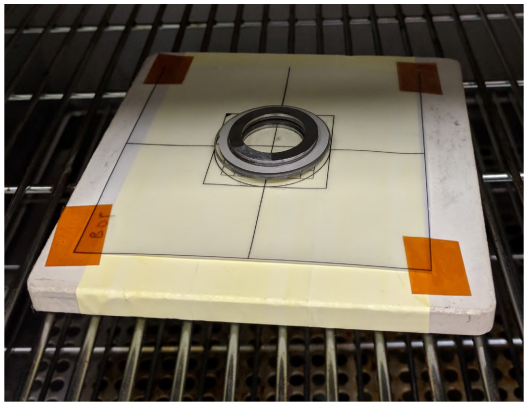

Figure 5.14. MPS Prototype Template and Assembly

- Bonding PZT with conductive epoxy
- Bonding most of the PZT electrode with non-conductive epoxy, and bonding a small area with conductive epoxy
- Using conductive silver ink on the glass and bonding the PZT to the glass with non-conductive mechanical epoxy
- Sputtering conductive metal film on the glass

- Sandwiching electrical wire between PZT and glass during bonding
- Using conductive tape to achieve the bond and electrical contact

5.4.4.1. Soldering wires to PZT. One of the most common ways to attach the wire was to solder the wire directly onto the exposed electrodes of the PZT. There are two forms of commercial electrodes available for PZT: nickel and silver-based. A brief study was conducted to find the best solder and flux. The solder used must have a melting temperature below the PZT Curie temperature; a higher soldering temperature could cause localized depoling of the PZT. The resulting mechanical joint should be secure. The flux used should be easy to clean. The solder and flux combination should be usable for both electrodes. Table 5.7 shows the solder and flux considered in the study; these were selected based on recommendations from PZT manufacturers. The study was conducted on all combinations of solder, flux, and electrode types.

Table 5.7. Solder and Flux

Solder Specifications		
AIM-SN100C [35]	Kester-331 [36]	Thermoflow TF604016 [37]
Sn 99.241, Cu 0.7, Ni 0.05, Ge0.009	Sn 96.5, Ag 3, Cu 0.5, Flux 3.3%	Sn 60 Pb 40
227°C	315°C	350°C
Flux		
Kester 2331-ZX [38]	Kester-951 [39]	Ruby Fluid [40]

The study results found that the most suitable solder and flux combination for both electrodes was AIM-SN100C and Kester 2331-ZX. Throughout the project, this solder-flux combination was used, and the following soldering technique was developed.

- Use soldering iron with a chisel tip at a temperature of 315 – 325°C. See Figure 5.15a.
- Strip and tin the wire using solder and flux.
- Clean the electrode of the PZT with 99% isopropyl alcohol.

- Ensure only a small area of PZT is wetted with the flux from the wire. Damp the tinned wire using the flux and mark the PZT where the wire is to be soldered. See Figure 5.15b.
- Use the side of the chisel tip to melt a small amount of solder on the soldering iron.
- Place the wire on the marked area and touch the solder to the wire and not the PZT. Solder will flow quickly from the iron to the wire and onto the PZT. In a good solder joint, solder flows rapidly in less than 1 second. See Figure 5.15c.
- If the solder joint is not secure, repeat the process, but never expose the PZT to the high temperature of the iron for more than 2 seconds, and allow sufficient time between each attempt for the PZT to cool down.

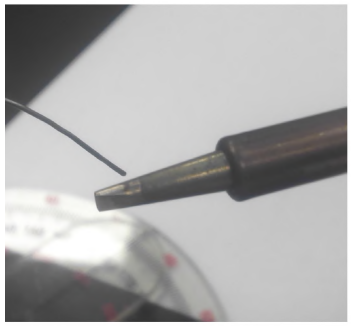

(a) Chisel Tip Solder Iron

(b) PZT Surface Preparation

(c) PZT Solder Joint

Figure 5.15. PZT-Wire Soldering Process

5.4.4.2. Co-firing of glass-PZT and electrode firing on glass. After exhausting several methods of attaching PZT to glass, it was determined that the best possible solution was to achieve a chemical and mechanical bond between PZT and glass. A subcontractor developed a method to co-fire PZT to the glass. ElectroScience ESL 9912-MM silver conductive paste was used for co-firing the PZT to the glass. The process involves screen printing the conductive paste and aligning the PZT ring with glass. The assembly is then subject to a specific curing schedule in a conveyor furnace with temperatures of up to 800°C. The temperatures in the process exceed the Curie temperature of the PZT and cause

a loss in polarization; this requires the PZT to be re-poled after the co-firing process. The subcontractor conducted numerous trials with ion-exchanged, non-ion-exchanged, and FQ glass.

The co-firing process was successful for non-ion-exchanged and FQ glass, and two samples of the co-fired PZT and glass were produced. The ion-exchanged glass did not withstand the high temperatures of the co-firing process in several trials and resulted in damage due to cracking or warping. Repoling of the PZT was never successful; some reasons that could have led to this include cracks in PZT due to high temperatures of the co-firing process. The repoling process may have failed due to the existing electrode on PZT disintegrating in the co-firing process and causing carbon residue resulting in an electrical path between the electrodes and causing a short. Due to limited resources, none of these have been thoroughly investigated or corroborated as the cause of the failure in repoling PZT. This method of assembly seems to be the most viable method to make long-lasting prototypes.

All the prototypes in this report have been built using glass co-fired with silver conductive paste, and then the PZT bonded to the glass using epoxy. An example of fired quartz glass received from the subcontractor is shown in Figure 5.16.

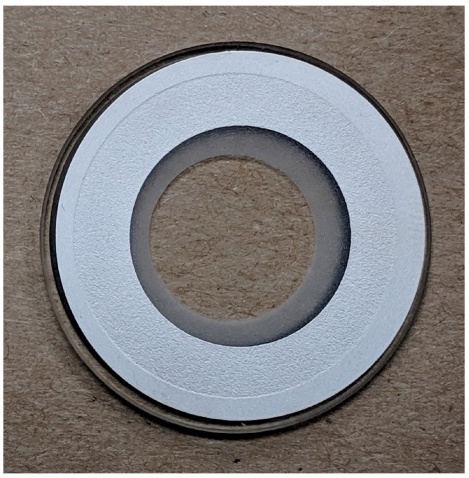

Figure 5.16. Silver Co-fired Quartz Glass

6. DESIGN PROTOTYPING AND TESTING

This section details optimization, prototype building, testing, and results for each design. For each design, the ANSYS optimization results and the output parameter's design sensitivities to input parameters are shown. The prototyping and testing details are then covered for the prototype. The four designs were tested for efficacy in removing solid and liquid contaminants. The solid contaminants range from 9.5 μm to 100 μm in diameter, and liquid contaminants have a viscosity range of 0.89 cPs to 70000 cPs.

6.1. SINGLE PZT SYSTEM

The Single PZT System (SPS) was the first design to be studied in detail due to its relative simplicity in design and prototyping. Figure 6.1 shows the design and a built SPS prototype. Some key lessons were learned during the design and development of this system. The initial analysis and optimization runs of the SPS design led to developing a more robust optimization analysis routine by identifying the number of design parameters and the need for a custom result analysis routine and output parameters that would be tracked in optimization. Several technical challenges were discovered during manufacturing that have guided many design decisions and the pursuit of manufacturing solutions to improve the other designs. Two SPS prototypes were built and tested. One of the prototypes was built based on the SPS design optimization while the second prototype was built with the SDS design rings, hereafter referred to as SPS Prototype 1 and SPS Prototype 2, respectively.

6.1.1. Analysis and Optimization of the SPS Design. The SPS design was the first design to be analyzed and optimized. The design geometry and the ANSYS model are shown in Figure 6.2. PZT4 was used in this design analysis. Due to the manufacturing limitations of the PZT ring, the PZT thickness cannot be modified and, therefore, was held constant during the design optimization. Design-space parameters and constraints used in optimization are shown in Tables 6.1 and 6.2. Optimization was carried out to maximize

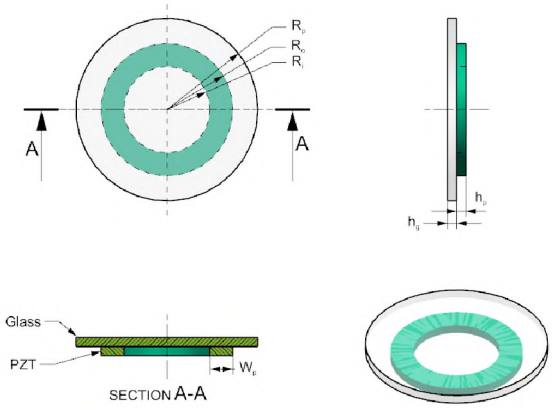

(a) SPS Design

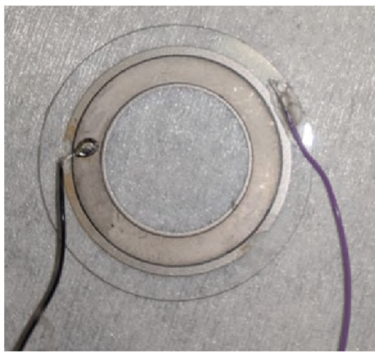

(b) SPS Prototype 1

Figure 6.1. Single PZT System (SPS)

Table 6.1. Prototype Design Space Dimensions

Parameter	Lower Bound	Upper Bound
r_i [mm]	8	8.9
w_p [mm]	0.5	5.4
V_0 [V]	-200	200
h_p [mm]	1	
r_g [mm]	15.875	

the normal surface acceleration on the glass surface within the field of view illustrated in Figure 6.3. The custom analysis and post-processing algorithm from section 4.2.4.2 was used for the result.

The ANSYS optimization routine calculates the output variables' sensitivity to change in the design variables for the input design space. Figure 6.4 shows the normalized sensitivities of the variables inner radius, r_i, the bias voltage, V_0, and the PZT width, w_p. From the figure, it is seen that the SPS design is most sensitive to the width of the PZT.

6.1.2. SPS Build Process. The two SPS prototypes built are based on the design optimization of the SPS design. Initially, a PZT ring was cut using a slurry mill to the optimization results' dimensions, then cleaned ultrasonically. A non-ion-exchanged glass with a co-fired silver electrode was cleaned and prepared for bonding. EPO-TEK 301-2FL was used to build SPS prototype and was selected because it can be cured at room

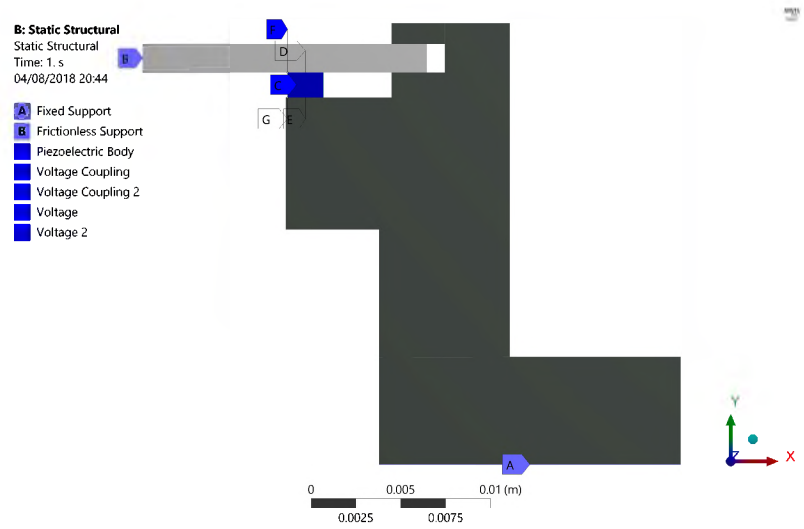

Figure 6.2. SPS Design FEM Representation

Figure 6.3. Area Investigated for Optimization of Normal Surface Acceleration

Table 6.2. Prototype Design Constraints

Parameter	Constraint
Surface acceleration	Maximize
Strain in PZT	Minimize
Equivalent stress in glass	$\leq$ 40 MPa
Equivalent stress in body	$\leq$ 62 MPa
Equivalent stress in cap	$\leq$ 62 MPa

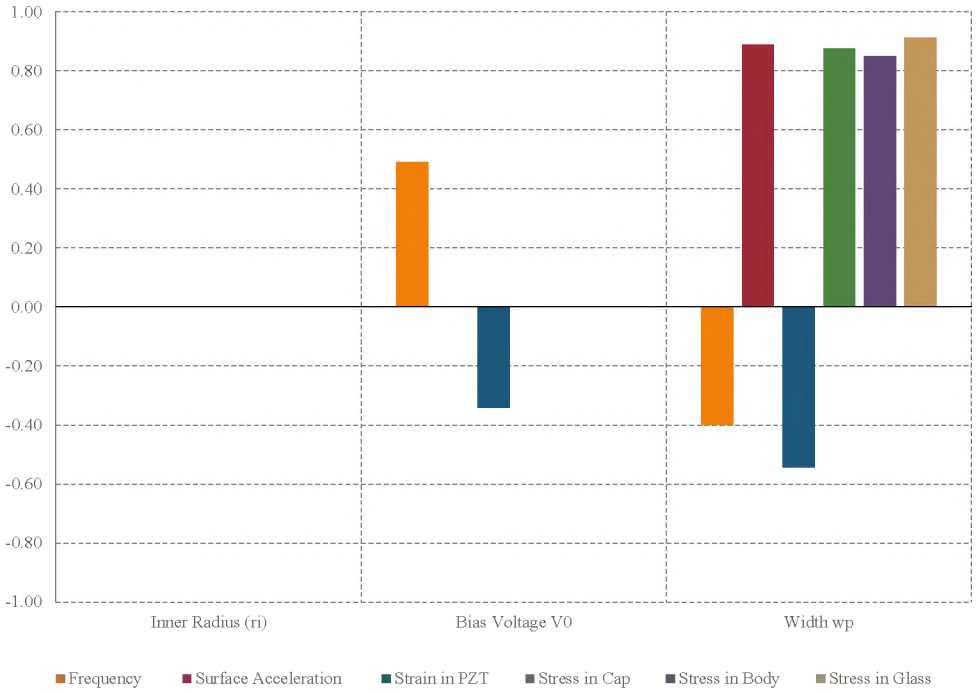

Figure 6.4. Impedance Spectrum from FEA for Prototype 1

temperature or low temperature in the oven, has a low viscosity, long pot life, and high storage modulus. EPO-TEK 301-2FL was used over EPO-TEK 353ND, which was used before, as it requires to be cured at high temperature, and has short pot life that was considered undesirable for the application at this stage. The epoxy glass transition temperature is one parameter that was initially neglected that was of significant importance for the application. It was later found during the epoxy studies that EPO-TEK 353ND was superior to EPO-TEK 301-2FL in bond quality and glass transition temperature. EPO-TEK 301-2FL was mixed and vacuum outgassed. A thin coating of epoxy was applied to one side of the PZT ring, and the PZT ring was visually aligned with the silver electrode on the glass. A 50 g mass was placed on top of the PZT to help with the bonding process and to achieve a thin bond-line with high-point contact between the PZT and the silver electrode. The epoxy was cured in an oven at 80°C for 3 hours. After cooling and visual inspection of the prototype, wire

Table 6.3. Prototype Dimensions

Parameter	Prototype 1	Prototype 2
R_i	8.81 mm	8 mm
R_o	12.06 mm	9.655 mm
R_g	15.875 mm	15.875 mm
w_p	3.25 mm	1.655 mm
h_g	0.5mm	0.5 mm
h_p	1.02 mm	1.02 mm
V_0	40 V	40 V
PZT	SM412-PZT4	SM412-PZT4
Glass	non-ion-exchanged glass	non-ion-exchanged glass

leads were attached to the prototype by soldering wires to the silver electrode on the glass and PZT. The geometric parameter values of the two prototypes built are shown in Table 6.3.

6.1.3. Analysis of the SPS Prototype. To aid in testing and to correlate to a numerical model, separate analysis simulations were performed. The analyses performed on this model were the same as those performed for design optimization. The analysis was conducted at the frequencies of interest, which were based on the prototype's impedance measurement. This analysis gives the response of the prototype under test conditions. The impedance spectrum from the ANSYS analysis for SPS Prototype 1 is shown in Figure 6.5. The Figures 6.6 and 6.7 show the total and the normal acceleration of the glass and PZT at 82 kHz, the first frequency of interest. Similarly, Figures 6.8 and 6.9 show the total and normal acceleration of the glass surface at a frequency of 6.8 MHz. These results give insight into the frequency response of the transducer at each test frequency, the magnitude of the acceleration on the surface, and the stress and strain behavior in the PZT and glass. This analysis identifies the frequencies at which the prototype can be driven for the maximum efficacy.

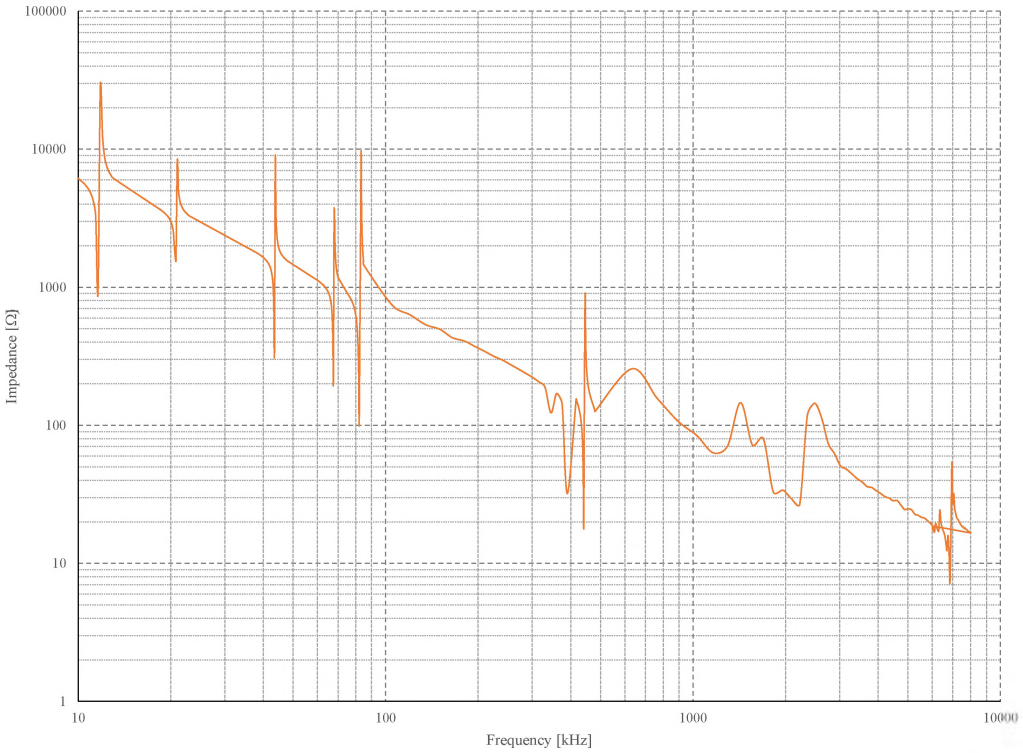

Figure 6.5. Impedance Spectrum from FEA for SPS Prototype 1

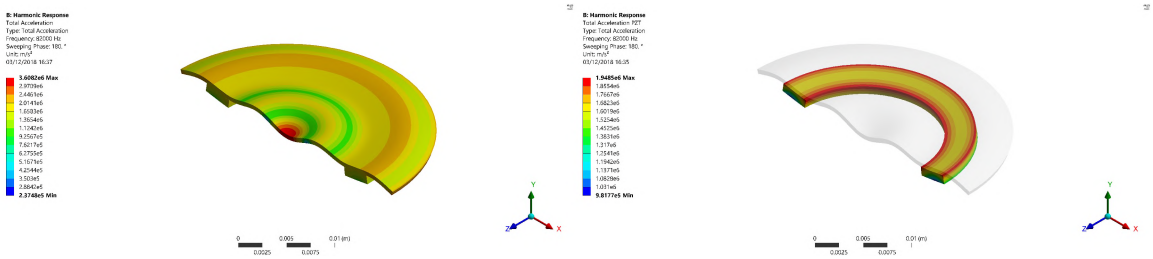

(a) Glass Surface (b) PZT

Figure 6.6. Prototype 1 - Total Acceleration Profile 82 kHz

The impedance spectrum from the ANSYS analysis for SPS prototype 2 is shown in Figure 6.10. Figures 6.11 and 6.12 show the total and the normal acceleration of the glass and the PZT at the first frequency of interest. Similarly, Figures 6.13 to 6.16 show the total and normal acceleration, at 82 kHz and 6.8 MHz, in the PZT and on the glass surface.

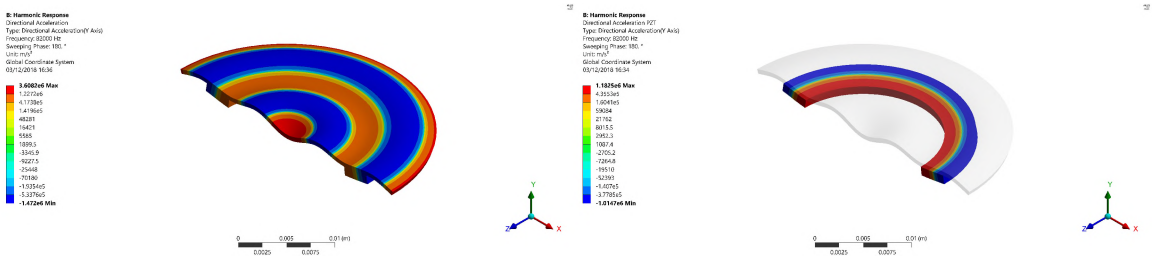

(a) Glass Surface (b) PZT

Figure 6.7. SPS Prototype 1 - Normal Y-Acceleration Profile 82 kHz

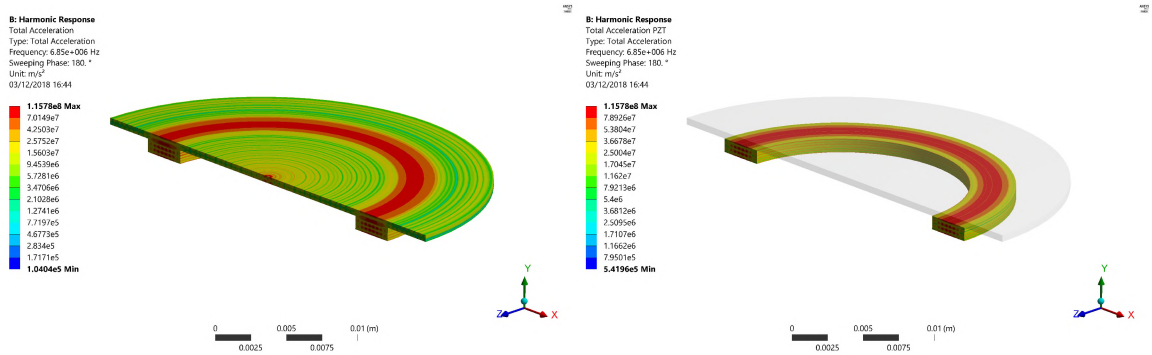

(a) Glass Surface (b) PZT

Figure 6.8. Prototype 1 - Total Acceleration Profile 6.8 MHz

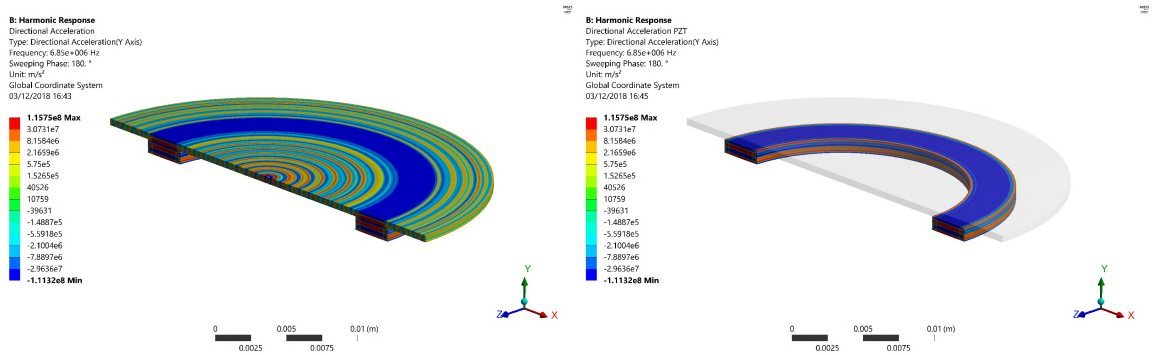

(a) Glass Surface (b) PZT

Figure 6.9. SPS Prototype 1 - Normal Y-Acceleration Profile 6.8 MHz

6.1.4. Impedance Spectroscopy of the SPS Prototype. Impedance spectroscopy is a commonly used technique to characterize, check the health, determine the quality factor, and identify the impedance of the prototype at the excitation frequencies [41]. The Butterworth-Van Dyke resonator (BVD) circuit model, shown in Figure 6.17, is the most

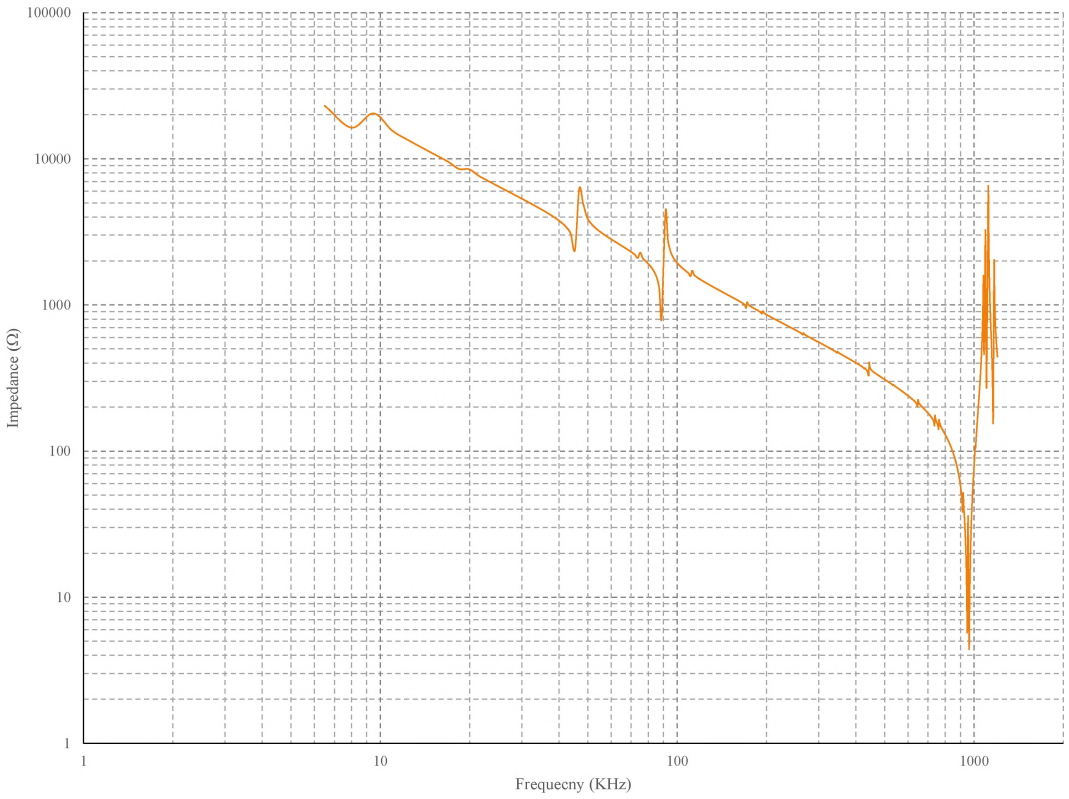

Figure 6.10. Impedance Spectrum from FEA for SPS Prototype 2

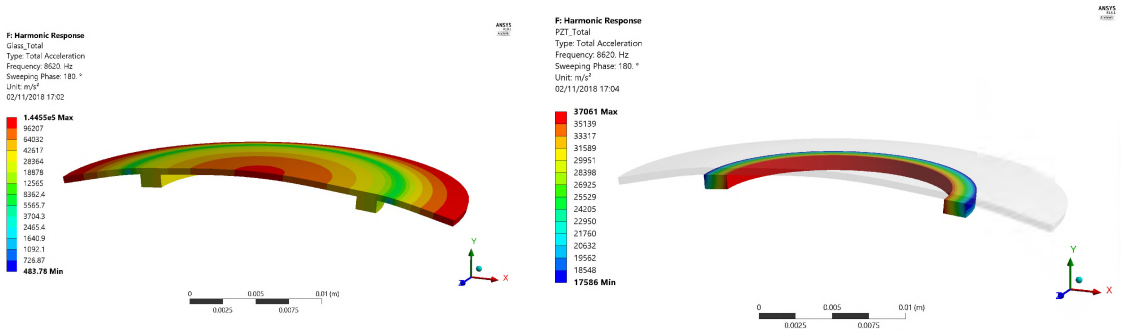

(a) Glass Surface

(b) PZT

Figure 6.11. SPS Prototype 2 - Total Acceleration Profile 7.6 kHz

commonly used model and is the recommended model for piezoelectric transducers [41]. The equivalent circuit consists of two parallel legs: (1) the C_0 parallel capacitance, and (2) the RLC series motional leg. At frequencies far away from any resonance/antiresonance frequencies, a piezoelectric structure behaves like a capacitor with $i(t) = i_C(t)$, and the mo-

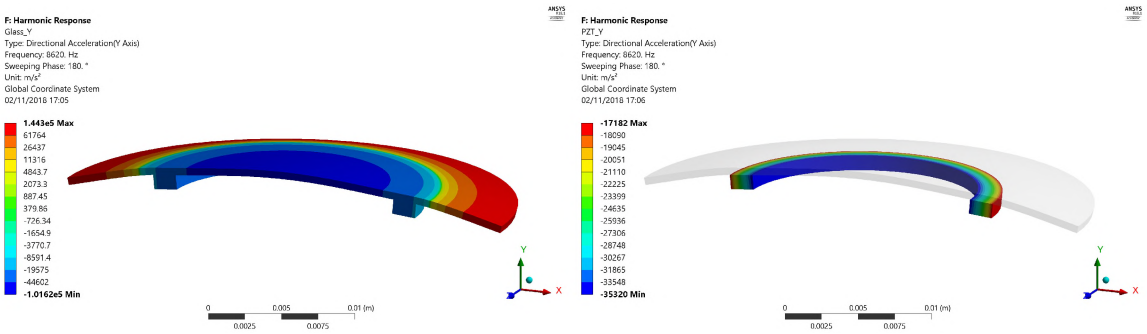

(a) Glass Surface (b) PZT

Figure 6.12. SPS Prototype 2 - Normal Y-Acceleration Profile 7.6 kHz

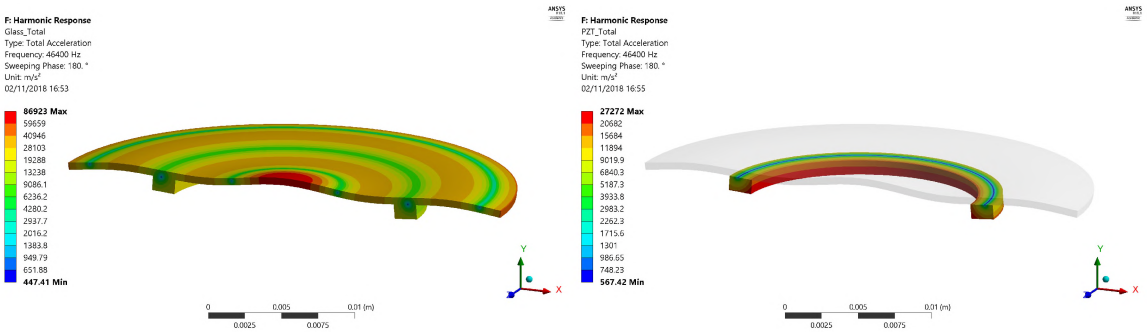

(a) Glass Surface (b) PZT

Figure 6.13. SPS Prototype 2 - Total Acceleration Profile 46 kHz

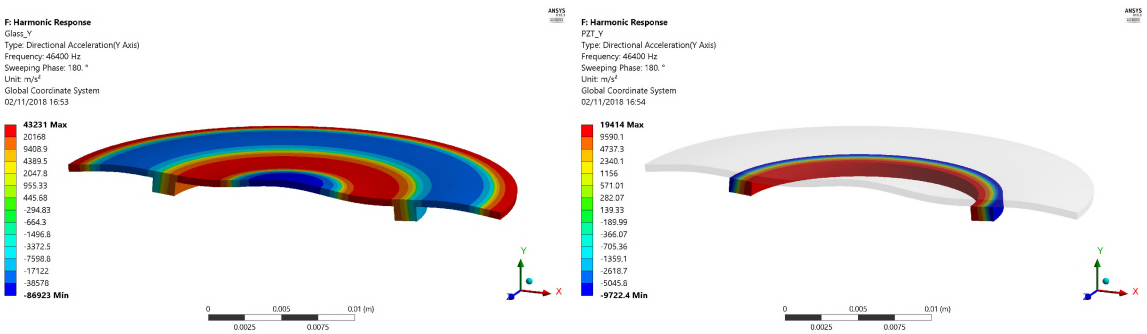

(a) Glass Surface (b) PZT

Figure 6.14. SPS Prototype 2 - Normal Y-Acceleration Profile 46 kHz

tional leg vanishes. Near a resonance-antiresonance frequency pair, however, the motional leg becomes apparent. At the resonance frequency, f_r, the current is dominated by the current in the motional leg referred to as the motional current, i_m, and $i(t) \approx i_m(t)$ [1]. A

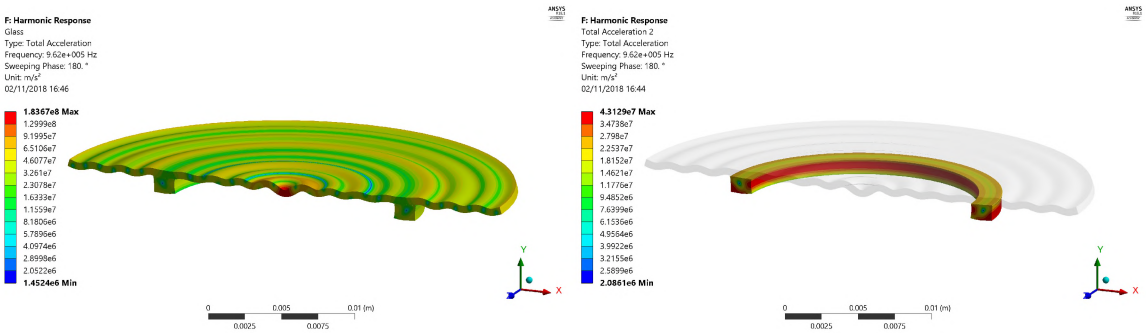

(a) Glass Surface (b) PZT

Figure 6.15. SPS Prototype 2 - Total Acceleration Profile 999 kHz

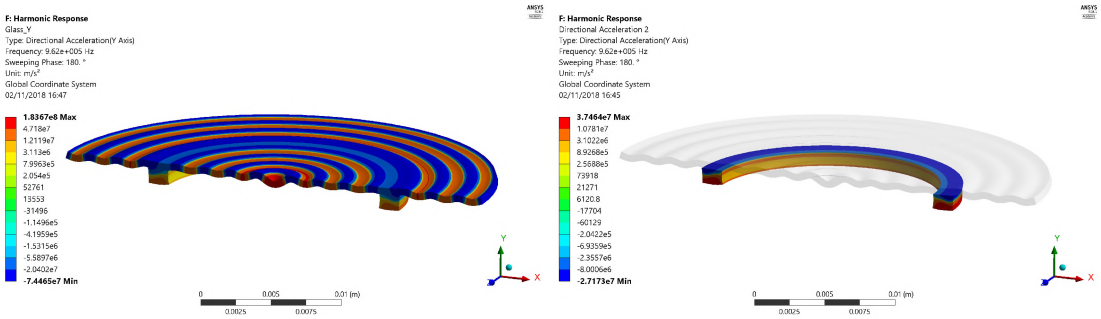

(a) Glass Surface (b) PZT

Figure 6.16. SPS Prototype 2 - Normal Y-Acceleration Profile 999 kHz

Python code was developed and used to estimate the equivalent circuit parameters. The code can be found in Appendix A2. The impedance is measured at a low electrical field using an HP4294A impedance analyzer. The measured impedance and estimated parameters help guide the testing of the prototypes by locating the resonance frequencies and determining the corresponding quality factor, Q.

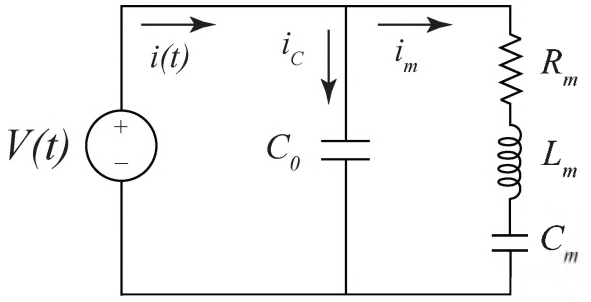

Figure 6.17. Butterworth-Van Dyke Resonator Circuit Model

6.1.4.1. SPS prototype 1. Impedance analysis was conducted in the frequency range of 5 kHz to 20 MHz, and an impedance spectrum was collected around each significant resonance-antiresonance pair. The full impedance spectrum for the SPS prototype is shown in Figure 6.18. Each of the modes was characterized by estimating the parameters of the cc -1.

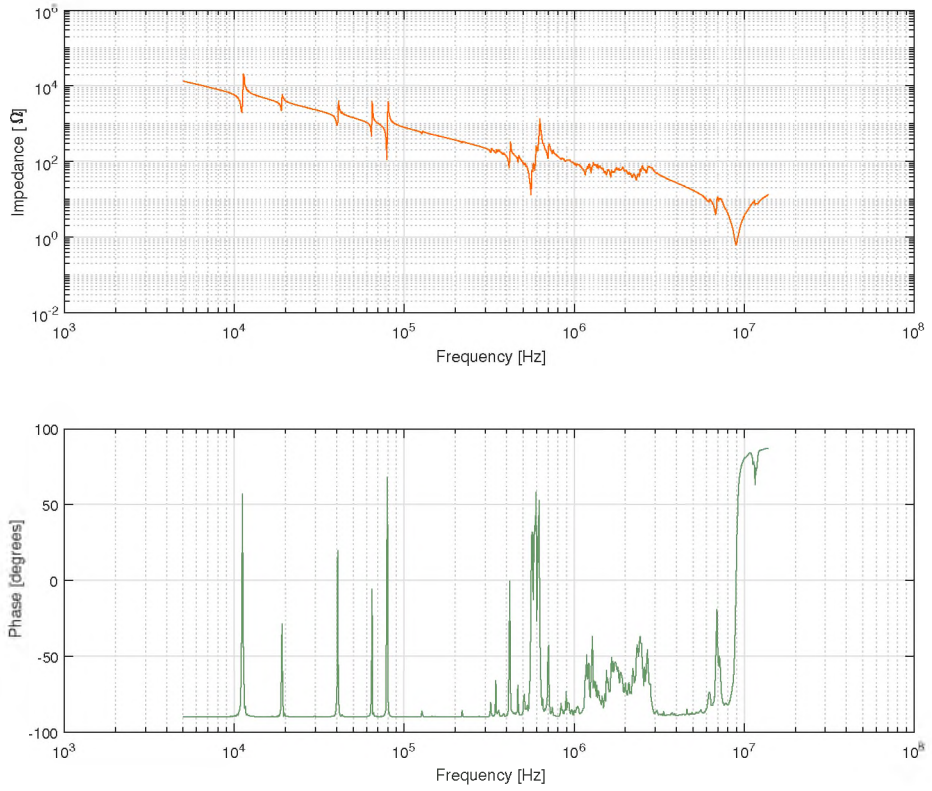

Figure 6.18. Impedance Spectrum - SPS Prototype 1

Table 6.4. SPS Prototype 1 Equivalent Circuit Parameters

Mode	f_r [kHz]	f_a [kHz]	C_0 [nF]	R_1 [Ω]	L_1 [H]	C_1 [pF]	Q_m
Mode 1	11.06	11.27	2.2954	1765.07	2.3268	80.98	91.61
Mode 2	18.98	19.1	2.2288	2643.17	2.6869	26.14	121.28
Mode 3	40.43	40.74	2.2776	618.4	0.4424	35.02	181.73
Mode 4	64.32	64.74	2.2823	389.33	0.2021	30.23	209.76
Mode 5	78.81	80.04	2.0460	89.05	0.0637	64.04	354.09
Mode 6	555.44	605.98	1.4605	16.39	0.0002	27.79	62.90
Mode 7	415.93	419.79	2.6099	92.14	0.0030	48.56	85.51

The equivalent circuit parameters for the SPS Prototype 1 based on the BVD circuit for modes one through six are tabulated in Table 6.4. The BVD model fails to converge for low Q_m modes (Mode 8), and they are not useful as they would have poor efficacy [41]. Figure 6.20 shows the BVD model fit across the entire impedance spectrum.

6.1.4.2. SPS prototype 2. Similarly to SPS Prototype 1, the impedance analysis was conducted in a frequency range of 5 kHz to 20 MHz. A detailed impedance spectrum was collected around each significant resonance peak. The full impedance spectrum for SPS Prototype 2 is shown in Figure 6.19. Each of the modes was characterized by its equivalent circuit model. Modes one through eight are shown in Appendix 3.42.

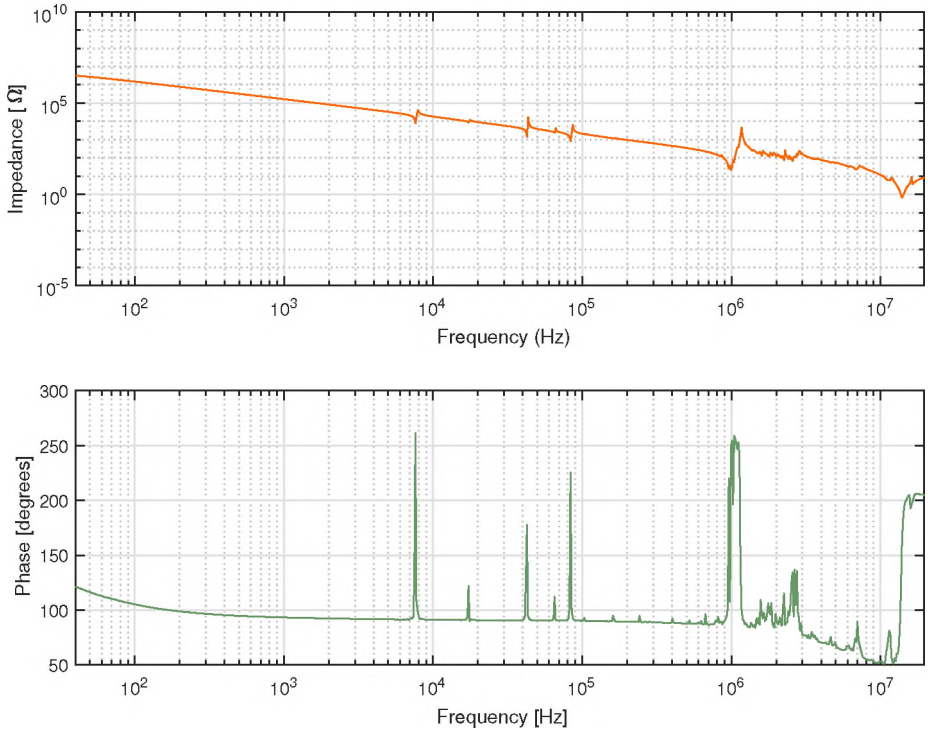

Figure 6.19. Impedance Spectrum - SPS Prototype 2

The equivalent circuit parameters for prototype 2 based on the BVD model were calculated for each mode, and are tabulated in Table 6.5. Similar to Mode 8 in SPS Prototype 1, Mode 2 of SPS Prototype 2 does not fit the BVD model.

Table 6.5. SPS Prototype 2 Equivalent Circuit Parameters

Mode	f_r [kHz]	f_a [kHz]	C_0 [nF]	R_1 [Ω]	L_1 [H]	C_1 [pF]	Q_m
Mode 1	7.65	7.77	0.9192	5733.37	15.32	28.20	128.55
Mode 3	42.80	43.41	0.88	1659.76	0.5438	25.42	88.12
Mode 4	84.21	85.56	0.812	335.16	0.136	26.26	214.7
Mode 5	999.835	1071.3	0.871	6.597	0.00019	132.24	182.45

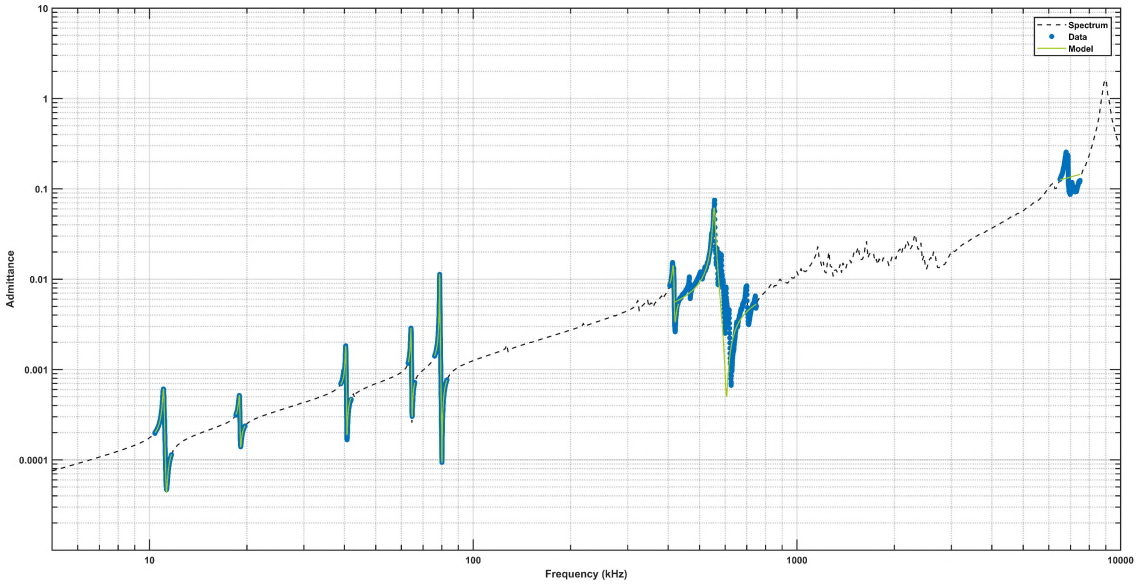

Figure 6.20. Admittance Spectrum Model Fit - SPS Prototype 1

6.1.4.3. Comparison of measured impedance and finite element analysis impedance of the SPS prototype. The impedances measured from SPS Prototype 1 and 2 were superimposed on the ANSYS FEM-model predicted impedance, and are shown in Figures 6.21 and 6.22 respectively. As seen in the figures, the FEA impedance closely follows the impedance spectrum measured by the impedance analyzer. There are some discrepancies with the measured frequency and amplitude of the ANSYS impedance prediction that arise due to factors which include the variation of material properties from the manufacturer's published values, and the aging effect on piezoelectric constants. The FEA model also assumes that the PZT ring is concentrically bonded to the glass, and the contact elements are used to represent the epoxy and bond stiffness. Damping is assumed to be constant,

but, in actuality, the damping is frequency and material dependent. All of these factors can contribute to the deviation of the measured impedance spectrum from that predicted by FEA.

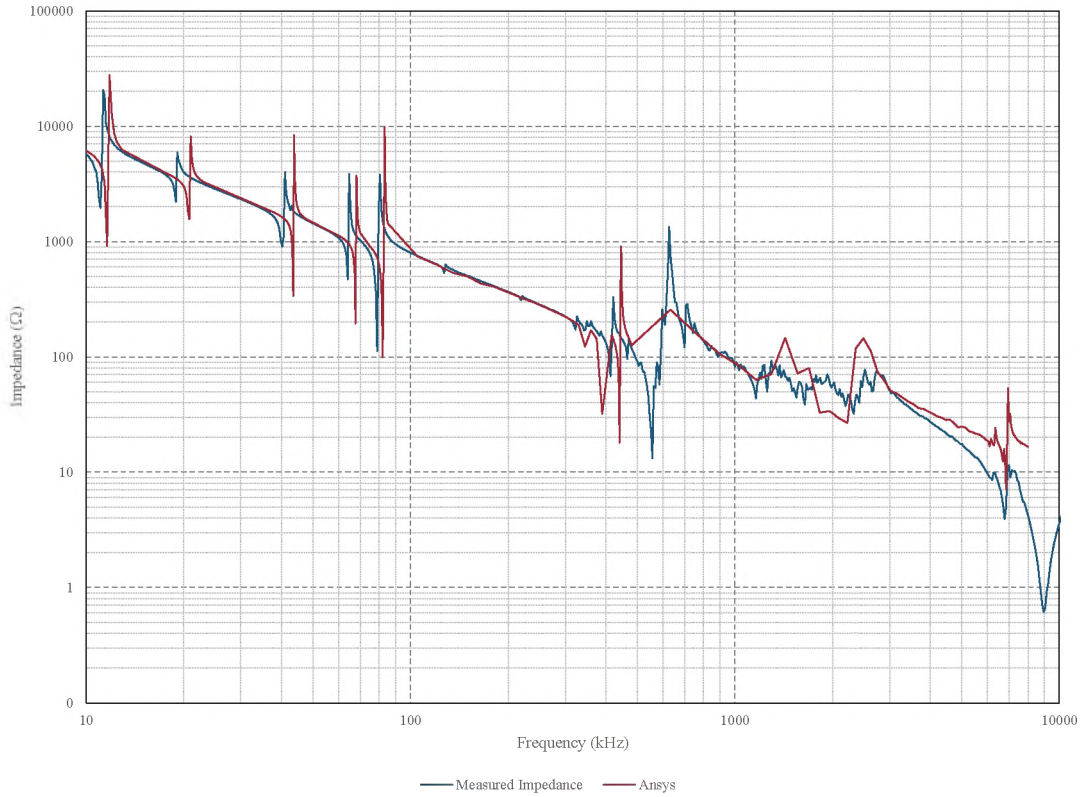

Figure 6.21. ANSYS and Measured Impedance - SPS Prototype 1

6.1.5. Testing Setup, Procedure and Measurements of the SPS Prototype. After building and characterizing the SPS prototypes, prototypes were tested for their efficacy at removing both solid and liquid contaminants. Contaminant tested include table salt, aluminum oxide, silicon carbide, water, mineral oil and toothpaste.

6.1.5.1. Test setup. The block diagram of the test setup for the SPS prototypes is shown in Figure 6.23. Figure 6.24 shows the electrical equivalent driving circuit of the setup. In this setup, an amplified sinusoidal signal from the source, V_1, is passed through the blocking capacitor, and the DC voltage, V_2, is passed through a diode before being combined with V_1. This is done to protect the AC amplifier from the DC power supply and vice versa. The combined signal is then applied to the prototype. In Figure 6.24,

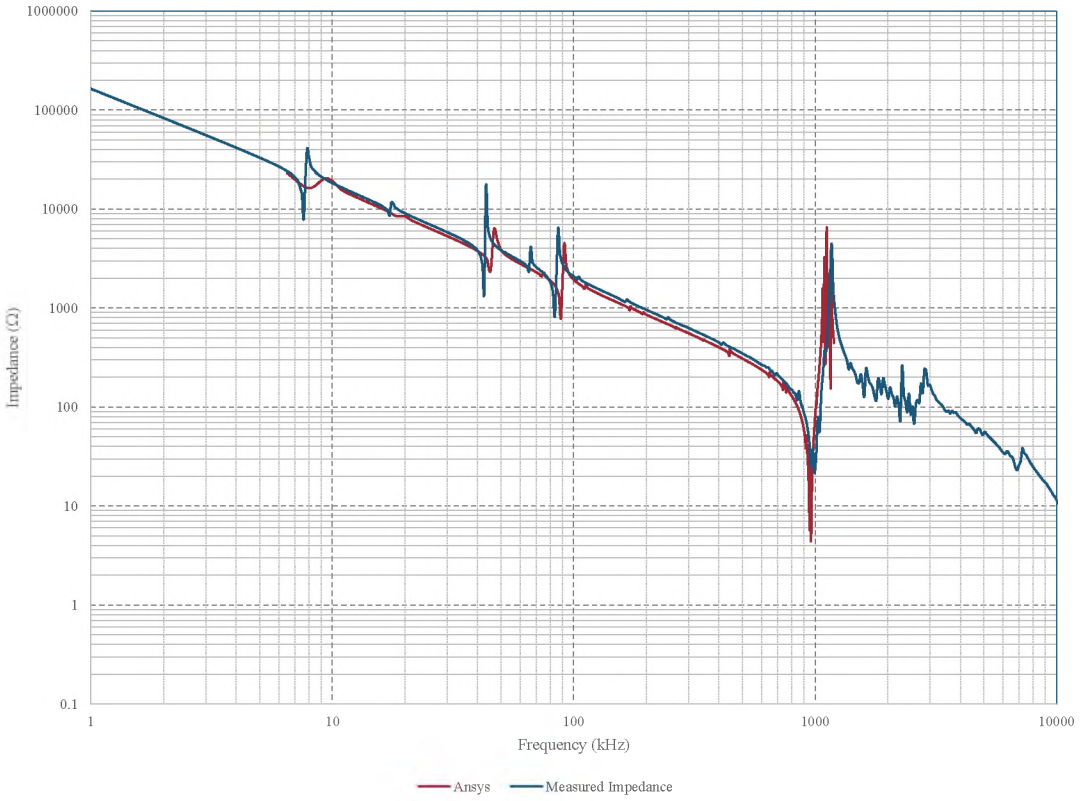

Figure 6.22. ANSYS and Measured Impedance - SPS Prototype 2

the transducer is shown as the BVD equivalent circuit model. In this figure, the values are for SPS Prototype 2 Mode 3 before the prototype was tested. The driving circuit is independent of the prototype and the structural mode being driven. The sinusoidal signal is generated from a Yokogawa FG120 Function generator and then amplified by an ENI 2100L RF amplifier. A BK precision 1740 DC power supply is used to supply the DC-bias. In addition to the driving circuit, a voltage probe from a TEK 460A oscilloscope is connected at TP1 to measure the input voltage, and a current probe is attached to the transducer's return path to measure the current. Additionally, two type T thermocouples are attached to each prototype. One of the thermocouples is attached to the PZT directly via cyanoacrylate (CA) glue. The other thermocouple is attached to the glass surface directly over the PZT. The temperature at both thermocouples is recorded every 200 milliseconds during each test.

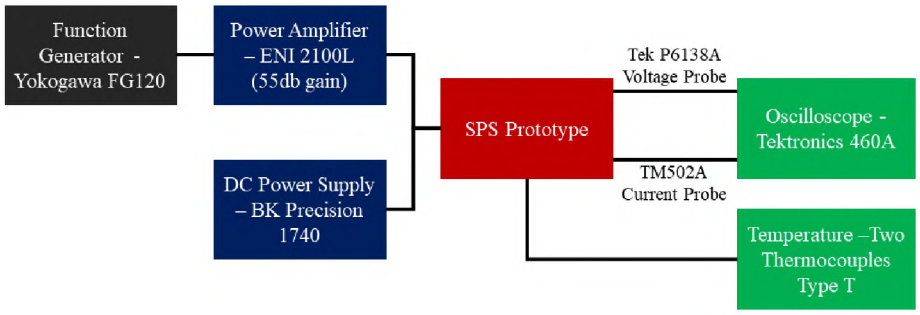

Figure 6.23. Test Setup Block Diagram

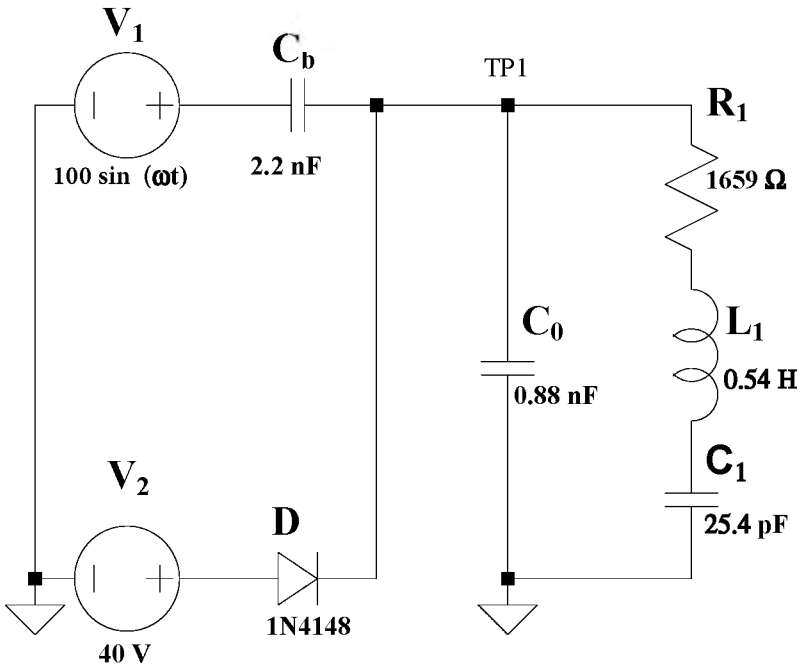

Figure 6.24. Electrical Drive Circuit and Equivalent BVD Prototype Model

6.1.5.2. Procedure. The contaminant is evenly distributed on the prototype surface. Then one of the modes identified by the impedance spectroscopy is selected, and the test frequency and the low input voltage are set on the signal generator. The frequency and amplitude are then adjusted around the mode's resonance until the contaminant particles start moving, and the phase between current and voltage measurement is minimized. The amplitude of the signal is gradually increased once the particles start moving to achieve either nebulization of the fluid or removal of the solid particles from the surface. The

prototype is put through a short duty cycle for each test. At each test point, data is recorded manually from the oscilloscope. A successful test requires anywhere from 10 to 50 cycles at varying signal amplitudes and frequencies. It is desired to keep the prototype from overheating; if a prototype reaches over 100°C, testing is immediately stopped in order to allow the prototype to cool down. In addition to the physical measurements, a video was recorded to capture nebulization and solid particle removal.

The impedance of mode 8 of SPS Prototype 1 (see Appendix 1 Figure 8) is approximately 10 Ω and the output impedance of the EIN 2100L RF power amplifier is 50 Ω; this would lead to a mismatch of impedance between the prototype and the amplifier. To ensure that the amplifier would always see a 50 Ω load, an LC compensation network was introduced between the prototype and drive circuit. The compensation network is shown in Figure 6.25. In this figure, the BVD equivalent circuit is shown for mode 3 of the SPS Prototype 2 as the equivalent circuit model fails to converge for mode 8 of SPS Prototype 1 [41].

After testing the first prototype, many issues were discovered. There was no set testing procedure, and the duty cycle for the tests was arbitrary because it relied on the tester turning the amplifier on and off. Subsequently, a LabVIEW program was developed, which can control the duty cycle and measure all of the interest parameters simultaneously during the test.

6.1.5.3. Measurements. At each test point, the voltage magnitude, current magnitude, and phase of the signal driving the prototype under test were measured along with the PZT and glass surfaces' temperatures. A test summary of the measurements for SPS Prototypes 1 and 2 is provided in Tables 6.7 and 6.8. The test frequency, voltage, current, power, and temperature in the tables were recorded after the contaminant was removed. Figure 6.26 shows Prototype 2 under test.

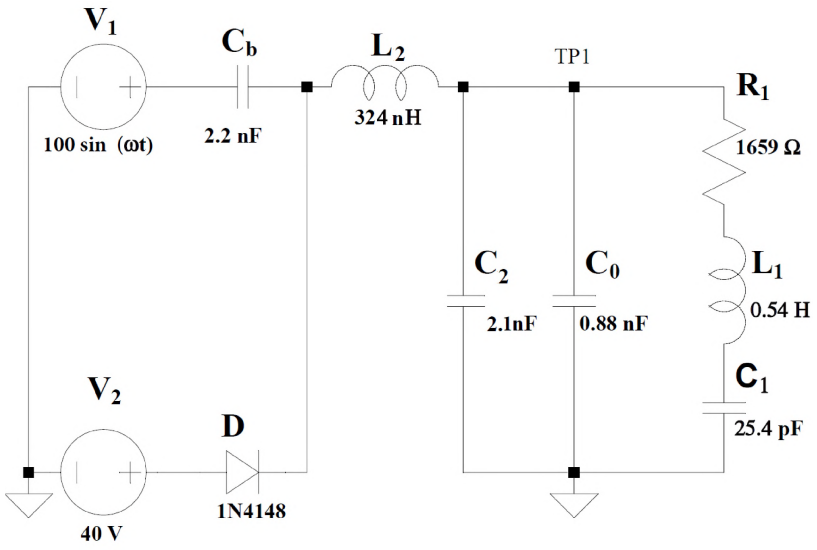

Figure 6.25. Electrical Drive Circuit with LC Compensation Network and Equivalent BVD Prototype Model

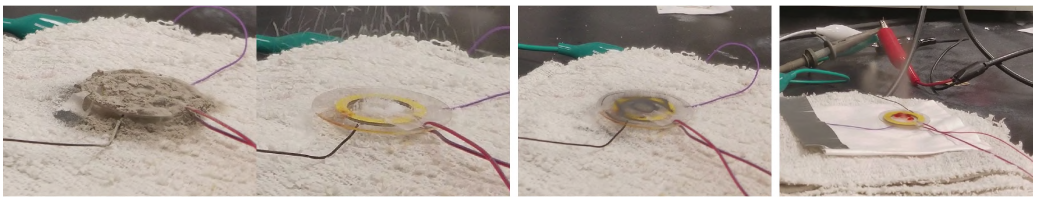

(a) Aluminum Oxide (b) Salt (c) Silicon Carbide (d) Water

Figure 6.26. SPS Prototype 2 - Test

6.1.6. SPS Prototype Efficacy Matrix. The performance of SPS Prototypes 1 and 2 is shown in Tables 6.6 and 6.9. Currently, there is no quantifiable method to measure the efficacy of the prototype. A visual inspection was performed to see if a contaminant was successfully removed during testing.

Table 6.6. Efficacy Matrix for SPS Prototype 1[1]

Contaminant	Density [kg/m^3]	Particle Size Viscosity	78.59 [kHz]	6.8 [MHz]
Water	1000	0.890 cps	Yes	Yes

[1] Color Code: Green = Success, Orange = Partial success, Red = Failure

Table 6.7. SPS Prototype 1 Test Data

Contaminant	**F [kHz]** Test Frequency	**V_p [V]** Voltage Amplitude	**I_p [A]** Current Amplitude	**S [VA]** Apparent Power	**P [W]** True Power	**Q [VAR]** Reactive Power	**T_{PZT} [°C]** Temp. of PZT	**ϕ [°]** Phase
Water ~ 0.06 g	78.59	114	1.28	145.92	95.34	-110.46	43.5	-49.2
Water ~ 0.06 g	78.59	132	1.84	242.88	158.70	-183.86	42.0	-49.2
Water ~ 0.06 g	6800	90	10.8	972	202.09	950.75	40.6	78

Table 6.8. SPS Prototype 2 Test Data

Contaminant	**F [kHz]** Test Frequency	**V_p [V]** Voltage Amplitude	**I_p [A]** Current Amplitude	**S [VA]** Apparent Power	**P [W]** True Power	**Q [VAR]** Reactive Power	**T_{PZT} [°C]** Temp. of PZT	**ϕ [°]** Phase
Table Salt ~ 0.06 g	42.8	44	0.138	6.07	6.05	-0.39	20.7	- 3.7
Silicon Carbide ~ 0.07 g	7.681	22	0.02	0.44	0.18	0.39	22.7	64.9
Silicon Carbide ~ 0.07 g	42.8	44	0.144	6.34	6.43	0.0	24.0	0
Aluminum Oxide ~ 0.19 g	7.681	29	0.02	0.58	-0.29	-0.50	24	-120
Aluminum Oxide ~ 0.19 g	42.8	78	0.162	12.63	12.61	0.86	33.0	3.9
Water ~ 0.06 g	980	26.8	2.04	54.67	52.55	-15.07	40.7	-16
Mineral Oil ~ 0.05 g	996	82	0.2	16.4	16.16	2.79	25.12	9.8
Toothpaste ~ 0.04 g	996	82	0.38	31.16	29.28	10.66	75	20

Table 6.9. Efficacy matrix for SPS Prototype 2[1]

Contaminant	Density [kg/m^3]	Particle Size Viscosity	7.68 [kHz]	42.8 [kHz]	998.36 kHz [kHz]
Water	1000 kg/m^3	0.890 cps	No	No	Yes
Salt	1234 kg/m^3	100 μm	Yes	Yes	No
Silicon Carbide	3210 kg/m^3	75 μm	Yes	Yes	No
Aluminum Oxide	3950 kg/m^3	9.5 μm	Partial	Partial	No
Mineral Oil	830 kg/m^3	700 cps	No	No	Partial
Toothpaste	1450 kg/m^3	70,000-10,0000 cps	No	No	Contaminant moves

[1] Color Code: Green = Success, Orange = Partial success, Red = Failure

6.1.7. SPS Prototype Design Remarks. The SPS design has shown good potential for the removal of contaminants. The lower frequency modes tend to work better in removing solid particles, while the megasonic frequency modes tend to move or nebulize fluid contaminants more easily.

6.2. MASS LOADED SINGLE PZT SYSTEM

The mass loaded PZT (MPS) system was the third prototype to be designed and analyzed. The added mass puts the PZT in compression in the in-plane (r,θ) direction due to the CTE mismatch between the PZT and metal. Figure 6.27 shows the critical parameters of the MPS design and the MPS prototype. The MPS design introduces one new variable: the thickness of the metal mass. The build process, test, and measurement procedure for the MPS prototype are precisely the same as used for the SPS design. One prototype was built according to dimensions in Table 6.10. This design was based on SPS Prototype 1 to avoid producing separate PZT rings.

6.2.1. Analysis of MPS Prototype. An ANSYS model of the prototype was developed to predict the prototype's behavior, aid in testing, and provide a correlating numerical model. The analyses of the model were based on the measured dimensions of the prototype. The analyses performed on this model were the same as those performed for design optimization. The impedance measurement of the prototype was used to determine the

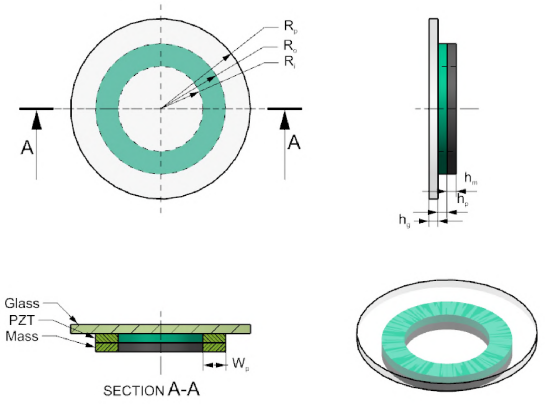

(a) MPS-Design

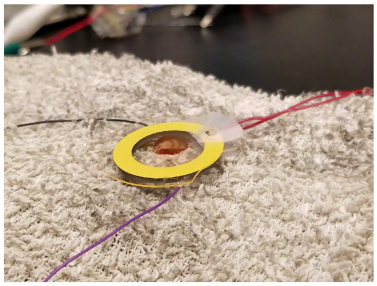

(b) MPS Prototype

Figure 6.27. MPS-Prototype

Table 6.10. MPS Prototype Dimensions

Parameter	MPS Protoype
R_i	8.70 mm
R_o	12.11 mm
R_g	15.875 mm
w_p	3.41 mm
h_g	0.5mm
h_m	1 mm
h_p	1.02 mm
V_0	40 V
PZT	SM412-PZT4
Glass	non-ion-exchanged glass

frequency range at which the analysis was conducted. Figure 6.28 shows the total and normal acceleration in the Y-axis of the prototype at 81.6 kHz. Similarly, Figures 6.29 and 6.30 show the total and normal acceleration of the PZT and the mass at 81.6 kHz.

6.2.2. Impedance Spectroscopy of the MPS Prototype. The MPS Prototype PZT ring was characterized before building the prototype, after assembly, and subsequently following testing. This allows quantification of the quality of prototype build and any possible damage from testing. Figure 6.31 shows the impedance spectrum of the MPS

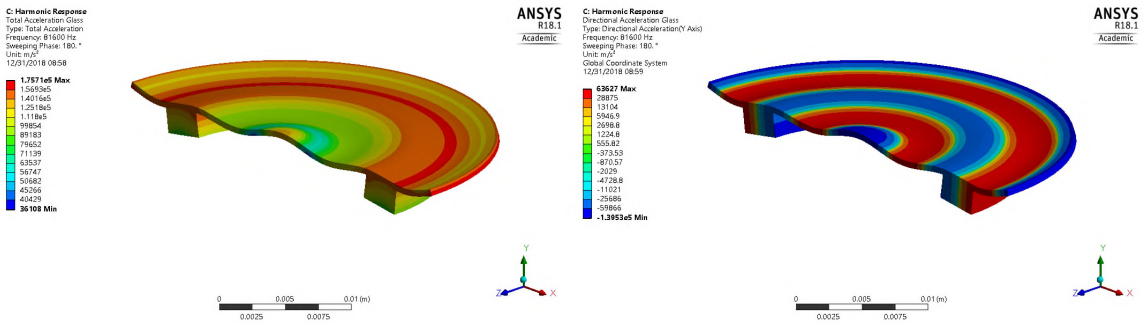

(a) Total Acceleration (b) Normal Y-Acceleration

Figure 6.28. MPS Prototype - Acceleration Profile of Glass 81.6 kHz

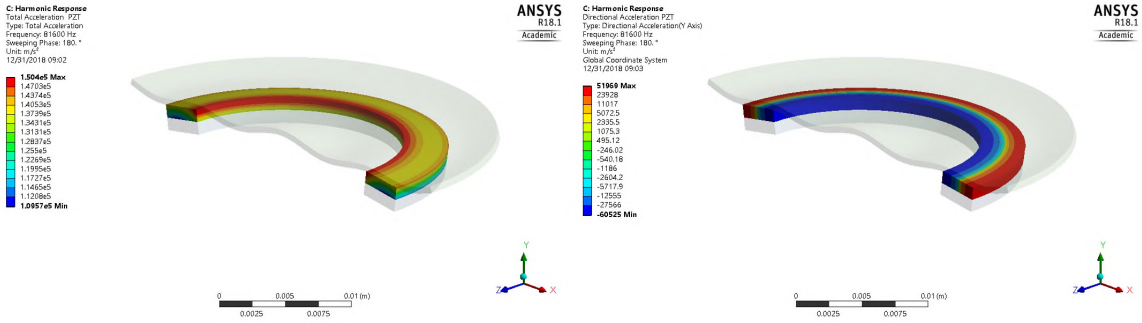

(a) Total Acceleration (b) Normal Y-Acceleration

Figure 6.29. MPS Prototype - Acceleration Profile of PZT 81.6 kHz

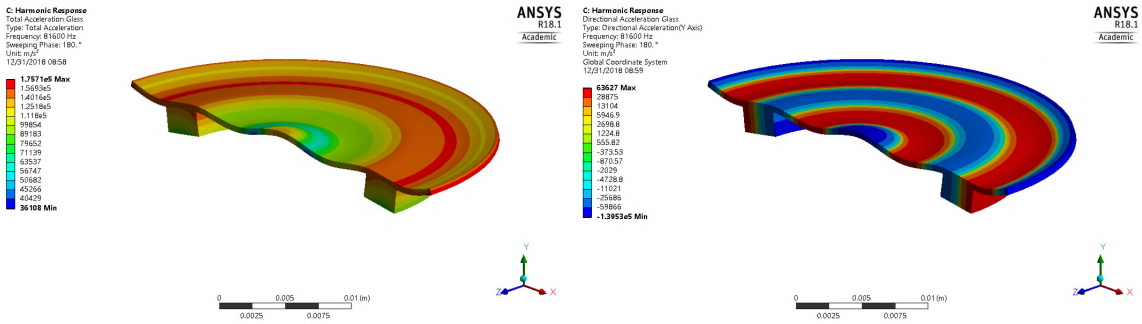

(a) Total Acceleration (b) Normal Y-Acceleration

Figure 6.30. MPS Prototype - Acceleration Profile Mass 81.6 kHz

Prototype immediately after it was built, and Figure 6.32 shows the corresponding BVD equivalent circuit parameters and model fit of Mode 1. The quality factor of the MPS Prototype was initially 225.

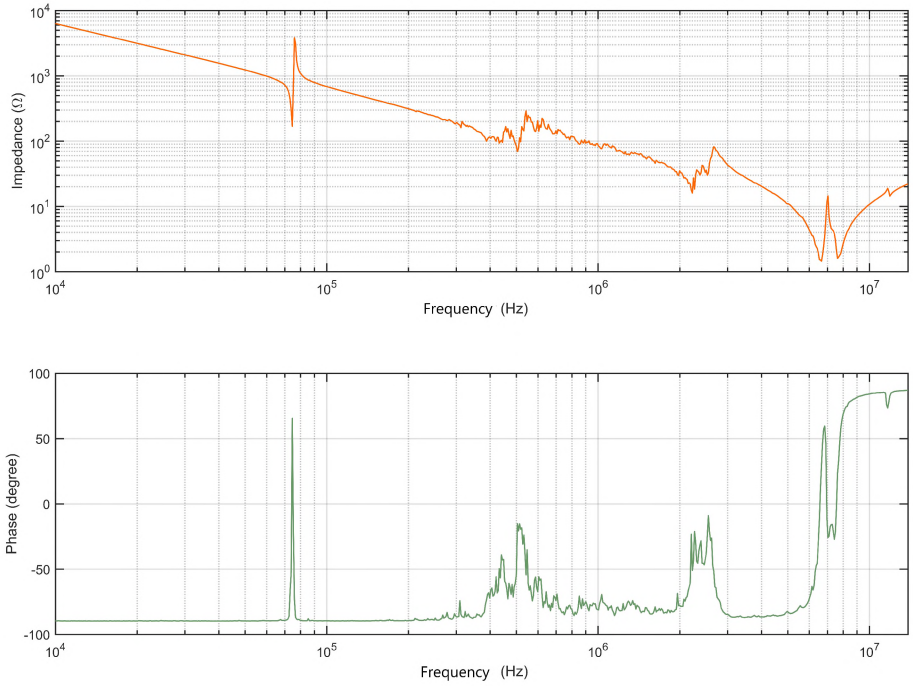

Figure 6.31. Impedance Spectrum of MPS Prototype

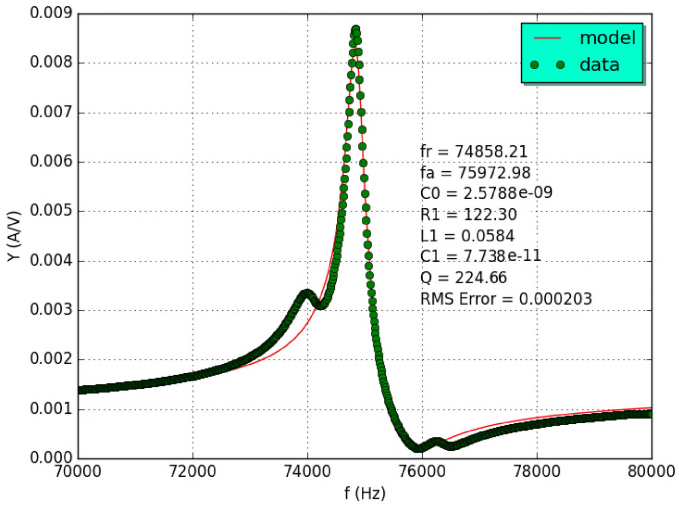

Figure 6.32. Mode 1 - Impedance of MPS Prototype Before Test

Figure 6.33 shows mode one after testing, which has a quality factor of 103. This 54% drop in quality factor corresponds to the damage to the MPS Prototype. The damage can be caused by cracks in the PZT, loss in epoxy strength, etc. Only a limited assessment could be made with the available resources.

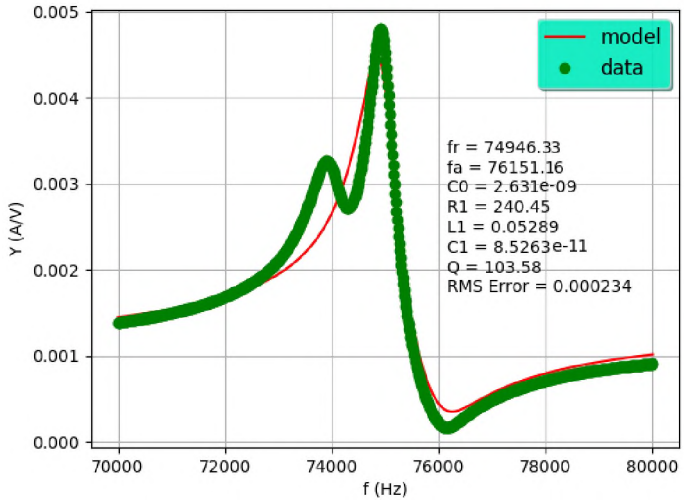

Figure 6.33. Mode 1 - Impedance of MPS Prototype After Test

6.2.3. Test Measurements of the MPS Prototype. As mentioned in Section 6.1.5, a new automated measurement system was developed in LabVIEW for testing this prototype. The system allows for rapid and simultaneous measurement of all of the test parameters. The system also controls the number of times the prototype is actuated and the amount of time it is actuated. In the process of testing this prototype, the prototype was subjected to over 100 cycles at varying frequencies and voltage amplitudes. Table 6.11 shows the measured parameters during testing. The table only includes the measurements when contaminant removal was achieved. Figure 6.34 shows the MPS prototype in test.

6.2.4. Efficacy Matrix of the MPS Prototype. The performance of the prototype is summarized in Table 6.12. See Section 6.1.6, a visual inspection of the prototype was performed to see if the contaminant was removed.

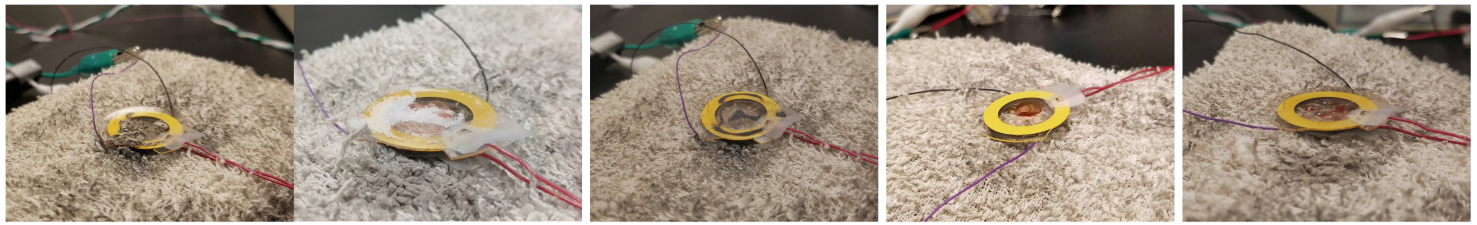

(a) Silicon Carbide (b) Salt (c) Aluminum Oxide (d) Water (e) Mineral Oil

Figure 6.34. MPS Prototype - Test

Table 6.11. MPS Prototype Test Data

Contaminant	**F [kHz]** Test Frequency	**V_p [V]** Voltage Amplitude	**I_p [A]** Current Amplitude	**S [VA]** Apparent Power	**P [W]** True Power	**Q [VAR]** Reactive Power	**T_{PZT} [°C]** Temp. of PZT	**ϕ [°]** Phase
Table Salt 0.06 g	74.6	24	0.76	18.24	14.18	8.92	22.7	- 51
Silicon Carbide 0.07 g	74.65	21	1.03	21.63	21.6	1.13	23.4	3
Aluminum Oxide 0.19 g	74.65	14	0.24	3.36	3.2	0.28	21.41	16.2
Water 0.06 g	74.4	32	1.5	48	22.6	42.3	35	61.9
Mineral Oil 0.05 g	75.47	15	1.06	15.9	15.89	0.45	27.71	1.6
Toothpaste 0.04 g	74.73	73	0.4	29.2	16.07	24.37	36.8	56.6

Table 6.12. Efficacy Matrix for MPS Prototype[2]

Contaminant	Density	Particle Size/Viscosity	74.8 kHz
Water	1000 kg/m^3	0.890 cps	Yes
Salt	1234 kg/m^3	100 μm	Yes
Silicon Carbide	3210 kg/m^3	75 μm	Yes
Aluminum Oxide	3950 kg/m^3	9.5 μm	Partial
Mineral Oil	830 kg/m^3	700 cps	Partial
Toothpaste	1450 kg/m^3	70,000-10,0000 cps	Partial

[2] Color Code: Green = Success, Orange = Partial success, Red = Failure

6.2.5. MPS Prototype Design Remarks. One of the significant outcomes of testing this prototype was the loss of quality factor. This led us to review the design and build process in-depth, and we found that the EPO-TEK 301-2FL has a glass temperature of approximately 45°C, after which the CTE dramatically rises. At several test cycles, the prototype's temperature exceeded the epoxy's glass transition temperature, which likely resulted in epoxy bond weakening. A weak epoxy bond would limit the extent to which the actuation from the PZT would be transmitted to the glass and consequently cause a loss of the prototype's quality factor. Overall, this prototype performed well at entirely removing or partially removing various contaminants until its failure after about 150 testing cycles.

6.3. RADIALLY SPLIT PZT SYSTEM

The Radially-Split PZT System (RPS) was the fourth prototype built and tested. The design could be realized in two ways: (1) using two PZT rings or (2) splitting the electrode on a single PZT element; for this prototype, the latter method is used. The design can drive the two PZT sectors in-phase, out-of-phase, and at different frequencies. Driving at different frequencies excites two axisymmetric modes. When driven in phase, a lower-frequency axisymmetric mode with a radial half-wavelength corresponding to the combined electrode width can be excited, and when driven 180° out-of-phase; a higher mode with radial wavelength roughly half the former can be excited. In theory, by alternating

between these two modes of excitation, potential radial node lines where contaminants might accumulate can be reduced or eliminated. Figure 6.35a shows the RPS design schematic, and Figure 6.35b shows the assembled prototype. Figure 6.36 shows the poling direction and the drive signal setup for the RPS prototype.

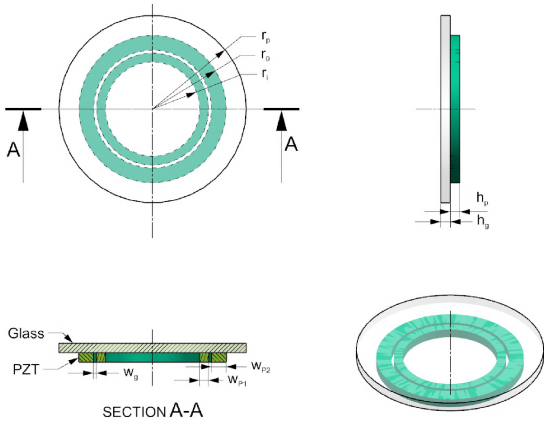

(a) RPS Design

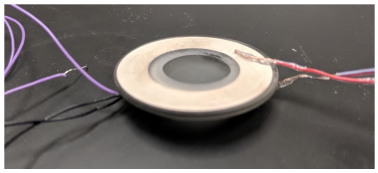

(b) RPS Prototype

Figure 6.35. Radially Split PZT System (RPS)

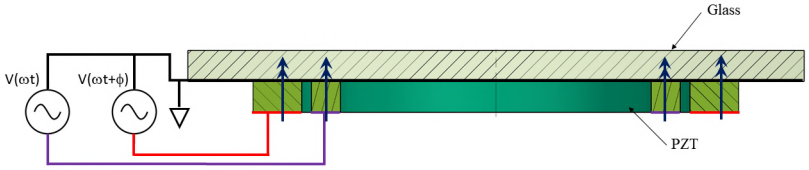

Figure 6.36. PZT Poling and Drive Signal - RPS

6.3.1. RPS Build Process. The RPS build process was similar to that used in the SPS design except with an additional step to separate the top PZT electrode. A tool similar to the tool used to cut the PZT was made to split the PZT electrode into two electrodes and is shown in Figure 6.37. Table 6.13 shows the geometric parameters of the RPS prototype. During the epoxy curing in the oven, the PZT ring shifted, causing it not to be concentric with the glass.

6.3.2. Analysis of the RPS Prototype. ANSYS simulations were performed to help visualize the behavior of the prototype and to aid in testing. The analyses performed on the prototypes are the same as those used to optimize the design. The model in this

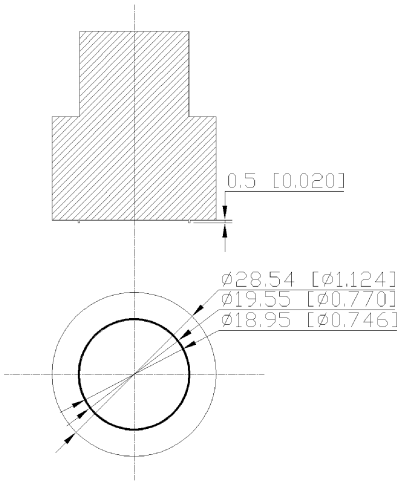

(a) RPS Electrode Separation Tool Design

(b) RPS Ring Cutting Tools

Figure 6.37. Radially Split PZT System (RPS)

Table 6.13. Radially Split PZT System (RPS) Design Parameters

Parameter	RPS Prototype	
r_i	Inner radius of PZT	8.35 mm
w_{p1}	Width of inner PZT ring	1.11 mm
w_{p2}	Width of outer PZT ring	2.38 mm
w_g	Gap between PZT electrodes	0.3 mm
r_o	Outer radius of PZT ($r_o = r_i + w_{p1} + w_g + w_{p2}$)	12.15 mm
r_g	Radius of glass	15.875 mm
h_g	Thickness of glass	1.51 mm
h_p	Thickness of PZT	1 mm

analysis accounts for the measured eccentricity of the prototype. Figure 6.38 shows the comparison of the driven mode and pattern observed on the prototype during the test when both the inner and outer electrode are driven at 88.436 kHz with a phase difference of 180° between inner and outer ring. The contaminant is removed from high acceleration regions and accumulates along the nodal lines of the mode. Figure 6.39 shows the comparison of the prototype and ANSYS model when the inner electrode of the prototype is driven at 485.525 kHz, and the outer electrode is driven at 77.777 kHz. Water nebulization is achieved with

these test frequencies. Figure 6.39b shows the prototype testing under polarized light for photoelasticity. The glass's optical birefringence causes the strain inside the glass to be visible and, therefore, is compared to the maximum principal strain from the ANSYS model.

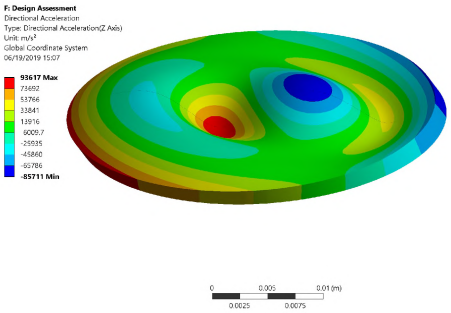

(a) Total Acceleration

(b) Prototype Under Test

Figure 6.38. Inner Electrode 88.436 kHz Phase 0° and Outer Electrode 88.436 kHz Frequency Phase 180°

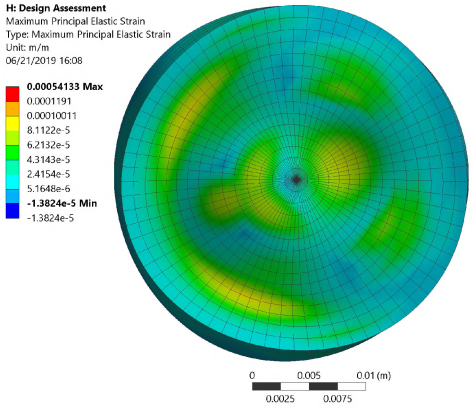

(a) Principal Strain

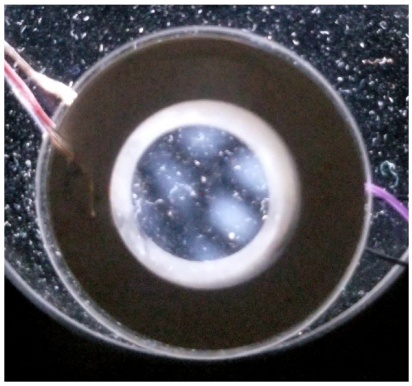

(b) Polarized Light - Maximum Principal Strain Pattern Visualized on Prototype

Figure 6.39. Inner Electrode 485.525 kHz Phase 0° and Outer Electrode 77.777 kHz Frequency Phase 0°

6.3.3. Impedance Spectroscopy of the RPS Prototype. As for all prototypes, the RPS prototype was characterized via impedance spectroscopy. Impedance spectroscopy was carried out on the bare PZT ring before assembly and on the prototype after assembly, both before and after testing. This quantifies the build's quality and helps assess the damage to the prototype due to testing. The total impedance spectra of the PZT before prototype assembly is shown in Figure 6.40, and each mode was characterized and is provided in Appendix

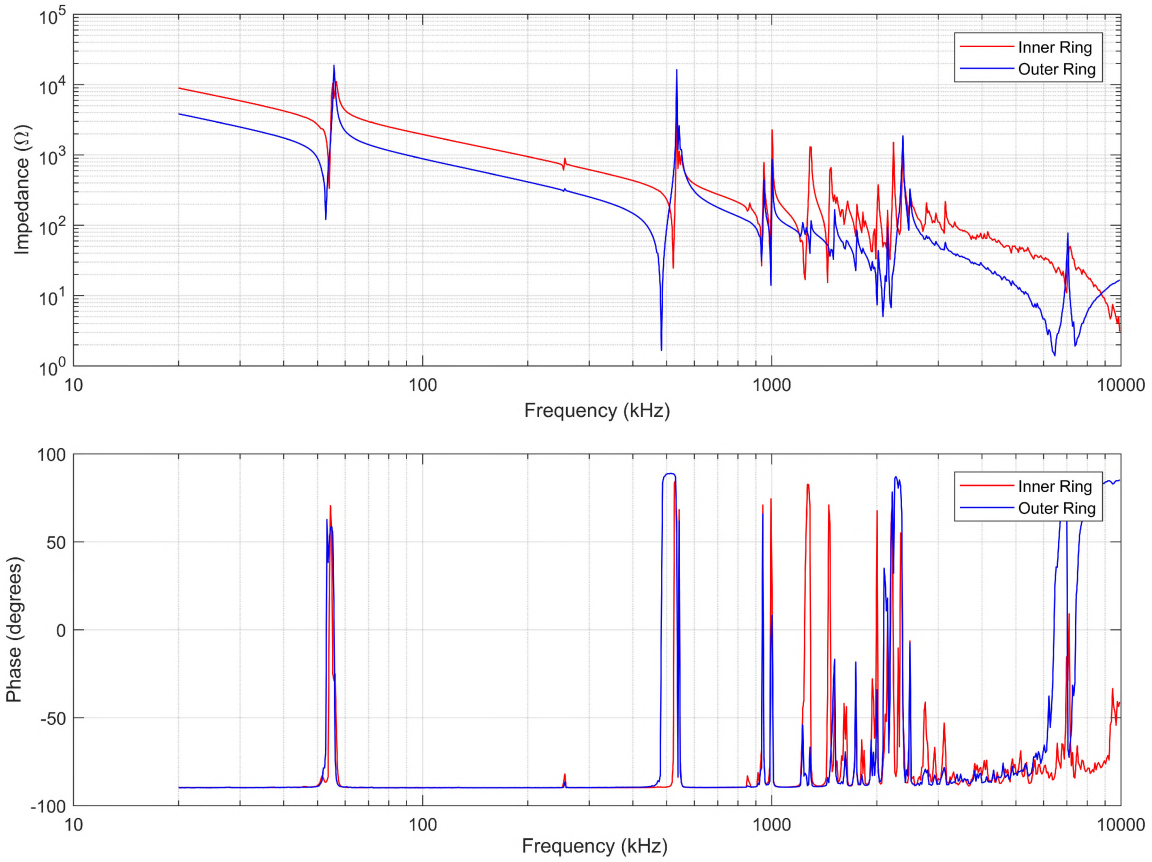

Figure 6.40. RPS Rings Impedance Spectrum Before Assembly

3.43.1. Figure 6.41 shows the comparison of the impedance spectrum of the prototype before, after initial, and after final testing. The corresponding mode characterizations are shown in Appendices 3.43.2, 3.43.3, and 3.43.4 respectively. The equivalent circuit parameters for the RPS Prototype based on the BVD circuit for modes one through eight are tabulated in Table 6.14. The BVD model fails to converge for low Q_m modes (Modes 2, 3 and 6), and they are not useful as they would have low efficacy. Most of the modes fail to converge after testing; this can be attributed to a loss in bond strength. Mode 1, which converges both before and after testing, shows that Q_m changes from 157.7 to 162.4 after the first set of tests and 73.6 after the final set of tests. This shows that there is damage to the prototype from testing and is consistent with the results seen in previous prototypes.

Table 6.14. Equivalent Circuit Parameters for RPS Prototype

Mode	f_r [kHz]	f_a [kHz]	C_0 [nF]	R_1 [Ω]	L_1 [H]	C_1 [pF]	Q_m
Mode 1	18.24	18.72	2.38	433.82	0.597	12.75	157.70
Mode 4	77.77	78.25	2.48	400.32	0.1351	0.031	164.87
Mode 5	88.43	88.99	2.43	163.16	0.1047	0.031	356.46
Mode 7	489.19	541.28	1.81	49.86	0.0003	0.407	16.03
Mode 8	1283.82	129.51	2.07	40.51	0.0004	0.036	82.94

6.3.4. Testing Setup, Procedure, and Measurements of the RPS Prototype.

After building and characterizing the RPS prototypes, prototypes were tested for their efficacy at removing both solid and liquid contaminants. Contaminant tested include table salt, aluminum oxide, silicon carbide, water, mineral oil and toothpaste. The testing process is similar to the SPS prototype, but an additional frequency source and amplifier are added to drive the PZT rings at different frequencies and amplitudes.

6.3.4.1. Test setup. The testing of the RPS prototype was carried out manually. Since the two rings of the RPS prototype can be driven by different frequency and phase signals, additional signal source and amplifier were added to the SPS design's test setup. The block diagram of setup and an equivalent driving circuit for the prototype is shown in Figure 6.42 and 6.43, respectively. In the test setup, a second channel of the signal generator and amplifier was used to drive one of the electrodes. An additional voltage probe was added to measure the voltage applied to the second ring. The equivalent circuit is shown in Figure 6.43, shows the two rings as equivalent BVD circuits highlighted by red and green blocks. The equivalent circuits for 77 kHz and 88 kHz are shown in Figure 6.43. The test point TP1 was used to measure the voltage input of the inner ring, and test point TP2 was used to measure the voltage input to the outer ring. The current was measured on the common return path at TP3.

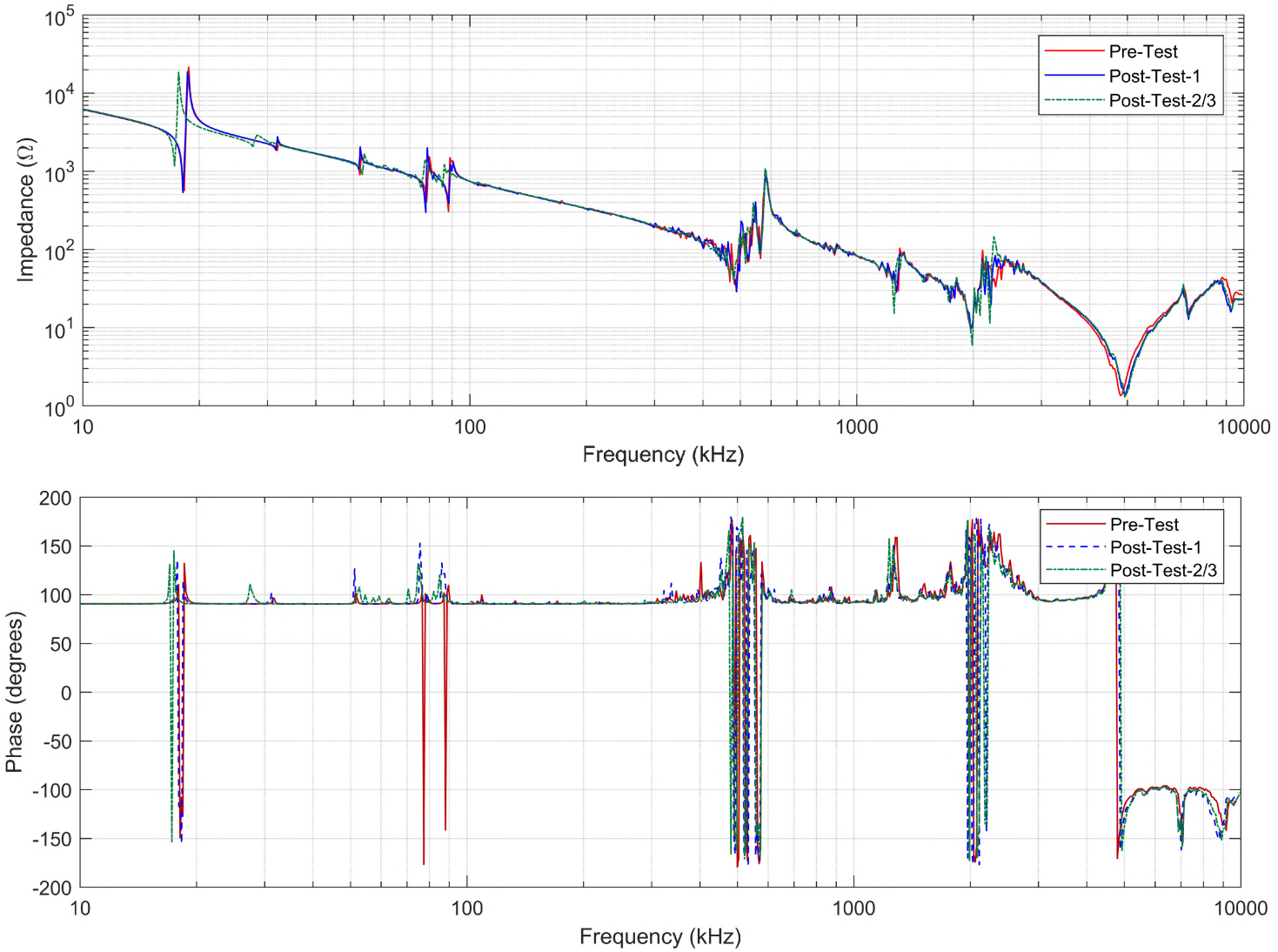

Figure 6.41. RPS Prototype Impedance Spectrum

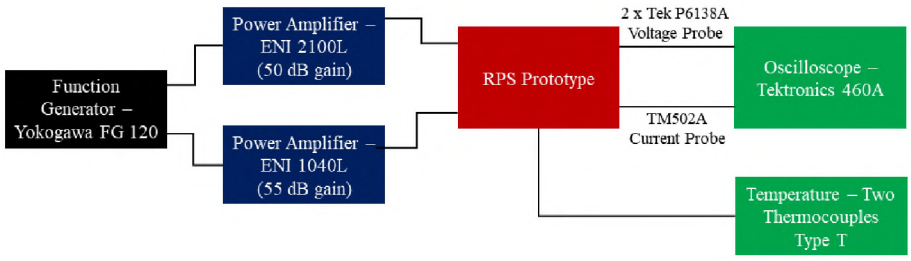

Figure 6.42. Test Setup Block Diagram

6.3.4.2. Procedure. The testing procedure is similar to the SPS prototype; the significant difference being that each electrode can be driven at different frequencies, amplitudes, and phases. Several tests were conducted on the RPS prototype. The first test involved driving both the prototype's electrodes at the same frequency, amplitude, and phase. This was done by connecting the two electrodes to the same source. In the next test, the frequency was kept the same, but the signal's phase and amplitude were varied. The amplitude supplied from the signal source was the same, but since two different amplifiers were used having different power gains of 50 dB and 55 dB, the applied voltage on the rings was different. The third test varied the frequency and amplitude of the source signal on each ring.

6.3.4.3. Measurements. At each test point, the voltage magnitude, current magnitude, and phase of the signal driving the prototype under test were measured along with the temperatures on the PZT and glass surfaces. Table 6.16 shows the test results of first test with the same frequency, amplitude, and phase. The second test involved varying the phase and amplitude. In the third test, the signal frequency supplied to the inner and outer electrodes was varied. Tables 6.17 and 6.18 show the measured data during the second and third testing sets. Figure 6.44 shows the RPS prototype test.

6.3.5. RPS Prototype Efficacy Matrix. The ability of the prototype to remove contaminants is summarized in Table 6.15. A visual inspection was performed to see if a contaminant was successfully removed during testing.

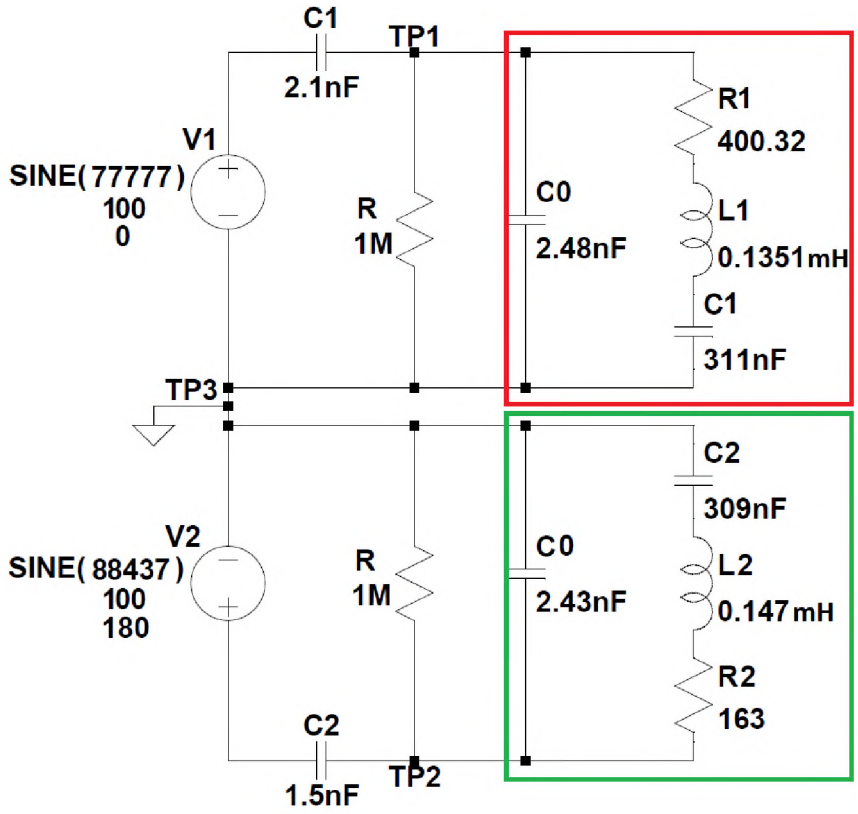

Figure 6.43. Electrical Drive Circuit and Equivalent BVD - RPS Prototype Model

Table 6.15. Efficacy Matrix for RPS Prototype [4]

Contaminant				**Table Salt**	**Silicon Carbide**	**Aluminum Oxide**	**Water**
Inner Ring		Outer Ring		1234 kg/m^3	3210 kg/m^3	3950 kg/m^3	1000 kg/m^3
Freq. [kHz]	Phase	Freq. [kHz]	Phase	100 μm	75 μm	9.5 μmm	0.890 cps
77.777	0	77.777	0	Yes	Yes	No	No
88.436	0	88.436	0	Partial	Yes	Partial	No
77.777	0	77.777	180	Yes	Yes	No	NA
77.777	180	77.777	0	Yes	Yes	No	NA
88.436	0	88.436	180	Yes	Yes	Partial	NA
88.436	180	88.436	0	Yes	Yes	Partial	NA
485.525	0	485.525	0	NA	NA	NA	Yes
485.525	0	485.525	180	NA	NA	NA	Yes
485.525	180	485.525	0	NA	NA	NA	Yes
77.777	0	485.525	0	Yes	Yes	Partial	Yes
485.525	0	77.777	0	Yes	Yes	Partial	Yes

[4]Color Code: Green = Success, Orange = Partial success, Red = Failure, Blue = Could not or did not test

(a) Silicon Carbide

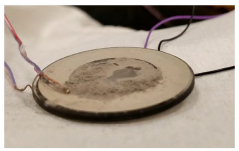

(b) Aluminum Oxide

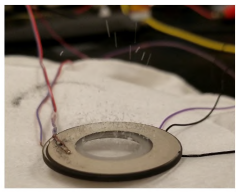

(c) Salt

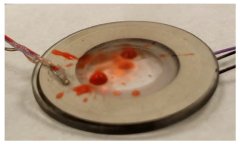

(d) Water

Figure 6.44. RPS Prototype Test

Table 6.16. RPS Prototype Test Data: Single Frequency, Amplitude, and Phase

Contaminant	**F [kHz]** Test Frequency	**V_p [V]** Voltage Amplitude	**I_p [A]** Current Amplitude	**ϕ [°]** Phase	**S [VA]** Apparent Power	**P [W]** True Power	**Q [VAR]** Reactive Power	**T_{PZT} [°C]** Temp. of PZT	**T_{glass} [°C]** Temp. of Glass
Aluminum Oxide 0.07 g	77.777	150	1.52	-83.08	228	27.47	-226.34	25.04	25.68
Aluminum Oxide 0.07 g	77.777	158	1.68	-85.6	265.44	20.36	-264.66	26.05	26
Aluminum Oxide 0.07 g	88.436	146	1.92	-81.32	280.32	42.30	-277.11	27.32	26.89
Water 0.06 g	88.436	146	2	-84.24	292	29.31	-290.53	26.6	25.34
Water 0.06 g	77.777	148	1.76	-78.44	260.48	52.19	-255.19	25.2	24.7
Table Salt 0.06 g	88.436	72	0.192	-83.76	13.824	1.50	-13.74	23.99	23.84
Table Salt 0.06 g	88.436	138	1.008	-62.6	139.104	64.02	-123.49	26.23	25.17
Table Salt 0.06 g	88.436	148	1.72	-77.6	254.56	54.66	-248.62	25.9	25.87
Table Salt 0.06 g	77.777	132	1.44	-79.96	190.08	33.14	-187.17	28.29	27.37
Silicon Carbide 0.07 g	77.777	35.6	0.16	-73.24	5.696	1.64	-5.45	22.55	22.51
Silicon Carbide 0.07 g	77.777	70.4	0.4	-69.04	28.16	10.07	-26.29	23	22.2
Silicon Carbide 0.07 g	77.777	106	0.8	-88.96	84.8	1.54	-84.79	23.08	22.36
Silicon Carbide 0.07 g	88.436	37.2	0.6	15.12	22.32	21.55	5.82	23.88	22.65
Silicon Carbide 0.07 g	88.436	75.2	0.272	-9.52	20.4544	20.17	-3.38	23.82	23.16
Silicon Carbide 0.07 g	88.436	106	0.384	-74.04	40.704	11.19	-39.13	23.69	23.37

Table 6.17. RPS Prototype Test Data: Single Frequency Different Amplitude and Phase[3]

Contaminant	F_i [kHz]	F_i [kHz]	Φ_i [°]	Φ_i [°]	V_{ip} [V]	V_{op} [V]	I_p [A]	ϕ_i [°]	S_i [VA]	S_o [VA]	P_i [W]	Q_i [VAR]	T_{PZT} [°C]	T_{Glass} [°C]
Silicon Carbide 0.07 g	77.777	77.777	0	180	198	61.6	0.896	99.08	177.41	55.19	-27.99	175.18	23	23
Silicon Carbide 0.07 g	77.777	77.777	180	0	198	62	0.992	102.56	196.42	61.50	-42.71	191.72	23.1	23.3
Silicon Carbide 0.07 g	88.436	88.436	0	180	188	52	1.184	102.24	222.59	61.57	-47.19	217.53	24	24.1
Silicon Carbide 0.07 g	88.436	88.436	180	0	208	52	2.42	19.76	503.36	125.84	473.72	170.17	23.4	23.5
Table Salt 0.06 g	88.436	88.436	180	0	192	8	0.82	82.56	157.44	6.56	20.39	156.11	23.5	23.5
Table Salt 0.06 g	88.436	88.436	0	180	206	49.8	2.5	132.76	515	124.5	-349.65	378.12	23.6	23.6
Table Salt 0.06 g	88.436	88.436	180	0	192	8	0.82	82.56	157.44	6.56	20.39	156.12	23.5	23.5
Table Salt 0.06 g	88.436	88.436	0	180	206	49.8	2.5	132.76	515	124.5	-349.65	378.12	23.6	23.6
Table Salt 0.06 g	77.777	77.777	180	0	206	61.6	1.04	101.92	214.24	64.064	-44.25	209.62	23.7	23.5
Table Salt 0.06 g	77.777	77.777	0	180	204	62.4	0.98	105.08	199.92	61.152	-52.01	193.03	24.7	23.9
Aluminum Oxide 0.07 g	77.777	77.777	0	180	210	61.6	0.96	103.96	201.6	59.136	-48.63	195.65	23.5	23.5
Aluminum Oxide 0.07 g	77.777	77.777	180	0	246	80.8	3.18	127.96	782.28	256.94	-481.19	616.78	24.5	24.5
Aluminum Oxide 0.07 g	88.436	88.436	0	180	238	72.8	3.58	22.76	852.04	260.624	785.69	329.63	24	24
Aluminum Oxide 0.07 g	88.436	88.436	180	0	206	46.4	2.48		510.88	115.072	510.88	0	25.1	25.1
Water 0.06 g	88.436	88.436	180	0	190	74.4	1.36	-179.48	258.4	101.184	-258.39	-2.35	23.4	23.4
Water 0.06 g	88.436	88.436	180	0	188	89.6	1.44	103.68	270.72	129.024	-64.03	263.04	25	25
Water 0.06 g	485.525	485.525	0	0	56	7.2	3.28	17.08	183.68	23.62	175.58	53.95	24.9	24.3
Water 0.06 g	485.525	485.525	0	0	88	35.2	2.28	5.16	200.64	80.26	199.83	18.05	27	27
Water 0.06 g	485.525	485.525	0	0	90	26.4	5.6	14.2	504	147.84	488.60	123.64	30	29
Water 0.06 g	485.525	485.525	0	180	82	43.2	5.96	130.96	488.72	257.472	-320.37	369.06	29	28
Water 0.06 g	485.525	485.525	180	0	82	41.6	5.76	130.72	472.32	239.62	-308.12	357.97	29	28

[3] F_i=Test frequency inner ring, F_o =Test frequency outer ring, Φ_i= Phase inner ring, Φ_o= Phase outer ring, V_{ip} = Voltage amplitude inner ring, V_{ip} = Voltage amplitude outer ring, I_p = Current amplitude, ϕ_i= Phase between current I_p and V_{ip}, S_i=Apparent power inner ring, S_o=Apparent power outer ring, P_i=True power inner ring, Q_i=Reactive power outer ring, T_{PZT}=Temperature of PZT, T_{glass}= Temperature of Glass

Table 6.18. RPS Prototype Test Data: Single Frequency Different Amplitude and Phase [3]

Contaminant	F_i [kHz]	F_i [kHz]	Φ_i [°]	Φ_i [°]	V_{ip} [V]	V_{op} [V]	I_p [A]	ϕ_i [°]	S_i [VA]	S_o [VA]	P_i [W]	Q_i [VAR]	T_{PZT} [°C]	T_{Glass} [°C]
Aluminum Oxide 0.07 g	77.777	485.525	0	0	228	88	9.44	105.72	2152.32	830.72	-583.14	2071.82	38	39
Aluminum Oxide 0.07 g	485.525	77.777	0	0	140	130	3.76	38.58	526.4	488.8	411.51	328.27	43	40
Silicon Carbide 0.07 g	77.777	485.525	0	0	232	94	9.92	-96.48	2301.44	932.48	-259.73	-2286.74	40	43
Silicon Carbide 0.07 g	485.525	77.777	0	0	118	120	3.12	48.72	368.16	374.4	242.89	276.67	24	26
Table Salt 0.06 g	77.777	485.525	0	0	232	72	9.98	-19.32	2315.36	718.56	2184.97	-766.02	40	40
Table Salt 0.06 g	485.525	77.777	0	0	96	104	2.56	136.36	245.76	266.24	-177.85	169.61	20	25
Water 0.06 g	485.525	582.37	0	0	116	147.2	2.8	65.28	324.8	412.16	135.826	295.04	50	45
Water 0.06 g	485.525	582.37	0	0	110	116	2.72	58.52	299.2	315.52	156.25	255.16	37	36
Water 0.06 g	485.525	77.777	0	0	86	52	2.32	71.12	199.52	120.64	64.56	188.79	22.3	22.3
Water 0.06 g	485.525	77.777	0	0	96	86	2.48	-60	238.08	213.28	119.04	-206.18	23.2	23.4
Water 0.06 g	77.777	485.525	0	0	230	40	8.32	107.92	1913.6	332.8	-588.79	1820.77	28	28
Water 0.06 g	77.777	485.525	0	0	258	150	7.52	-20.12	1940.16	1128	1821.76	-667.39	45	43

[3] F_i=Test frequency inner ring, F_o =Test frequency outer ring, Φ_i= Phase inner ring, Φ_o= Phase outer ring, V_{ip} = Voltage amplitude inner ring, V_{ip} = Voltage amplitude outer ring, I_p = Current amplitude, ϕ_i= Phase between current I_p and V_{ip}, S_i=Apparent power inner ring, S_o=Apparent power outer ring, P_i=True power inner ring, Q_i=Reactive power outer ring, T_{PZT}=Temperature of PZT, T_{glass}= Temperature of Glass

6.3.6. RPS Prototype Design Remarks. Building this prototype requires an extra step in manufacturing the ring to separate the electrodes. The testing of the prototype requires an additional signal to drive the prototype at separate frequencies or amplitudes. The test setup also requires additional instrumentation. The prototype is suitable for the removal of a variety of contaminants, and the conclusion from the previous testing holds true that low frequencies work better for solids, and higher frequencies work better for liquids. The RPS prototype electrodes may be driven at a single frequency in-phase or out-of-phase at the same or at different amplitudes, or at two different frequencies at the same or at different amplitudes, and in or out-of-phase.

As seen in previous prototypes and mentioned above, the resonance frequencies shift downwards after only a few minutes of testing done a few seconds at a time. A reduction in resonance frequency indicates an overall loss of elastic stiffness, which is compatible with structural degradation, and most likely due to softening or separation in the epoxy layer. The reduction in Q_m, observed in previous prototypes, is also consistent with structural degradation. Therefore, the previous conclusion regarding the necessity of developing a more robust interface between the PZT and glass applies to this latest prototype as well.

6.4. SUPPORT DRIVEN SYSTEM

The support driven system (SDS) was the third design to be built and tested. Various improvements were made in the build process based on the experience from previous prototypes. Figure 6.45 shows the SDS design schematic and the prototype, which has two PZT rings and masses attached to the glass. Figure 6.46 shows that both PZT rings in this prototype are poled in the same direction. The electrode surfaces bonded to the lens surface are driven with the same harmonic signal; an outer electrode of the metal mass is driven with the opposite polarity causing the two rings to expand and contract 180 degrees out-of-phase such that they create a push-pull effect on the glass surface.

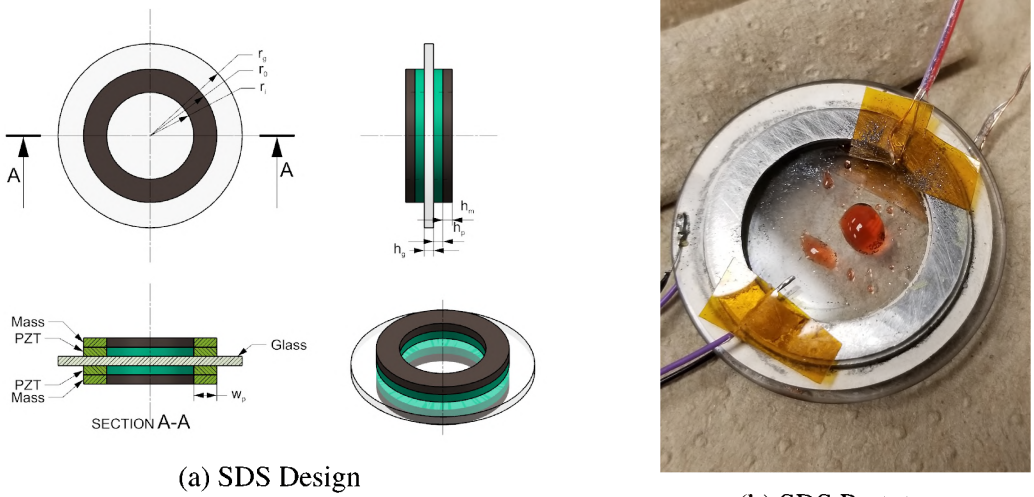

(a) SDS Design

(b) SDS Prototype

Figure 6.45. Support Driven System-SDS

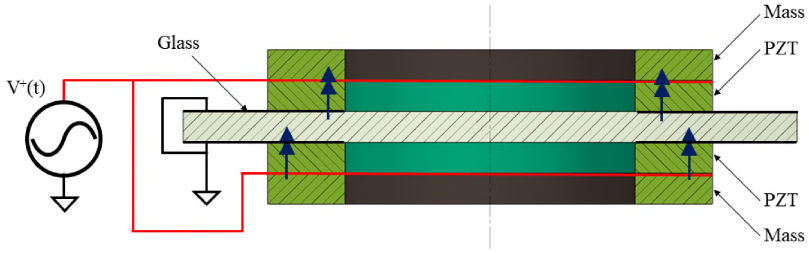

Figure 6.46. PZT Poling and Drive Signal-SDS

6.4.1. SDS Prototype Build Process. Building the SDS Prototype is a multi-step process. Each PZT and mass is attached separately to the glass. Visual alignment of each PZT and mass to the glass is accomplished using a printed template. EPO-TEK-323LP epoxy was used in this build. Wires were attached to the glass via soldering. EPO-TEK-H20E was used to attach wires to the top and bottom steel mass. One of the major challenges of building this prototype is aligning and controlling the tolerances of the mass and the PZT. Table 6.19 provides the dimensions of the prototype.

6.4.2. Impedance Spectroscopy of SDS Prototype. Impedance spectroscopy was conducted on each PZT ring at various stages of the prototype and build process. Both PZT rings were characterized separately at three stages: before bonding to the glass, assembly,

Table 6.19. SDS Prototype Dimensions

Parameter	Mass-1	PZT-1	Glass	PZT-2	Mass-2
R_o	12.31 mm	12.88 mm	15.77 mm	12.74 mm	12.18 mm
R_i	8.63 mm	8.67 mm	-	8.63 mm	8.97 mm
w	3.68 mm	4.21 mm	-	4.12 mm	3.21 mm
h	0.81 mm	1.01 mm	1.58 mm	1 mm	0.83 mm
m	1.45 g	2.02 g	2.68g	2.00 g	1.39 g

and after testing of the prototype. Figures 6.47 and 6.48 show the impedance spectrum of rings 1 and 2 for a frequency range of 10 kHz to 40 MHz. Figures 6.49 and 6.50 show the first two modes of the rings, and Table 6.20 provides the equivalent circuit parameters of these rings.

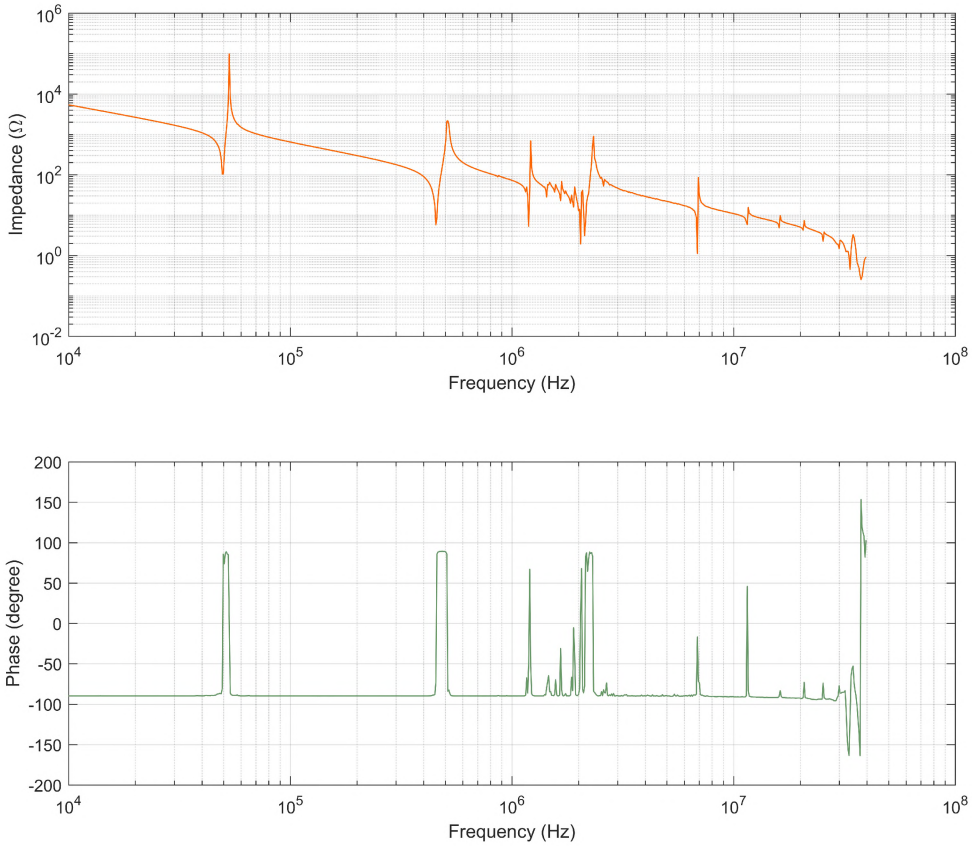

Figure 6.47. SDS Prototype - Impedance of Ring 1 Pre-Build

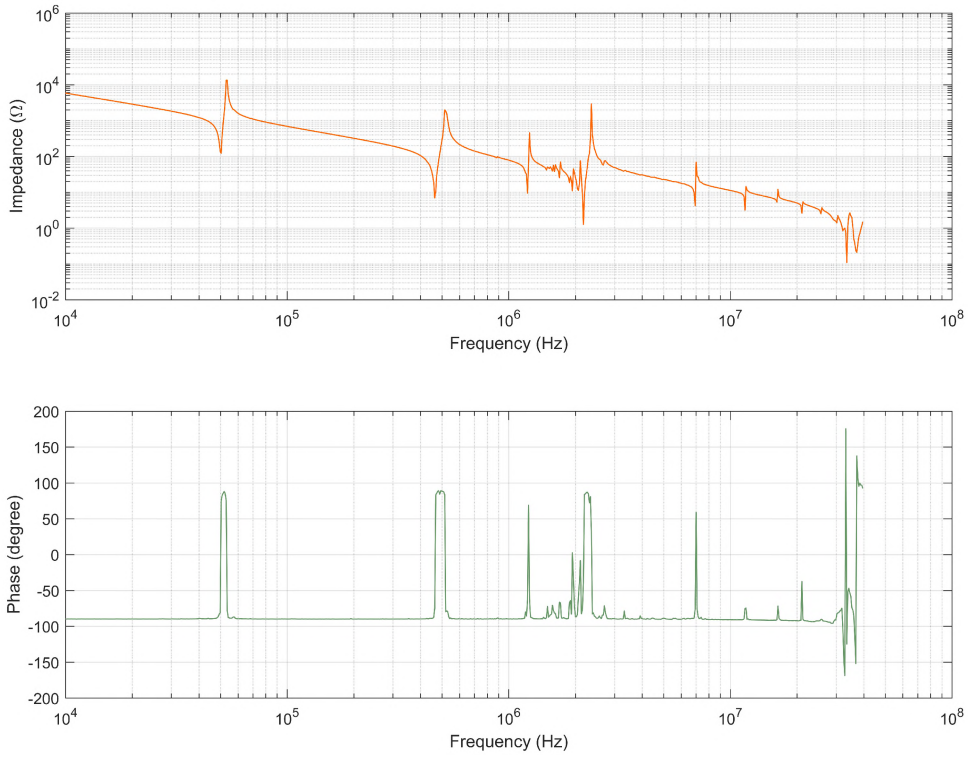

Figure 6.48. SDS Prototype - Impedance of Ring 2 Pre-Build

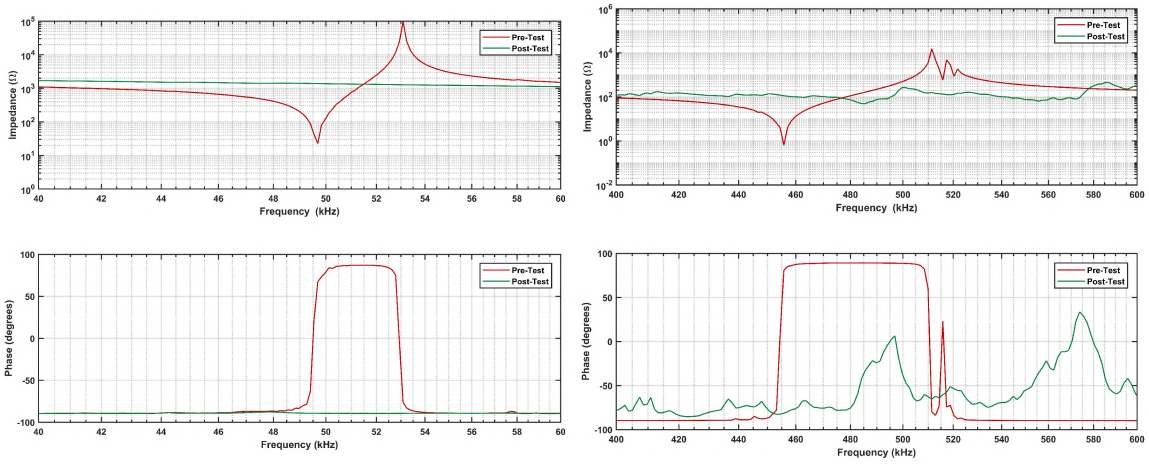

(a) Mode 1

(b) Mode 2

Figure 6.49. SDS Prototype - Ring 1 - Impedance Spectrum

Figures 6.51 and 6.52 compare the impedance spectrum of the rings before and after testing. The comparison shows that the impedance shifted and is lower in magnitude after testing.

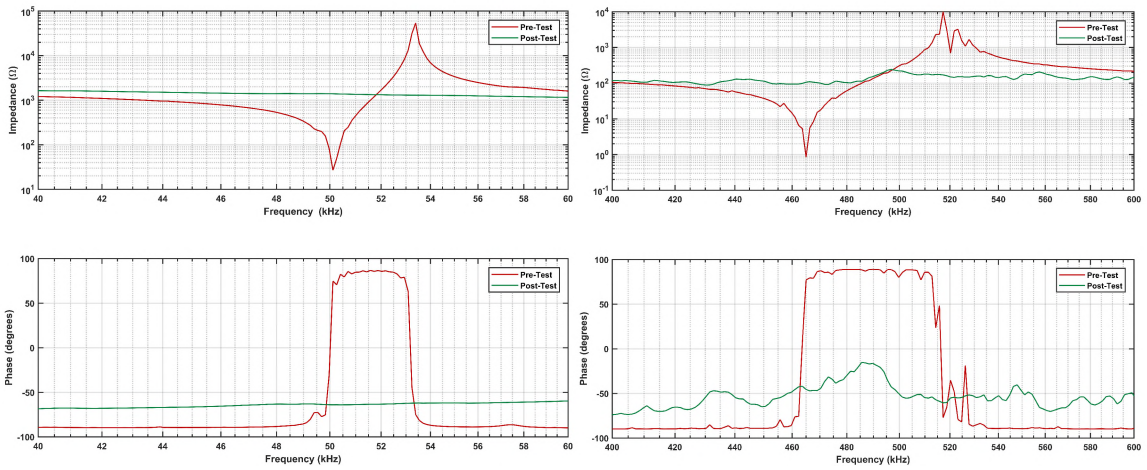

(a) Mode 1 (b) Mode 2

Figure 6.50. SDS Prototype - Ring 2 - Impedance Spectrum

Table 6.20. Equivalent Circuit Parameters for SDS Prototype

Mode	f_r [kHz]	f_a [kHz]	C_0 [nF]	R_1 [Ω]	L_1 [H]	C_1 [pF]	Q_m
Ring 1 Mode 1	49.6	52.8	2.51	18.02	0.0303	33.86	525.21
Ring 1 Mode 2	455.7	510.8	2.05	0.62	0.0002	52.79	1066.82
Ring 2 Mode 1	50.16	53.1	2.33	23.53	0.0357	28.19	478.24
Ring 2 Mode 2	464.98	512.99	1.90	0.996	0.00028	41.36	830.21

6.4.3. Analysis of the SDS Prototype. The SDS prototype was analyzed in ANSYS. Impedance spectroscopy of the prototype revealed several modes of interest. Due to the limitations of the BVD circuit model [41], not every mode could be fully characterized. Figures 6.53 and 6.54 show the total acceleration and normal acceleration response of the prototype at 74.6 kHz. A frequency of 74 kHz was used to remove solid contaminants during testing. Figures 6.55 and 6.56 show the total and normal acceleration response of the prototype at 665 kHz. The frequency of 665 kHz was used to remove fluid contaminants in testing.

6.4.4. Testing Setup, Procedure and Measurements of the SDS Prototype. The prototype's test setup is similar to that of the previous prototype and is shown in the block diagram in Figure 6.23. The electrical equivalent driving circuit for the setup has two BVD

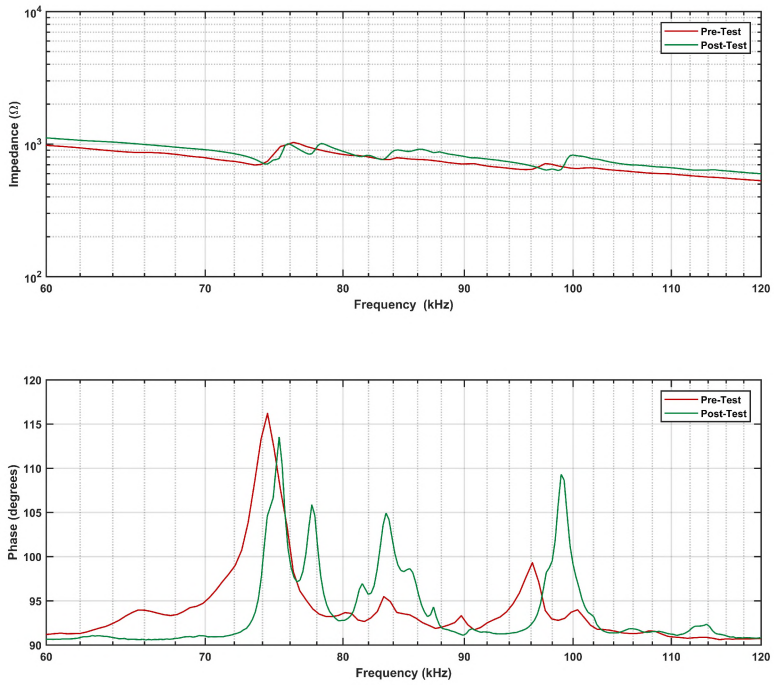

(a) Ring 1 - 20 kHz to 120 kHz

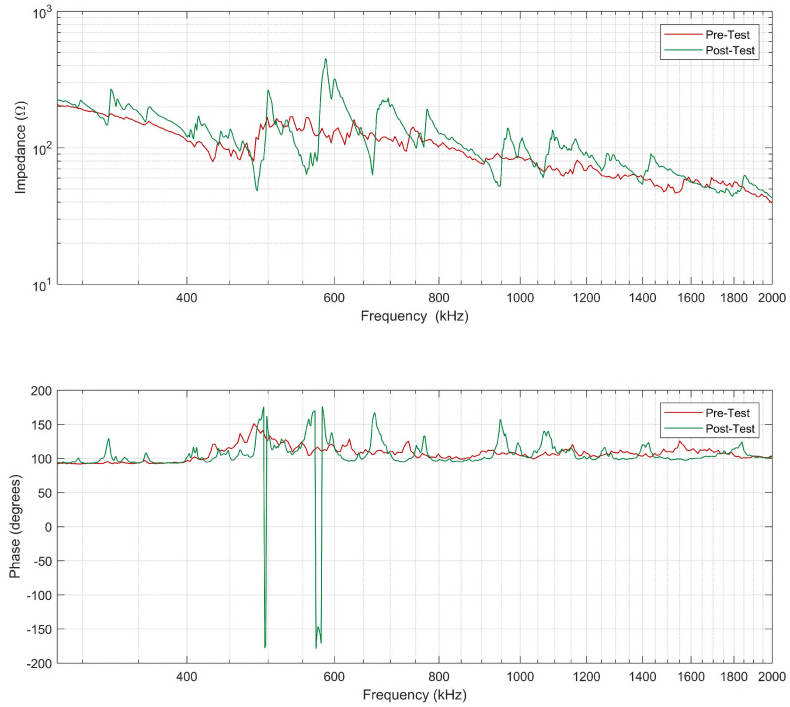

(b) Ring 1 - 280 kHz to 2 MHz

Figure 6.51. SDS Prototype - Impedance Comparison of Ring 1 Pre and Post Test

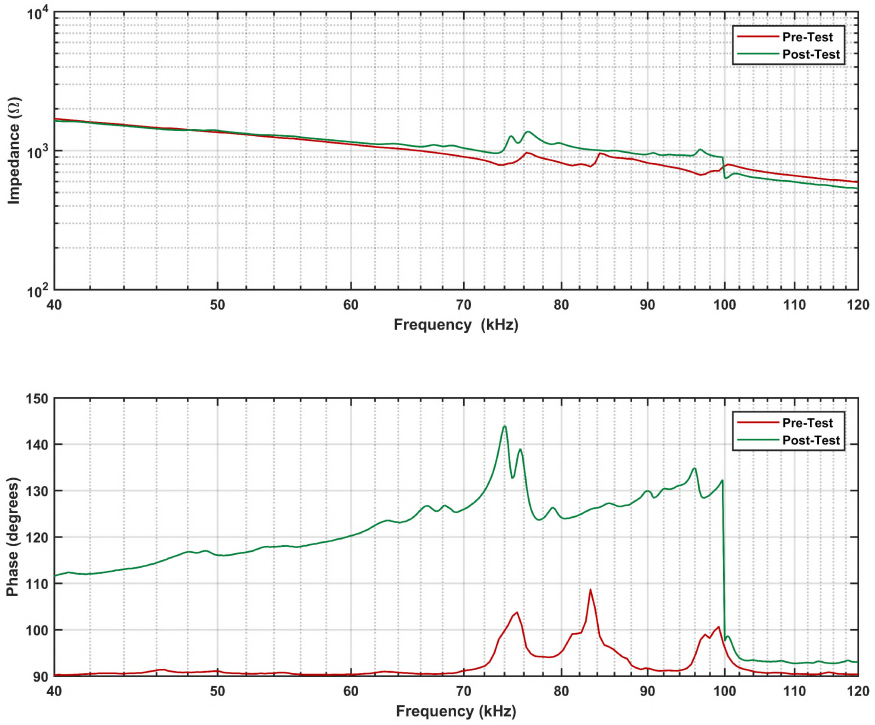

(a) Ring 2 - 20 kHz to 120 kHz

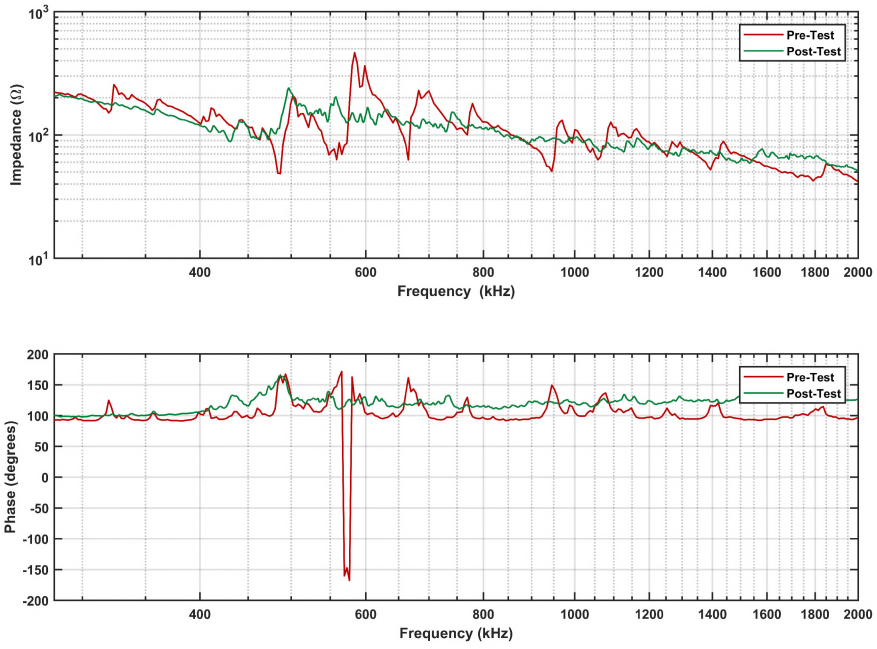

(b) Ring 2 - 280 kHz to 2 MHz

Figure 6.52. SDS Prototype - Impedance Comparison of Ring 2 Pre and Post Test

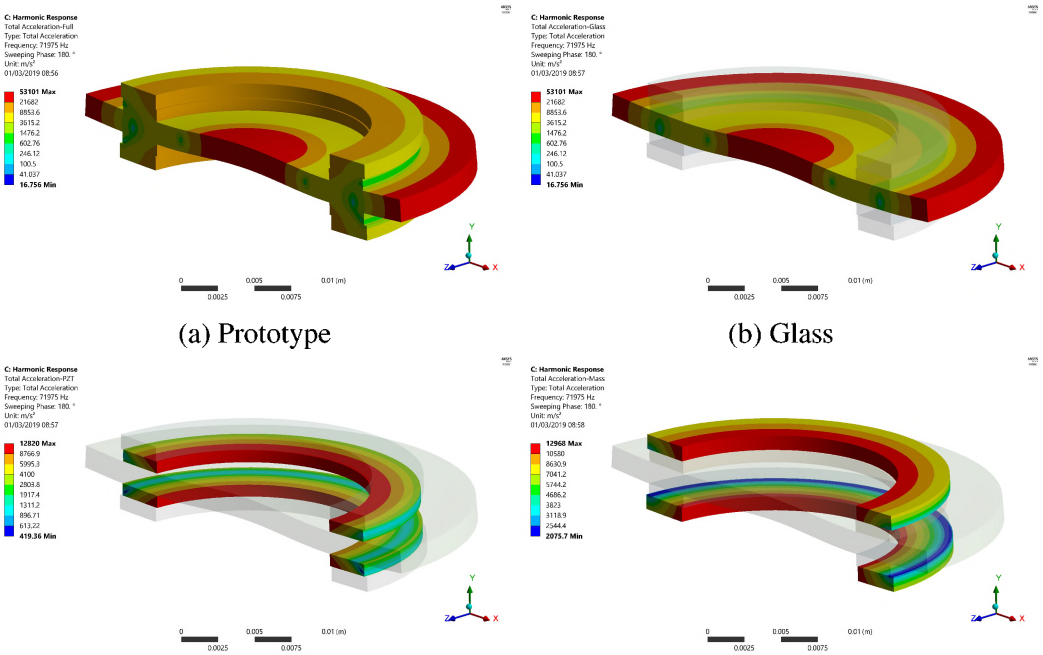

(a) Prototype (b) Glass

(c) PZT (d) Mass

Figure 6.53. SDS Prototype - Total Acceleration at 74.6 kHz

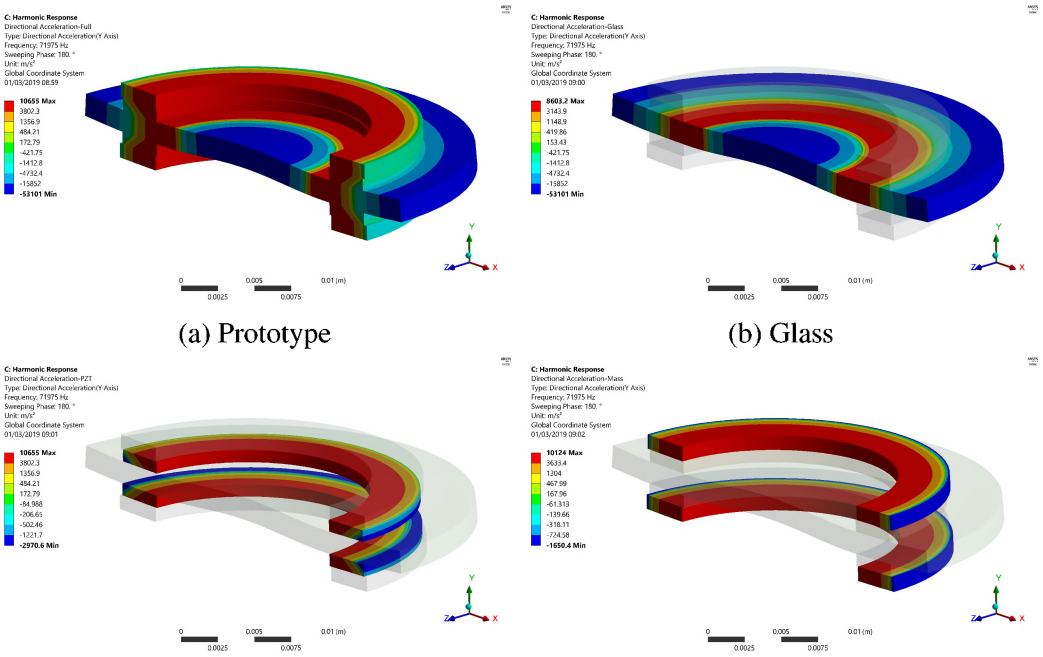

(a) Prototype (b) Glass

(c) PZT (d) Mass

Figure 6.54. SDS Prototype - Normal Y-Acceleration at 74.6 kHz

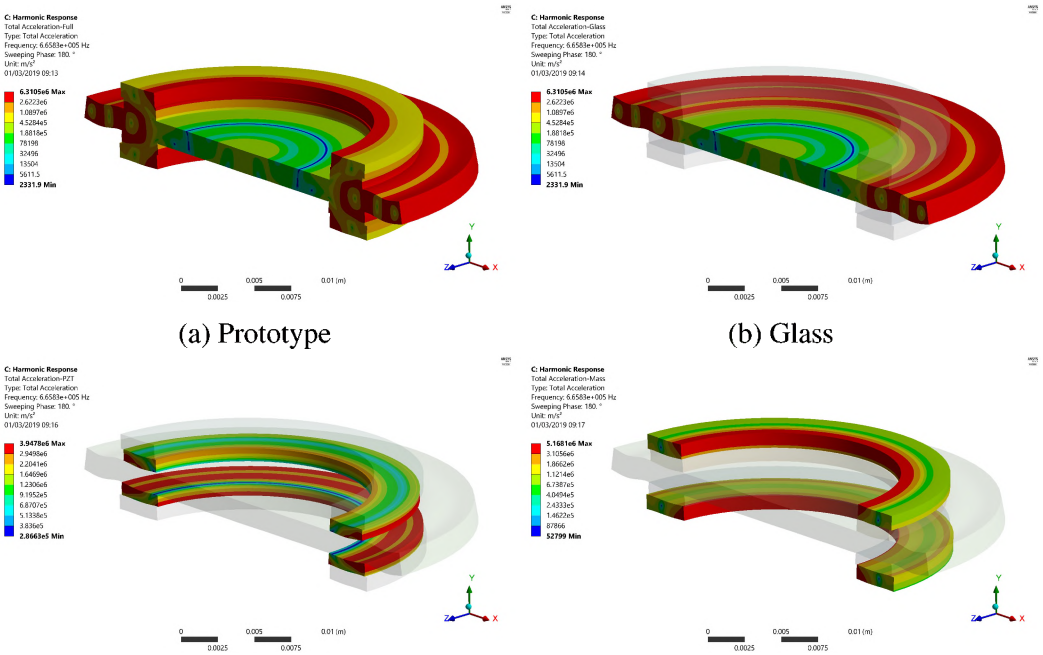

(a) Prototype (b) Glass

(c) PZT (d) Mass

Figure 6.55. SDS Prototype - Total Acceleration at 665.9 kHz

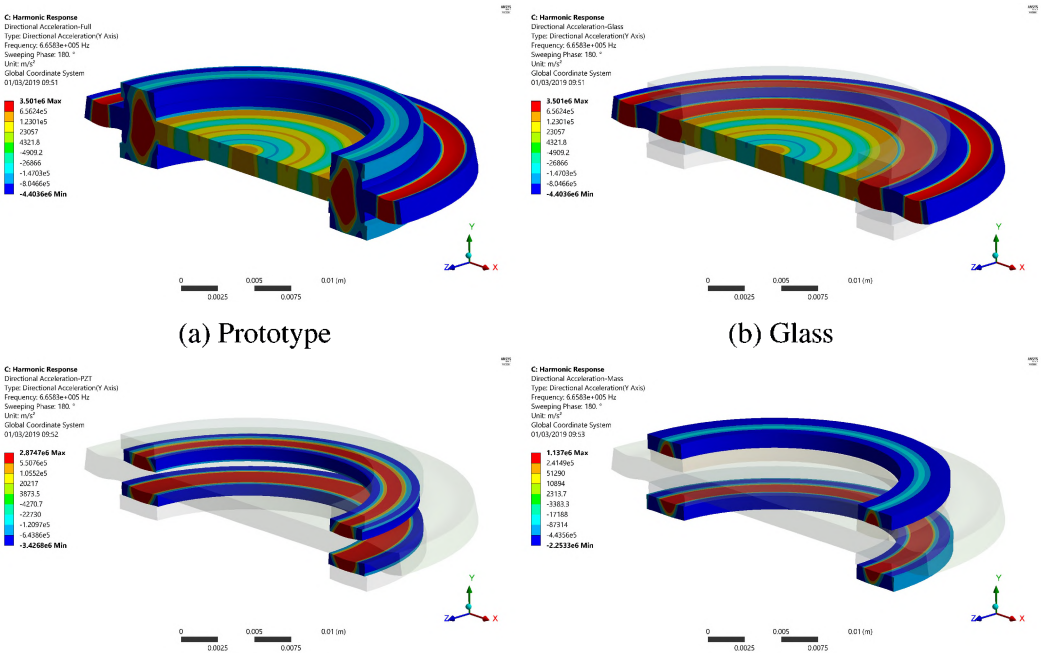

(a) Prototype (b) Glass

(c) PZT (d) Mass

Figure 6.56. SDS Prototype - Normal Y-Acceleration at 665.9 kHz

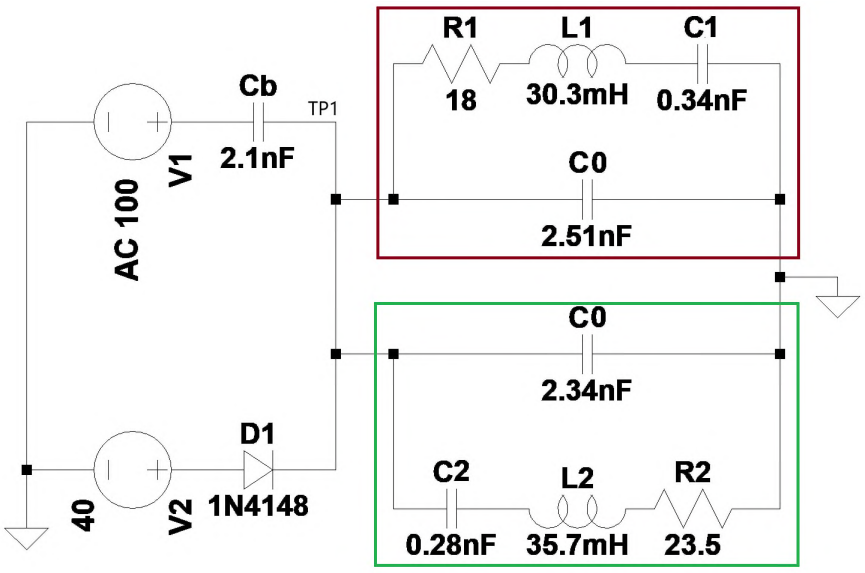

Figure 6.57. Equivalent Electrical Circuit of the SDS Prototype in Test

equivalent circuits, each representing the two separate PZT rings, and is shown in Figure 6.57. The drive circuit works the same as described in Section 6.1.5. In Figure 6.57, the values are for Prototype, and the two PZT's are identified by Red and Green rectangles. The driving circuit is independent of the mode and prototype driven.

The tests were conducted on several contaminants, including water, salt, silicon carbide, mineral oil, and toothpaste. The parameters recorded were the test frequency, voltage, current, apparent power, true power, reactive power, and the phase between voltage and current, and temperature. Table 6.22 shows the data collected at each test where the best cleaning result was achieved. Each contaminant required more than ten tests at different voltage and frequency settings. During each test, a burst of two to three seconds was used with a delay of five seconds between bursts. Figure 6.59 shows the SDS Prototype under test.

6.4.5. Efficacy Matrix of the SDS Prototype. The ability of the prototype to remove contaminants is summarized in Table 6.21.

Table 6.21. Efficacy Matrix for SDS Prototype[5]

Contaminant	Density	Particle Size/Viscosity	74.8 kHz	484 kHz	583 kHz	665.9 kHz
Water	1000 kg/m^3	0.890 cps	No	Yes	Yes	Yes
Table Salt	1234 kg/m^3	100 μm	Partial	NA	NA	NA
Silicon Carbide	3210 kg/m^3	75 μm	Yes	NA	NA	NA
Mineral Oil	830 kg/m^3	700 cps	NA	NA	NA	Yes
Toothpaste	1450 kg/m^3	70,000-10,0000 cps	NA	NA	NA	Partial

[5]Color Code: Green = Success, Orange = Partial success, Red = Failure,Blue = Could not or did not test

6.4.6. SDS Prototype Design Remarks. Building this prototype is more complicated than any of the other designs tested, but as seen from the efficacy matrix, the prototype is the most successful of the designs tested in contaminant removal. The SDS prototype is capable of being driven at several different frequencies and power settings. After prolonged testing, the prototype started to heat up rapidly, and the current waveform showed the distinct and repetitive ringing phenomenon shown in Figure 6.58. The phenomenon became more prominent in continued testing. As seen in Figure 6.58b, prolonged testing led to a voltage graph showing some variation from a clean sinusoidal signal. This led to the conclusion that the prototype was being damaged with each additional actuation cycle.

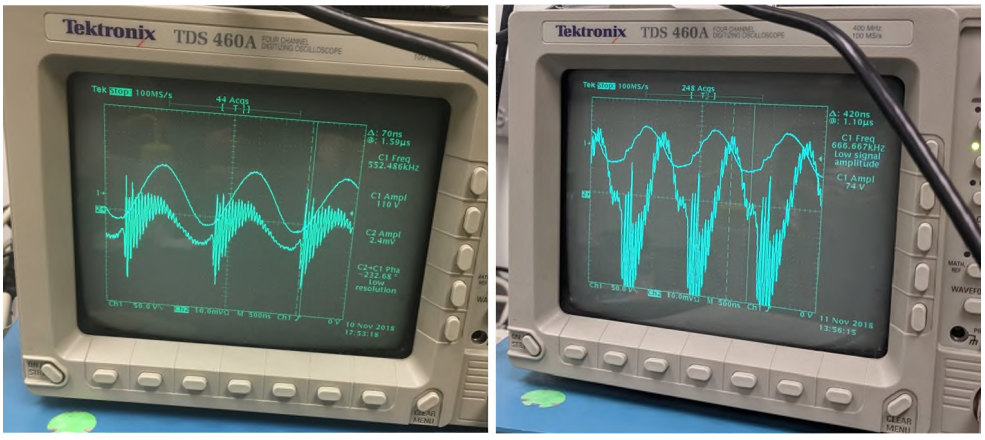

(a) Voltage and Current Waveforms After Initial Testing

(b) Voltage and Current Waveforms After Additional Cycles

Figure 6.58. Voltage and Current Waveforms

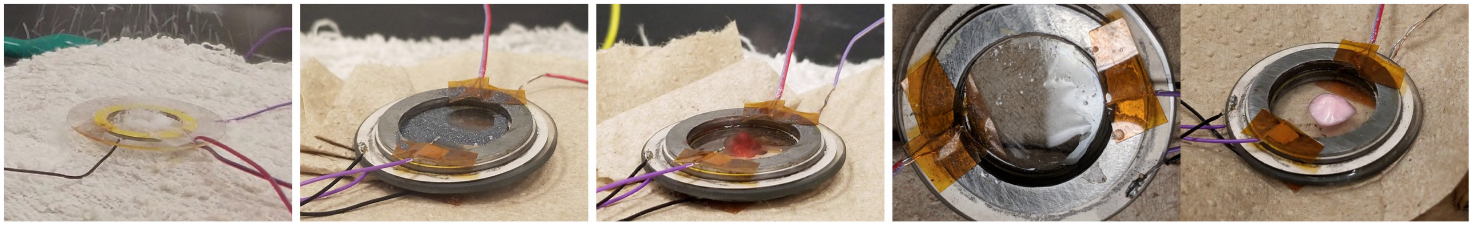

(a) Salt (b) Silicon Carbide (c) Water (d) Mineral Oil (e) Toothpaste

Figure 6.59. SDS Prototype

Table 6.22. SDS Prototype Test Data

Contaminant	**F [kHz]** Test Frequency	**V_p [V]** Voltage Amplitude	**I_p [A]** Current Amplitude	**S [VA]** Apparent Power	**P [W]** True Power	**Q [VAR]** Reactive Power	**T_{PZT} [°C]** Temp. of PZT	**ϕ [°]** Phase
Table Salt 0.06 g	74.24	31.45	0.75	24.07	-1.12	24.04	24.52	70.73
Silicon Carbide 0.07 g	74.29	31.2	0.765	23.85	-13.46	-19.66	24.16	73.22
Water 0.06 g	665.96	22	2.94	66.37	7.58	-65.94	49.47	61.9
Mineral Oil 0.05 g	665.96	37	1.62	59.99	59.74	-5.46	61.24	-12.65
Toothpaste 0.04 g	665.96	38	4.91	-97.71	-179.1	60.53	64.12	-97.71

7. ANALYTICAL MODELS FOR CIRCULAR PLATE WITH ECCENTRIC PRESSURE LINE LOAD AND ECCENTRIC MOMENT LINE LOAD

Analytical models for piezoelectric actuators are desirable for a relatively simple formulation that can help analyze actuators rapidly compared to FEM models that are numerical and computationally expensive. A limited amount of work has been accomplished in the area of circular plates with line loads. Several models exist for piezoelectric motors, but most of them consider the force acting concentric to the stator [42, 43, 44]. The model presented is for an eccentrically loaded free circular plate. Soedel and Powder present the general approach to the off axes line loads applied to rectangular plates using Cartesian coordinates [45]. The formulation presented here expands the general approach to polar coordinates by describing an eccentric line load applied to a circular plate with free boundaries.

7.1. FREE VIBRATION OF CIRCULAR PLATE

The equation of motion describing transverse vibration of a circular plate is given by Equation (7.1). [45]

$$D\nabla^4 u_3 + \rho h \ddot{u}_3 = q(r,\theta,t) \tag{7.1}$$

where $q(r,\theta,t)$ denotes a general force applied, and Equation (7.2) is the laplacian biharmonic operator in polar coordinates:

$$\nabla^2(\cdot) = \frac{\partial^2(\cdot)}{\partial r^2} + \frac{\partial(\cdot)}{\partial r} + \frac{1}{r}\frac{\partial^2(\cdot)}{\partial \theta^2} \tag{7.2}$$

Where, D is the bending stiffness of the plate, ρ density of the plate, and h is the plate's thickness. In the unforced ($q = 0$) free vibration of the plate, the solution can be assumed to be separable in temporal harmonic solution.

$$u_3(r,\theta,t) = U_3(r,\theta)e^{j\omega t} \tag{7.3}$$

Then, substituting Equation (7.3) into Equation (7.1) it yields:

$$D\nabla^4 U_3(r,\theta) - \rho h\omega^2 U_3(r,\theta,t) = 0 \tag{7.4}$$

rearranging Equation (7.4).

$$(\nabla^2 + \lambda^2)(\nabla^2 - \lambda^2)U_3(r,\theta) = 0 \tag{7.5}$$

where,

$$\lambda^2 = \frac{\rho h\omega^2}{D} \tag{7.6}$$

This is the spatial domain equation whose solution is also the same as that of Equation (7.7).

$$(\nabla^2 \pm \lambda^2)U_3(r,\theta) = 0 \tag{7.7}$$

Applying separation of variables on the spatial domain:

$$U_3(r,\theta) = R(r)\Theta(\theta) \tag{7.8}$$

Substituting Equation (7.8) into Equation (7.7) and dividing by $R(r)$ and $\Theta(\theta)$.

$$r^2\left[\left(\frac{d^2R}{dr^2} + \frac{1}{r}\frac{dR}{dr}\right)\frac{1}{R} \pm \lambda^2\right] = \frac{-1}{\theta}\frac{d^2\Theta}{d\theta^2} \tag{7.9}$$

A solution exists to the Equation (7.9) if both sides of the equations equate to a constant k^2. Therefore,

$$\frac{d^2\Theta}{d\theta^2} + k^2\Theta = 0 \tag{7.10}$$

$$\frac{d^2R}{dr^2} + \frac{1}{r}\frac{dR}{dr} + \left(\pm\lambda^2 - \frac{k^2}{r^2}\right) = 0 \tag{7.11}$$

The azimuthal Equation (7.10) is second order ordinary differential equation whose solution is given by,

$$\Theta(\theta) = A\cos(k\theta) + B\sin(k\theta) \tag{7.12}$$

In the radial direction. Let,

$$\xi = \begin{cases} \lambda r & for + \lambda^2 \\ j\lambda r & for - \lambda^2 \end{cases}$$

Therefore, Equation (7.11) becomes,

$$\frac{d^2R}{d\xi^2} + \frac{1}{\xi}\frac{dR}{d\xi} + \left(1 - \frac{k^2}{\xi^2}\right) = 0 \tag{7.13}$$

This is a Bessel's equation of fractional order whose solution is given by

$$R(r) = A_1J_k(\lambda r) + A_2I_k(\lambda r) + A_3Y_k(\lambda r) + A_4K_k(\lambda r) \tag{7.14}$$

7.2. BOUNDARY CONDITIONS

There are no boundaries in the azimuthal direction. Boundary conditions on the edge of the circular plate in this model are free in radial directions.

7.2.1. Azimuthal Solution. Since the plate in this case is closed in azimuthal θ-direction, any solution must have a maximum period of 2π. Therefore k, must be integers $n = 1, 2, 3, ...$ and therefore the Equation (7.14) and Equation (7.12) become,

$$\Theta(\theta) = A\cos(n\theta) + B\sin(n\theta) \tag{7.15}$$

$$R(r) = A_1 J_n(\lambda r) + A_2 I_n(\lambda r) + A_3 Y_n(\lambda r) + A_4 K_n(\lambda r) \tag{7.16}$$

7.2.2. Radial Solution. At the center $r = 0$, Bessel functions Y and K are singular, so $A_3 = A_4 = 0$. Thus, the free vibration solution reduces to:

$$U_3(r, \theta) = [A_1 J_n(\lambda r) + A_2 I_n(\lambda r)](A\cos(n\theta) + B\sin(n\theta)) \tag{7.17}$$

The boundary conditions are given by:

$$M_{rr} = -D\left[\frac{\partial^2 u_3}{\partial r^2} + \nu\left(\frac{1}{r}\frac{\partial u_3}{\partial r} + \frac{1}{r^2}\frac{\partial^2 u_3}{\partial \theta^2}\right)\right] = 0 \tag{7.18}$$

and

$$V_{r3} = -D\left[\frac{\partial \nabla^2 u_3}{\partial r} + \frac{1-\nu}{r^2}\frac{\partial^2}{\partial \theta^2}\left(\frac{\partial u_3}{\partial r} - \frac{u_3}{r}\right)\right] = 0 \tag{7.19}$$

Substitution of (7.17) into Equations (7.18) and (7.19) yields the generalized eigenvalue problem given by:

$$\begin{bmatrix} a_{11} & a_{12} \\ a_{21} & a_{22} \end{bmatrix}\begin{pmatrix} A_1 \\ A_2 \end{pmatrix} = \begin{pmatrix} 0 \\ 0 \end{pmatrix} \tag{7.20}$$

where,

$$a_{11} = J_n(\lambda r)(-n^2\nu - (\lambda r)^2 + \nu n + n^2 - n) + J_{n+1}(\lambda r)(-\nu\lambda r) + \lambda r) \tag{7.21}$$

$$a_{12} = I_n(\lambda r)(-n^2\nu + (\lambda r)^2 + \nu n + n^2 - n) + I_{n+1}(\lambda r)(\nu\lambda r) - \lambda r) \tag{7.22}$$

$$a_{21} = J_n(\lambda r)(\nu n^3 - n(\lambda r)^2 - n^2\nu - n^3 + n^2) + J_{n+1}(\lambda r)(-n^2\nu\lambda r + (\lambda r)^3 + n^2\lambda r) \tag{7.23}$$

$$a_{22} = I_n(\lambda r)(\nu n^3 + n(\lambda r)^2 - n^2\nu - n^3 + n^2) + I_{n+1}(\lambda r)(n^2\nu\lambda r + (\lambda r)^3 - n^2\lambda r) \tag{7.24}$$

For nontrivial solutions A_1 and A_2, the determinant of the coefficient matrix must equal to zero. This will yield an eigenvalue equation that can be solved numerically for each value of the azimuthal mode number, n, which is equal to the number of diametrical node lines in the mode. The mnth natural frequency is given by,

$$\omega_{mn} = \frac{\lambda_{mn}^2}{a^2}\sqrt{\frac{D}{\rho h}} \tag{7.25}$$

where λ_{mn} is the mnth eigenvalue, and where m denotes the number of radial node-lines for a particular value of n. Assuming A_1 as unity and substituting into Equation (7.20), A_2 can be found for any combination of m and n.

7.3. ECCENTRIC LOAD FORMULATION

In general, the solution to line load in the direction of coordinate axes is presented in *Vibrations of Plates and Shells*[45]. Stanisics and Soedel explore a detailed discussion of line loads acting asymmetrically to the coordinate axis [46]. In the paper by Soedel and Powder, the authors go to significant trouble to define the scaling factor required to project the component of the load to an arbitrary normal of the curve [46]. The paper goes into

great detail to develop a scaling factor for a curve $y = f(x)$ describing a line load acting on a rectangular plate. Here, a similar scaling factor is developed in polar coordinates for an eccentric line load acting on a circular plate.

7.3.1. Eccentric Load Location. First, the location of the eccentric load is derived as a function of the azimuthal direction. Figure 7.1 shows the geometry of an eccentric load with a center located at (x_0, y_0). The eccentric load location is defined by:

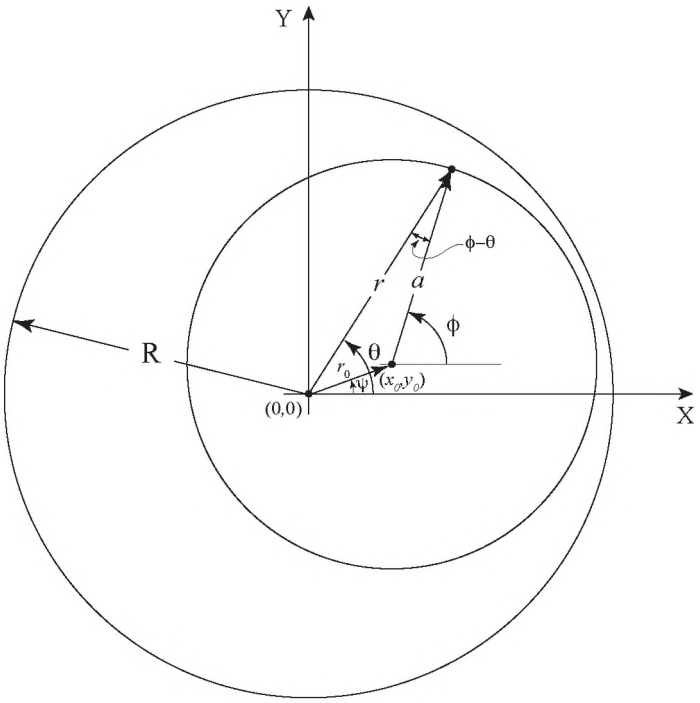

Figure 7.1. Geometry of Eccentric Circles

$$(x - x_0)^2 + (y - y_0)^2 = a^2 \tag{7.26}$$

letting,

$$x = r\cos\theta \tag{7.27}$$

$$y = r\sin\theta \tag{7.28}$$

Therefore, Equation (7.26) becomes:

$$(r\cos\theta - x_0)^2 + (r\sin\theta - y_0)^2 = a^2 \tag{7.29}$$

Expanding and collecting,

$$r(\theta) = x_0\cos\theta + y_0\sin\theta + \sqrt{(x_0\cos\theta + y_0\sin\theta)^2 + a^2 - x_0^2 - y_0^2} \tag{7.30}$$

Only the positive radical has been chosen since both it and the negative option describe the same curve only in opposite directions with increasing θ.

7.3.2. Pressure Line Load. The Equation (7.30) is the definition of eccentric load location but its vector magnitude $r(\theta)$ is not normal to the circular curve it describes, but the vector of length, a, from the origin of the eccentric circle at (x_0, y_0) is. Therefore, the relation between the angle of ψ to θ must be found. From the law of Sines:

$$\frac{r_0}{\sin(\phi - \theta)} = \frac{a}{\sin(\phi - \theta)} \tag{7.31}$$

$$\phi = \theta + \arcsin\left(\frac{r_0}{a}\sin(\theta - \psi)\right) \tag{7.32}$$

where ψ and r_0 is given by:

$$r_0 = \sqrt{x_0^2 + y_0^2} \tag{7.33}$$

$$\psi = \arctan\left(\frac{y_0}{x_0}\right) \tag{7.34}$$

The geometry of the curve relative to the two angles is shown in Figure 7.2 where the component of Δr normal to curve is given by,

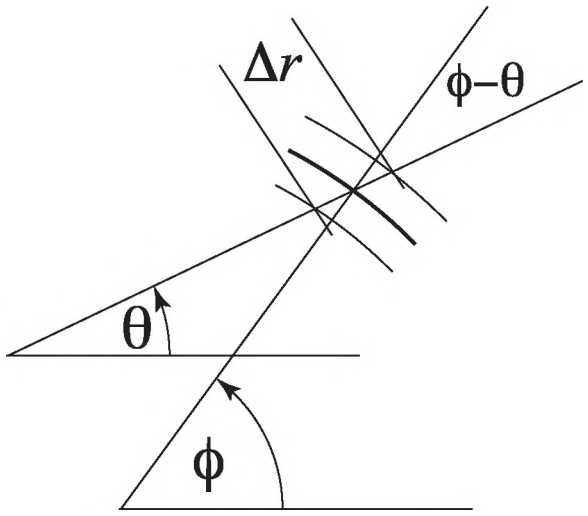

Figure 7.2. Geometry of the Curve Described Relative to θ and ϕ

$$\Delta r\cos(\phi-\theta)=\Delta r\cos\left(arcsin\left(\frac{r_0}{a}\sin(\theta-\psi)\right)\right) \tag{7.35}$$

Using the trigonometric identity $\cos(\arcsin(x))=\sqrt{1-x^2}$, therefore:

$$\Delta r\cos(\phi-\theta)=\Delta r\sqrt{1-\left(\frac{r_0}{a}\right)^2\sin^2(\theta-\psi)} \tag{7.36}$$

Thus, a force per unit length applied along a line defined by $r(\theta)$ may be expressed as,

$$q(r,\theta,t)=\lim_{\Delta r\to 0}\frac{Q(r,\theta,t)}{r\sqrt{1-\left(\frac{r_0}{a}\right)^2\sin^2(\theta-\psi)}}\left(\frac{H(r-r(\theta))-H(r-r(\theta)-\Delta r)}{\Delta r}\right) \tag{7.37}$$

Hence,

$$q(r,\theta,t)=\frac{Q(r,\theta,t)}{r\sqrt{1-\left(\frac{r_0}{a}\right)^2\sin^2(\theta-\psi)}}\delta(r-r(\theta)) \tag{7.38}$$

where, $Q(r,\theta,t)$ represents a line load applied along the curve defined by $r(\theta)$ given by Equation (7.30).

7.3.3. Two Pressure Line loads. An extension of the single pressure line load model is two pressure line loads. The line loads are separated by a small Δr and act in opposite direction. The two loads combined create a moment load on the plate. The forcing for this formulation is given by,

$$q(r,\theta,t) = \frac{Q(r,\theta,t)}{r\sqrt{1-\left(\frac{r_0}{a}\right)^2\sin^2(\theta-\psi)}}\delta(r-r(\theta)) - \frac{Q(r,\theta,t)}{r\sqrt{1-\left(\frac{r_0}{a}\right)^2\sin^2(\theta-\psi)}}\delta(r-r(\theta)-\Delta r) \tag{7.39}$$

7.3.4. Eccentric Piezoelectric Moment Load Formulation. The force exerted by the PZT ring due to the lamina's expansion and contraction produces a moment load on the plate. Here, the analytical model's formulation is extended to moment loading and follows a similar procedure to the line load shown above. The eccentric load location is defined by Equation (7.30), and the applied moment due to piezoelectric lamina is given by [45, 47],

$$M^a_{rr} = -e_{31}\left(\frac{h_p+h_g}{2}\right)v_0\,\delta(r-r(\theta))\mathrm{e}^{\mathrm{j}\omega t} \tag{7.40}$$

$$M^a_{\theta\theta} = -e_{31}\left(\frac{h_p+h_g}{2}\right)v_0\,\delta(r-r(\theta))\mathrm{e}^{\mathrm{j}\omega t} \tag{7.41}$$

7.4. STEADY STATE HARMONIC FORCED SOLUTION TO PRESSURE LINE LOADS

From Soedel, the equation of motion for transverse vibration of a circular plate with applied pressure load is given by [45]:

$$L_3(u_3) - c\dot{u}_3 - \rho h\ddot{u}_3 = -q_3 \tag{7.42}$$

where, the $L_3(u_3)$ is Love's operator and is defined by Equation (7.1), the viscous damping parameter c is introduced by replacing the force $q(r,\theta,t)$ with $q_3 - c\dot{u}_3$. Since the free circular plate's mode shape and natural frequencies are known, the forced solution of the circular plate under load can be found using the modal expansion technique. The type and magnitude of force govern the number of modes that participate in the circular plate's vibration. The general solution may be written:

$$u_3(r,\theta,t) = \sum_{m=0}^{\infty}\sum_{n=1}^{\infty} \eta_{mn}(t) U_3(r,\theta) \tag{7.43}$$

Substituting Equation (7.43) into Equation (7.42) results in,

$$\sum_{m=0}^{\infty}\sum_{n=1}^{\infty} \left[\eta_{mn} L_3(U_{3mn}) - c\dot{\eta}_{mn} U_{3mn} - \rho h \ddot{\eta}_{mn} U_{3mn}\right] \tag{7.44}$$

Substitution of (7.4) into (7.44) yields:

$$\sum_{m=0}^{\infty}\sum_{n=1}^{\infty} \left[\rho h \ddot{\eta}_{mn} + c\dot{\eta}_{mn} + \rho h \omega_{mn}^2 \eta_{mn}\right] U_{3mn} = q_3 \tag{7.45}$$

The double sum can be collapsed to a single sorted summation so that $(m,n) \rightarrow (k)$. Hence, $(0,2) \rightarrow (1)$, and $(1,0) \rightarrow (2)$, etc.

$$\sum_{k=1}^{\infty} \left[\rho h \ddot{\eta}_k + c\dot{\eta}_k + \rho h \omega_k^2 \eta_k\right] U_{3k} = q_3 \tag{7.46}$$

Since the natural modes U_{3k} are orthogonal they have the same property that is utilized in Fourier series, multiplying by U_{3n} and integrating both sides over the surface of the plate and exploiting the orthogonality of modes yields:

$$\sum_{k=1}^{\infty} \left[\rho h \ddot{\eta}_k + c\dot{\eta}_k + \rho h \omega_k^2 \eta_k\right] \int_r \int_\theta U_{3k}\, U_{3n}\, r\, d\theta dr = \int_r \int_\theta q_3\, U_{3n}\, r\, d\theta dr \tag{7.47}$$

Using the condition of modal orthogonality:

$$\int_r \int_\theta U_{3k}\, U_{3n}\, r\, d\theta dr = \begin{cases} 0 & \text{if k} \neq \text{n} \\ N_n = \int_r \int_\theta U_{3n}^2 r\, d\theta dr & \text{if k} = \text{n} \end{cases}$$

Hence, all the terms vanish except when $k = n$. This results in a second order ordinary differential equation that remains to be solved for the modal participation factor of mode n,

$$\ddot{\eta}_n + 2\zeta_n \omega_n \dot{\eta}_n + \omega_n^2 \eta_n = F_n \tag{7.48}$$

and where,

$$F_n = \frac{1}{\rho h N_n} \int_r \int_\theta q_3\, U_{3n}\, r\, d\theta dr \tag{7.49}$$

$$\zeta_n = \frac{c}{2\rho\omega_n} \tag{7.50}$$

where, q_3 is given by Equation (7.38) and (7.39) for the pressure line loads and two pressure line loads respectively, and defined as $q_3 = q(r, \theta, t)\mathrm{e}^{\mathrm{j}\omega \mathrm{t}}$. The steady state harmonic motion is of the most interest, as the transient part is usually short and of least significance. Since forcing is assumed to be harmonic, the solution will be harmonic and the solution to the Equation (7.48) is given by:

$$\eta_n = \Lambda_n \mathrm{e}^{\mathrm{j}(\omega \mathrm{t} - \phi_\mathrm{n})} \tag{7.51}$$

where,

$$\Lambda_n = \frac{F_p}{\sqrt{(\omega_n^2 - \omega^2)^2 + 4\zeta_n^2 \omega_n^2 \omega^2}} \tag{7.52}$$

$$\phi_n = \arctan\left(\frac{2\zeta_n \omega_n \omega}{\omega_n^2 - \omega^2}\right) \tag{7.53}$$

The solution is evaluated in the Maple mathematical analysis tool as manual integration of the equations is nontrivial. Appendix A4 and Appendix A5 show the solutions for single pressure line load, and two opposite pressure line loads, respectively. The Equation (7.52) is the general harmonic solution; this equation is evaluated twice to account for the sine and cosine part of the mode shape. The response to the forced solution is therefore given by,

$$u_3(r,\theta,t) = \sum_{n=1}^{\infty} \left[U_{3n}(r,\theta)\cos n\theta \Lambda_n^c + U_{3n}(r,\theta)\sin n\theta \Lambda_n^s \right] \mathrm{e}^{\mathrm{j}(\omega \mathrm{t} - \phi_\mathrm{n})} \tag{7.54}$$

where, Λ_n^c and Λ_n^s are the magnitude response from forcing due to the sine and cosine mode shapes.

7.5. STEADY STATE HARMONIC FORCED SOLUTION TO ECCENTRIC MOMENT LOAD

From Soedel and Tzou [45, 47], the equation of motion for transverse vibration of a circular plate with applied moment load is given by,

$$L_3(M_{ij}) - c\dot{u}_3 - \rho h\ddot{u}_3 = -q_3 - L_z(M_{ij}^a) \tag{7.55}$$

where the $L_3(u_3)$ is Love's operator and is defined by Equation (7.1). The viscous damping parameter c is introduced by replacing the force $q(r,\theta,t)$ with $-q_3 - L_3(M_{ij}^a) - c\dot{u}_3$. $L_3(M_{ij}^a)$ is Love's operator on the applied moment per unit length due to the deformation of the piezoelectric lamina. Therefore, the Equation (7.55) becomes:

$$D\nabla^4 u_3 + c\dot{u}_3 + \rho h\ddot{u}_3 = q_3 + \left(2\frac{1}{r}\frac{\partial M_{rr}^a}{\partial r} + \frac{\partial^2 M_{rr}^a}{\partial r^2} - \frac{1}{r}\frac{\partial M_{\theta\theta}^a}{\partial r} + \frac{1}{r^2}\frac{\partial^2 M_{\theta\theta}^a}{\partial \theta^2} \right) \tag{7.56}$$

Here, $M_{r\theta}$ and $M_{\theta r}$ are zero since the piezoelectric laminae will not induce the twisting moments. Applying modal expansion similarly to the Equations (7.43) to (7.48) yields,

$$\ddot{\eta}_n + 2\zeta_n\omega_n\dot{\eta}_n + \omega_n^2\eta_n = F_n \tag{7.57}$$

where,

$$F_n = \frac{1}{\rho h N_n}\int_r\int_\theta\left(2\frac{1}{r}\frac{\partial M_{rr}^a}{\partial r} + \frac{\partial^2 M_{rr}^a}{\partial r^2} - \frac{1}{r}\frac{\partial M_{\theta\theta}^a}{\partial r} + \frac{1}{r^2}\frac{\partial^2 M_{\theta\theta}^a}{\partial\theta^2}\right)U_{3n}\, r\, d\theta dr \tag{7.58}$$

$$\zeta_n = \frac{c}{2\rho h\omega_n} \tag{7.59}$$

and where the transverse loading, q_3 is considered negligible. The steady state harmonic motion is of the most interest, as the transient part is usually short and of least significance. Since forcing is assumed to be harmonic, the solution will be harmonic and the solution to the Equation (7.57) is given by:

$$\eta_n = \Lambda_n e^{j(\omega t - \phi_p)} \tag{7.60}$$

where,

$$\Lambda_n = \frac{F_n}{\sqrt{(\omega_n^2 - \omega^2)^2 + 4\zeta_n^2\omega_n^2\omega^2}} \tag{7.61}$$

$$\phi_n = \arctan\left(\frac{2\zeta_n\omega_n\omega}{\omega_n^2 - \omega^2}\right) \tag{7.62}$$

The solution is evaluated in the Maple mathematical analysis tool as manual integration of the equations is nontrivial. Appendix A6 shows the solutions for moment line load. The Equation (7.61) is the general harmonic solution; this equation is evaluated twice to account for the sine and cosine part of the mode shape. The response to the forced solution

is therefore given by,

$$u_3(r,\theta,t) = \sum_{n=1}^{\infty} \left[U_{3n}(r,\theta)\ \cos n\theta\ \Lambda_n^c + U_{3n}(r,\theta)\ \sin n\theta\ \Lambda_n^s \right] e^{j(\omega t - \phi_n)} \tag{7.63}$$

where, Λ_n^c and Λ_n^s are the magnitude response from forcing due to the cosine and sine mode shapes, respectively.

7.6. FREQUENCY RESPONSE

The frequency response of the plate for both the pressure line load and moment line load is calculated by separating the complex Equations (7.54) and (7.63) into real and imaginary parts and then taking the magnitude and phase to recast them in polar form.

$$\mathrm{Re}(u_3(r,\theta,t)) = \sum_{n=1}^{\infty} \left[U_{3n}(r,\theta) \cos n\theta\ \Lambda_n^c \cos\phi_n + U_{3n}(r,\theta) \sin n\theta\ \Lambda_n^s \cos\phi_n \right] \tag{7.64}$$

$$\mathrm{Im}(u_3(r,\theta,t)) = \sum_{n=1}^{\infty} \left[U_{3n}(r,\theta) \cos n\theta\ \Lambda_n^c \sin\phi_n + U_{3n}(r,\theta) \sin n\theta\ \Lambda_n^s \sin\phi_n \right] \tag{7.65}$$

Therefore, magnitude and phase of the response at any point on the plate is given by,

$$|u_3(r,\theta,t)| = \sqrt{(\mathrm{Re}(u_3(r,\theta,t))^2 + \mathrm{Im}(u_3(r,\theta,t))^2} \tag{7.66}$$

$$\angle u_3(r,\theta,t) = \arctan\left(\frac{\mathrm{Im}(u_3(r,\theta,t))}{\mathrm{Re}(u_3(r,\theta,t))} \right) \tag{7.67}$$

7.7. ANALYTICAL AND FINITE ELEMENT MODEL COMPARISONS

The analytical models are compared to the results of similar models developed in ANSYS for both the pressure line load and line moment models. ANSYS captures the 3-D plate's behavior, whereas the analytical model is limited to shell and thin plate theory. The geometric and material properties used in both the analytical and ANSYS model are the same and shown in Table 7.1.

Table 7.1. Geometric and Material Values

Parameter	Pressure Line Load	Moment load
Radius of the plate, a	15.875 mm	15.875 mm
Thickness of the plate, h_g	1.5875 mm	1.5875 mm
Thickness of the PZT, h_p	-	1 mm
Location of the center of eccentricity in X, x_0	2.0 mm	2.0 mm
Location of the center of eccentricity in Y, y_0	1.5 mm	1.5 mm
Location of the center of eccentricity in radial, r_0	2.5 mm	2.5 mm
Location of the center of eccentricity in angle, ψ	0.6435 rads	0.6435 rads
Line pressure, Q	10 N-m/m	-
Young's modulus, E	72 GPa	72 GPa
Density, ρ	2200 kg/m^3	2200 kg/m^3
Poisson's ratio, ν	0.17	0.17
Piezo constant, e_{31}	-	-135 m/v
Voltage, v_0	-	10 V

A two-dimensional shell model was mapped meshed using quadratic elements. Modal analysis was conducted to check for mesh convergence. The discrepancy in the analytical and FEM model's natural frequency is within 1% for the first ten modes and increases for higher frequency modes. A comparison of the first two modes is shown in Figure 7.3, and the frequency of the first five modes is shown in Table 7.2.

A pressure line load and moment load are applied to the geometry, and a harmonic mode superposition solution is used to solve for the plate's response in the frequency range of 4 kHz to 500 kHz. The pressure loading and moment loading as represented in ANSYS

Table 7.2. Natural Frequencies

Mode	Analytical Frequency [Hz]	ANSYS [Hz]
Mode 1	9499.3	9511.5
Mode 2	14401.8	14417
Mode 3	21830.9	21567
Mode 4	33612.5	32932
Mode 5	38061.1	37015

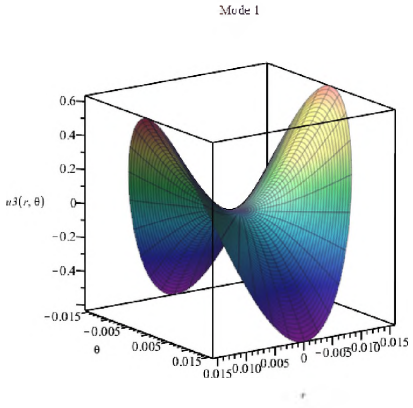

(a) Maple Mode 1

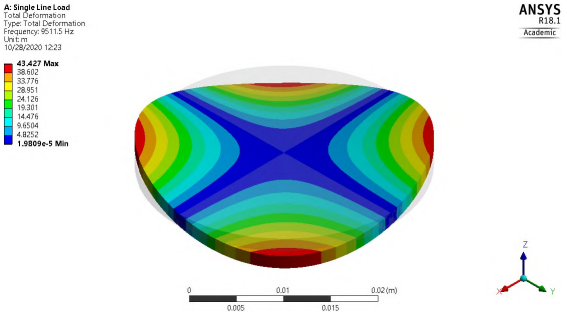

(b) ANSYS Mode 1

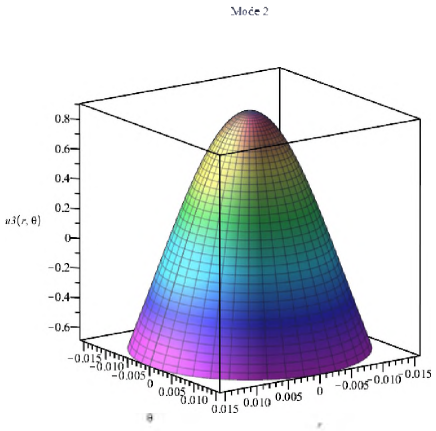

(c) Maple Mode 2

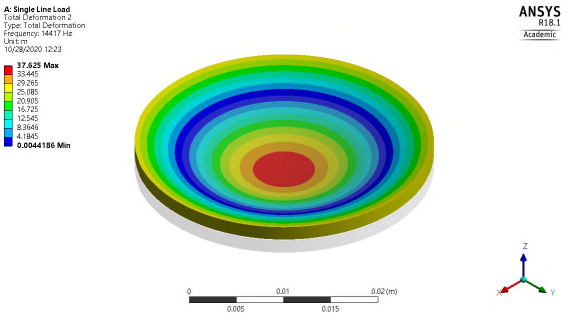

(d) ANSYS Mode 2

Figure 7.3. First Two Modes of the Circular Plate

are shown in Figure 7.4; frequency response is calculated at the center of the circular plate and on its edge. The magnitude and phase response from the analytical model is compared to the ANSYS results.

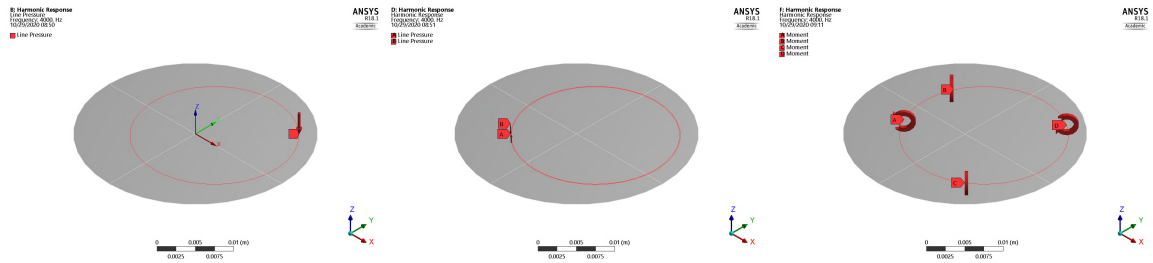

(a) Pressure Line Load (b) Two Pressure Line Loads (c) Moment Load

Figure 7.4. ANSYS Loading Models

Figure 7.5 and Figure 7.6 show the ANSYS and analytical model's comparison for a single pressure line load. The analytical and ANSYS models closely follow each other and match with reasonable accuracy at the resonate frequencies. There are discrepancies due to the ANSYS model accounting for the 3-dimensional and shear effects, and the damping models are different. Similarly, results are seen for two-line load models in Figure 7.7 and Figure 7.8 and the moment loading in Figure 7.9 and Figure 7.10.

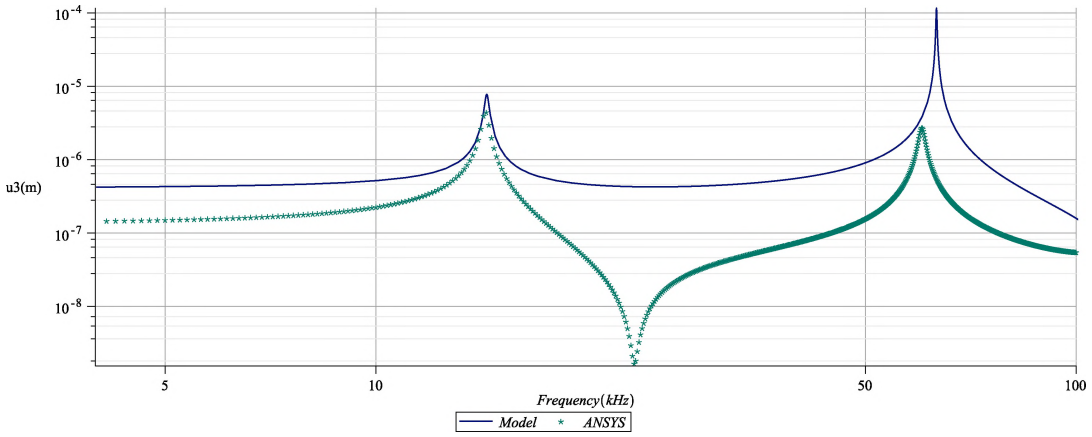

Figure 7.5. Frequency Response of Eccentric Pressure Line Load at the Center of the Circular Plate

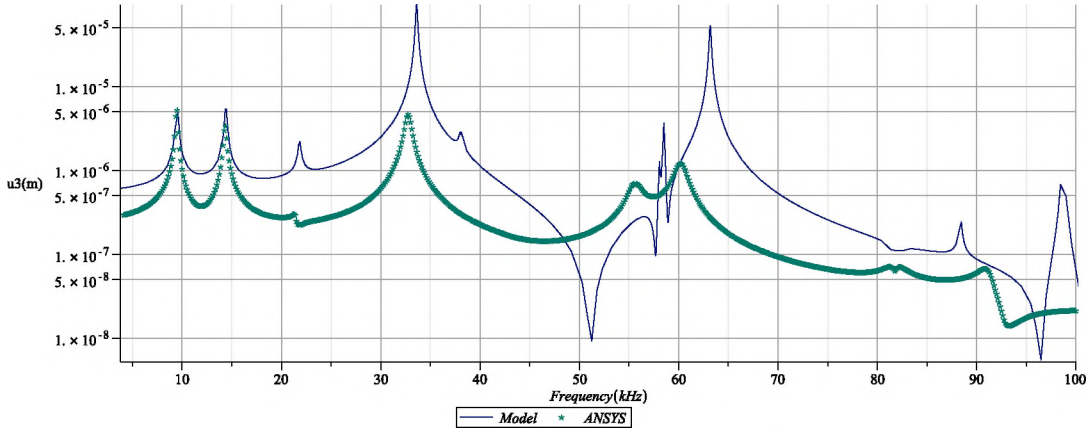

Figure 7.6. Frequency Response of Eccentric Pressure Line Load at the Edge of the Circular Plate

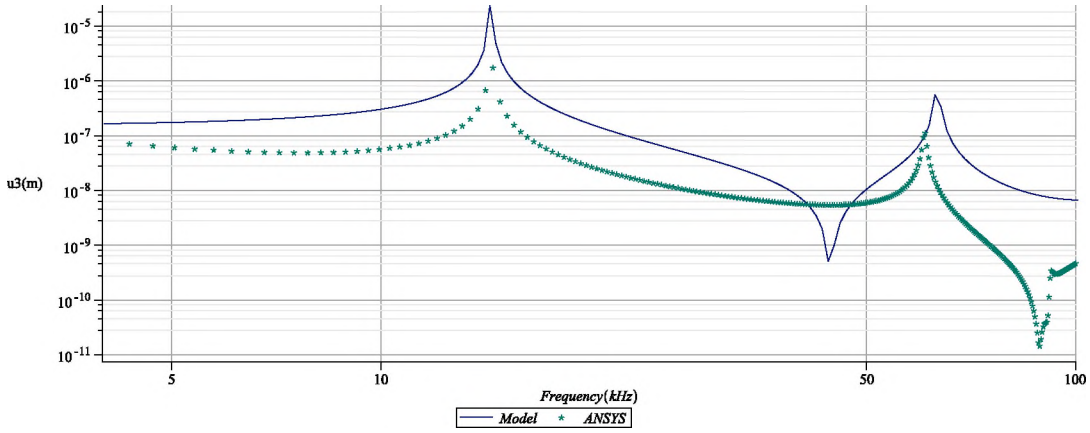

Figure 7.7. Frequency Response of Eccentric to Two Pressure Line Loads at the Center of the Circular Plate

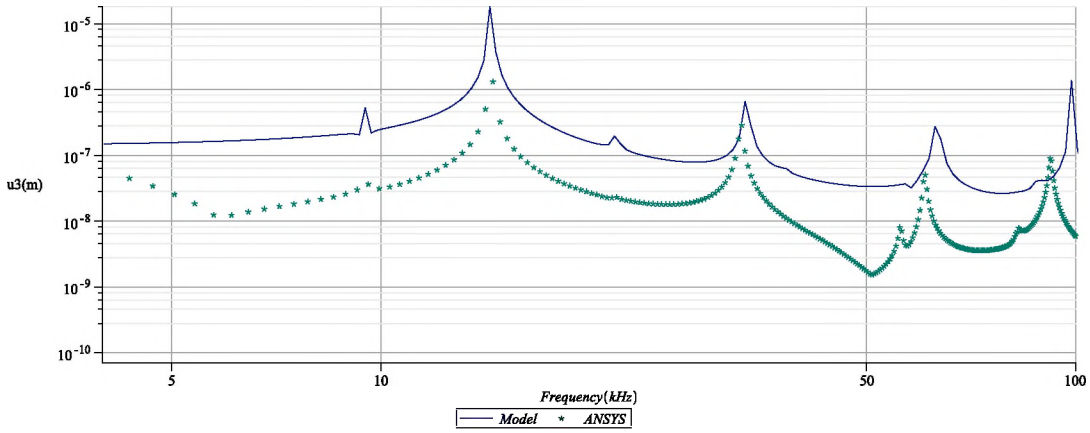

Figure 7.8. Frequency Response of Eccentric to Two Pressure Line Loads at the Edge of the Circular Plate

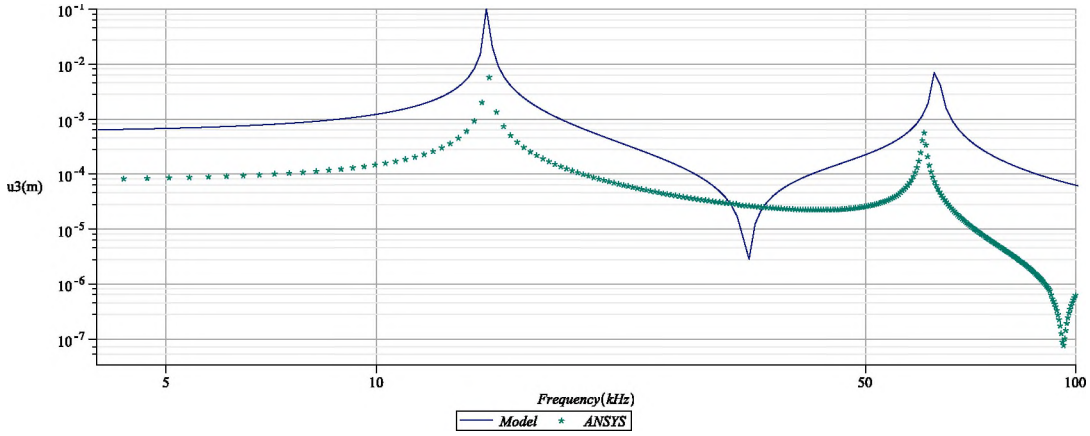

Figure 7.9. Frequency Response of Eccentric Moment Line Load at the Center of the Circular Plate

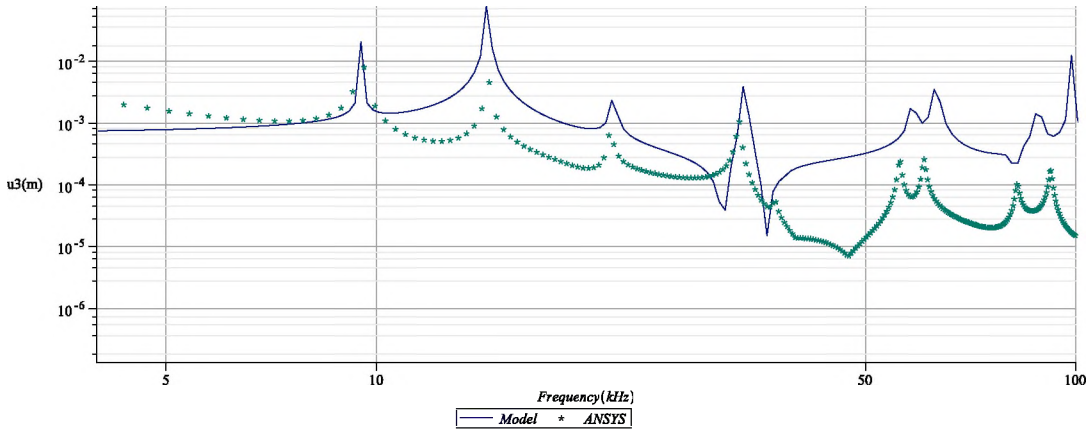

Figure 7.10. Frequency Response of Eccentric Moment Line Load at the Edge of the Circular Plate

8. CONCLUSIONS

Most of the objectives laid out in the study have been met. A thorough understanding of the forces of adhesion for solids and liquids has been accomplished. A review of current technologies used in the industry for removing contaminants from a surface has been conducted. The use of structural modes by PZT excitation to remove contaminants on a glass surface were validated. Four designs were developed that take advantage of axisymmetric and thickness mode excitation so that the designs could be driven at varying frequencies and surface accelerations on the glass.

ANSYS was used to design and optimize each prototype. Each optimization and design used a custom results algorithm to optimize the normal surface acceleration on the glass surface in the lens field-of-view. These optimizations facilitate rapid insight into each design's behavior. The predicted sensitivity of the design variables to the optimization constraints and goals allows for rapid design selection. The optimization techniques developed here can be used on any cleaning actuator designs and would allow for a fast evaluation of a design's potential and to discover design flaws without the need of building a physical prototype.

Four proposed designs have been prototyped and tested. Each of the prototypes had unique manufacturing issues that led to further studies or developments. The very first prototype resulted in stress concentrations in the fused quartz lens, due to the eccentricities in the assembly, motivating an ANSYS study that was conducted to understand how the stress in the glass was affected by eccentricity. This was the motivation to develop analytical models that could help analyze eccentric loads on circular plates.

The SPS prototype was the first to be built and tested. Testing of the prototype was initially done via manual control and hand recording test results, which proved inefficient and resulted in poor control of the test. A LabView system was developed to automate testing and data collection. The SPS prototype, one of the simplest designs proposed in the

project, helped overcome several optimization, design, and development challenges. The testing of prototypes resulted in the loss of mechanical quality factor. An investigation of the type of epoxy used and the bond thickness was undertaken as a result of the prototype failure; results of this study led to choosing EPO-TEK 323-LP for future prototypes. The SPS, MPS, RPS, and SDS prototypes had success in removing various solid contaminants in the ultrasonic frequency range, and liquid contaminants in the megasonic frequency range.

To make more reliable prototypes, the critical task of studying the bond of PZT to glass must be initiated. A detailed study of glass, bonding material, co-firing, and re-poling the PZT after the co-firing process needs to be undertaken. Multiple prototypes need to be put through efficacy testing, destructive, and nondestructive. These prototypes should be tested to fatigue failure to quantify the life of the prototypes. Driving prototypes efficiently will require tracking the resonance and implementation of resonant switch-mode circuit. Finally, a protocol needs to be established to quantify the efficacy and to compare the actuator designs.

APPENDIX A.

PROGRAMING SCRIPTS

1. ANSYS MATERIAL CONVERSION SCRIPT

```
%%
clc
clear all
close all
%% Permittivity of free space
format long g
ep0=8.854e-12;

%%
prompt = 'Do you want to enter PZT Data or Load ...
Stanrdard PZT Data? Y/N [N]: ';
str = input(prompt,'s');
if isempty(str)
    str = 'N';
end
if str=='N'||str=='n'
    load('PZT_DATA');
    prompt = 'Select PZT type? BaTi03/PZT-4/PZT-5A...
    /PZT-5H/PZT-8/PKI-502 [PZT-5A]: ';
    str = input(prompt,'s');
    str=upper(str);
    if isempty(str)
        str = 'PZT-5A';
    end
    if strcmp(str,'BATI03')
        i=1;
```

```
27      elseif strcmp(str,'PZT-4')
28          i=2;
29      elseif strcmp(str,'PZT-5A')
30          i=3;
31      elseif strcmp(str,'PZT-5H')
32          i=4;
33      elseif strcmp(str,'PZT-8')
34          i=5;
35      elseif strcmp(str,'PKI-502')
36          i=6;
37      end
38      Se=zeros(6,6);
39      d=zeros(6,3);
40
41      Se(1,1) = PZT(5,i);
42      Se(1,2) = PZT(7,i);
43      Se(1,3) = PZT(8,i);
44      Se(3,3) = PZT(6,i);
45      Se(4,4) = PZT(9,i);
46      Se(6,6) = 2*(Se(1,1)-Se(1,2));
47      Se(2,1)=Se(1,2);
48      Se(2,2)=Se(1,1);
49      Se(2,3)=Se(1,3);
50      Se(3,1)=Se(1,3);
51      Se(3,2)=Se(1,3);
52      Se(5,5)=Se(4,4);
53      Ce=Se^-1;
54
55      d(1,3) = PZT(2,i);
```

```
56      d(3,3) = PZT(3,i);
57      d(5,1) = PZT(4,i);
58      d(4,2) = d(5,1);
59      d(2,3) = d(1,3);
60      e=Se^-1*d;
61
62      kpt(1,1) = PZT(10,i);
63      kpt(2,2) =kpt(1,1) ;
64      kpt(3,3) = PZT(11,i);
65      ept=kpt*ep0;
66      eps=ept-(d'*Se^-1*d);
67      kps=eps/ep0;
68      rho = PZT(1,i);
69
70  else
71
72      %% Density
73      prompt = 'Density :';
74      rho = input(prompt);
75
76      %% Strength Data
77      prompt = 'Do you want to enter Compliance? Y/N...
78      [Y]: ';
79      str = input(prompt,'s');
80      if isempty(str)
81          str = 'Y';
82      end
83
84      if str=='Y'||str=='y'
```

```
85          Se=zeros(6,6);
86          prompt = 'Se11 :';
87          Se(1,1) = input(prompt);
88          prompt = 'Se12 :';
89          Se(1,2) = input(prompt);
90          prompt = 'Se13 :';
91          Se(1,3) = input(prompt);
92          prompt = 'Se33 :';
93          Se(3,3) = input(prompt);
94          prompt = 'Se44 :';
95          Se(4,4) = input(prompt);
96          prompt = 'Se66 :';
97          Se66 = input(prompt);
98          if isempty(Se66)
99              Se(6,6) = 2*(Se(1,1)-Se(1,2));
100         else
101             Se(6,6)=Se66;
102         end
103         Se(2,1)=Se(1,2);
104         Se(2,2)=Se(1,1);
105         Se(2,3)=Se(1,3);
106         Se(3,1)=Se(1,3);
107         Se(3,2)=Se(1,3);
108         Se(5,5)=Se(4,4);
109         Ce=Se^-1;
110
111     elseif str=='n'||str=='N'
112         prompt = 'Do you want to enter Stiffness?...
113         Y/N [Y]: ';
```

```
114         str = input(prompt,'s');
115         if isempty(str)
116             str = 'Y';
117         end
118         if str=='Y'||str=='y'
119             Ce=zeros(6,6);
120             prompt = 'Ce11 :';
121             Ce(1,1) = input(prompt);
122             prompt = 'Ce12 :';
123             Ce(1,2) = input(prompt);
124             prompt = 'Ce13 :';
125             Ce(1,3) = input(prompt);
126             prompt = 'Ce33 :';
127             Ce(3,3) = input(prompt);
128             prompt = 'Ce44 :';
129             Ce(4,4) = input(prompt);
130             prompt = 'Ce66 :';
131             Ce(6,6) = input(prompt);
132             Ce(2,1)=Ce(1,2);
133             Ce(2,2)=Ce(1,1);
134             Ce(2,3)=Ce(1,3);
135             Ce(3,1)=Ce(1,3);
136             Ce(3,2)=Ce(1,3);
137             Ce(5,5)=Ce(4,4);
138             Se=Ce^-1;
139
140         elseif str=='n'||str=='N'
141             fprintf('enter Ortho\n');
142             prompt = 'Ex :';
```

```
143             Ex = input(prompt);
144             prompt = 'Ey=Ez :';
145             Ez = input(prompt);
146             prompt = 'vxy :';
147             vxy = input(prompt);
148             prompt = 'vyz=vxz :';
149             vyz = input(prompt);
150             prompt = 'Gxy :';
151             Gxy = input(prompt);
152             prompt = 'Gyz=Gxz :';
153             Gxz = input(prompt);
154             Se=zeros(6,6);
155             Se(1,1)= 1/Ex;
156             Se(1,2) = -vxy/Ex;
157             Se(1,3) = -vyz/Ez;
158             Se(3,3) = 1/Ez;
159             Se(4,4) = 1/Gxy;
160             Se(6,6) = 1/Gxz;
161             Se(2,1)=Se(1,2);
162             Se(2,2)=Se(1,1);
163             Se(2,3)=Se(1,3);
164             Se(3,1)=Se(1,3);
165             Se(3,2)=Se(1,3);
166             Se(5,5)=Se(4,4);
167             Ce=Se^-1;
168         end
169     end
170     clear Ex Ez vxy vyz Gxy Gxz
171
```

```
172     %% Coupling Data
173     prompt = 'Do you want to enter Piezoelectric...
174     coupling matrix relating strain? Y/N [Y]: ';
175     str = input(prompt,'s');
176     if isempty(str)
177         str = 'Y';
178     end
179
180     if str=='Y'||str=='y'
181         d=zeros(6,3);
182         prompt = 'd15 :';
183         d(5,1) = input(prompt);
184         d(4,2) = d(5,1);
185         prompt = 'd31 :';
186         d(1,3) = input(prompt);
187         d(2,3) = d(1,3);
188         prompt = 'd33 :';
189         d(3,3) = input(prompt);
190         e=Se^-1*d;
191
192     elseif  str=='n'||str=='N'
193         fprintf('Enter Piezoelectric coupling...
194         matrix relating stress\n');
195         e=zeros(6,3);
196         prompt = 'e15 :';
197         e(5,1) = input(prompt);
198         e(4,2) = e(5,1);
199         prompt = 'e31 :';
200         e(1,3) = input(prompt);
```

```
201         e(2,3) = e(1,3);
202         prompt = 'e33 :';
203         e(3,3) = input(prompt);
204     end
205
206     %% Permittivity Data
207     prompt = 'Do you want to enter relative...
208     Permittivity matrix at constant stress? Y/N [Y]: ';
209     str = input(prompt,'s');
210     if isempty(str)
211         str = 'Y';
212     end
213
214
215     if str=='Y'||str=='y'
216         kpt=zeros(3,3);
217         prompt = 'kpt11 :';
218         kpt(1,1) = input(prompt);
219         kpt(2,2) =kpt(1,1) ;
220         prompt = 'kpt33 :';
221         kpt(3,3) = input(prompt);
222         ept=kpt*ep0;
223         eps=ept-(d'*Se^-1*d);
224         kps=eps/ep0;
225
226     elseif str=='n'||str=='N'
227         fprintf('Enter Relative Permittivity...
228         matrix at constant  strain\n');
229
```

```
230         kps=zeros(3,3);
231         prompt = 'kps11 :';
232         kps(1,1) = input(prompt);
233         kps(2,2) =kps(1,1);
234         prompt = 'kps33 :';
235         kps(3,3) = input(prompt);
236     end
237 end
238
239
240 %% Anysy Transformatiom
241 % X axis
242 Cex=Ce;
243 Cex(1,1)=Ce(3,3);
244 Cex(1,2)=Ce(1,3);
245 Cex(1,3)=Ce(1,3);
246 Cex(2,1)=Ce(1,3);
247 Cex(2,2)=Ce(1,1);
248 Cex(2,3)=Ce(1,2);
249 Cex(3,1)=Ce(1,3);
250 Cex(3,2)=Ce(1,2);
251 Cex(3,3)=Ce(1,1);
252 Cex(4,4)=Ce(4,4);
253 Cex(5,5)=Ce(6,6);
254 Cex(6,6)=Ce(4,4);
255
256 ex=zeros(6,3);
257 ex(1,1)=e(3,3);
258 ex(2,1)=e(1,3);
```

```
259 ex(3,1)=e(1,3);
260 ex(4,2)=e(4,2);
261 ex(6,3)=e(5,1);
262
263 kpsx=kps;
264 kpsx(1,1)=kps(3,3);
265 kpsx(3,3)=kps(1,1);
266
267 % Y axis
268 Cey=Ce;
269 Cey(1,2)=Ce(1,3);
270 Cey(1,3)=Ce(1,2);
271 Cey(2,1)=Ce(1,3);
272 Cey(2,2)=Ce(3,3);
273 Cey(2,3)=Ce(1,3);
274 Cey(3,1)=Ce(1,2);
275 Cey(3,2)=Ce(1,3);
276 Cey(3,3)=Ce(1,1);
277 ey=zeros(6,3);
278 ey(1,2)=e(1,3);
279 ey(2,2)=e(3,3);
280 ey(3,2)=e(1,3);
281 ey(4,1)=e(4,2);
282 ey(5,3)=e(5,1);
283 kpsy=kps;
284 kpsy(2,2)=kps(3,3);
285 kpsy(3,3)=kps(1,1);
286
287 % Z axis
```

```
288 Cez=Ce;
289 Cez(4,4)=Ce(6,6);
290 Cez(6,6)=Ce(5,5);
291 ez=e;
292 ez(4,2)=0;
293 ez(5,1)=0;
294 ez(5,2)=e(4,2);
295 ez(6,1)=e(5,1);
296 kpsz=kps;
297
298 %% Output Format
299 clear prompt str
300 prompt = 'Axis of Polorizarion? X/Y/Z [Z]: ';
301 axis = input(prompt,'s');
302 if isempty(axis)
303     axis = 'Z';
304 end
305 prompt = 'Ansys Workbench(W) Format or APDL(A)...
306  Format? W/A [W]: ';
307 str = input(prompt,'s');
308 if isempty(str)
309     str = 'W';
310 end
311 %% Ansys APDL output
312 if str=='A'||str=='a'
313     prompt = 'Ansys APDL(A)Format Material Number?...
314     [1]: ';
315     MATID = input(prompt);
316     if isempty(MATID)
```

```
317         MATID = 1;
318     end
319     clc
320     fprintf('ANSYS APDL INPUT in %c axis and...
321     Material ID %d \n\n',axis,MATID);
322     fprintf('/COM, Density \n');
323     fprintf('MP,DENS,%d,%6.2f \n\n',MATID,rho);
324
325
326     if axis=='z'||axis=='Z'
327         fprintf('/COM, Stiffness \n');
328         fprintf('TB,ANEL,%d,1,0 \n',MATID);
329         fprintf('TBDATA,1,%10.4f,%10.4f,%10.4f\n',...
330         Cez(1,1),Cez(1,2),Cez(1,3));
331         fprintf('TBDATA,7,%10.4f,%10.4f\n',Cez(2,2)...
332         ,Cez(2,3));
333         fprintf('TBDATA,12,%10.4f\n',Cez(3,3));
334         fprintf('TBDATA,16,%10.4f\n',Cez(4,4));
335         fprintf('TBDATA,19,%10.4f\n',Cez(5,5));
336         fprintf('TBDATA,21,%10.4f\n\n',Cez(6,6));
337
338         fprintf('/COM, Piezo Matrix \n');
339         fprintf('TB,piez,%d \n',MATID);
340         fprintf('TBDATA,3,%6.4f\n',ez(1,3));
341         fprintf('TBDATA,6,%6.4f\n',ez(2,3));
342         fprintf('TBDATA,9,%6.4f\n',ez(3,3));
343         fprintf('TBDATA,14,%6.4f\n',ez(5,2));
344         fprintf('TBDATA,16,%6.4f\n\n',ez(6,1));
345
```

```
346         fprintf('/COM, Permittivity Matrix \n');
347         fprintf('MP,PERX,%d,%6.2f \n',MATID,...
348         kpsz(1,1));
349         fprintf('MP,PERY,%d,%6.2f \n',MATID,...
350         kpsz(2,2));
351         fprintf('MP,PERZ,%d,%6.2f \n\n',MATID,...
352         kpsz(3,3));
353
354     elseif axis=='y'||axis=='Y'
355         fprintf('/COM, Stiffness \n');
356         fprintf('TB,ANEL,%d,1,0 \n',MATID);
357         fprintf('TBDATA,1,%10.4f,%10.4f,%10.4f\n',...
358         Cey(1,1),Cey(1,2),Cey(1,3));
359         fprintf('TBDATA,7,%10.4f,%10.4f\n',Cey(2,2),...
360         Cey(2,3));
361         fprintf('TBDATA,12,%10.4f\n',Cey(3,3));
362         fprintf('TBDATA,16,%10.4f\n',Cey(4,4));
363         fprintf('TBDATA,19,%10.4f\n',Cey(5,5));
364         fprintf('TBDATA,21,%10.4f\n\n',Cey(6,6));
365
366         fprintf('/COM, Piezo Matrix \n');
367         fprintf('TB,piez,%d \n',MATID);
368         fprintf('TBDATA,2,%6.4f\n',ey(1,2));
369         fprintf('TBDATA,5,%6.4f\n',ey(2,2));
370         fprintf('TBDATA,8,%6.4f\n',ey(3,2));
371         fprintf('TBDATA,10,%6.4f\n',ey(4,1));
372         fprintf('TBDATA,15,%6.4f\n\n',ey(5,3));
373
374         fprintf('/COM, Permittivity Matrix \n');
```

```
375         fprintf('MP,PERX,%d,%6.2f \n',MATID,...
376         kpsy(1,1));
377         fprintf('MP,PERY,%d,%6.2f \n',MATID,...
378         kpsy(2,2));
379         fprintf('MP,PERZ,%d,%6.2f \n\n',MATID,...
380         kpsy(3,3));
381
382     elseif axis=='X'||axis=='x'
383         fprintf('/COM, Stiffness \n');
384         fprintf('TB,ANEL,%d,1,0 \n',MATID);
385         fprintf('TBDATA,1,%10.3f,%10.3f,%10.3f\n',...
386         Cex(1,1),Cex(1,2),Cex(1,3));
387         fprintf('TBDATA,7,%10.3f,%10.3f\n',Cex(2,2)...
388         ,Cex(2,3));
389         fprintf('TBDATA,12,%10.3f\n',Cex(3,3));
390         fprintf('TBDATA,16,%10.3f\n',Cex(4,4));
391         fprintf('TBDATA,19,%10.3f\n',Cex(5,5));
392         fprintf('TBDATA,21,%10.3f\n\n',Cex(6,6));
393
394         fprintf('/COM, Piezo Matrix \n');
395         fprintf('TB,piez,%d \n',MATID);
396         fprintf('TBDATA,1,%6.4f\n',ex(1,1));
397         fprintf('TBDATA,4,%6.4f\n',ex(2,1));
398         fprintf('TBDATA,7,%6.4f\n',ex(3,1));
399         fprintf('TBDATA,11,%6.4f\n',ex(4,2));
400         fprintf('TBDATA,18,%6.4f\n\n',ex(6,3));
401
402         fprintf('/COM, Permittivity Matrix \n');
403         fprintf('MP,PERX,%d,%6.2f \n',MATID,...
```

```
404         kpsx(1,1));
405         fprintf('MP,PERY,%d,%6.2f \n',MATID,...
406         kpsx(2,2));
407         fprintf('MP,PERZ,%d,%6.2f \n\n',MATID,...
408         kpsx(3,3));
409     end
410     %% Ansys Workbench output
411 elseif str=='W'||str=='w'
412     clc
413     fprintf('ANSYS Workbench INPUT in %c axis \n\n...
414     ',axis);
415     if axis=='z'||axis=='Z'
416         fprintf('/COM, Stiffness \n');
417         Cez
418         fprintf('/COM, Piezo Matrix \n');
419         ez
420         fprintf('/COM, Permittivity Matrix \n');
421         kpsz
422         fprintf('/COM, Density \n');
423         rho
424     elseif axis=='y'||axis=='Y'
425         fprintf('/COM, Stiffness \n');
426         Cey
427         fprintf('/COM, Piezo Matrix \n');
428         ey
429         fprintf('/COM, Permittivity Matrix \n');
430         kpsy
431         fprintf('/COM, Density \n');
432         rho
```

```
433
434     elseif axis=='X'||axis=='x'
435         fprintf('/COM, Stiffness \n');
436         Cex
437         fprintf('/COM, Piezo Matrix \n');
438         ex
439         fprintf('/COM, Permittivity Matrix \n');
440         kpsx
441         fprintf('/COM, Density \n');
442         rho
443
444     end
445 end
```

2. EQUIVALENT CIRCUIT MODEL - PYTHON

```
1 ####################--
2 # File: eqcirc2.py
3 # Equivalent Circuit Parameter Estimator for Piezoelectric ...
     Structures
4 # Author: D. S. Stutts
5 # Associate Professor of Mechanical Engineering
6 # 282 Toomey Hall
7 # 400 W. 13th St.
8 # Rolla, MO 65409-0050
9 # Email: stutts@mst.edu
10 # Original release: eqcirc2.py Version 0.1.0 3-29-2015
11 # Modified and renamed to eqcirc2.py to input impedance ...
     4-17-2015:DSS
12 # Now also automatically determines the number of points to ...
     process.
13 ####################--
14 """
15 This program calculates the equivalent
16 circuit parameters from frequency-impedance magnitude
17 magnitude data stored in the standard
18 HP4294A Impedance Analyser output data
19 format.
20
21 An image of the equivalent circuit may be
22 found here:
23 http://web.mst.edu/¬stutts/piezoequivcircuit0.png
```

```
24
25 The program first calculates the approximate
26 equivalent circuit parameters for a single
27 resonance-antiresonance frequency pair.
28 It then uses the Levenberg-Marquardt (LM)
29 nonlinear least squares algorithm to
30 optimize the model in the least squares
31 sense.  The LM algorithm is invoked
32 via a call to leastsq(rez, z0, args=(yy, xx),
33 full_output=1) from the scipy.optimize library.
34
35 See: http://docs.scipy.org/doc/scipy-0.14.0/
36 reference/generated/scipy.optimize.leastsq.html
37 for more information.
38
39 eqcirc2.py calculates the following outputs stdout:
40
41 (1) fr (the resonance frequency)
42 (2) fa (the anti-resonance frequency)
43 (3) C0 (the parallel capacitance)
44 (4) R1 (the motional resistance)
45 (5) L1 (the motional inductance)
46 (6) C1 (the motional capacitance)
47 (7) Q (the series R1L1C1 resonance
48        quality factor = 1/2zeta)
49 (8) RMS Error
50
51 A graph of the data and model is also produced.
52
```

```
53 Example call: python eqcirc2.py inputdatafile.txt
54
55 The graph may be saved in PNG format, and the text
56 may be redirected from stdout to a file like so:
57
58 python eqcirc2.py inputdatafile.txt > outdata.txt
59
60  # This code is copyrighted by the author, but released under ...
       the MIT
61  # license:
62
63 Copyright (c) 2015 eqcirc2.py
64
65 S&T and the University of Missouri Board of Curators
66 license to you the right to use, modify, copy, and distribute ...
      this
67 code subject to the MIT license:
68
69 Permission is hereby granted, free of charge, to any person ...
      obtaining a copy
70 of this software and associated documentation files (the ...
      "Software"), to deal
71 in the Software without restriction, including without ...
      limitation the rights
72 to use, copy, modify, merge, publish, distribute, sublicense, ...
      and/or sell
73 copies of the Software, and to permit persons to whom the ...
      Software is
74 furnished to do so, subject to the following conditions:
```

```
75
76 The above copyright notice and this permission notice shall ...
     be included
77 in all copies or substantial portions of the Software.
78
79 THE SOFTWARE IS PROVIDED "AS IS", WITHOUT WARRANTY OF ANY ...
     KIND, EXPRESS OR
80 IMPLIED, INCLUDING BUT NOT LIMITED TO THE WARRANTIES OF ...
     MERCHANTABILITY,
81 FITNESS FOR A PARTICULAR PURPOSE AND NONINFRINGEMENT. IN NO ...
     EVENT SHALL
82 THE AUTHORS OR COPYRIGHT HOLDERS BE LIABLE FOR ANY CLAIM, ...
     DAMAGES OR OTHER
83 LIABILITY, WHETHER IN AN ACTION OF CONTRACT, TORT OR ...
     OTHERWISE, ARISING
84 FROM, OUT OF OR IN CONNECTION WITH THE SOFTWARE OR THE USE OR ...
     OTHER
85 DEALINGS IN THE SOFTWARE.
86
87 The author kindly requests that any publications benefitting ...
     from the use
88 of this software include the following citation:
89
90 @Misc{eqcirc1_2015,
91 author =   {Stutts, D. S.},
92 title = {{eqcirc2.py}: {Equivalent Circuit Parameter Estimator
93 for Piezoelectric Structures.}},
94 howpublished = {\url{https://github.com/MSTESG/EQCIRC1.git}},
95 year = {2015}}
```

```
96
97 """
98
99
100 from pylab import *
101 from scipy.optimize import leastsq
102 #from matplotlib import pyplot
103 # Initialize some lists:
104 ydat = []
105 x = []
106 xx = []
107 yy = []
108 zdat = []
109 # Define functions:
110 def y(f, z):  # Admittance model
111     return 0.2e1 * np.pi * f * np.sqrt(0.4e1 * z[0] ** 2*z[3]**2*
112     z[1] ** 2 * np.pi ** 2 * f ** 2 + (
113     -0.4e1 * z[0] * z[3] * z[2] * np.pi ** 2 * f ** 2
114     + z[0]+z[3])**2)*((-0.4e1 * z[3]*z[2]*np.pi ** ...
          2*f**2+0.1e1)**2
115     + 0.4e1*z[1]**2*z[3]**2*np.pi**2*f**2)**(-0.1e1/0.2e1)
116
117
118 def C0_i(Ymin, Ymax, fr, fa):  # Parallel capacitance estimate
119     return np.sqrt(0.2e1*(fa ** 2 - fr**2)*Ymin**2/np.pi**2/fa**4
120     + 0.2e1*np.sqrt((fa ** 2 - f ** 2)**2/np.pi**4/fa**8*Ymin**4
121     + 0.4e1*Ymin**2*Ymax**2/np.pi**4/fa**4))/0.4e1
122
123
```

```
124 def R1_i(Ymin, Ymax, fr, fa, C0):  # Motional resistance estimate
125     return (-0.4e1*np.pi**2*fr**2*C0**2+Ymax**2)**(-0.1e1/0.2e1)
126
127
128 def L1_i(fr, fa, C0):  # Motional inductance estimate
129     return 0.1e1 / np.pi ** 2 / (fa ** 2 - fr ** 2) / C0 / 0.4e1
130
131
132 def C1_i(fr, fa, C0):  # Motional capacitance estimate
133     return (fa ** 2 / fr ** 2 - 1) * C0
134
135
136 def rez(z, ydat, f):  # Residual function
137     return ydat - y(f, z)
138
139 # Input data file on command line:
140 infile = sys.argv[1]
141 data = open(infile, "r")  # get array out of input file
142 numline = 0
143 # Count the number of lines in the data file:
144 for line in data:
145     numline +=1
146
147 # Calculate the number of magnitude data points:
148 data = open(infile, "r") # Reload
149 nummagpts = (numline - 1 - 26)/2
150 linecount = 0
151   # read the 21st through total lines from the data file
152   # and fill x,y lists with floating point numbers:
```

```
153 for line in data:
154     if linecount > 20 and linecount < nummagpts+21:
155         x.append(map(float, (line[0:31]).split())[0])
156         zdat.append(map(float, (line[0:31]).split())[1])
157     linecount += 1
158 xx = array(x)
159 zin = array(zdat)
160
161 yy = 1/zin
162
163 # Locate Ymax, fr, Ymin, and fa:
164 f = 0
165 Ymax = 0
166 imax = len(x)
167 kmax = 0
168 for k in range(imax):
169     if yy[k] > yy[kmax]:
170         kmax = k
171
172 Ymax = yy[kmax]
173 fr = x[kmax]
174
175 kmin = kmax
176
177 for k in xrange(kmin, imax):
178     if yy[k] < yy[kmin]:
179         kmin = k
180
181 Ymin = yy[kmin]
```

```
182 fa = x[kmin]
183
184 print "Ymax = ", Ymax, " at fr = ", fr, "\n"
185 print "Ymin = ", Ymin, " at fa = ", fa, "\n"
186
187 # Estimate initial parameter values:
188
189 C0i = C0_i(Ymin, Ymax, fr, fa)
190 R1i = R1_i(Ymin, Ymax, fr, fa, C0_i(Ymin, Ymax, fr, fa))
191 L1i = L1_i(fr, fa, C0_i(Ymin, Ymax, fr, fa))
192 C1i = C1_i(fr, fa, C0_i(Ymin, Ymax, fr, fa))
193 """
194 # Print the initial values: (uncomment if you want
195 # to see the approximate values)
196 print "fr = ", fr,"\n"
197 print "fa = ", fa,"\n"
198 print "C0i = ", C0i,"\n"
199 print "R1i = ", R1i,"\n"
200 print "L1i = ", L1i,"\n"
201 print "C1i = ", C1i,"\n"
202 Qi = 1/(R1i*np.sqrt(C1i/L1i))
203 print "Qi = ", Qi,"\n"
204 """
205 # Create initial guess array:
206 z0 = [C0i, R1i, L1i, C1i]
207
208 # Find the best values:
209 output = leastsq(rez, z0, args=(yy, xx), full_output=1)
210
```

```
211 C0 = output[0][0]
212 R1 = output[0][1]
213 L1 = output[0][2]
214 C1 = output[0][3]
215 Q = 1 / (R1 * np.sqrt(C1 / L1))
216 fr = 1 / np.sqrt(L1 * C1) / 0.2e1 / np.pi
217 fa = np.sqrt((C0 + C1) / C0 / C1 / L1) / np.pi / 0.2e1
218
219 # Print the results:
220 print "fr = ", fr, "\n"
221 print "fa = ", fa, "\n"
222 print "C0 = ", C0, "\n"
223 print "R1 = ", R1, "\n"
224 print "L1 = ", L1, "\n"
225 print "C1 = ", C1, "\n"
226 print "Q = ", Q, "\n"
227
228 # Put the optimal values in an array:
229 coeffs = [C0, R1, L1, C1]
230
231 # Calculate RMS error:
232
233 rmserr = sqrt(sum((yy-y(xx,coeffs))**2)/len(xx))
234
235 # Calculate plot annotation positions:
236 dely = (Ymax-Ymin)/20
237 noteymax = 0.7*Ymax
238 # Plot the model and the data:
239 plt.plot(xx, y(xx, coeffs), 'r-', label='model')
```

```
240 plt.plot(xx, yy, 'go', label='data')
241 plt.annotate('fr = '+str(fr),xy=(fa,noteymax))
242 plt.annotate('fa = '+str(fa),xy=(fa,noteymax-dely))
243 plt.annotate('C0 = '+str(C0),xy=(fa,noteymax-2*dely))
244 plt.annotate('R1 = '+str(R1),xy=(fa,noteymax-3*dely))
245 plt.annotate('L1 = '+str(L1),xy=(fa,noteymax-4*dely))
246 plt.annotate('C1 = '+str(C1),xy=(fa,noteymax-5*dely))
247 plt.annotate('Q = '+str(Q),xy=(fa,noteymax-6*dely))
248 plt.annotate('RMS Error = '+str(rmserr),xy=(fa,noteymax-7*dely))
249
250 legend = plt.legend(loc='upper right', shadow=True, ...
       fontsize='large')
251 xlabel('f (Hz)')
252 ylabel('Y (A/V)')
253 grid(True)
254 # Put a nice background color on the legend:
255 legend.get_frame().set_facecolor('#00FFCC')
256 # Save plot as PNG:
257 plotname = infile.split('.')[0]+"model"
258 plt.savefig(plotname)
259 plt.show()
```

3. CUSTOM RESULT PROGRAM - ANSYS

```
1 !   Commands inserted into this file will be executed ...
      immediately after the ANSYS /POST1 command.
2
3 !   Active UNIT system in Workbench when this object was ...
      created:  Metric (m, kg, N, s, V, A)
4 !   NOTE:  Any data that requires units (such as mass) is ...
      assumed to be in the consistent solver unit system.
5 !               See Solving Units in the help system for ...
      more information.
6
7
8 /POST26 ! Enter Time-History Post Prossessor
9 PRCPLX,1! Set output as  Amplitude and Phase for complex Variable
10 PLCPLX,0! Display Amplitude Information only for complex Variable
11
12 SOLU,2,NCMSS,,SSCount! Find Number of Substeps (Store--->2)
13 STORE,MERGE ! Stores data in the database for the defined ...
      variables
14 *GET,SStep,VARI,2,EXTREM,VMAX,,! Store Number of Substepst to ...
      SStep Parameter
15
16 *DIM,FREQ,ARRAY,SStep,1! Define a vector to Store Frequency ...
      list (FREQ)
17 VGET,FREQ(1,1,1),1,,0   ! Populate Frequency Vector (FREQ)
18 FINISH! Exit Time-History Post Prossessor
19
```

```
20 /POST1! Enter  General Post Prossessor
21 !*********** Post Processing Variable Input *****************
22 XL= 0.008! ARG 1 Edge of Glass
23 YL= 0.023447! ARG 2  Surfacwe of Glass
24 DM=2e-5! ARG 3 Mesh Size/2
25 MATID=GlassMat! ARG 4 Material ID
26
27 !********** Post Processing Variabel Generation ***************
28 *GET,NMAX,NODE,0,NUM,MAX    ! Get Maximum Node Number in ...
     Model (Store ---> NMAX)
29 *DIM,AC,ARRAY,SStep ! Intilaize Accelration Storage Vector  ...
     AMPL (Store ---> ACA)
30 *DIM,NMASK,ARRAY,NMAX   ! Intilaize Mask Vector (NMASK of ...
     size  NMAX)
31
32 !******** Selection of Nodes on Glass Surface ...
     ********************
33 ESEL,S,MAT,,MATID! Select Elements Assocatied with Glass Material
34 NSLE,S! Select Nodes Associated with Elements
35 NSEL,R,LOC,X,0,XL! Select Nodes from 0 to Edge of Glass
36 NSEL,R,LOC,Y,YL-DM,YL+DM! Select Nodes from top of Glass Surface
37
38 !************** Get Information for Nodes on Gkass Surface
39 *GET,NDCNT,NODE,0,COUNT  ! Count Number of Active Nodes
40 *VGET,NMASK(1),NODE,1,NSEL ! Identify which nodes are actives ...
     and which are deactive
41
42 !************** Get Information for Nodes on Gkass Surface
43 *GET,NDCNT,NODE,0,COUNT ! Count Number of Active Nodes
```

```
*VGET,NMASK(1),NODE,1,NSEL ! Identify which nodes are actives ...
    and which are deactive

!***********************
*DO,J,1,SStep,1! Loop thru each Substep
    SET,1,J,ACEL,3  ! Select Substep and set for Amplitude
    *DEL,ACV    ! Clear Accel Vector
    *DIM,ACV,ARRAY,NMAX,1   ! Setup Substep Accel Vector    ...
       for Entire Model (ACVR)
    *VMASK,NMASK(1) ! Set NMASK Array  as Mask Vector
    *VGET,ACV(1,1),NODE,1,U,Y   ! GET NODAL ACCEL IN Y and ...
       mask the array
    *VSCFUN,ACY,SUM,ACV(1)! Divde the Accel Sum by total ...
       number of  active nodes to get Avg. Accel
    AC(J,1)=ACY/NDCNT
    ALLSEL
*ENDDO

!************** Clear Unnessacary  Variables ...
    *******************************
*DEL,ACV
*DEL,ACY

!************* Search for Max Acceleration Amplitude ...
    ************************
*VSCFUN,ACMAX,MAX,AC! Search Maximum Acceleration
*VSCFUN,ACMAXL,LMAX,AC ! Search Location of Maximum Acceleration

R_A=ACMAX
```

```
R_F=FREQ(ACMAXL)
R_S=ACMAXL

ALLSEL

!************ Plot Frequecy Response******************
! Create Table  Vectors and Copy Array Data
*DIM,ACT,TABLE,SStep,1
*DIM,FT,TABLE,SStep,1

*MFUN,ACT,COPY,AC
*MFUN,FT,COPY,FREQ

! Plot Setup
/AXLAB,X,Frequency(Hz)! X-Label
/AXLAB,Y,Acceleration(m/s^2) ! Y-Label
/GRID,1! Grid On
/GTHK,CURVE,1! Curve Thickness
/GMARKER,1,3,1! Marker  ON
/GROPT,CURL,1! Legend Loc
/SHOW,PNG! Plot  Grpahics
*VPLOT,FT,ACT! Plot Freq Response
/SHOW,! Put in Workbench


SET,1,ACMAXL,0,AMPL ! Load  Amplitude Results for frequency ...
    where maximum Acceleration occurs
!******************** Strain in Top PZT ...
    *******************************
```

```
CMSEL,S,PZT! Select nodes in Top PZT
NSORT,EPEL,Y,0,0! Load and sort Strain results for  Normal Y ...
    elastic strain
*GET,EY,SORT,0,MAX! Find the Max Strain Result
NUSORT! Restore Sort Result
ALLSEL


!******************** Stress in Cap ...
    *******************************
 CMSEL,S,Cap! Select nodes in Cap
 NSORT,S,EQV,0,0! Load and sort Stress results for  ...
     Equivalent elastic stress
 *GET,SC,SORT,0,MAX! Find the Max Stress Result
 ALLSEL


!******************** Stress in Body ...
    *******************************
 CMSEL,S,Body   ! Select nodes in Body
 NSORT,S,EQV,0,0! Load and sort Stress results for  ...
     Equivalent elastic stress
 *GET,SB,SORT,0,MAX! Find the Max Stress Result
 ALLSEL


!******************** Stress in Glass ...
    *******************************
 CMSEL,S,Glass  ! Select nodes in Glass
```

```
117 NSORT,S,EQV,0,0 Load and sort Stress results for  Equivalent ...
       elastic stress
118 *GET,SG,SORT,0,MAX! Find the Max Stress Result
119 ALLSEL
120
121 R_EY=EY
122 R_SC=SC
123 R_SB=SB
124 R_SG=SG
```

4. ANALYTICAL PRESSURE LINE LOAD MODEL - MAPLE

```
1
2 # Circular Plate With Eccentric Force Model
3 # Y. Anklesaria & D. S. Stutts
4 # 11-1-2017 Update7/6/2020
5 # Load Libraries and Functions
6 restart:
7 with(LinearAlgebra):with(plots):with(VectorCalculus)
8     :with(ArrayTools):
9 read "multiroot2.mpl":
10 read "CicrularPlateModes.mpl":
11 Assume(r, real, theta, real,A[1], realcons, A[2],
12     realcons, A[3], realcons, A[4], realcons, beta,
13     realcons, ri, realcons, ro, realcons, x0,
14     realcons,y0,realcons,Q,realcons):
15 global ND:=10:
16 Nmodes:=50:
17 QL:=10: # Load
18 opts := coords = cylindrical, labels = [r, theta,
19     u3(r,theta)], shading = Zhue, grid = [200, 200]:
20     # Options for 3-D Plots
21 opts2:= labels = [Frequency(kHz), "u3(m)"],
22     color = "Niagara Navy",gridlines=true,size=[0.7,0.4]:
23 opts3:=labels = [Frequency(kHz), Phase('m')],
24     style=point,symbol = asterisk, symbolsize = 5,
25     color = "BlueGreen",gridlines=true,size=[0.7,0.4]:
26 # Integration Procedure
```

```
approxint := proc( expr, r::name=numeric..numeric,
    { numsamples::integer := 10000} )
    local f, randvals;
    f := `if`( type(expr,procedure), expr,
    unapply(expr,lhs(r)) );
    randomize();
    randvals := LinearAlgebra:
    -RandomVector(numsamples,generator=evalf(rhs(r)),
        datatype=float[8]);
    (add( f(randvals[i]), i=1..numsamples )/numsamples)
    * (rhs(rhs(r)) - lhs(rhs(r)));
end proc:
# Material Properties
# Glass
Y__g:=72e9: #Young's modulus [N/m^2]
nu__g:=0.17: #Poisson's ratio
rho__g:= 2200: #Density [kg/m^3]
# PZT
Y__p:=73e9: #Young's modulus [N/m^2]
rho__p:= 7800: # Density [kg/m^3]
# Geometry Dimensions
# Glass Dimensions
r__g:=0.625*25.4e-3: # Radius of Glass [m]
h__g:=(1/16)*25.4e-3: # Thickness of Glass [m]
# PZT Dimesions
r__po:=12e-3: # Outer Radius of  PZT  [m]
r__pi:=10e-3: #  Inner Radius of PZT[m]
r__p:= (r__po+r__pi)/2: # Mean radius of the PZT [m]
h__p:= 1e-3: # Thickness of the PZT [m]
```

```
x0:=2.0e-3:# Eccentricity of PZT in X-axis from the
    center of Glass [m]
y0:=1.5e-3:# Eccentricity of PZT in Y-axis from the
    center of Glass [m]
r__0:=sqrt(x0^2+y0^2): # Radial Eccentricity of PZT
    from the center of Glass [m]
psi__0:=arctan(y0/x0): # Angle Eccentricity of PZT
    from the center of Glass [m]
# Bending Stiffness & Mode Shape of Free Circular Plate
Dd:=unapply((E*h^3)/(12(1-nu^2)),E,h,nu):
    # Stiffness of the plate
U3c:=unapply((A1*BesselJ(n,lambda*r)+A2*BesselI(n,lambda*r))
    *cos(n*(theta)),A1,A2,n,lambda,r,theta);
U3s:=unapply((A1*BesselJ(n,lambda*r)+A2*BesselI(n,lambda*r))
    *sin(n*(theta)),A1,A2,n,lambda,r,theta);
# Roots of the Circular Plate
EV:=freeSolidDiskModes(nu__g,0.5,30,10):
EV:
# Frequency & Mode Shapes
# Frequency in rad/s
omega:=[seq(EV[1,i]^2/(r__g^2)*sqrt(Dd(Y__g,h__g,nu__g)/
    (rho__g*h__g)),i=1..Size(EV)[2])]:
# Frequency in Hz
Freq:= omega/(2.0*Pi);
Umc:=[seq(U3c(1,EV[3,i],EV[2,i],EV[1,i]/r__g,r,theta,0),
    i=1..Size(EV)[2])]:
Ums:=[seq(U3s(1,EV[3,i],EV[2,i],EV[1,i]/r__g,r,theta,0),
    i=1..Size(EV)[2])]:
mn1,mn2:=Size(omega):
```

```
for k from 1 to 5 do
#plot3d([r,theta,Umc[k]],r=0..r__g,theta=0..2*Pi,
    opts,title=typeset("Mode ",k));
#plot3d([r,theta,Ums[k]],r=0..r__g,theta=0..2*Pi,
    opts,title=typeset("Mode ",k));
od;
# Eccentric Force & Location
# Radial Location of PZT wrt to the center of the
    circular disk
Rpzt:=unapply(x*cos(theta)+y*sin(theta)+sqrt((x*
    cos(theta)+y*sin(theta))^2+a^2-x^2-y^2),x,y,a,r,theta);
Pn:=unapply((Q0*Dirac(r-Rpzt(x,y,a,r,theta)))/(r*
    sqrt(1-(r0/a)^2*sin(theta-psi)^2)),Q0,x,y,a,r0,psi,r,theta);
# Eccentric Harmonic Load With Q0 amplitude
P:=unapply(exp(I*Omega*t)*Pn(Q0,x,y,a,r0,psi,r,theta)
    ,Q0,x,y,a,r0,psi,Omega,t,r,theta):
# Force Solution
if (Nmodes>mn2) then Nmodes:=mn2 else Nmodes:=Nmodes
    end if: # identify the number of modes in eigenproblem
    and compare the number of modes used in modal solution
for k from 1 to Nmodes do
Nk[k]:=int(int(U3c(1,EV[3,k],EV[2,k],EV[1,k]/r__g,
    r,theta)^2*r,r=0..r__g),theta=0..2*Pi):
od:
Fkc:=unapply(approxint(int(U3c(1,A2,n,lambda,r,theta)
    *Pn(QL, x0, y0, r__p,r__0,psi__0,r,theta)*r,r=0..r__g),
    theta=0..2*3.1415926535897),A2,n,lambda):
Fks:=unapply(approxint(int(U3s(1,A2,n,lambda,r,theta)*
    Pn(QL, x0, y0, r__p,r__0,psi__0,r,theta)*r,r=0..r__g),
```

```
    theta=0..2*3.1415926535897),A2,n,lambda):
for k from 1 to Nmodes do
Fkcn[k]:=Fkc(EV[3,k],EV[2,k],(EV[1,k]/r__g))/
    (rho__g*h__g*Nk[k]):
Fksn[k]:=Fks(EV[3,k],EV[2,k],(EV[1,k]/r__g))/
    (rho__g*h__g*Nk[k]):
od:
beta:=2*rho__g*h__g*omega[1]*0.01
for k from 1 to Nmodes do
zeta[k]:=beta/(2*rho__g*h__g*omega[k]):
lambdac[k] := (Fkcn[k]/sqrt((omega[k]^2-Omega^2)^2+
    (2*zeta[k]*Omega*omega[k])^2)):
lambdas[k] := (Fksn[k]/sqrt((omega[k]^2-Omega^2)^2+
    (2*zeta[k]*Omega*omega[k])^2)):
Phi[k]:= arctan((2*zeta[k]*Omega*omega[k])/(omega[k]^2
    -Omega^2)):
etac[k]:=lambdac[k]*Re(exp(I*(Omega*t-Phi[k]))):
etas[k]:=lambdas[k]*Re(exp(I*(Omega*t-Phi[k]))):
od:
# Frequency Response
Y1:=unapply(add((U3c(1,EV[3,i],EV[2,i],(EV[1,i]/r__g),
    r,theta)*lambdac[i]*cos(Phi[i]))+(U3s(1,EV[3,i],
    EV[2,i],(EV[1,i]/r__g),r,theta)*lambdas[i]*
    cos(Phi[i])),i=1..Nmodes),Omega,r,theta):
Y2:=unapply(add((U3c(1,EV[3,i],EV[2,i],(EV[1,i]/r__g)
    ,r,theta)*lambdac[i]*sin(Phi[i]))+(U3s(1,EV[3,i],
    EV[2,i],(EV[1,i]/r__g),r,theta)*lambdas[i]*
    sin(Phi[i])),i=1..Nmodes),Omega,r,theta):
# Static Response Plot
```

```
Umc:=unapply((add(U3c(1,EV[3,i],EV[2,i],(EV[1,i]/r__g),
    r,theta)*lambdac[i],i=1..Nmodes)),Omega,r,theta):
    # Modal Magnitude of response
Ums:=unapply((add(U3s(1,EV[3,i],EV[2,i],(EV[1,i]/r__g),
    r,theta)*lambdas[i],i=1..Nmodes)),Omega,r,theta):
    # Modal Magnitude of response
Um:=unapply(Umc(Omega,r,theta)+Ums(Omega,r,theta),
    Omega,r,theta):
for k from 1 to 3 do
plot3d([r,theta,Um(omega[k]*2*Pi,r,theta)],r=0..r__g,
    theta=0..2*Pi,opts);
od
# Animate Response Plot
Ut:=unapply((add((U3c(1,EV[3,i],EV[2,i],(EV[1,i]/r__g)
    ,r,theta,Pi/2)*etac[i])+(U3s(1,EV[3,i],EV[2,i],
    (EV[1,i]/r__g),r,theta,Pi/2)*etas[i]),i=1..Nmodes)),
    Omega,r,theta,t):# Time plot:
animate(plot3d,[[r,theta,Ut(omega[1],r,theta,t)],
    r=0..r__g,theta=0..2*Pi,opts],t=0..1,frames=60);
#animate(plot3d,[[r,theta,Ut(55800*2*Pi,r,theta,t)]
    ,r=0..r__g,theta=0..2*Pi,opts],t=0..1,frames=60);
# Frequency Response Center
Range:=0..200:
Y1c:=Y1(Omega,0,0):
Y2c:=Y2(Omega,0,0):
Yc:=unapply((Y1c^2+Y2c^2)^0.5,Omega):
Pc:=unapply(arctan(Y2c,Y1c),Omega):
MYc:=loglogplot(Yc(Omega*2*Pi*1000),Omega=Range,opts2):
MPc:=semilogplot(Pc(Omega*2*Pi*1000),Omega=Range,opts2):
```

```
172
173 # Frequency Response Edge
174 Y1e:=Y1(Omega,r__g,0):
175 Y2e:=Y2(Omega,r__g,0):
176 Ye:=unapply((Y1e^2+Y2e^2)^0.5,Omega):
177 Pe:=unapply(arctan(Y2e,Y1e),Omega):
178 MYe:=loglogplot(Ye(Omega*2*Pi*1000),Omega=Range,opts2):
179 MPe:=semilogplot(Pe(Omega*2*Pi*1000),Omega=Range,opts2):
180
181 # Load ANSYS Data
182 Ansys:=ImportMatrix("ANSYS/ANSYSOneload.csv"):
183 m,n:=Size(Ansys):
184 F:=Ansys[1..m,1]/1000:
185 Yac:=Ansys[1..m,2]:
186 Pac:=Ansys[1..m,3]:
187 Pac:=Pac*(Pi/180.):
188 AYc:=loglogplot(F,Yac,opts3):
189 APc:=plot(F,Pac,opts3):
190 Yae:=Ansys[1..m,4]:
191 Pae:=Ansys[1..m,5]:
192 Pae:=Pae*(Pi/180.):
193 AYe:=loglogplot(F,Yae,opts3):
194 APe:=semilogplot(F,Pae,opts3):
195 # Comparison of ANSYS vs Model Center
196 display({MYc,AYc},legend=[Model,ANSYS],title="Center
197     -AMPL",titlefont = ["HELVATIC", 20]);
198 display({MPc,APc},legend=[Model,ANSYS],title="Center
199     -PHS",titlefont = ["HELVATIC", 20]);
200 # Comparison of ANSYS vs Model Edge
```

```
display({MYe,AYe},legend=[Model,ANSYS],title="Edge
    -AMPL",titlefont = ["HELVATIC", 20]);
display({MPe,APe},legend=[Model,ANSYS],title="Edge
-PHS",titlefont = ["HELVATIC", 20]);
```

5. ANALYTICAL TWO PRESSURE LINE LOADS MODEL - MAPLE

```
1
2 # Circular Plate with 2 Opposing Eccentric Force Loads
3 # Y. Anklesaria & D. S. Stutts
4 # 4-15-2020 Update 7-8-2020
5 # Load Libraries and Functions
6 restart:
7 with(LinearAlgebra):with(plots):with(VectorCalculus)
8     :with(ArrayTools):
9 read "multiroot2.mpl":
10 #read "circularplatemodes.mpl":
11 read "CicrularPlateModes.mpl":
12 Assume(r, real, theta, real,A[1], realcons, A[2],
13     realcons, A[3], realcons, A[4], realcons, beta,
14     realcons, ri, realcons, ro, realcons, x0,realcons,
15     y0,realcons,Q,realcons):
16 ND:=10:
17 Nmodes:=20: # number of modes used in modal solution
18 QL:=10: # Load
19 opts := coords = cylindrical, labels = [r, theta, u3],
20     shading = Zhue, grid = [200, 200]: # Options for 3-D Plots
21 opts2:= labels = [Frequency(kHz), "u3(m)"],
22     color = "Niagara Navy",gridlines=true,size=[0.7,0.4]:
23 opts3:=labels = [Frequency(kHz), Phase('m')],style=point,
24     symbol = asterisk, symbolsize = 5, color = "BlueGreen",
25     gridlines=true,size=[0.7,0.4]:
26 # Integration Procedure
```

```
approxint := proc( expr, r::name=numeric..numeric,
    { numsamples::integer := 10000} )
    local f, randvals;
    f := `if`( type(expr,procedure), expr,
        unapply(expr,lhs(r)) );
    randomize();
    randvals := LinearAlgebra:-RandomVector(numsamples,
        generator=evalf(rhs(r)),datatype=float[8]);
    (add( f(randvals[i]), i=1..numsamples )/numsamples)
        * (rhs(rhs(r)) - lhs(rhs(r)));
end proc:
# Material Properties
# Glass
Y__g:=72e9: #Young's modulus [N/m^2]
nu__g:=0.17: #Poisson's ratio
rho__g:= 2200: #Density [kg/m^3]
# PZT
Y__p:=73e9: #Young's modulus [N/m^2]
rho__p:= 7800: #Density [kg/m^3]
# Geometry Dimensions
# Glass Dimensions
r__g:=0.625*25.4e-3: # Radius of Glass [m]
h__g:=(1/16)*25.4e-3: # Thickness of Glass [m]
# PZT Dimesions
r__po:=11.05e-3: # Outer Radius of  PZT [m]
r__pi:=10.95e-3: # Inner Radius of PZT [m]
r__p:= (r__po+r__pi)/2: #Mean radius of the PZT [m]
h__p:= 1e-3:# Thickness of the PZT [m]
x0:=2.0e-3: # Eccentricity of PZT in X-axis from the
```

```
56     center of Glass [m]
57 y0:=1.5e-3: # Eccentricity of PZT in y-axis from the
58     center of Glass [m]
59 r__0:=sqrt(x0^2+y0^2): # Radial Eccentricity of PZT
60     from the center of Glass [m]
61 psi__0:=arctan(y0/x0): # Angle Eccentricity of PZT
62     from the center of Glass [m]
63 # Bending Stiffness & Mode Shape of Free Circular Plate
64 Dd:=unapply((E*h^3)/(12(1-nu^2)),E,h,nu): # Stiffness of the ...
     plate
65 U3c:=unapply((A1*BesselJ(n,lambda*r)+A2*BesselI(n,lambda*r))
66     *cos(n*theta),A1,A2,n,lambda,r,theta);
67 U3s:=unapply((A1*BesselJ(n,lambda*r)+A2*BesselI(n,lambda*r))
68     *sin(n*theta),A1,A2,n,lambda,r,theta);
69 # Roots of the Circular Plate
70 EV:=freeSolidDiskModes(nu__g,0.5,20,10):
71
72 # Frequency & Mode Shapes
73 # Frequency in rad/s
74 omega:=[seq(EV[1,i]^2/(r__g^2)*sqrt(Dd(Y__g,h__g,nu__g)/
75     (rho__g*h__g)),i=1..Size(EV)[2])]:
76 # Frequency in Hz
77 Freq:= omega/(2.0*Pi);
78 Umc:=[seq(U3c(1,EV[3,i],EV[2,i],EV[1,i]/r__g,r,theta)
79     ,i=1..Size(EV)[2])]:
80 Ums:=[seq(U3s(1,EV[3,i],EV[2,i],EV[1,i]/r__g,r,theta,0)
81     ,i=1..Size(EV)[2])]:
82 mn1,mn2:=Size(omega):
83 for k from 1 to 5 do
```

```
plot3d([r,theta,Umc[k]],r=0..r__g,theta=0..2*Pi,
    opts,title=typeset("Mode ",k));
#plot3d([r,theta,Ums[k]],r=0..r__g,theta=0..2*Pi,
    opts,title=typeset("Mode ",k));
od
# Eccentric Force & Location
# Radial Location of PZT wrt to the center of the circular disk
Rpzt:=unapply(x*cos(theta)+y*sin(theta)+sqrt((x*cos(theta)+
    y*sin(theta))^2+a^2-x^2-y^2),x,y,a,r,theta);
Pn:=unapply((Q0*Dirac(r-Rpzt(x,y,a,r,theta)))/(r*
    sqrt(1-(r0/a)^2*sin(theta-psi)^2))-Q0*Dirac(r-Rpzt(x,y,a,r,theta)
    -(r__po-r__pi))/(r*sqrt(1-(r0/a)^2*sin(theta-psi)^2))
    ,Q0,x,y,a,r0,psi,r,theta);
# Eccentric Harmonic Load With Q0 amplitude
P:=unapply(exp(I*Omega*t)*Pn(Q0,x,y,a,r0,psi,r,theta)
    ,Q0, x, y, a, r0, psi, r, theta,Omega,t):
# Force Solution
if (Nmodes>mn2) then Nmodes:=mn2 else Nmodes:=Nmodes
    end if: # identify the number of modes in eigenproblem
    and compare the number of modes used in modal solution
for k from 1 to Nmodes do
Nk[k]:=int(int(U3c(1,EV[3,k],EV[2,k],EV[1,k]/r__g,r,theta)^2
    *r,r=0..r__g),theta=0..2*Pi):
od:
Fkc:=unapply(approxint(int(U3c(1,A2,n,lambda,r,theta)
    *Pn(QL, x0, y0, r__p,r__0,psi__0,r,theta)*r,r=0..r__g),
    theta=0..2*3.1415926535897),A2,n,lambda):
Fks:=unapply(approxint(int(U3s(1,A2,n,lambda,r,theta)*
    Pn(QL, x0, y0, r__p,r__0,psi__0,r,theta)*r,r=0..r__g),
```

```
113     theta=0..2*3.1415926535897),A2,n,lambda):
114 for k from 1 to Nmodes do
115 Fkcn[k]:=Fkc(EV[3,k],EV[2,k],(EV[1,k]/r__g))/(rho__g*h__g*Nk[k]):
116 Fksn[k]:=Fks(EV[3,k],EV[2,k],(EV[1,k]/r__g))/(rho__g*h__g*Nk[k]):
117 od:
118 beta:=2*rho__g*h__g*omega[1]*0.01
119 ;
120 for k from 1 to Nmodes do
121 zeta[k]:=0.001;#beta/(2*rho__g*h__g*omega[k]):
122 lambdac[k] := (Fkcn[k]/sqrt((omega[k]^2-Omega^2)^2+
123     (2*zeta[k]*Omega*omega[k])^2)):
124 lambdas[k] := (Fksn[k]/sqrt((omega[k]^2-Omega^2)^2+
125     (2*zeta[k]*Omega*omega[k])^2)):
126 Phi[k]:= arctan((2*zeta[k]*Omega*omega[k])/(omega[k]^2
127     -Omega^2)):
128 etac[k]:=lambdac[k]*Re(exp(I*(Omega*t-Phi[k]))):
129 etas[k]:=lambdas[k]*Re(exp(I*(Omega*t-Phi[k]))):
130 od:
131
132
133 # Frequency Response
134 Y1:=unapply(add((U3c(1,EV[3,i],EV[2,i],(EV[1,i]/r__g),
135     r,theta)*lambdac[i]*cos(Phi[i]))+(U3s(1,EV[3,i],
136     EV[2,i],(EV[1,i]/r__g),r,theta)*lambdas[i]*cos(Phi[i])),
137     i=1..Nmodes),Omega,r,theta):
138 Y2:=unapply(add((U3c(1,EV[3,i],EV[2,i],(EV[1,i]/r__g),
139     r,theta)*lambdac[i]*sin(Phi[i]))+(U3s(1,EV[3,i],
140     EV[2,i],(EV[1,i]/r__g),r,theta)*lambdas[i]*sin(Phi[i])),
141     i=1..Nmodes),Omega,r,theta):
```

```
142 # Static Response Plot
143 Umc:=unapply((add(U3c(1,EV[3,i],EV[2,i],(EV[1,i]/r__g),
144     r,theta)*lambdac[i],i=1..Nmodes)),Omega,r,theta):
145     # Modal Magnitude of response
146 Ums:=unapply((add(U3s(1,EV[3,i],EV[2,i],(EV[1,i]/r__g),
147     r,theta)*lambdas[i],i=1..Nmodes)),Omega,r,theta):
148     # Modal Magnitude of response
149 Um:=unapply(Umc(Omega,r,theta)+Ums(Omega,r,theta),
150     Omega,r,theta):
151 for k from 1 to 1 do
152 #plot3d([r,theta,Um(omega[2],r,theta)],r=0..r__g,
153     theta=0..2*Pi,opts);
154 od
155 # Animate Response Plot
156 Ut:=unapply((add((U3c(1,EV[3,i],EV[2,i],(EV[1,i]/r__g),
157     r,theta,Pi/2)*etac[i])+(U3s(1,EV[3,i],EV[2,i],
158     (EV[1,i]/r__g),r,theta,Pi/2)*etas[i]),i=1..Nmodes)),
159     Omega,r,theta,t):# Time plot:
160 #animate(plot3d,[[r,theta,Ut(omega[2],r,theta,t)],
161     r=0..r__g,theta=0..2*Pi,opts],t=0..1,frames=60);
162 #animate(plot3d,[[r,theta,Ut(55800*2*Pi,r,theta,t)],
163     r=0..r__g,theta=0..2*Pi,opts],t=0..1,frames=60);
164 # Frequency Response Center
165 Range:=4..200:
166 Y1c:=Y1(Omega,0,0):
167 Y2c:=Y2(Omega,0,0):
168 Yc:=unapply((Y1c^2+Y2c^2)^0.5,Omega):
169 Pc:=unapply(arctan(Y2c,Y1c),Omega):
170 MYc:=loglogplot(Yc(Omega*2*Pi*1000),Omega=Range,opts2):
```

```
MPc:=semilogplot(Pc(Omega*2*Pi*1000),Omega=Range,opts2):
# Frequency Response Edge
Y1e:=Y1(Omega,r__g,0):
Y2e:=Y2(Omega,r__g,0):
Ye:=unapply((Y1e^2+Y2e^2)^0.5,Omega):
Pe:=unapply(arctan(Y2e,Y1e),Omega):
MYe:=loglogplot(Ye(Omega*2*Pi*1000),Omega=Range,opts2):
MPe:=semilogplot(Pe(Omega*2*Pi*1000),Omega=Range,opts2):
# Load ANSYS Data
Ansys:=ImportMatrix("ANSYS/ANSYSTwoLoad.csv"):
m,n:=Size(Ansys):
F:=Ansys[1..m,1]/1000:
Yac:=Ansys[1..m,2]:
Pac:=Ansys[1..m,3]:
Pac:=Pac*(-Pi/180.):
AYc:=loglogplot(F,Yac,opts3):
APc:=plot(F,Pac,opts3):
Yae:=Ansys[1..m,4]:
Pae:=Ansys[1..m,5]:
Pae:=Pae*(-Pi/180.):
AYe:=loglogplot(F,Yae,opts3):
APe:=semilogplot(F,Pae,opts3):
# Comparison of ANSYS vs Model Center
display({MYc,AYc},legend=[Model,ANSYS],title="Center
    -AMPL",titlefont = ["HELVATIC", 20]);
display({MPc,APc},legend=[Model,ANSYS],title="Center
    -PHS",titlefont = ["HELVATIC", 20]);
# Comparison of ANSYS vs Model Edge
display({MYe,AYe},legend=[Model,ANSYS],title="Edge
```

```
200     -AMPL",titlefont = ["HELVATIC", 20]);
201 display({MPe,APe},legend=[Model,ANSYS],title="Edge
202     -PHS",titlefont = ["HELVATIC", 20]);
203 #
```

6. ANALYTICAL MOMENT LINE LOAD MODEL - MAPLE

```
1
2 # Circullar Plate with Line Moment Eccentric Load
3 # Y. Anklesaria & D. S. Stutts
4 # 4-25-2020 Update 7-9-2020
5 # Load Libraries and Functions
6 restart:
7 with(LinearAlgebra):with(plots):with(VectorCalculus)
8     :with(ArrayTools):
9 read "multiroot2.mpl":
10 read "CicrularPlateModes.mpl":
11 Assume(r, real, theta, real,A[1], realcons, A[2],
12     realcons, A[3], realcons, A[4], realcons, beta,
13     realcons, ri, realcons, ro, realcons, x0,
14     realcons,y0,realcons,Q,realcons):
15 ND:=10:
16 Nmodes:=20: # number of modes used in modal solution
17 QL:=10: # Load
18 opts := coords = cylindrical, labels = [r, theta, u3],
19     shading = Zhue, grid = [200, 200]: # Options for 3-D Plots
20 opts2:= labels = [Frequency(kHz), "u3(m)"],
21     color = "Niagara Navy",gridlines=true,size=[0.7,0.4]:
22 opts3:=labels = [Frequency(kHz), Phase('m')],style=point,
23     symbol = asterisk, symbolsize = 5, color = "BlueGreen",
24     gridlines=true,size=[0.7,0.4]:
25 # Integration Procedure
26 approxint := proc( expr, r::name=numeric..numeric,
```

```
27      { numsamples::integer := 10000} )
28      local f, randvals;
29      f := `if`( type(expr,procedure), expr,
30          unapply(expr,lhs(r)) );
31      randomize();
32      randvals := LinearAlgebra:-RandomVector(numsamples,
33          generator=evalf(rhs(r)),datatype=float[8]);
34      (add( f(randvals[i]), i=1..numsamples )/numsamples) *
35          (rhs(rhs(r)) - lhs(rhs(r)));
36 end proc:
37 # Material Properties
38 # Glass
39 Y__g:=72e9: #Young's modulus [N/m^2]
40 nu__g:=0.17: #Poisson's ratio
41 rho__g:= 2200: #Density [kg/m^3]
42 # PZT
43 Y__p:=73e9: #Young's modulus [N/m^2]
44 rho__p:= 7800: #Density [kg/m^3]
45 E31:=15.080:
46 V0:=200:
47 # Geometry Dimensions
48 # Glass Dimensions
49 r__g:=0.625*25.4e-3: # Radius of Glass [m]
50 h__g:=(1/16)*25.4e-3: # Thickness of Glass [m]
51 # PZT Dimesions
52 r__po:=11.05e-3: # Outer Radius of  PZT [m]
53 r__pi:=10e-3: #  Inner Radius of PZT[m]
54 r__p:= (r__po+r__pi)/2: #Mean radius of the PZT [m]
55 h__p:= 1e-3:# Thickness of the PZT [m]
```

```
x0:=3.5e-3:# Eccenetircity of PZT in X-axis from
    center of Glass
y0:=4.5e-3:# Eccenetircity of PZT in Y-axis from
    center of Glass
r__0:=sqrt(x0^2+y0^2):
psi__0:=arctan(y0/x0):
# Bending Stiffness & Mode Shape of Free Circular Plate
Dd:=unapply((E*h^3)/(12(1-nu^2)),E,h,nu): # Stiffness of the ...
    plate
U3c:=unapply((A1*BesselJ(n,lambda*r)+A2*BesselI(n,lambda*r))
    *cos(n*theta),A1,A2,n,lambda,r,theta);
U3s:=unapply((A1*BesselJ(n,lambda*r)+A2*BesselI(n,lambda*r))
    *sin(n*theta),A1,A2,n,lambda,r,theta);
# Roots of the Circular Plate
EV:=freeSolidDiskModes(nu__g,0.5,20,10):
# Frequency & Mode Shapes
# Frequency in rad/s
omega:=[seq(EV[1,i]^2/(r__g^2)*sqrt(Dd(Y__g,h__g,nu__g)/
    (rho__g*h__g)),i=1..Size(EV)[2])]:
# Frequency in Hz
Freq:= omega/(2.0*Pi);
Umc:=[seq(U3c(1,EV[3,i],EV[2,i],EV[1,i]/r__g,r,theta),
    i=1..Size(EV)[2])]:
Ums:=[seq(U3s(1,EV[3,i],EV[2,i],EV[1,i]/r__g,r,theta,0),
    i=1..Size(EV)[2])]:
mn1,mn2:=Size(omega):
for k from 1 to 1 do
#plot3d([r,theta,Umc[k]],r=0..r__g,theta=0..2*Pi,
    opts,title=typeset("Mode ",k));
```

```
#plot3d([r,theta,Ums[k]],r=0..r__g,theta=0..2*Pi,
    opts,title=typeset("Mode ",k));
od
# Eccentric Force & Location
# Radial Location of PZT wrt to the center of the circular disk
Rpzt:=unapply(x*cos(theta)+y*sin(theta)+sqrt((x*cos(theta)+
    y*sin(theta))^2+a^2-x^2-y^2),x,y,a,r,theta);
# Eccentric Harmonic Line Moment Load With Q0 amplitude
Mrr:=-e31*((h__g+h__p)/2)*V*Dirac(r-Rpzt(x,y,a,r,theta));
Mtt:=-e31*((h__g+h__p)/2)*V*Dirac(r-Rpzt(x,y,a,r,theta));
Mks:=unapply((2/r)*diff(Mrr,r)+diff(Mrr,r$2)-(1/r)
    *diff(Mtt,r)+(1/r^2)*diff(Mtt,theta$2),e31,V,x,y,a,
    r0,psi,r,theta);
# Force Solution
if (Nmodes>mn2) then Nmodes:=mn2 else Nmodes:=Nmodes
    end if: # identify the number of modes in eigenproblem
    and compare the number of modes used in modal solution
for k from 1 to Nmodes do
Nk[k]:=int(int(U3c(1,EV[3,k],EV[2,k],EV[1,k]/r__g,
    r,theta)^2*r,r=0..r__g),theta=0..2*Pi):
od:
Fkc:=unapply(approxint(int(U3c(1,A2,n,lambda,r,theta)
    *Mks(E31,V0,x0, y0, r__p,r__0,psi__0,r,theta)*r,r=0..r__g)
    ,theta=0..2*3.1415926535897),A2,n,lambda):
Fks:=unapply(approxint(int(U3s(1,A2,n,lambda,r,theta)
    *Mks(E31,V0,x0, y0, r__p,r__0,psi__0,r,theta)*r,r=0..r__g)
    ,theta=0..2*3.1415926535897),A2,n,lambda):
for k from 1 to Nmodes do
Fkcn[k]:=Fkc(EV[3,k],EV[2,k],(EV[1,k]/r__g))/(rho__g*h__g*Nk[k]):
```

```
Fksn[k]:=Fks(EV[3,k],EV[2,k],(EV[1,k]/r__g))/(rho__g*h__g*Nk[k]):
od:
beta:=2*rho__g*h__g*omega[1]*0.01
;
for k from 1 to Nmodes do
zeta[k]:=0.001;#beta/(2*rho__g*h__g*omega[k]):
lambdac[k] := (Fkcn[k]/sqrt((omega[k]^2-Omega^2)^2+
    (2*zeta[k]*Omega*omega[k])^2)):
lambdas[k] := (Fksn[k]/sqrt((omega[k]^2-Omega^2)^2+
    (2*zeta[k]*Omega*omega[k])^2)):
Phi[k]:= arctan((2*zeta[k]*Omega*omega[k])/(omega[k]^2
    -Omega^2)):
etac[k]:=lambdac[k]*Re(exp(I*(Omega*t-Phi[k]))):
etas[k]:=lambdas[k]*Re(exp(I*(Omega*t-Phi[k]))):
od:
# Frequency Response
Y1:=unapply(add((U3c(1,EV[3,i],EV[2,i],(EV[1,i]/r__g),
    r,theta)*lambdac[i]*cos(Phi[i]))+(U3s(1,EV[3,i],
    EV[2,i],(EV[1,i]/r__g),r,theta)*lambdas[i]*
    cos(Phi[i])),i=1..Nmodes),Omega,r,theta):
Y2:=unapply(add((U3c(1,EV[3,i],EV[2,i],(EV[1,i]/r__g),
    r,theta)*lambdac[i]*sin(Phi[i]))+(U3s(1,EV[3,i],
    EV[2,i],(EV[1,i]/r__g),r,theta)*lambdas[i]*
    sin(Phi[i])),i=1..Nmodes),Omega,r,theta):
# Static Response Plot
Umc:=unapply((add(U3c(1,EV[3,i],EV[2,i],(EV[1,i]/r__g),
    r,theta)*lambdac[i],i=1..Nmodes)),Omega,r,theta):
    # Modal Magnitude of response
Ums:=unapply((add(U3s(1,EV[3,i],EV[2,i],(EV[1,i]/r__g),
```

```
142     r,theta)*lambdas[i],i=1..Nmodes)),Omega,r,theta):
143     # Modal Magnitude of response
144 Um:=unapply(Umc(Omega,r,theta)+Ums(Omega,r,theta),Omega,r,theta):
145 for k from 1 to 1 do
146 #plot3d([r,theta,Um(omega[2],r,theta)],r=0..r__g,theta=0..2*Pi,opts);
147 od
148 # Animate Response Plot
149 Ut:=unapply((add((U3c(1,EV[3,i],EV[2,i],(EV[1,i]/r__g),
150     r,theta,Pi/2)*etac[i])+(U3s(1,EV[3,i],EV[2,i],
151     (EV[1,i]/r__g),r,theta,Pi/2)*etas[i]),i=1..Nmodes)),
152     Omega,r,theta,t):# Time plot:
153 #animate(plot3d,[[r,theta,Ut(omega[2],r,theta,t)],
154     r=0..r__g,theta=0..2*Pi,opts],t=0..1,frames=60);
155 #animate(plot3d,[[r,theta,Ut(55800*2*Pi,r,theta,t)],
156     r=0..r__g,theta=0..2*Pi,opts],t=0..1,frames=60);
157 # Frequency Response Center
158 Range:=4..200:
159 Y1c:=Y1(Omega,0,0):
160 Y2c:=Y2(Omega,0,0):
161 Yc:=unapply((Y1c^2+Y2c^2)^0.5,Omega):
162 Pc:=unapply(arctan(Y2c,Y1c),Omega):
163 MYc:=loglogplot(Yc(Omega*2*Pi*1000),Omega=Range,opts2):
164 MPc:=semilogplot(Pc(Omega*2*Pi*1000),Omega=Range,opts2):
165 # Frequency Response Edge
166 Y1e:=Y1(Omega,r__g,0):
167 Y2e:=Y2(Omega,r__g,0):
168 Ye:=unapply((Y1e^2+Y2e^2)^0.5,Omega):
169 Pe:=unapply(arctan(Y2e,Y1e),Omega):
170 MYe:=loglogplot(Ye(Omega*2*Pi*1000),Omega=Range,opts2):
```

```
MPe:=semilogplot(Pe(Omega*2*Pi*1000),Omega=Range,opts2):
# Load ANSYS Data
Ansys:=ImportMatrix("ANSYS/ANSYSMoment.csv"):
m,n:=Size(Ansys):
F:=Ansys[1..m,1]/1000:
Yac:=Ansys[1..m,2]:
Pac:=Ansys[1..m,3]:
Pac:=Pac*(-Pi/180.):
AYc:=loglogplot(F,Yac,opts3):
APc:=plot(F,Pac,opts3):
Yae:=Ansys[1..m,4]:
Pae:=Ansys[1..m,5]:
Pae:=Pae*(-Pi/180.):
AYe:=loglogplot(F,Yae,opts3):
APe:=semilogplot(F,Pae,opts3):
# Comparison of ANSYS vs Model Center
display({MYc,AYc},legend=[Model,ANSYS],title="Center
    -AMPL",titlefont = ["HELVATIC", 20]);
display({MPc,APc},legend=[Model,ANSYS],title="Center
    -PHS",titlefont = ["HELVATIC", 20]);
# Comparison of ANSYS vs Model Edge
display({MYe,AYe},legend=[Model,ANSYS],title="Edge
    -AMPL",titlefont = ["HELVATIC", 20]);
display({MPe,APe},legend=[Model,ANSYS],title="Edge
    -PHS",titlefont = ["HELVATIC", 20]);
```

APPENDIX B.

IMPEDANCE SPECTRUM

1. SPS - PROTOTYPE 1

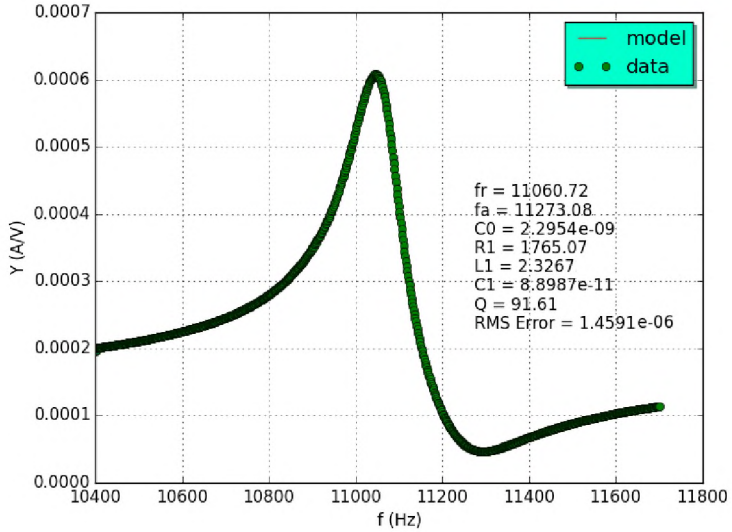

Figure 1. Prototype 1 - Mode 1

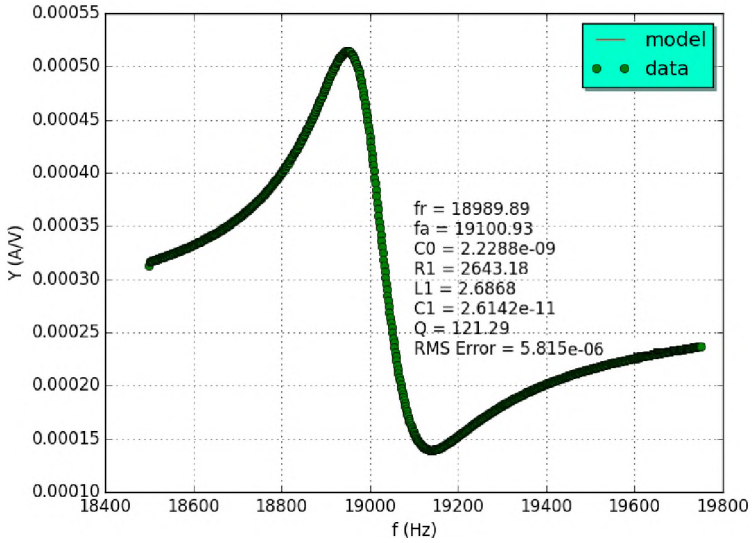

Figure 2. Prototype 1 - Mode 2

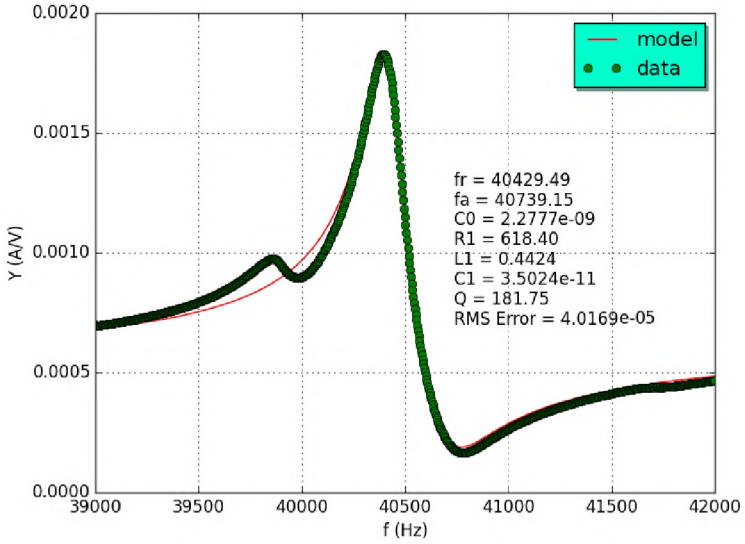

Figure 3. Prototype 1 - Mode 3

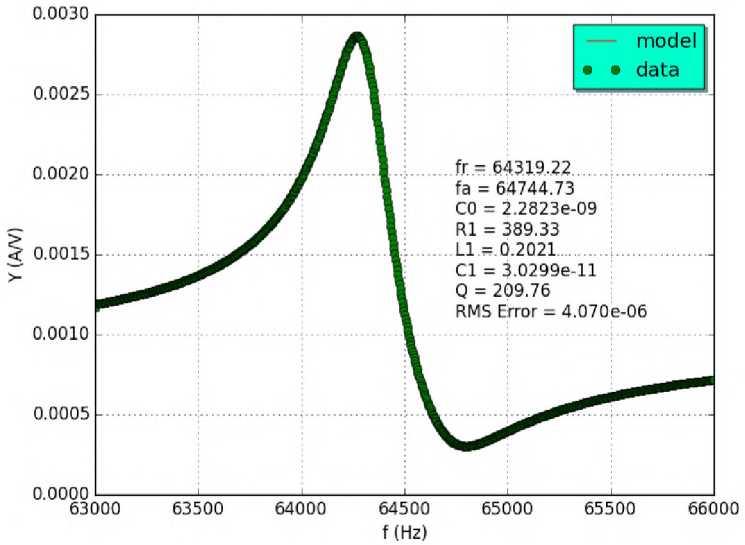

Figure 4. Prototype 1 - Mode 4

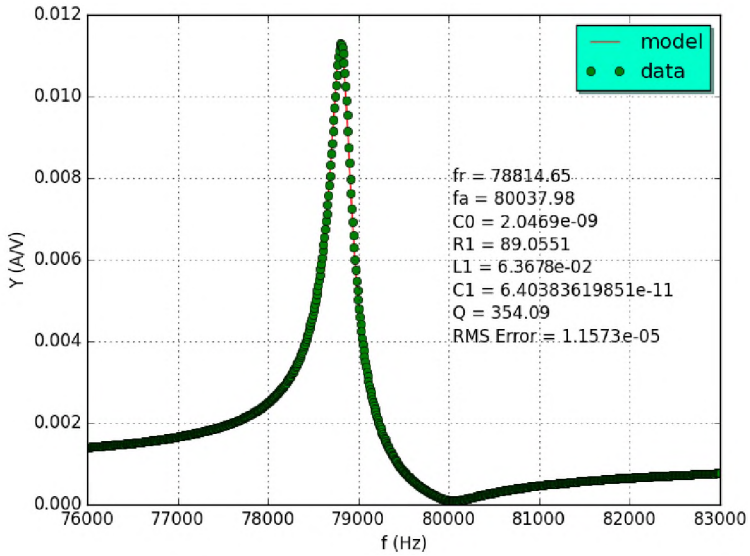

Figure 5. Prototype 1 - Mode 5

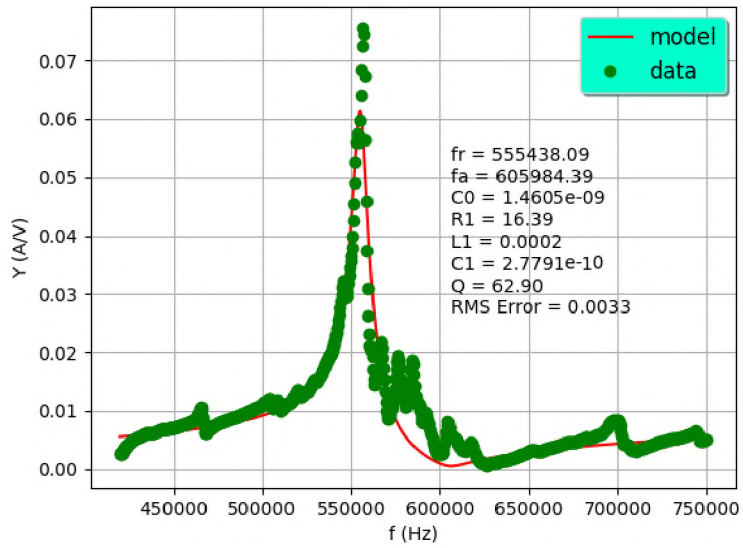

Figure 6. Prototype 1 - Mode 6

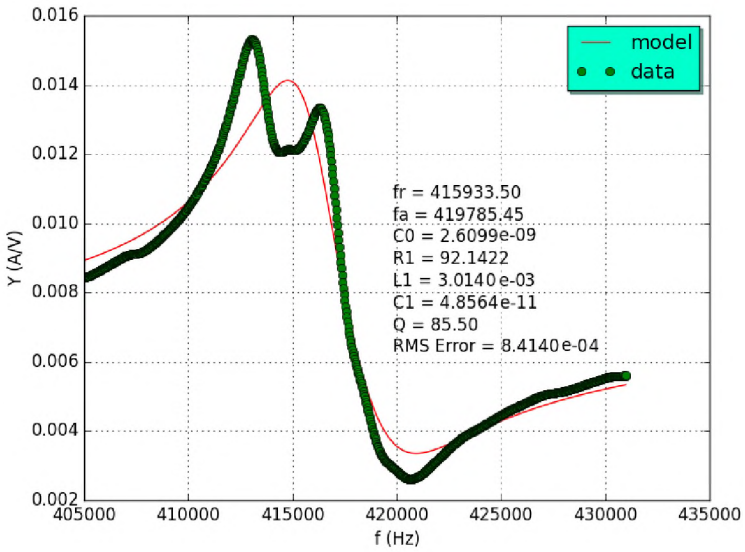

Figure 7. Prototype 1 - Mode 7

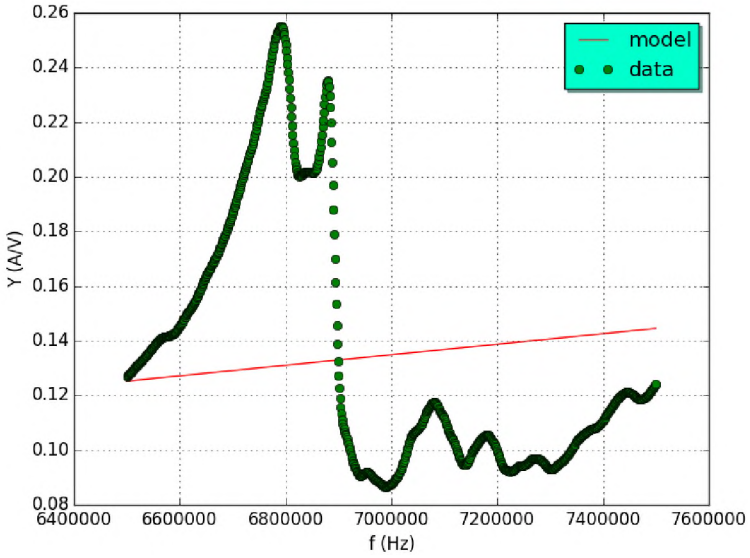

Figure 8. Prototype 1 - Mode 8

2. SPS - PROTOTYPE 2

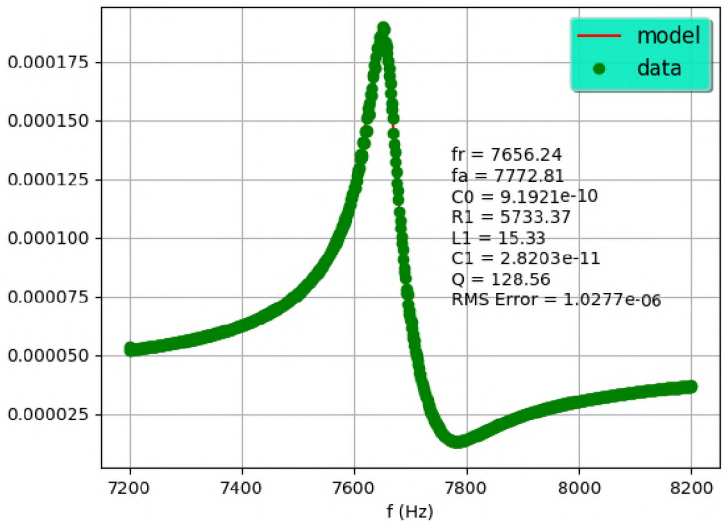

Figure 9. Prototype 2 - Mode 1

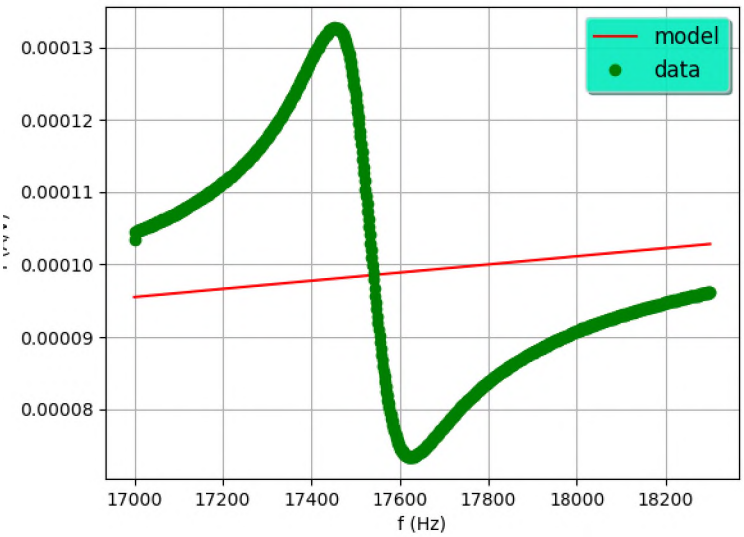

Figure 10. Prototype 2 - Mode 2

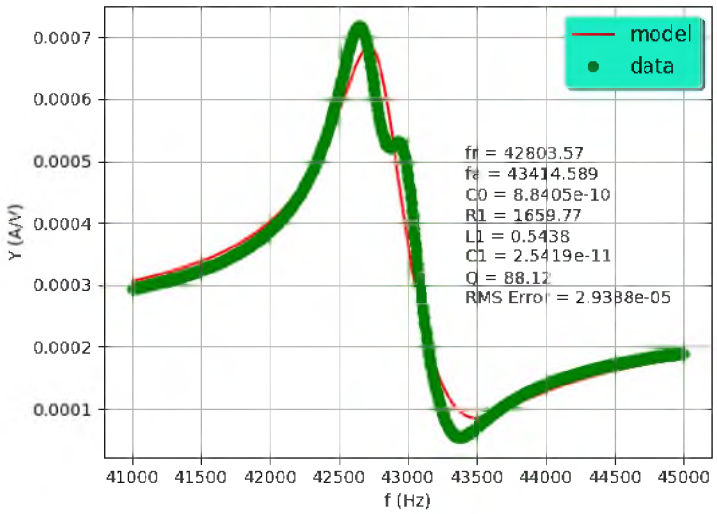

Figure 11. Prototype 2 - Mode 3

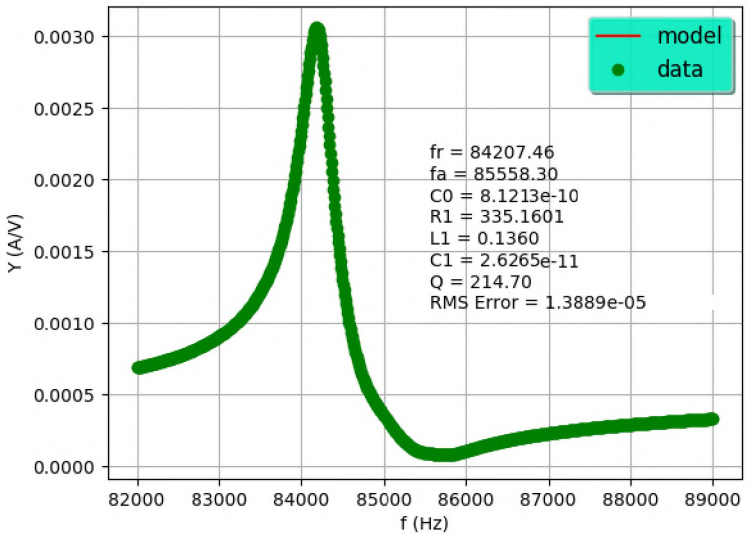

Figure 12. Prototype 2 - Mode 4

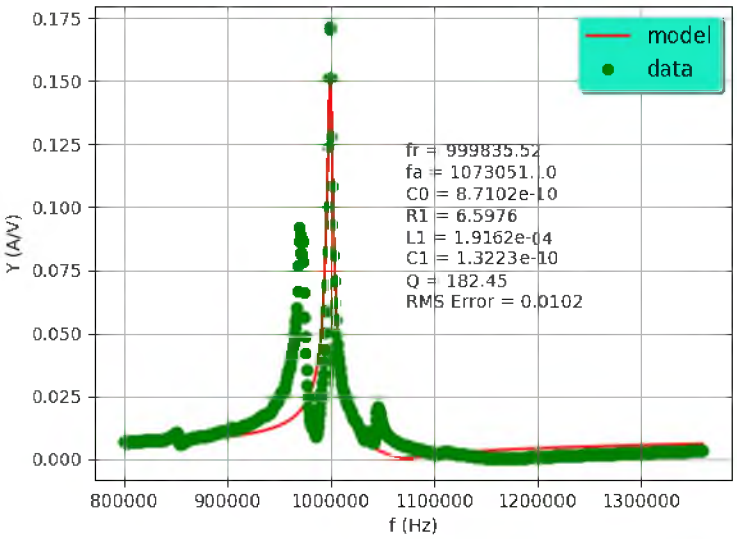

Figure 13. Prototype 2 - Mode 5

3. RPS -PROTOTYPE IMPEDANCE

3.1. RING MODES BEFORE PROTOTYPE ASSEMBLY

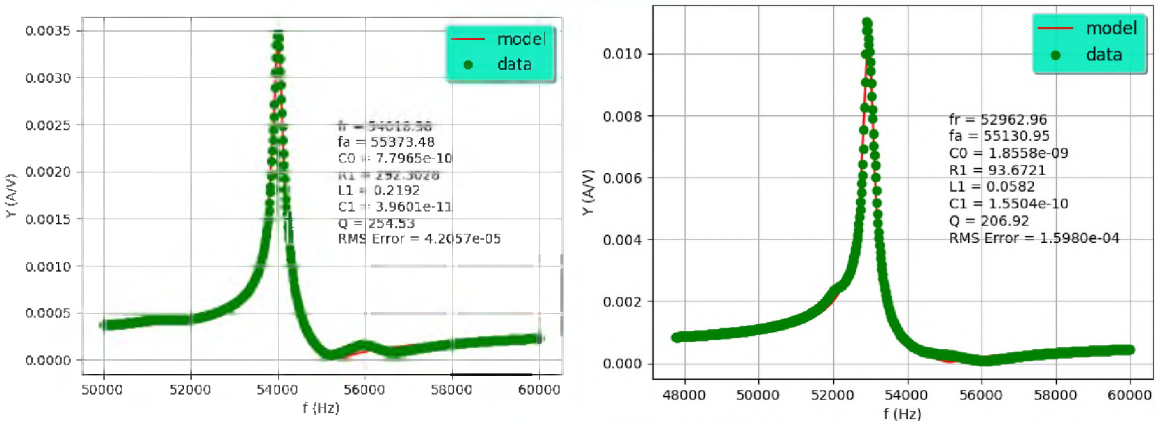

(a) Inner Ring - Mode 1

(b) Outer Ring - Mode 1

Figure 14. Impedance Spectrum Mode 1

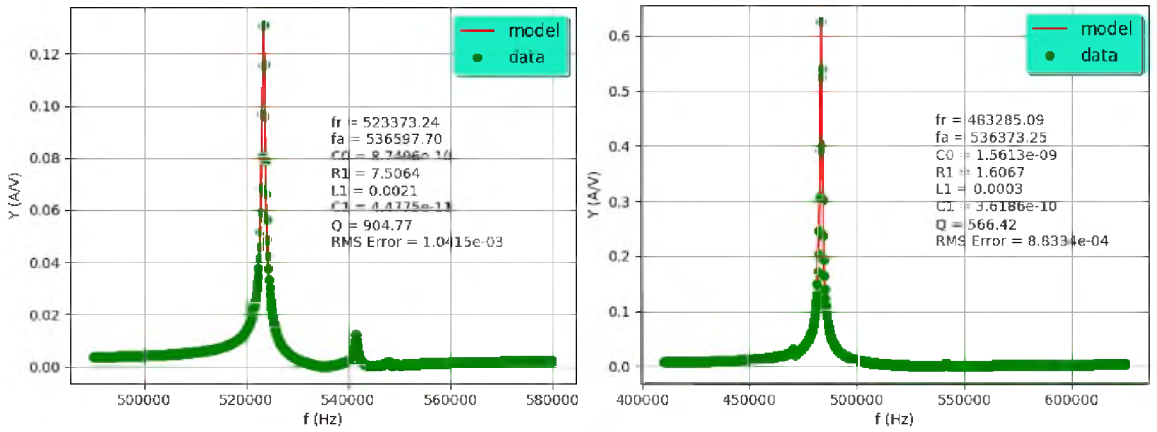

(a) Inner Ring - Mode 2

(b) Outer Ring - Mode 2

Figure 15. Impedance Spectrum Mode 2

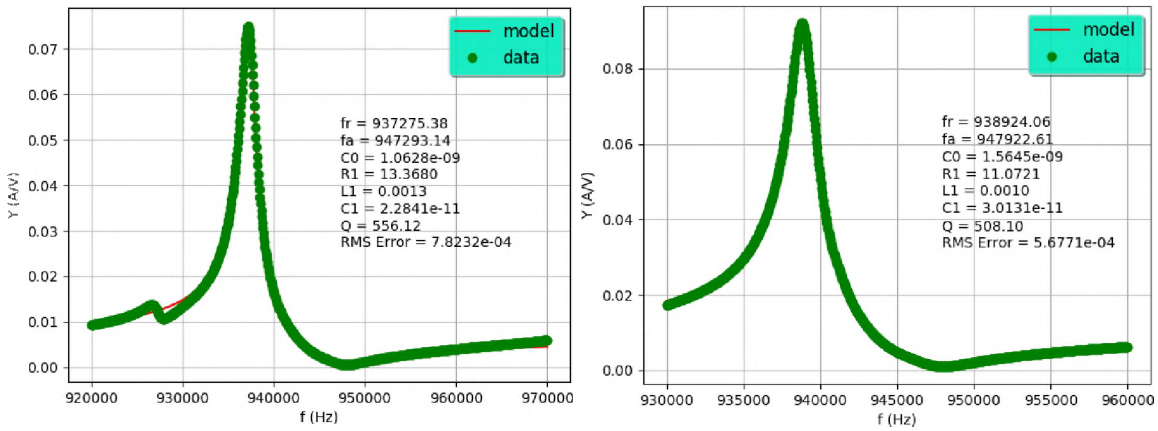

(a) Inner Ring - Mode 3 (b) Outer Ring - Mode 3

Figure 16. Impedance Spectrum Mode 3

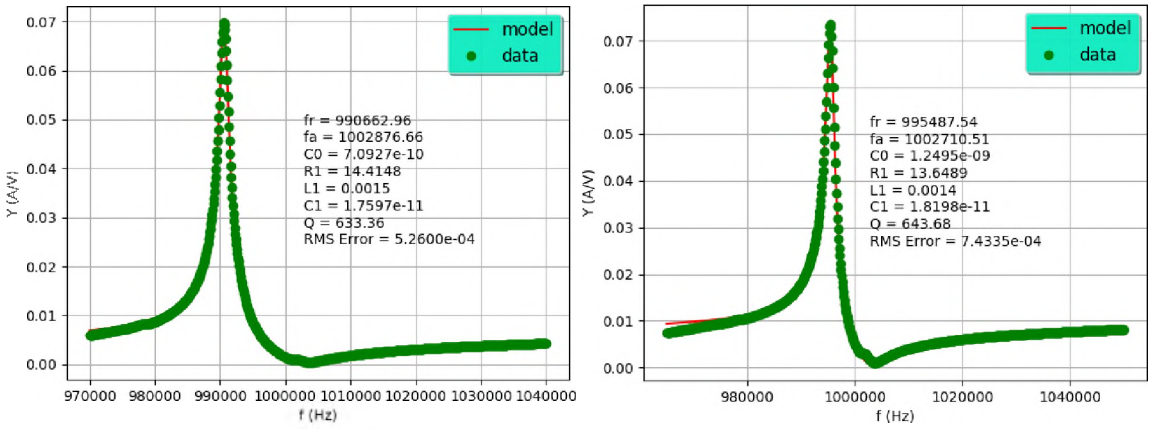

(a) Inner Ring - Mode 4 (b) Outer Ring - Mode 4

Figure 17. Impedance Spectrum Mode 4

3.2. RPS - RING MODES AFTER PROTOTYPE ASSEMBLY

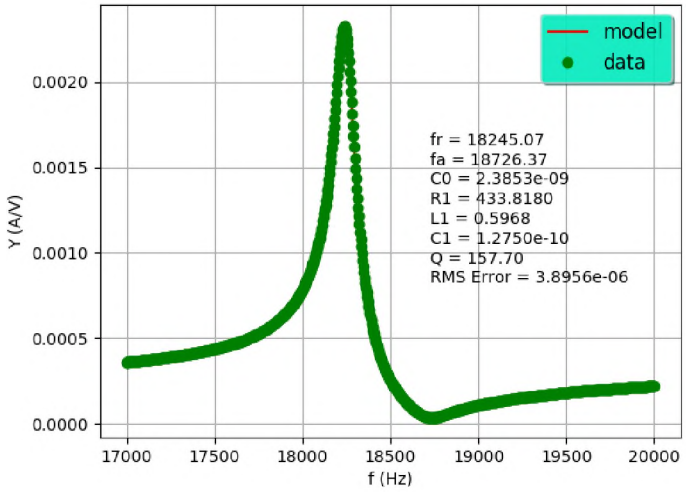

Figure 18. RPS Prototype Mode-1

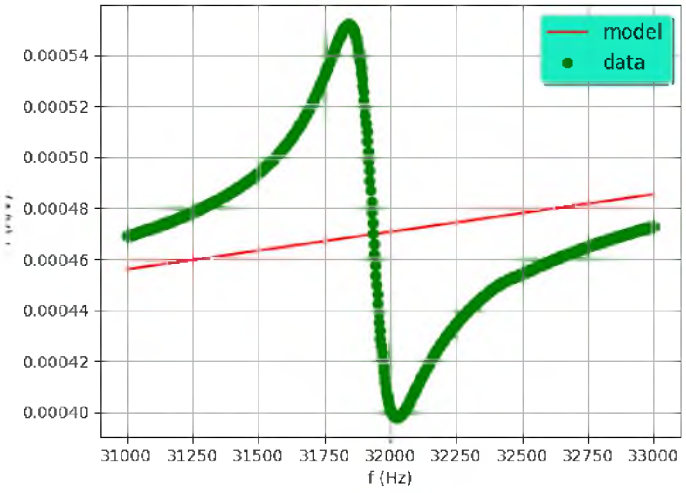

Figure 19. RPS Prototype Mode-2

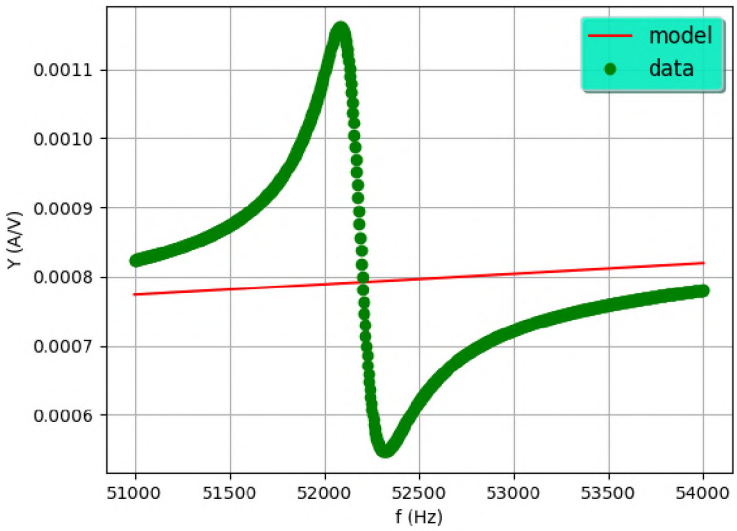

Figure 20. RPS Prototype Mode-3

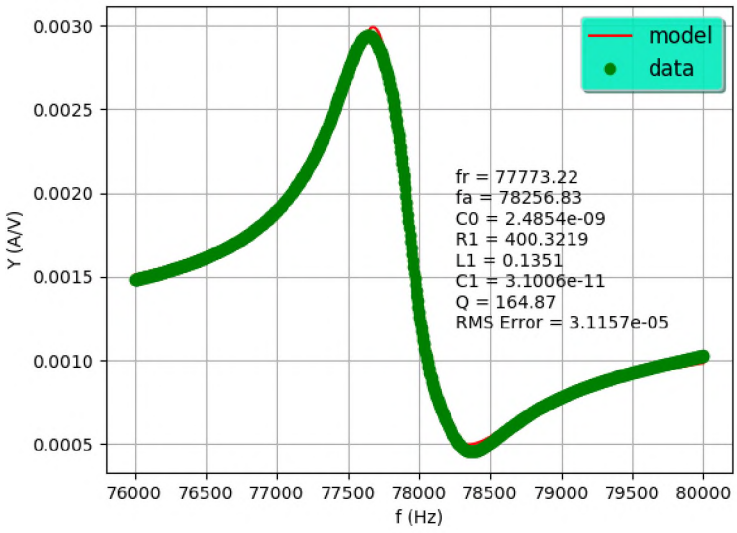

Figure 21. RPS Prototype Mode-4

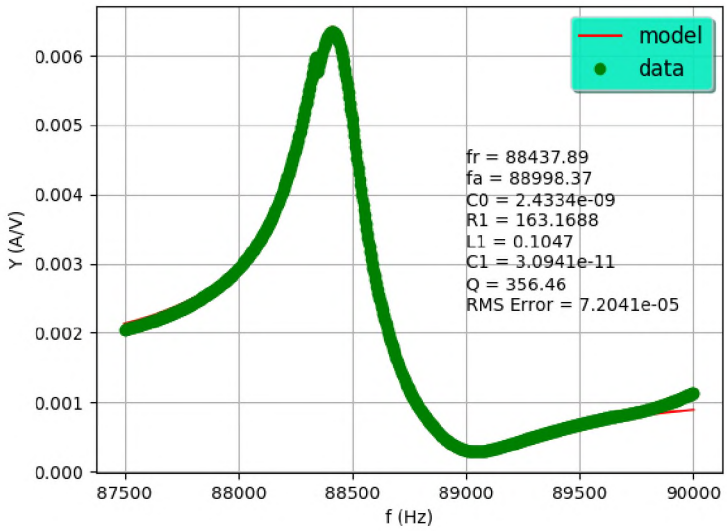

Figure 22. RPS Prototype Mode-5

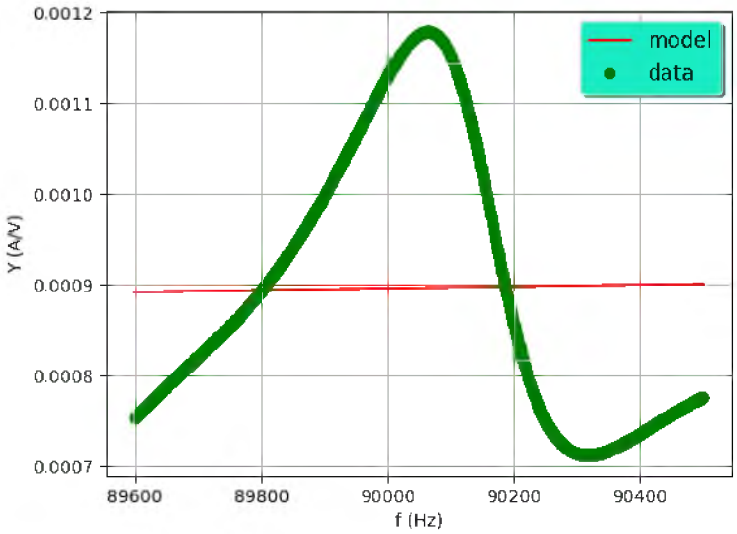

Figure 23. RPS Prototype Mode-6

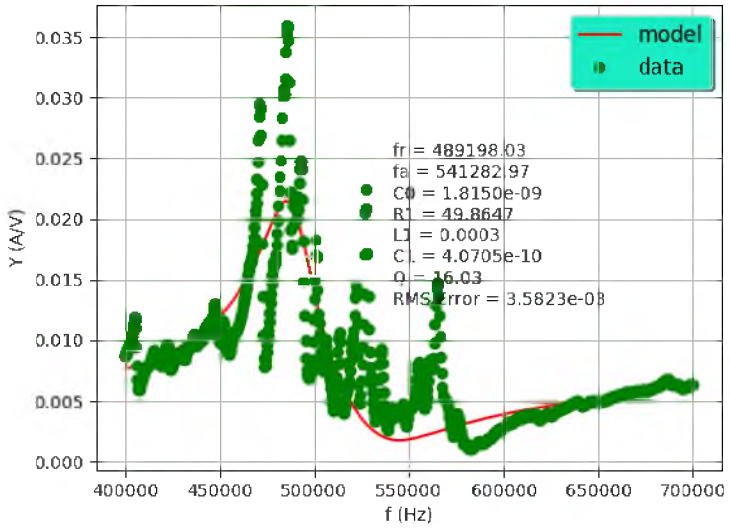

Figure 24. RPS Prototype Mode-7

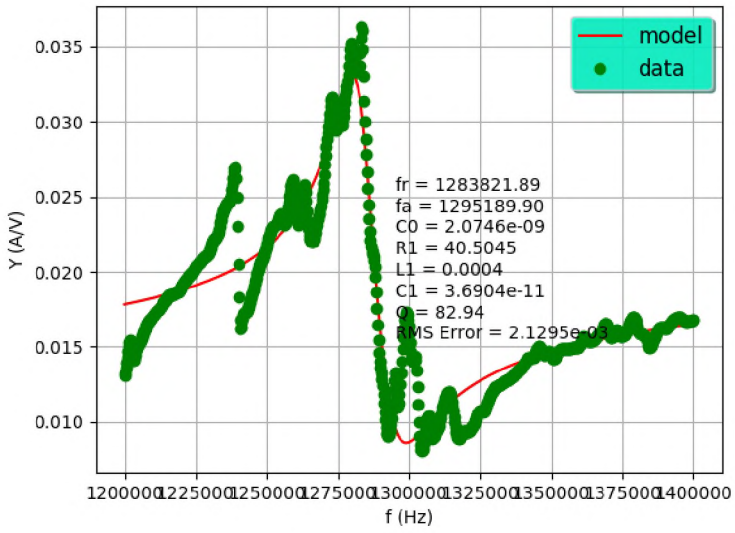

Figure 25. RPS Prototype Mode-8

3.3. RPS -RING MODES AFTER TESTING SINGLE FREQUENCY

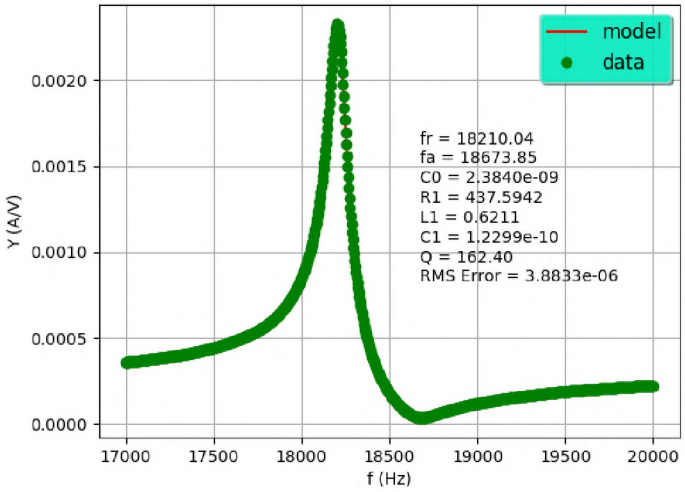

Figure 26. RPS Prototype Post Test-1 Mode-1

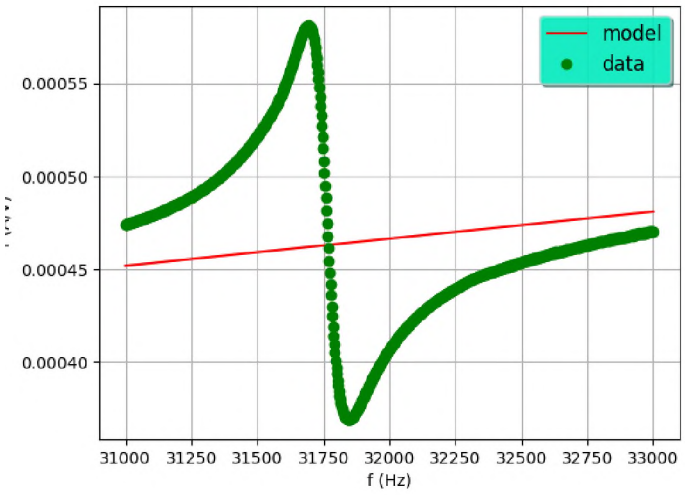

Figure 27. RPS Prototype Post Test-1 Mode-2

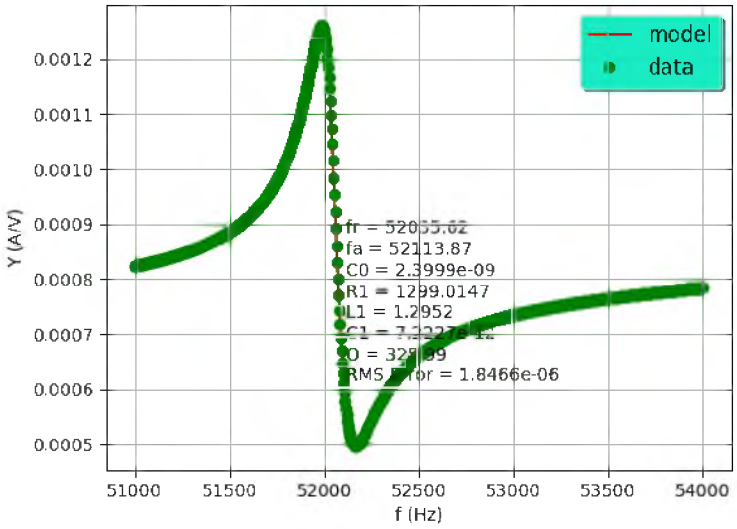

Figure 28. RPS Prototype Post Test-1 Mode-3

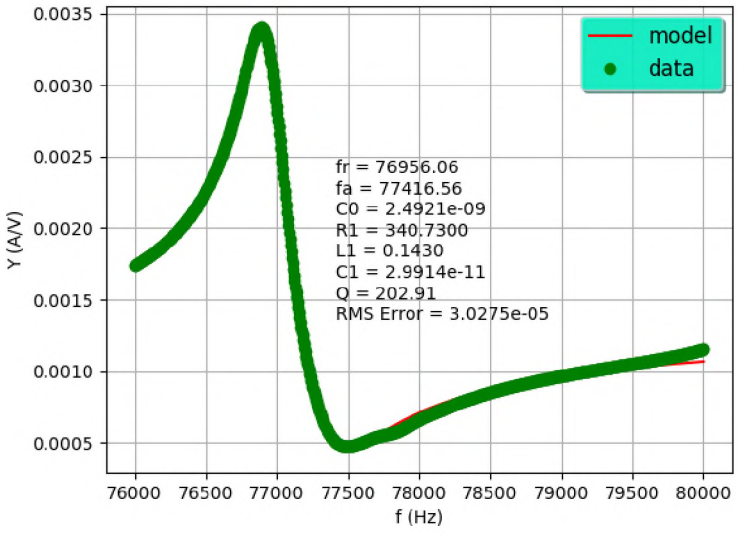

Figure 29. RPS Prototype Post Test-1 Mode-4

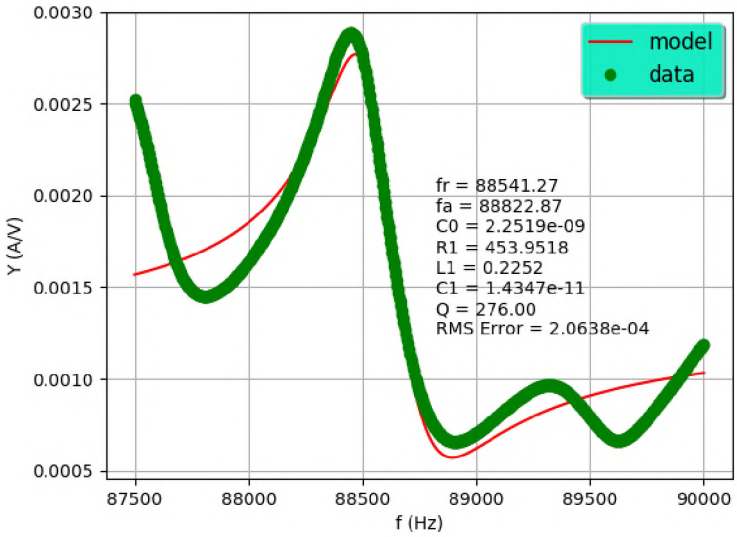

Figure 30. RPS Prototype Post Test-1 Mode-5

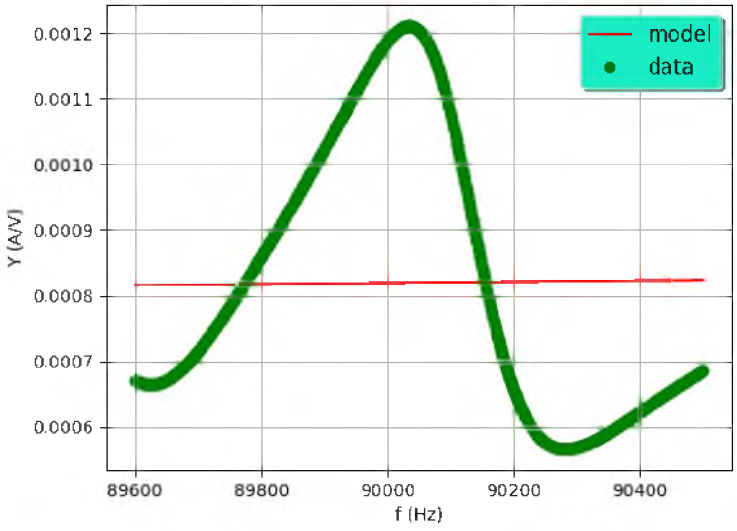

Figure 31. RPS Prototype Post Test-1 Mode-6

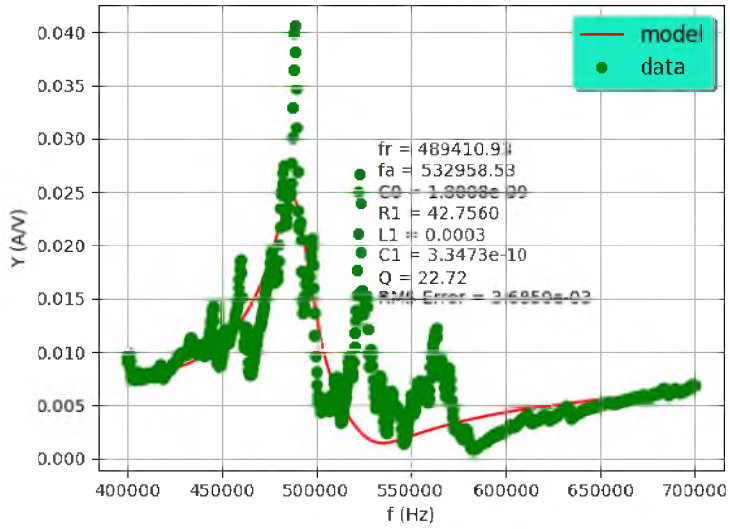

Figure 32. RPS Prototype Post Test-1 Mode-7

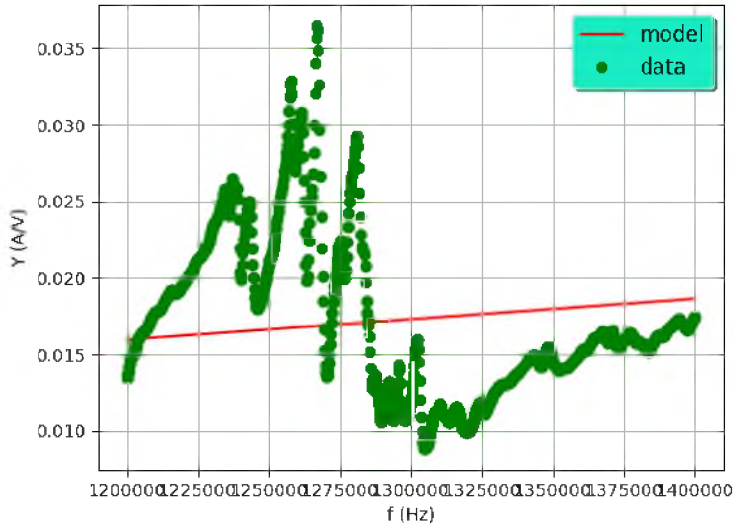

Figure 33. RPS Prototype Post Test-1Mode-8

3.4. RPS - RING MODES AFTER TESTING MULTI FREQUENCY

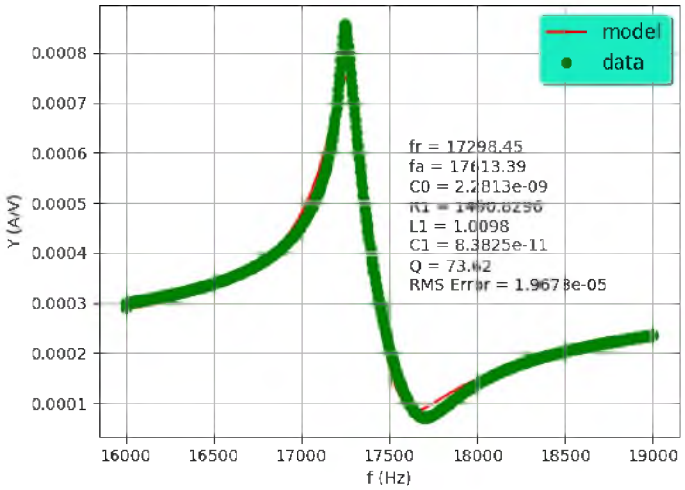

Figure 34. RPS Prototype Post Test-2/3 Mode-1

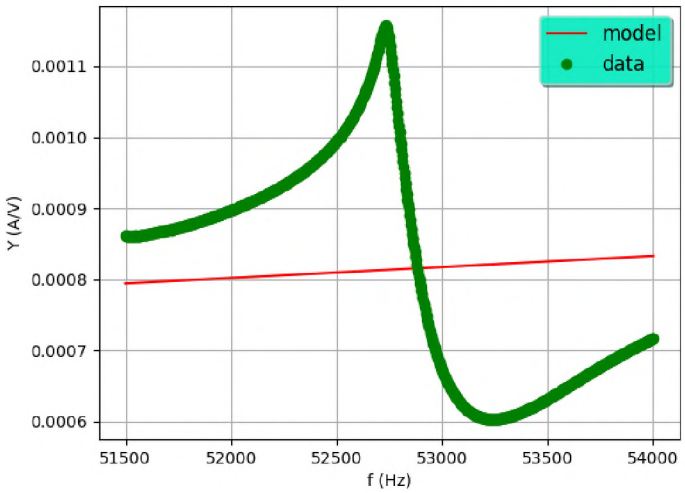

Figure 35. RPS Prototype Post Test-2/3 Mode-2

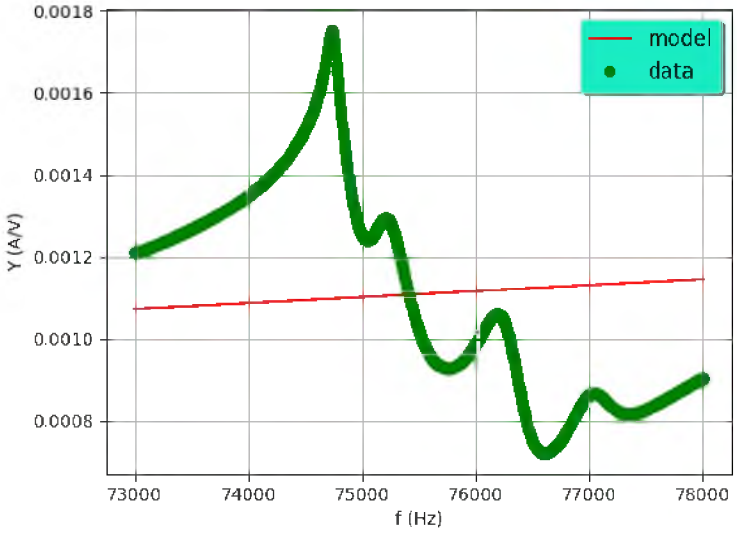

Figure 36. RPS Prototype Post Test-2/3 Mode-3

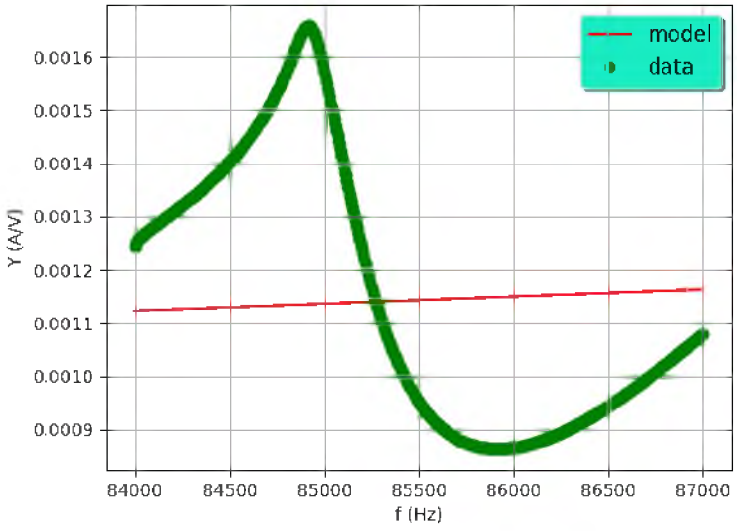

Figure 37. RPS Prototype Post Test-2/3 Mode-4

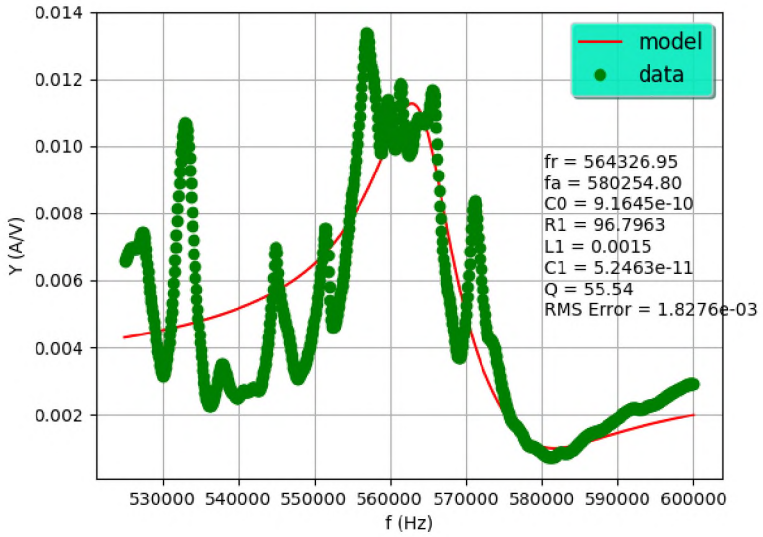

Figure 38. RPS Prototype Post Test-2/3 Mode-5

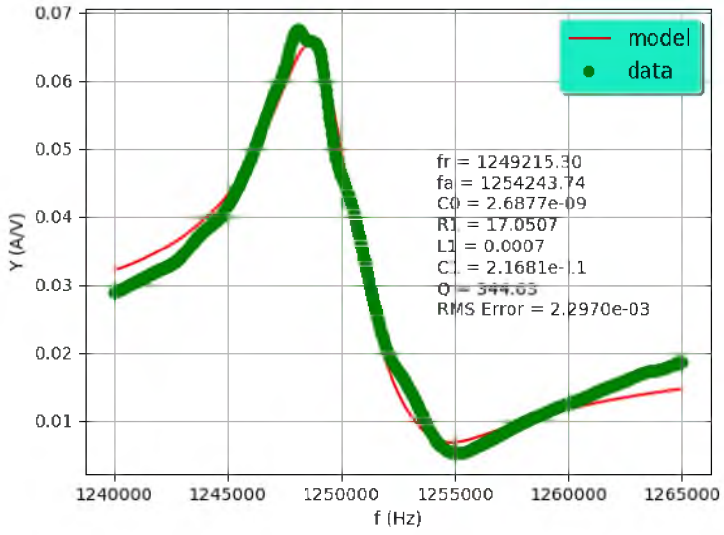

Figure 39. RPS Prototype Post Test-2/3 Mode-6

REFERENCES

[1] D. S. Stutts and Y. A. Anklesaria, "Lens Cleaner Project Phase I Report," 2015.

[2] R. A. Bowling, "An analysis of particle adhesion on semiconductor surfaces," *Journal of the Electrochemical Society*, vol. 132, pp. 2208–2214, 1985.

[3] K. Mittal, Ed., *Particles on Surface Detection, Adhesion, and Removal.* Springer, 1988.

[4] A. Busnaina and G. Gale, "Ultrasonic and megasonic particle removal," in *Precision Cleaning*, 1995, pp. 347–359.

[5] G. Kumar, S. Smith, R. Jaiswal, and S. Beaudoin, "Scaling of van der waals and electrostatic adhesion interactions from the micro- to the nano-scale," *Journal of Adhesion Science and Technology*, vol. 22, no. 5-6, pp. 407–428, 2008. [Online]. Available: https://doi.org/10.1163/156856108X305714

[6] O. R. Walton, "Adhesion of lunar dust," NASA, Tech. Rep. NASA/CR-2007-214685, 2007.

[7] S. Cravens, "Dynamic particle rejection on optical lenses using piezoelectric elements," Masters Thesis, 2011.

[8] A. J. James, B. Vukasinovic, M. K. Smith, and A. Glezer, "Vibration-induced drop atomization and bursting," *Fluid Mechanics*, vol. 476, pp. 1 – 28, 2003.

[9] T. D. Donnelly, J. Hogan, A. Mugler, N. Schommer, M. Schubmehl, A. J. Bernoff, and B. Forrest, "An experimental study of micron-scale droplet aerosols produced via ultrasonic atomization," *Physics of Fluids*, vol. 16, no. 8, pp. 2843 – 2851, August 2004.

[10] B. Vukasinovic, M. K. Smith, and A. Glezer, "Spray characterization during vibration-induced drop atomization," *Physics of Fluids*, vol. 16, no. 2, pp. 306–316, 2004. [Online]. Available: https://doi.org/10.1063/1.1632907

[11] A. Yule and Y. Al-Suleimani, "On droplet formation from capillary waves on a vibrating surface," in *Proceedings of the Royal Society of London A: Mathematical, Physical and Engineering Sciences*, vol. 456, no. 1997. The Royal Society, 2000, pp. 1069–1085.

[12] H. Krupp and G. Sperling, "Theory of adhesion of small particles," *Journal of Applied Physics*, vol. 37, no. 11, 1966.

[13] O. Walton, "Review of adhesion fundamentals for micron scale particles," *KONA Powder and Particle Journal*, no. 26, pp. 129–135, 2008.

[14] G. Brereton and B. Bruno, "Particle removal by focused ultrasound," *Journal of Sound and Vibration*, vol. 173, no. 5, pp. 683 – 698, 1994. [Online]. Available: http://www.sciencedirect.com/science/article/pii/S0022460X84712533

[15] H. Takizawa and S. Kawai, "Camera and image pick-up device unit having an optical member that is vibrated to remove dust," Patent US US7 280 145B2, 2002.

[16] S. Kawai, "Dust removal camera," Patent US US7 724 299B2, 2000.

[17] A. Qi, J. R. Friend, and L. Y. Yeo, "Investigation of saw atomization," in *2009 IEEE International Ultrasonics Symposium*, Sept 2009, pp. 787–790.

[18] ANSYS, *ANSYS Mechanical APDL Coupled-Field Analysis Guide*, 17th ed., 2016.

[19] ANSYS, *ANSYS Mechanical APDL Element Reference*, 14th ed., 275 Technology Drive, Canonsburg, PA 15317, Nov. 2011.

[20] ANSYS, *ANSYS Mechanical APDL Contact Technology Guide*, 17th ed., 2016.

[21] ANSYS, *ANSYS Mechanical APDL Theory Reference*, 17th ed., 275 Technology Drive, Canonsburg, PA 15317, November 2016.

[22] (2006, Jan.) Cornung eagle xg amlcd glass substratesmaterial information. [Online]. Available: http://www.delta-technologies.com/downloads/Eagle\%20XG.pdf

[23] J. Barber, *Elasticity*. Springer, 2010.

[24] A. C. Ugural, *Stresses in Beams, Plates, and Shells, Third Edition (Applied and Computational Mechanics)*. CRC Press, 2009.

[25] C. A. Klein, "Characteristic strength, weibull modulus, and failure probability of fused silica glass," *Optical Engineering*, vol. 48, no. 11, pp. 1 – 10 – 10, 2009. [Online]. Available: https://doi.org/10.1117/1.3265716

[26] A. Pandey, M. K. Singhal, J. Kovacich, and C. Rau, "Fatigue time-to-failure prediction methodology for glass (fused quartz) material under cyclic loading," in *SAE 2016 World Congress and Exhibition*. SAE International, apr 2016. [Online]. Available: https://doi.org/10.4271/2016-01-0388

[27] Steiner & martins inc. pzt sm412 material properties. [Online]. Available: http://www.steminc.com/piezo/PZ_property.asp

[28] (2017) EPO-TEK 353-ND. [Online]. Available: http://www.epotek.com/site/administrator/components/com_products/assets/files/Style_Uploads/353ND.pdf

[29] (2007) EPO-TEK 301-2FL. [Online]. Available: http://www.epotek.com/site/administrator/components/com_products/assets/files/Style_Uploads/301-2FL.pdf

[30] (2017) EPO-TEK 323LP. [Online]. Available: http://www.epotek.com/site/administrator/components/com_products/assets/files/Style_Uploads/323LP.pdf

[31] (2015) EPO-TEK 353-ND. [Online]. Available: http://www.epotek.com/site/administrator/components/com_products/assets/files/Style_Uploads/H20E.pdf

[32] T. P. INC. (2009) Pelco colloidal silver product numbers. 16031, 16034. [Online]. Available: https://www.tedpella.com/technote_html/16031,%2034%20TN.pdf

[33] ElectroScience ESL 9912-MM. [Online]. Available: http://www.electroscience.com/sites/default/files/datasheets/9912-MM.pdf

[34] J. Friend and D. Stutts. (1995) Bonding suggestions for the piezoelectric motor system. [Online]. Available: http://web.mst.edu/~piezo/MotorAnalysis/BondingNote/BondingNote.html#fn0

[35] Aim sn 100c. [Online]. Available: https://www.aimsolder.com/sites/default/files/alloy_sn100c_tds.pdf

[36] Kester-331. [Online]. Available: https://www.kester.com/products/product/331-flux-cored-wire

[37] Thermoflow-tf604016. [Online]. Available: https://www.americanradiosupply.com/thermoflow-qq-200-lead-free-solder-tf604016-1lb-roll/

[38] Kester-2331-zx. [Online]. Available: https://www.kester.com/products/product/2331-zx-soldering-flux

[39] Kester-951. [Online]. Available: https://www.kester.com/products/product/951-soldering-flux

[40] Ruby fluid. [Online]. Available: http://rubyfluidflux.com/uploads/TDS_RubyFluid.pdf

[41] A. Meitzler, H. Tiersten, A. Warner, D. Berlincourt, G. Couqin, and F. Welsh III, "IEEE standard on piezoelectricity," 1988.

[42] J. Friend and D. Stutts, "The dynamics of an annular piezoelectric motor stator," *Journal of Sound and Vibration*, vol. 204, no. 3, pp. 421 – 437, 1997. [Online]. Available: http://www.sciencedirect.com/science/article/pii/S0022460X9690944X

[43] T. Sashida and T. Kenjo, "An introduction to ultrasonic motors," 1994.

[44] S. Ueha, Y. Tomikawa, M. Kurosawa, and N. Nakamura, *Ultrasonic Motors: Theory and Applications*, ser. Monographs in electrical and electronic engineering. Clarendon Press, 1993. [Online]. Available: https://books.google.com/books?id=gOlSAAAAMAAJ

[45] W. Soedel, *Vibrations of shells and plates*, ser. @Mechanical engineering. New York: Dekker, 1981, no. 10.

[46] W. Soedel and D. Powder, "A general dirac delta function method for calculating the vibration response of plates to loads along arbitrarily curved lines," *Journal of Sound and Vibration*, vol. 65, no. 1, pp. 29–35, 1979.

[47] H. Tzou, *Piezoelectric Shells Sensing, Energy Harvesting, and Distributed Control*, 2nd ed., G. M. L. Gladwell, Ed. Springer, 2019, vol. 247.

VITA

Yezad H. Anklesaria was born in Mumbai, India, to Hoshang and Katty Anklesaria on November 24, 1984. Yezad graduated from Patuck Jr.College in June 2002, and enrolled in Shri Bhagubhai Maftlal Polytechnic and received the Diploma in Mechanical Engineering. He then joined the undergraduate program in Aerospace Engineering at the University of Missouri-Rolla (now the Missouri University of Science and Technology) and received his Bachelors of Science degree in July of 2009. Following that, he continued his education at Missouri S&T in pursuit of his Masters of Science in Aerospace Engineering, receiving the degree in July 2012. In May 2021, he received his PhD degree in Aerospace Engineering from Missouri S&T. Yezad was a member of the Missouri S&T Satellite Research team and co-founded the Balloon Satellite Program. He was also the Vice President of the International Students' Club, Event Coordinator for the India Association, Graduate Teaching Assistant for the Mechanical Engineering Mechanical Systems Laboratory, and Multimedia Technician at the C. L. Wilson Library Multimedia Center.